



HAL
open science

Dual-rotation C-arm cone-beam tomographic acquisition and reconstruction frameworks for low-contrast detection in brain soft-tissue imaging

Aymeric Reshef

► To cite this version:

Aymeric Reshef. Dual-rotation C-arm cone-beam tomographic acquisition and reconstruction frameworks for low-contrast detection in brain soft-tissue imaging. Medical Imaging. Télécom ParisTech, 2018. English. NNT: 2018ENST0044 . tel-02077743v2

HAL Id: tel-02077743

<https://hal.science/tel-02077743v2>

Submitted on 27 Apr 2021

HAL is a multi-disciplinary open access archive for the deposit and dissemination of scientific research documents, whether they are published or not. The documents may come from teaching and research institutions in France or abroad, or from public or private research centers.

L'archive ouverte pluridisciplinaire **HAL**, est destinée au dépôt et à la diffusion de documents scientifiques de niveau recherche, publiés ou non, émanant des établissements d'enseignement et de recherche français ou étrangers, des laboratoires publics ou privés.



EDITE - ED 130

Doctorat ParisTech

THÈSE

pour obtenir le grade de docteur délivré par

TELECOM ParisTech

Spécialité « Signal et Images »

présentée et soutenue publiquement par

Aymeric RESHEF

le 25 septembre 2018

Dual-rotation C-arm cone-beam tomographic acquisition and reconstruction frameworks for low-contrast detection in brain soft-tissue imaging

Directrice de thèse : Pr. **Isabelle BLOCH**

Co-encadrement de la thèse :

Saïd Ladjal, TELECOM ParisTech **Cyril RIDDELL**, GE Healthcare

Jury

M. Emil SIDKY, Professeur, University of Chicago (USA)

M. Laurent DESBAT, Professeur, TIMC-IMAG, Université Grenoble-Alpes (La Tronche)

Mme Irène BUVAT, Directeur de recherche, Laboratoire IMIV, Inserm/CEA (Orsay)

M. Dimitris VISVIKIS, Directeur de recherche, LaTIM, Inserm U1101 (Brest)

M. Saïd LADJAL, Maître de conférences, TELECOM ParisTech (Paris)

M. Cyril RIDDELL, Ingénieur de recherche, GE Healthcare (Buc)

Rapporteur

Rapporteur

Examinatrice

Président du Jury

Examineur

Examineur

TELECOM ParisTech

École de l'Institut Mines-Télécom - Membre de ParisTech

Et de là sortant, nous revîmes
les étoiles.

Dante, *La Divine Comédie*

On m'a dit qu'après avoir rédigé mon manuscrit de thèse, le plus dur serait fait. C'est inexact. En réalité, le plus dur est de trouver la formule pour remercier tous ceux qui, de près ou de loin, m'ont accompagné jusqu'ici.

Une thèse n'est rien sans son encadrement, et à ce titre je remercie les personnes qui ont pris part à ce travail : Cyril, Yves, Saïd, Isabelle, cette expérience eût été bien différente sans vous ! Je suis reconnaissant aux membres du jury d'avoir pris le temps de lire et de commenter mes travaux de recherche : merci donc à Dimitris Visvikis, Irène Buvat, Laurent Desbat, et Emil Sidky, pour vos relectures bienveillantes.

J'ai passé le plus clair de mon temps de travail à GE Healthcare à Buc. Je remercie l'équipe qui m'a accueilli là-bas : Michel Grimaud a été mon manager au début de ma thèse, et je le remercie de m'avoir reçu dans son équipe. Valérie Desnoux a ensuite été manager de cette équipe, et je la remercie de m'avoir gardé jusqu'au bout de mon contrat ! Mes remerciements s'étendent à l'ensemble des ingénieurs permanents, consultants, doctorants, et stagiaires, qui ont partagé mon quotidien. J'ai eu le bonheur de rejoindre une autre équipe juste après mon contrat de thèse, et c'est auprès d'elle que j'ai achevé la rédaction de ce manuscrit. Je remercie chaleureusement Didier Verot, ainsi que toute son équipe, pour m'avoir si bien accueilli dans cette équipe Qualité Image.

Un grand merci aux amis de toujours, aux amis d'enfance, aux amis de lycée : ne changez rien, j'ai encore besoin de vos grains de folie ! Un grand merci à vous qui avez brouillé les frontières entre collègues et amis : sans vous, les "perfect weeks" n'existeraient pas, pas plus que mes excès de cafés résultant de nos pauses interminables mais (disons-le) salutaires ! Un merci immense également à l'Atelier Vermeer, à tous les peintres formidables auprès de qui j'ai pu m'évader pendant la thèse. Quoi qu'on en dise, si cette thèse est écrite et soutenue aujourd'hui, c'est en grande partie grâce à vous.

Des noms de professeurs traversent aussi mon esprit : professeurs de mathématiques, d'histoire, de grec ancien, et tant d'autres, soyez remerciés !

Cette thèse a bénéficié d'un financement dans le cadre des bourses CIFRE. Si elle avait eu d'autres sponsors, nul doute que l'on aurait pu nommer : (i) l'Adada, pour tous ces afterworks passés là-bas, pour les Miam's et les Ralph, pour la bonne ambiance qui y règne, et pour les bières que l'on y boit ; (ii) le café Caron (et avant lui, Selecta), sans qui toutes nos pauses au travail n'auraient pas pu avoir lieu.

Enfin, et avant toute chose, un merci chaleureux à ma famille : ce travail lui est dédié.

Table of contents

List of Figures	vii
List of Tables	xi
1 Interventional neuroradiology: a clinical context	1
1.1 Pathologies and treatments	2
1.1.1 Restoring blood flow	2
1.1.1.1 Balloon angioplasty and stent	2
1.1.1.2 Mechanical thrombectomy	3
1.1.2 Aneurysm coiling	4
1.1.3 Embolization of arteriovenous malformation	5
1.2 Enabling INR procedures with imaging	6
1.2.1 Pre-operative imaging	6
1.2.2 Per-operative imaging: the INR suite	9
1.2.2.1 2D imaging	10
1.2.2.2 3D imaging	11
1.3 Goal of this thesis	13
1.3.1 Contributions	13
1.3.2 Thesis outline	14
2 Imaging with C-arm systems	17
2.1 2D X-ray imaging	18
2.1.1 System description	18
2.1.2 X-ray production	21
2.1.2.1 Bremsstrahlung	21
2.1.2.2 Characteristic radiations	22
2.1.2.3 Off-focal radiation, collimation	23
2.1.3 X-ray attenuation	24
2.1.3.1 Interactions with matter	24

2.1.3.2	Beer's law	25
2.1.3.3	Intensities, dose	25
2.1.3.4	Polychromaticity and beam hardening	26
2.1.4	Image formation	28
2.1.4.1	Primary intensities, scattered intensities	28
2.1.4.2	Flat-panel detector technology	28
2.1.5	Real-time image guidance	29
2.1.5.1	Imaging modes	29
2.1.5.2	Field of view and binned modes	30
2.1.5.3	Exposure management	30
2.1.6	Artifacts	31
2.1.6.1	Scattered intensities	31
2.1.6.2	Non-uniform pixel response	32
2.2	3D X-ray imaging	33
2.2.1	Principles of circular computed tomography	34
2.2.1.1	Geometries	34
2.2.1.2	Filtered backprojection	38
2.2.1.3	Semi-discrete formulation	39
2.2.1.4	Iterative reconstruction	40
2.2.2	Image quality assessment	42
2.2.2.1	The Catphan [®] 500 phantom	42
2.2.2.2	Spatial resolution	43
2.2.2.3	Contrast resolution	43
2.2.3	Factors impacting low-contrast detection in C-arm CBCT	45
2.2.3.1	Quantum noise	45
2.2.3.2	Detector non-idealities	45
2.2.3.3	X-ray beam	46
2.2.3.4	Scatter	47
2.2.3.5	Sampling	49
2.2.4	Discussion	50
3	Virtual bow-tie C-arm CBCT	53
3.1	A matter of noise	54
3.1.1	Impact of analog-to-digital conversion	54
3.1.1.1	Principle of analog-to-digital conversion	54
3.1.1.2	Ramp-based quantization	55
3.1.1.3	Actual ramp-based ADC	57
3.1.1.4	Quantization and low-contrast detection	58
3.1.2	Influence of dose increase	60
3.1.2.1	Experiments and results	60
3.1.2.2	Conclusion	60
3.2	Virtual bow-tie via the dual-rotation framework	62
3.2.1	Acquisition	62
3.2.1.1	Assumptions	62
3.2.1.2	Parameters	63
3.2.1.3	Virtual bow-tie	64

3.2.2	Reconstruction	64
3.2.2.1	Analytical reconstruction	64
3.2.2.2	Energy minimization	65
3.2.2.3	Ramp filtering operators	65
3.2.3	Experiments	66
3.2.3.1	Simulations	66
3.2.3.2	Acquisitions, reconstructions	66
3.2.3.3	Image quality measures	67
3.2.4	Results	69
3.2.4.1	Simulations	69
3.2.4.2	Real phantom data	69
3.3	Discussion and conclusion	75
4	Direct reconstruction for virtual bow-tie C-arm CBCT	77
4.1	Filtered backprojection, backprojection-filtration	78
4.1.1	Challenges of dual-rotation direct reconstruction	78
4.1.2	Backprojection-filtration methods: a literature review	78
4.2	K -pass Hilbert-transformed DBP (DBP-HT- K)	80
4.2.1	Parallel-beam case	80
4.2.1.1	Notations	80
4.2.1.2	Angular splitting	81
4.2.1.3	Differentiated backprojection	84
4.2.2	Divergent-beam case	85
4.2.2.1	Resampling formula for the fan-beam case	85
4.2.2.2	Semi-discrete fan-beam BPF formula	86
4.2.2.3	Extension to C-arm CBCT	88
4.2.3	Simulations	89
4.2.3.1	Planar geometries	89
4.2.3.2	CBCT reconstruction of a uniform cylinder	91
4.2.3.3	CBCT reconstruction of a head	93
4.3	Application to virtual bow-tie C-arm CBCT	96
4.3.1	Principle	96
4.3.2	Validation on phantom acquisitions	97
4.3.2.1	Experiments	97
4.3.2.2	Results	98
4.4	Discussion	103
4.5	Proofs of the theorems	104
4.5.1	Proof of Theorem 4.2.1	104
4.5.2	Proof of Theorem 4.2.3	104
4.5.3	Proof of Theorem 4.2.4	105
4.5.4	Proof of Theorem 4.2.6	108
4.5.5	Proof of Theorem 4.2.7	108

5	From virtual bow-tie to region-of-interest C-arm CBCT	111
5.1	Challenges of ROI imaging	112
5.1.1	ROI imaging: a literature review	112
5.1.1.1	<i>A priori</i> knowledge	113
5.1.1.2	Knowledge from additional data	116
5.1.2	Proposed dual-rotation acquisition	117
5.2	Iterative reconstruction	118
5.2.1	Adapting the virtual bow-tie framework	118
5.2.2	Experiments and results	118
5.2.2.1	Catphan [®] CTP 515	118
5.2.2.2	Uniform head phantom	120
5.2.3	Discussion	122
5.3	Direct reconstruction	122
5.3.1	Adapting the Hilbert-transformed DBP	122
5.3.1.1	Hilbert-transformed DBP and angular sampling	122
5.3.1.2	Experiments	125
5.3.1.3	Results	126
5.3.1.4	Discussion	127
5.3.2	View-wise BPF solution	129
5.3.2.1	Standard scheme	129
5.3.2.2	Sped-up reconstruction through a dual-resolution strategy	130
5.3.2.3	Experiments	131
5.3.2.4	Results	132
5.4	Discussion	140
6	Conclusion	141
6.1	Outcomes of this work	141
6.2	Perspectives	143
6.2.1	Engineering perspectives	143
6.2.2	Theoretical perspectives	144
6.2.2.1	Improved scatter correction	144
6.2.2.2	Applications of DBP-HT- <i>K</i>	145
A	Proof of the fan-beam DBP-HT formula	149
A.1	Step 1: find the actual differentiated function	149
A.2	Step 2: find the residual integral	151
A.3	Step 3: deduce the corrective terms	152
B	Publications	155
B.1	Journals (with review committee)	155
B.2	Conferences (with review committee)	155
B.3	Invited talk	156
B.4	Supervised Master's theses	156

C	French summary	157
C.1	Contexte clinique	157
C.2	Imagerie sur arceau interventionnel	159
C.2.1	Généralités et imagerie 2D	159
C.2.2	Imagerie 3D	160
C.2.3	Qualité image des faibles contrastes	161
C.3	Bow-tie virtuel en tomographie conique rayons X	162
C.3.1	Une question de bruit	162
C.3.2	Bow-tie virtuel par rotation double	163
C.4	Une reconstruction directe pour le bow-tie virtuel	165
C.4.1	Rétro-projection différenciée à K passes de Hilbert	165
C.4.2	Application au bow-tie virtuel	167
C.5	Du bow-tie virtuel à l'imagerie de régions d'intérêt	168
C.5.1	Reconstruction itérative	168
C.5.2	Reconstruction directe	169
C.6	Conclusion	170
C.6.1	Contributions	170
C.6.2	Perspectives	171
Bibliography		173

List of Figures

1.1	Carotid artery stenting of a stenosis	2
1.2	Stroke frequency by mechanism	3
1.3	Medtronic's Solitaire™ Platinum revascularization device	4
1.4	Aneurysm coiling	5
1.5	Arteriovenous malformation (AVM) embolization	6
1.6	The Revolution CT scanner (GE Healthcare, Chicago, IL, USA)	7
1.7	Influence of windowing on image visualization	8
1.8	NECT to detect signs of bleeding and ischemic stroke events	9
1.9	Example of INR suite	10
1.10	C-arm biplane system for INR procedures	12
1.11	Volume rendering of a 3D DSA	13
1.12	Performance comparison between diagnostic CT and C-arm CBCT for soft-tissue imaging	14
2.1	Photographs of commercially available C-arm systems	19
2.2	Main components of a 2D X-ray imaging system	20
2.3	GE Healthcare IGS 730 monoplane system	20
2.4	Coolidge X-ray tube	21
2.5	Schematic of an X-ray spectrum produced by an X-ray tube	22
2.6	Illustration of off-focal radiation	23
2.7	Contribution of coherent scattering, Compton scattering and photo- electric effect to the total attenuation	24
2.8	Examples of linear attenuation coefficients as a function of the photon energy	26
2.9	Attenuation of an X-ray spectrum through different thicknesses of copper	27
2.10	Contribution of scattered radiations to the image formation	27
2.11	Photograph of GE Innova 4100 flat-panel detector	28
2.12	Indirect conversion detector steps	29

2.13	Toy example for contrast loss in presence of scatter	31
2.14	Non-uniform flat-panel detector pixel response correction	33
2.15	3D cone-beam computed tomography on a C-arm system	35
2.16	Parallel-beam circular tomographic acquisition geometry	36
2.17	Divergent-beam circular tomographic acquisition geometries	37
2.18	Cone-beam artifact reduction with iFDK	41
2.19	The Catphan [®] 500 phantom	42
2.20	IGS 740 C-arm CBCT of the Catphan [®] CTP 528 module	43
2.21	Comparison between an IGS 740 C-arm CBCT and a diagnostic CT of the Catphan [®] CTP 515 module	44
2.22	Factors impacting low-contrast detection in C-arm CBCT	44
2.23	Illustration of a bow-tie filter	47
2.24	Influence of scatter on image quality	48
3.1	Example of a quadratic ramp	56
3.2	Actual ADC conversion	57
3.3	Effect of quantization on low-contrast detection	59
3.4	Influence of dose on low-contrast detection of a Catphan [®] CTP 515	61
3.5	Dual-rotation acquisition	63
3.6	Single- and dual-rotation reconstructions of the Catphan [®] 528 spatial resolution module	68
3.7	Simulation setting in parallel-beam geometry	69
3.8	Simulation of equivalent noise distribution in dual-rotation	70
3.9	Full-volume single- and dual-rotation iterative reconstruction	72
3.10	Noise radial standard deviation for the single- and dual-rotation reconstructed images of the CTP 515	73
3.11	Comparison between dual-rotation CBCT and diagnostic CT	73
3.12	Reconstructed images from acquisitions with a wider 3D FOV height	74
3.13	Iterative reconstructions of the soft-tissue head phantom	74
4.1	Backprojection-filtration over an angular subset	82
4.2	Extended support for filtering a backprojection over an angular subset	83
4.3	General reconstruction flowchart for the splitting BPF method	84
4.4	Practical BPF reconstruction	85
4.5	Parallel-beam reconstructions of a uniform disk	90
4.6	Fan-beam reconstructions of a uniform disk from 1440 views uniformly spread over 360°	90
4.7	Fan-beam reconstructions of a uniform disk from 45 views uniformly spread over 360°	91
4.8	CBCT direct reconstruction of a uniform cylinder	92
4.9	CBCT direct reconstruction of a numerical Defrise phantom	93
4.10	Noise-free CBCT direct reconstruction of a head	94
4.11	Noisy CBCT direct reconstruction of a head	95
4.12	General dual-rotation direct reconstruction flowchart	97
4.13	Dual-rotation direct reconstruction of a head	99
4.14	Dual-rotation direct reconstruction of a head: relative errors	100

4.15	Dual-rotation direct reconstruction of the CTP 515 LCD module	101
4.16	Dual-rotation direct reconstruction of the head phantom	102
5.1	Truncation in ROI imaging	112
5.2	Padding, truncation and Fourier-based filtering	114
5.3	Dual-rotation ROI imaging of the Catphan [®] 515 module	119
5.4	Dual-rotation ROI imaging: deviations from the mean line profile values	120
5.5	Dual-rotation ROI imaging of a head phantom consisting of a skull with uniform soft tissues	121
5.6	Deviations from mean profile values along the line profile from Figure 5.5	121
5.7	Angular sampling, resolution and image support	124
5.8	Hilbert-transformed DBP-based dual-rotation reconstruction for ROI imaging	126
5.9	Dual-rotation reconstruction with DBP-HT without and with optimal smoothing of DBP _F	128
5.10	Merging step in dual-rotation ROI direct reconstruction	129
5.11	Flowchart of the multiresolution dual-rotation direct reconstruction	130
5.12	Mean relative error as a function of the number of full-FOV projections	132
5.13	Dual-rotation direct reconstruction for ROI imaging: circular, full-scan, fan-beam geometry with linear detector	133
5.14	Dual-rotation direct reconstruction for ROI imaging: circular, full-scan, cone-beam geometry with flat-panel detector	135
5.15	Dual-rotation direct reconstruction of a head: relative errors	136
5.16	Mean relative error as a function of the angular sampling and the resolution of the backprojection of the full-FOV projections	137
5.17	ROI direct reconstruction of the Catphan [®] 515 LCD module using different resolution factors for the full-FOV, subsampled spin	137
5.18	ROI reconstruction using two additional full-FOV projections	138
5.19	ROI reconstruction of a clinical C-arm CBCT acquisition of a head using 37 additional full-FOV projections	139
6.1	Improved scatter correction using dual-rotation acquisitions	144
6.2	Influence of out-of-FOV structures on FDK and DBP-HT-2	146
6.3	General flowchart for dynamic ROI update	147

List of Tables

2.1	Detector sizes for different clinical fields	28
2.2	Available binning modes for each FOV and each detector size	30
2.3	Tomographic acquisition parameters of IGS 7x systems	33
3.1	Ramp specifications in IGS 540 (CBCT modes)	58
3.2	CNR of single- and dual-rotation reconstructions of the CTP 515 . .	67
3.3	Dose-area products	71
4.1	Operator $F^{(n)}$ and the corresponding formulation of the $F_{\alpha}^{(n)}$	82
5.1	Optimal smoothing parameter σ and corresponding MRE for each angular subsampling ratio s	127

Interventional neuroradiology: a clinical context

This introductory chapter presents the clinical context of this thesis. It describes the main pathologies and treatments in interventional neuroradiology, and shows how imaging modalities are used in this context. The observation that 3D X-ray imaging with C-arm systems performs poorly compared to diagnostic X-ray computed tomography (CT) in terms of head soft-tissue imaging, is at the origin of this work, whose goals are given at the end of this chapter.

Contents

1.1 Pathologies and treatments	2
1.1.1 Restoring blood flow	2
1.1.1.1 Balloon angioplasty and stent	2
1.1.1.2 Mechanical thrombectomy	3
1.1.2 Aneurysm coiling	4
1.1.3 Embolization of arteriovenous malformation	5
1.2 Enabling INR procedures with imaging	6
1.2.1 Pre-operative imaging	6
1.2.2 Per-operative imaging: the INR suite	9
1.2.2.1 2D imaging	10
1.2.2.2 3D imaging	11
1.3 Goal of this thesis	13
1.3.1 Contributions	13
1.3.2 Thesis outline	14

Interventional radiology (Wible, 2017) refers to minimally invasive image-based technologies and procedures used in the diagnosis and treatment of diseases by inserting devices directly in the vascular system or by inserting needles inside the body to reach the location of the intervention. This discipline bridges the

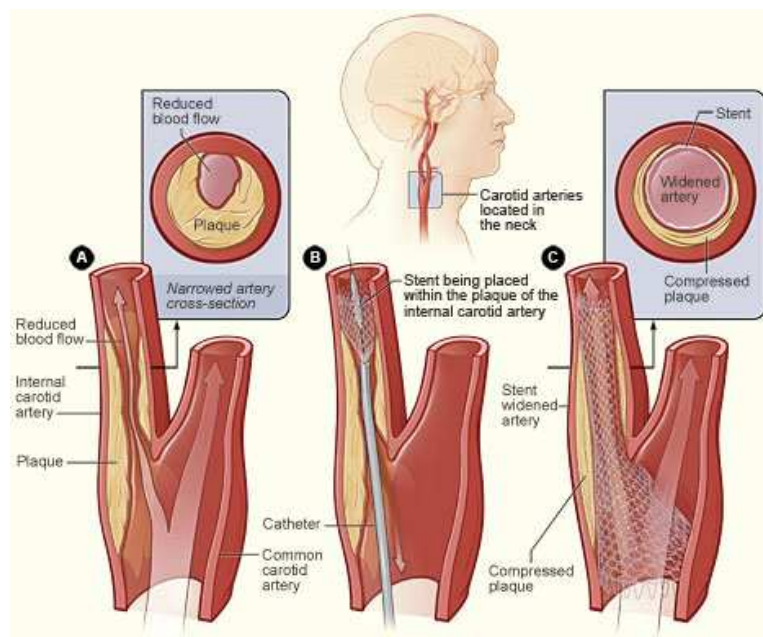


Figure 1.1 – Carotid artery stenting of a stenosis (National Heart, Lung and Blood Institute, 2018).

gap between pre-operative diagnostic steps and surgical procedures that are more invasive for the patient.

Interventional neuroradiology (INR) focuses on diseases of the head, neck and spine. In the following, we describe the main vascular diseases and interventional procedures involved in INR. All interventional procedures listed below require the clinician to insert a thin guidewire from the access point (typically, the femoral artery in the groin) to the location of the pathology via the arterial tree. A thin flexible tube, called a catheter, is then pushed over the wire and navigated through the blood vessels until it reaches the vascular territory of interest. Contrast agent and therapeutic devices are brought through the catheter, depending on the procedure.

1.1 Pathologies and treatments

1.1.1 Restoring blood flow

1.1.1.1 Balloon angioplasty and stent

A *stenosis* is a narrowing of a vessel that may even lead to vessel obstruction. In case of a calcified arterial stenosis, the narrowing is due to atherosclerotic plaques on the inner walls of arteries (Figure 1.1). In a first stage, the vessel wall enlarges to include the presence of deposit, while keeping a normal cross section size, thus maintaining a normal blood flow. At some point, the cross section narrows, and the reduced blood flow can create imbalance between oxygen and nutrient demand and supply.

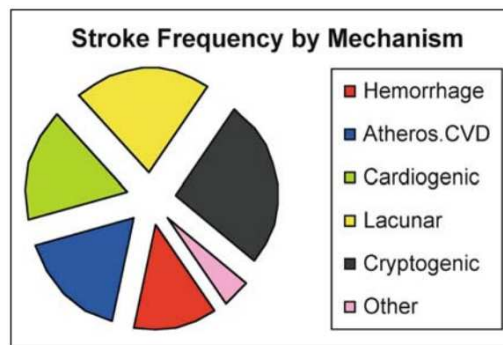


Figure 1.2 – Stroke frequency by mechanism (CVD stands for cardiovascular disease) (González et al., 2011).

In order to restore the original blood flow in a stenotic vessel, a balloon is threaded over the guidewire up to the lesion, and inflated for several seconds in order to compress atherosclerotic plaques. The balloon is removed when the blood flow is correctly restored. The risk of re-stenosis can be reduced by further expanding a thin mesh tube of (metallic) wires called a *stent*, that is wrapped around the balloon and remains in the vessel after the balloon is removed (Figure 1.1).

1.1.1.2 Mechanical thrombectomy

When a blood clot obstructs the blood flow through the vascular tree, the disease is called a *thrombosis*. In the brain, thromboses are responsible for ischemic *stroke* events. 87% of all strokes are ischemic strokes (Benjamin et al., 2017).

Many stroke patients have carotid atherosclerosis, indicating a link between cardiac and cerebrovascular disease (González et al., 2011). A carotid plaque is dangerous not only because of its stenotic effects, but also because it may rupture or dissect at the atherosclerotic wall, showering debris into the bloodstream, leading to multiple embolic cerebral infarcts downstream. The ruptured, ulcerated plaque can also be a source of thrombus formation. Intracranial or aortic atherosclerosis are other causes for ischemic stroke, along with cardiac abnormalities (Figure 1.2).

Globally, hypertension is the most significant risk factor for stroke, both ischemic and hemorrhagic. Elevation in blood pressure plays a large role in the development of vascular disease, including coronary heart disease, ventricular failure, atherosclerosis of the aorta and cerebrovascular arteries, as well as small vessel occlusion. Diabetes mellitus ranks highly as a stroke risk factor. Stroke is the number-one cause of long-term disability and the fifth leading cause of death in the United States (Yang et al., 2017).

Mechanical thrombectomy consists in inserting a medical device in the vascular tree up to the thrombus location. Many devices have been proposed; among them, stent retrievers are the most commonly used (Fanous & Siddiqui, 2016; Zaidat et al., 2018; Baek et al., 2017). An example of stent retriever is shown in Figure 1.3.

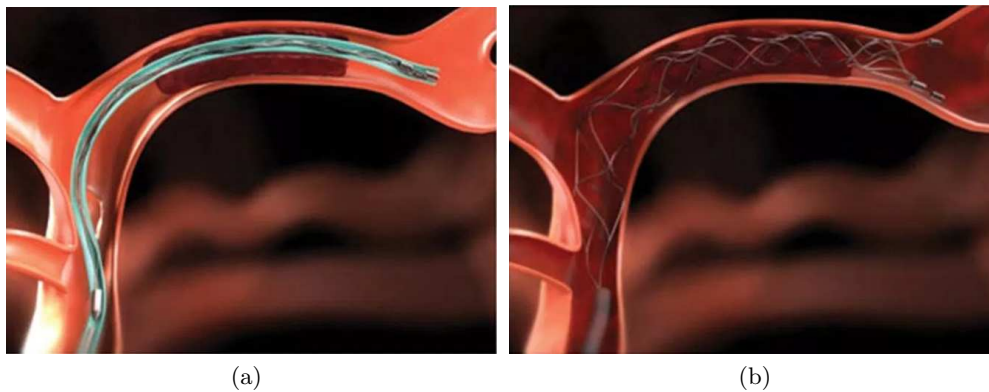


Figure 1.3 – Medtronic’s Solitaire[™] Platinum revascularization device. (a) A catheter is navigated through the thrombus and a stent retriever is brought through the catheter. (b) once the catheter is removed, the stent is opened and catches the thrombus. Once caught by the stent, the entire apparatus with the clot is removed from the body out a small puncture in the femoral artery at the groin (Medtronic, 2018).

Mechanical thrombectomy has several advantages over chemical thrombolysis (González et al., 2011), which consists in delivering drugs that fluidify blood. First, it lessens and may even preclude the use of thrombolytics, in this manner reducing the risk of intracranial hemorrhage (ICH). Second, by avoiding the use of thrombolytics it may be possible to extend the treatment window beyond six hours. Also, clot retrieval devices may provide faster restoration of blood flow.

This procedure is now recommended by the American Stroke Association for stroke patients “older than 18 years with non-significant pre-stroke disability” within six hours of onset of symptoms (Powers et al., 2018). Indeed, recent clinical studies showed the clinical benefits of performing mechanical clot removal as compared to chemical thrombolysis (Berkhemer et al., 2015; Bracard et al., 2016; Nogueira et al., 2018; Mulder et al., 2018), suggesting that the time window for mechanical thrombectomy could even be further extended to up to 24 hours. Still, the clinical outcome improves as the procedure is performed closer to the onset of symptoms: indeed, ischemic stroke patients are expected to lose millions of neurons per minute, causing the brain to age more than three times faster than a normal brain. Hence, despite wider time windows to treat ischemic strokes, the phrase “time is brain” is still valid (Saver, 2006; Zivelonghi & Tamburin, 2018).

1.1.2 Aneurysm coiling

An *aneurysm* is an abnormal inflation similar to a bubble or a balloon on the wall of a blood vessel (Figure 1.4). The ballooning develops because of a weakness of the vessel wall, which is inflated by arterial blood pressure. If not treated, an aneurysm may rupture, leading to internal hemorrhage. A ruptured aneurysm is a medical emergency. The incidence of spontaneous aneurysmal subarachnoid hemorrhage is 6–10 per 100,000 patients per year (Murphy & Robertson, 2013), and the prevalence of intracranial aneurysms is between 1% and 5% of the pop-

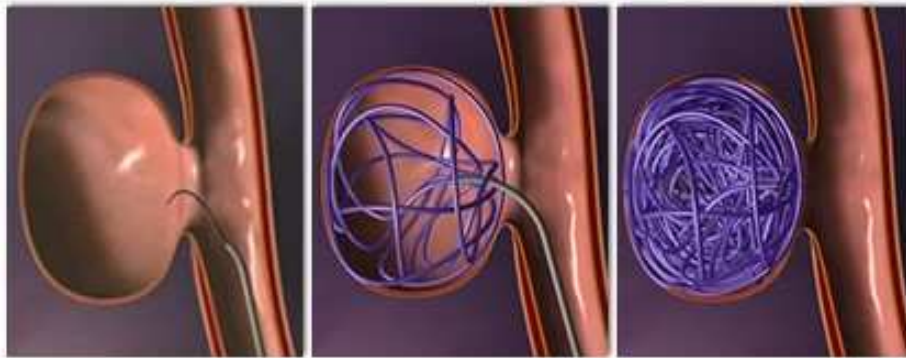


Figure 1.4 – Aneurysm coiling (Society of NeuroInterventional Surgery (SNIS), 2018). From left to right: a coil is brought to the aneurysm location by a micro-catheter and deployed in the aneurysm. The process is repeated until the aneurysm is filled by the coils (Society of NeuroInterventional Surgery (SNIS), 2018).

ulation.

In order to isolate the aneurysmal cavity from the normal blood flow circulation, the aneurysm is filled with metallic *coils* that are inserted during the endovascular procedure. Once the coils block the normal blood flow from entering the aneurysm, the risk of rupture is removed. Coiling procedures may be complemented by a stenting procedure to help the coils fit in the aneurysm.

In absence of complicated procedure, the hospital stay is usually one to two days. Recovery after the operation usually takes five to seven days. For a complicated surgery or endovascular treatment, or if an aneurysm has bled into the brain, hospitalization may last from one to four weeks, depending on the patient's medical condition and any complications caused by the hemorrhage (American Stroke Association, 2018).

1.1.3 Embolization of arteriovenous malformation

Brain arteriovenous malformations (AVMs) are rare and heterogeneous vascular abnormalities. AVMs are formed of an abnormal connection between arteries and veins. Arterial blood shunts directly into veins instead of going through a bed of capillaries, leading more blood flowing through and abnormal blood pressure in the brain (Figure 1.5). Prevalence is approximately 18 per 100,000 adults with an incidence of approximately 1.3 per 100,000 adults per year (Murphy & Robertson, 2013). The causes of AVMs are unknown.

Embolization is generally performed to treat AVMs. A catheter is inserted in one of the feeding arteries to the AVM, through which an embolization agent is injected, such as small particles or a glue-like substance, in order to block the artery and reduce blood flow into the AVM.

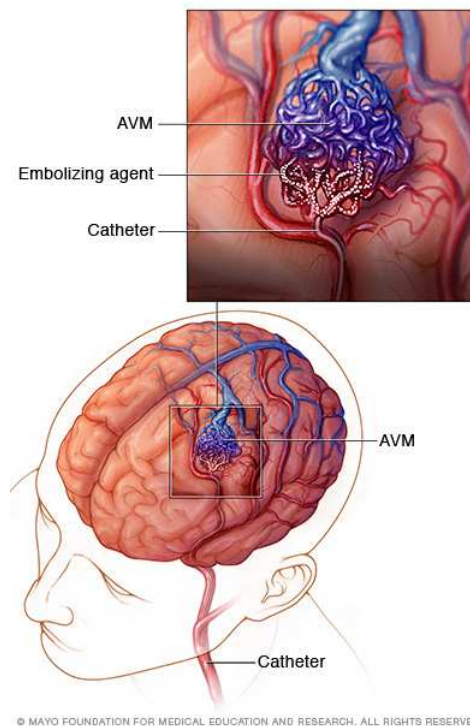


Figure 1.5 – Arteriovenous malformation (AVM) embolization (Mayo Clinic, 2018).

1.2 Enabling INR procedures with imaging

Minimally invasive procedures are made possible by the development of imaging systems both for diagnosis and real-time image guidance. In the following, we describe the commonly used diagnostic imaging modalities and we present the INR suite that is used during endovascular procedures.

1.2.1 Pre-operative imaging

There exists different pre-operating imaging modalities that can be used to plan INR procedures. The choice of each modality depends on the clinical task. Ultrasound imaging, for example, is a low-cost, real-time imaging solution that can be used to detect intracranial arterial occlusions (Hurst & Rosenwasser, 2007) and for basic examinations. Ultrasound can also be an option to monitor interventional procedures as a per-operative modality. It is also used to screen newborns and to check premature infants for signs of intracranial hemorrhage (Sartor, 2002). One interest of ultrasound imaging is that it does not require radiation exposure. However, the obtained images are operator-dependent, and the acoustic window restrictions prevent from using this modality for accurate imaging of the vascular anatomy of the brain (Wible, 2017). Moreover, ultrasound waves do not propagate well through the skull, making it a difficult imaging modality for INR procedures in the brain.

By contrast, magnetic resonance imaging (MRI) can provide a fully three-

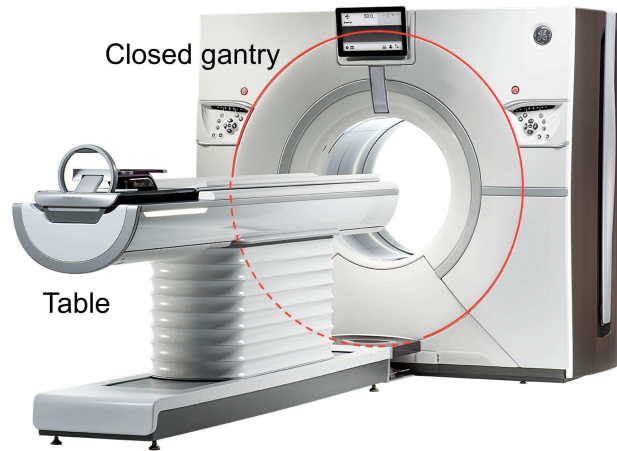


Figure 1.6 – The Revolution CT scanner (GE Healthcare, Chicago, IL, USA).

dimensional image of the brain. It is the best tool for tissue characterization (Wible, 2017), with excellent contrast resolution for soft-tissue imaging. Magnetic resonance angiography (MRA) also provides a three-dimensional map of the brain vessels. However, by design, MRA is not robust to mixed blood flow phases, yielding potential false detections of stenoses (Hurst & Rosenwasser, 2007). MRI can be used to diagnose intracranial aneurysms, carotid stenoses and AVMs. Diffusion-weighted imaging (DWI) may also be useful in the characterization of ischemic stroke events (Hurst & Rosenwasser, 2007). However, the effective utilization of MRI in INR procedures is still a research topic (Chalela et al., 2007; Menjot et al., 2017; Simonsen et al., 2018). The main drawbacks of MRI are the limited spatial resolution of the reconstructed images and its cost. Moreover, MRI is a time-consuming imaging modality.

X-ray computed tomography (CT) is widely used for diagnostic imaging in INR (Figure 1.6). CT scanners outnumber magnetic resonance imagers. Diagnostic CT can provide a fully three-dimensional image of the brain. It is a digital, computer-based imaging modality, where the body anatomy of interest – here, the head – is scanned with X-rays that pass across the imaged region (Sartor, 2002). A detector records X-ray attenuations along projections obtained around the patient, and an algorithm reconstructs a gray-valued image of the scanned body section. The gray levels are related to the tissue densities. Visual interpretation of sectional images is facilitated by selecting portions of the density scale (windows) that modulate the image contrast (Figure 1.7).

The CT modality is the primary imaging modality for the diagnosis of ischemia and intracranial hemorrhage (Hurst & Rosenwasser, 2007). CT imaging further spreads between contrast-enhanced CT (CECT), where an iodinated contrast agent is injected in the blood vessels, and non-enhanced CT (NECT), that is used for soft-tissue imaging in the brain. CT perfusion (CTp) is a functional imaging mode using contrast enhancement that provides maps of the blood vol-

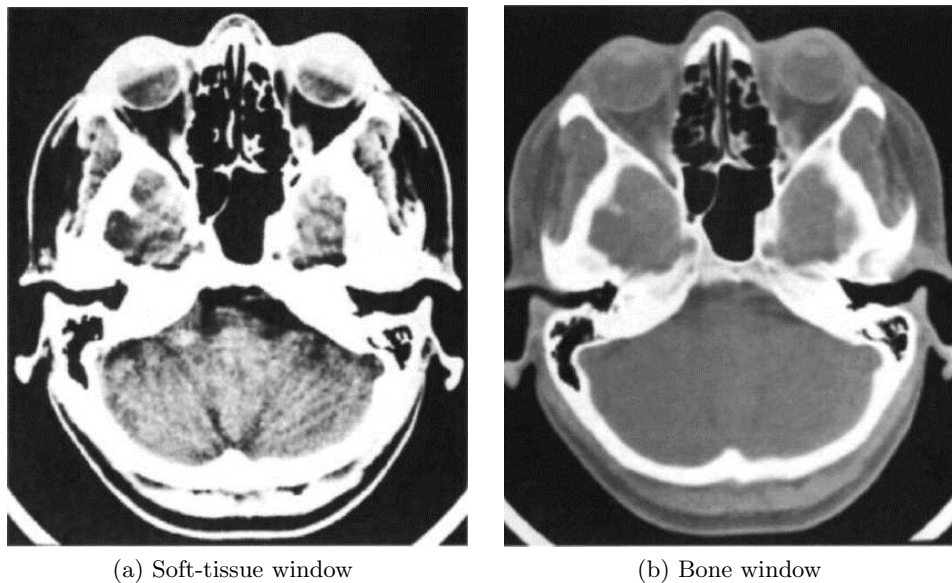


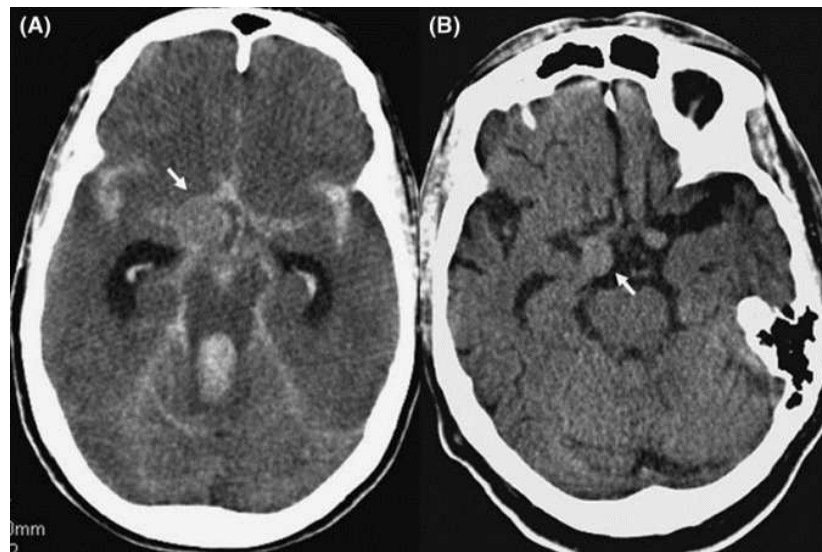
Figure 1.7 – Influence of windowing on image visualization. Case of an axial CT scan of a head (Sartor, 2002).

ume and of the blood perfusion within the brain. As for MRI, in the case of strokes, the benefits of CTP in terms of estimation of the impacted brain territory are still a research topic.

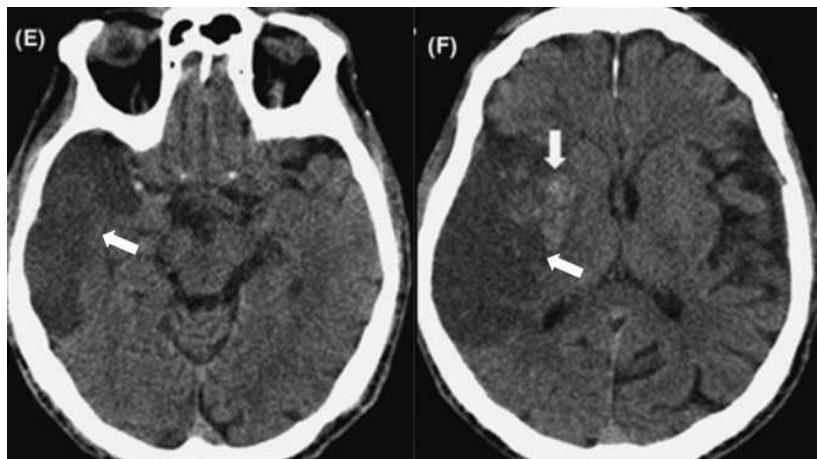
CT scanners accurately demonstrate the vascular anatomy and offer superior spatial resolution than MRI. They allow brain soft-tissue imaging with good contrast resolution. Acquisition and image reconstruction times are also much lower than with MRI. In particular, CT scanners are used in clinical routine for the detection of signs of bleeding, for example, the diagnosis of nontraumatic hemorrhage and the evaluation of unruptured or ruptured aneurysms. They also remain the gold standard for the diagnosis of ischemic strokes (Hurst & Rosenwasser, 2007).

Examples of NECT brain soft-tissue images are shown in Figure 1.8. In Figure 1.8a, the left image shows an axial slice of a brain with a ruptured aneurysm. The arrow shows the location of the aneurysm. The hyper-densities (light grey structures) leaving from the aneurysm are signs of bleeding. In comparison, the right image in Figure 1.8a shows an axial slice of a brain with an unruptured intracranial aneurysm (arrow). In Figure 1.8b, one can observe in two axial slices of a brain a vast hypo-dense territory (darker grey area shown with the arrows), that is characteristic of the infarct zone induced by an ischemic stroke event.

CT imaging involves the use of X-rays, which are a form of ionizing radiation. Although it is known that exposure to such radiation increases the risk of cancer, the amount of X-rays used in CT imaging (or in the interventional room, see Section 1.2.2) remains low, and its associated risks are orders of magnitude smaller than the lifetime risk of dying from cancer in the US (US Food and Drug Administration, 2017).



(a) Signs of bleeding



(b) Ischemia

Figure 1.8 – NECT to detect signs of bleeding and ischemic stroke events (Hurst & Rosenwasser, 2007).

1.2.2 Per-operative imaging: the INR suite

Once the patient is diagnosed a disease that can be treated via minimally invasive procedures, he is brought to the INR suite (Figure 1.9). The INR suite consists of two main rooms:

- a control room (Figure 1.9a), from which the clinician and assistants can monitor the imaging system and review recorded images;
- an exam room (Figure 1.9b), where the patient lies on a table and the clinician performs the procedure itself under the guidance of the imaging system; protective screens to block X-ray radiations and large display monitors are part of the accessories surrounding the clinician within the exam



(a) View from the control room (left) and schematic view of the interventional room (right)



(b) Example of INR exam room (CHRU de Nancy, 2018)

Figure 1.9 – Example of INR suite (CHRU de Nancy, 2018).

room.

1.2.2.1 2D imaging

The main component of the INR suite is the image guidance system, called an interventional C-arm system. It allows visualizing the patient's anatomy by the means of X-rays to perform minimally invasive interventions. Interventional tools

are navigated under live control of the imaging system, which provides two-dimensional, low-dose, real-time X-ray videos (known as fluoroscopic images) when the clinician presses the X-ray pedal. In INR procedures, it is often convenient to get X-ray images from two C-arm systems displaying real-time X-ray images from two different orientations (Figure 1.10a).

The imaging system displays projective images, showing contrasts between dense anatomical structures such as bones and interventional devices, that are designed with radio-opaque materials, super-imposing over an undifferentiated background composed of soft tissues and blood vessels. In order to see the vascular tree, contrast agent (iodine) is injected directly in the artery. However, this information quickly fades away and many injections are required during the procedure. However, due to the toxicity of iodine, it is desirable to reduce contrast media usage as much as possible, especially in the navigation phase.

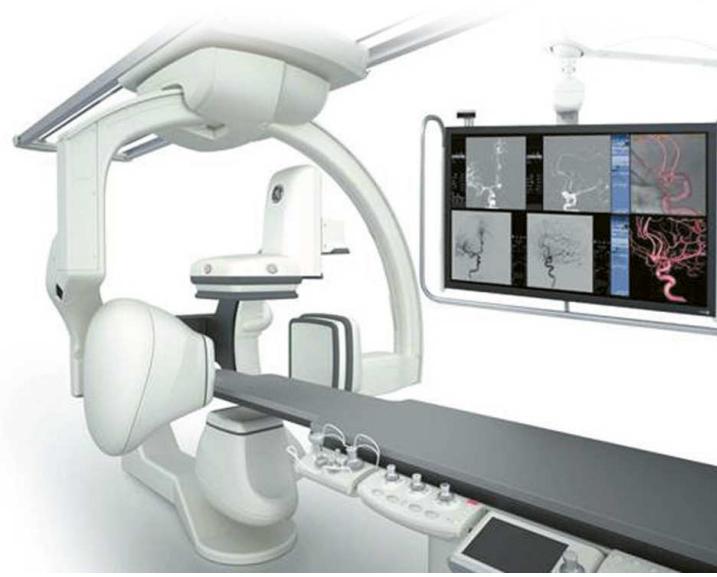
To this end, roadmapping solutions have been proposed, which consist in using previously acquired data containing vessels filled with contrast media, and combining this information with live fluoroscopic images. In addition, fluoroscopic images can be displayed in subtracted mode, where a mask averaging multiple frames of the static patient anatomy (like the skull) is subtracted from live images, so that focus can be made on injected vessels, roadmap information, and device navigation over a flat background (Figure 1.10b).

Endovascular therapy always starts with an angiographic mapping of the vessels (Sartor, 2002). Digital subtraction angiography (DSA, Figure 1.10c) provides a sequence of high-dose X-ray projections of iodinated contrast agent injected in the vascular tree. Again, the first, non-injected frames of the DSA can be used as a mask that is subtracted from the subsequent frames, leaving only the image of the contrast agent propagating in the vascular tree.

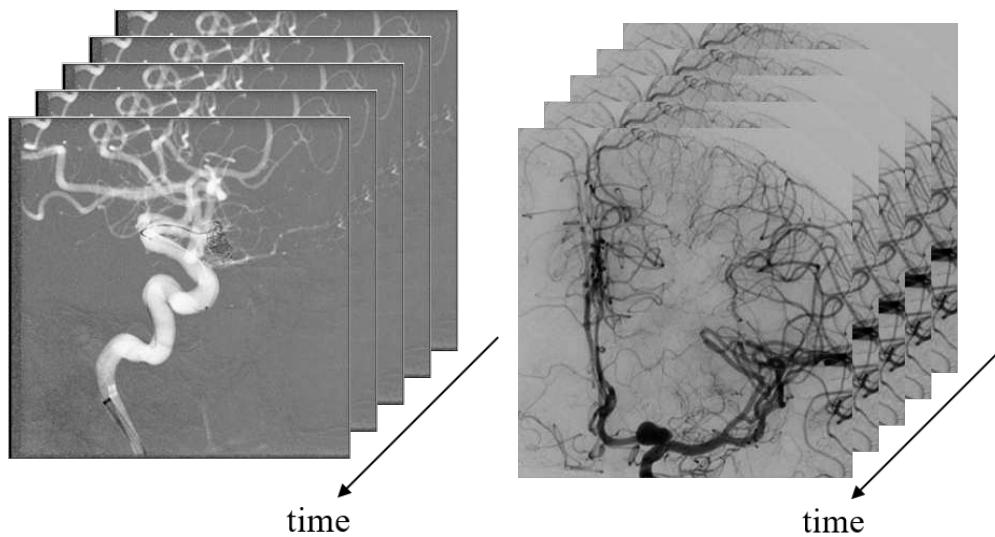
1.2.2.2 3D imaging

Historically, C-arm systems have been designed for 2D real-time imaging only. However, it is now possible to provide a fully three-dimensional image of the head as well. Interventional C-arm cone-beam CT (CBCT) is now routinely used for vascular imaging (Anxionnat et al., 1998). 3D imaging does not suffer from the ambiguities of 2D X-ray projections, which superimpose three-dimensional information onto a single plane. Three-dimensional subtracted angiography is now used to characterize the size of an aneurysm before a coiling procedure (Orth et al., 2008). Figure 1.11 shows a volume rendering of such a 3D image.

As with diagnostic CT, interventional C-arm systems can also provide 3D images without injection of iodinated contrast agent, bringing soft tissue imaging in the interventional room. Hence, patients need not be transferred to a CT scanner. However, current interventional C-arm CBCT images lack reliability, and may miss low-contrast information that only diagnostic CT would reveal, such as signs of bleeding and ischemic stroke events. Figure 1.12 shows two axial slices of a brain. The slices come from a diagnostic CT scanner in Figure 1.12a. Hyper-densities can be identified as abnormalities in the distribution of grey and white matters. A C-arm CBCT of the same patient is shown in Figure 1.12b. The images are much more difficult to interpret: indeed, the abnormalities from



(a) IGS 630 biplane C-arm system (GE Healthcare, Chicago, IL, USA)



(b) Subtracted fluoroscopy with roadmapping (white vessels)

(c) Digital subtraction angiography (DSA)

Figure 1.10 – A C-arm biplane system for INR procedures (a) provides 2D real-time image guidance through fluoroscopic images (b) or high-dose imaging such as digital subtraction angiography (DSA, (c)).

Figure 1.12a are barely distinguishable from errors originating from the imaging system. There are multiple sources of artifacts in C-arm CBCT images; in order to identify them, one must dig into the different parts of the 2D and 3D imaging chains. The main components of these imaging chains will be the topic of the next chapter. In particular, we will point out the main factors impacting soft-tissue imaging, whether they come from the acquisition workflow or from the system

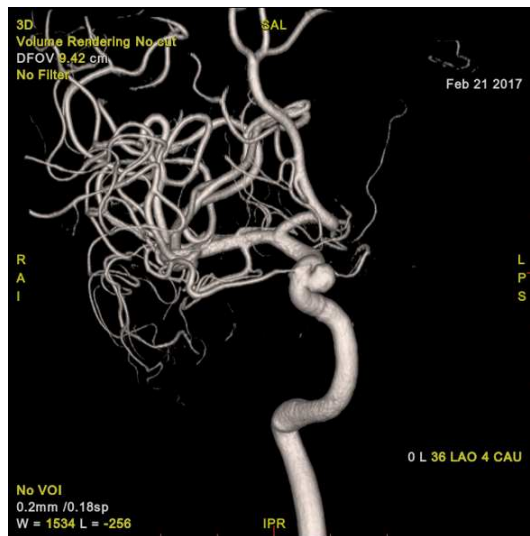


Figure 1.11 – Volume rendering of a three-dimensional digital subtraction angiography.

imaging chain.

1.3 Goal of this thesis

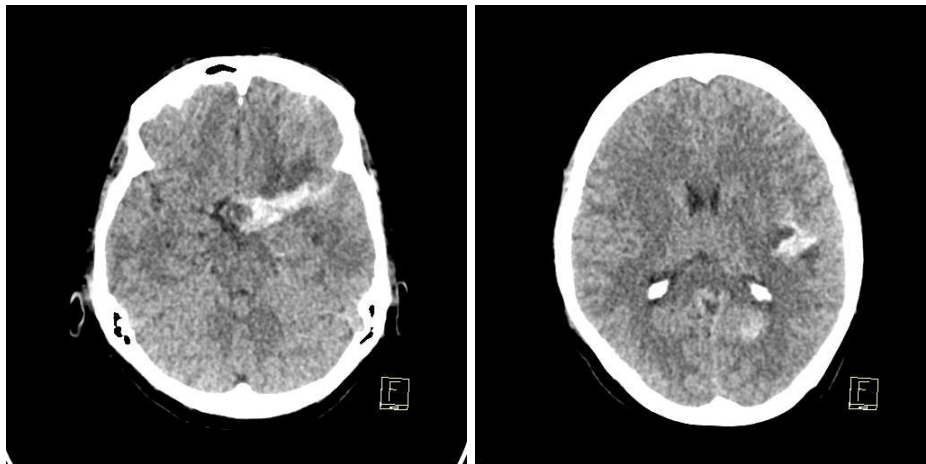
1.3.1 Contributions

As presented in this quick overview of INR procedures, soft-tissue imaging is essential to assess that no sign of bleeding appears after the procedure is completed. It is also necessary at a diagnostic and planning stage in the case of ischemic stroke events, in order to evaluate the presence and the extent of infarction in the brain.

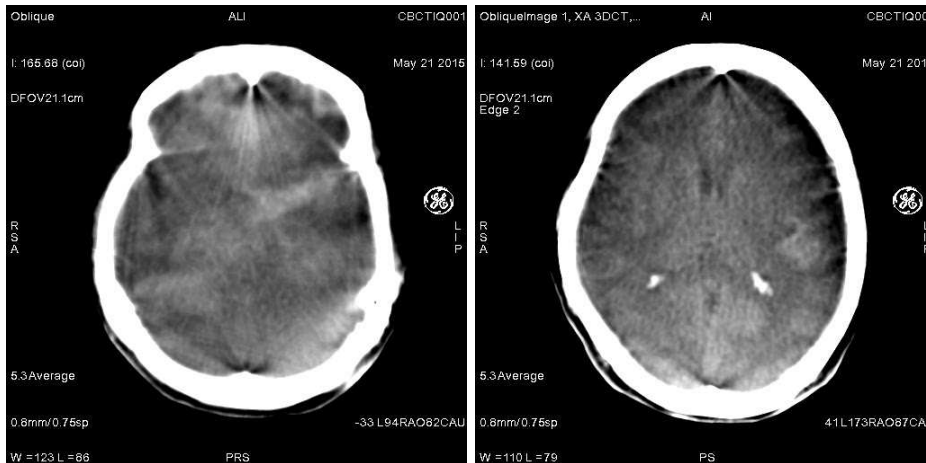
Current clinical workflows require to bring patients to a diagnostic CT scanner first, and then to transfer them to an INR suite, which further delays the mechanical thrombectomy. Moreover, the assessment of the clinical outcome often requires to bring back the patient in a diagnostic CT scanner, which is also time-consuming. Thus, there would be an interest to have access to high-quality soft-tissue imaging directly within the INR suite.

The goal of this thesis is to reduce the gap between diagnostic CT and interventional C-arm CBCT in terms of brain soft-tissue imaging. Taking diagnostic CT scanners as our gold standard, we study the specificities of the C-arm imaging chain, that is primarily designed for two-dimensional real-time image guidance. We identify the key factors impacting low-contrast resolution in C-arm CBCT, namely, scattered intensities, sampling, and dose. Without any hardware modification, we propose to use a set of two C-arm CBCT acquisitions, that we call a dual-rotation acquisition, in order to increase low-contrast detection. We use this acquisition to mimic X-ray beam modulation achieved in diagnostic CT by the means of bow-tie filters.

The flexibility that we leave on the design of this acquisition puts more effort on the reconstruction part. An iterative reconstruction strategy based on previous works ([Langet et al., 2015](#)) is proposed ([Reshef et al., 2016, 2017a](#)), that



(a) CT slices



(b) C-arm CBCT slices

Figure 1.12 – Performance comparison between diagnostic CT images (a) and interventional C-arm CBCT images (b) in terms of soft-tissue imaging.

is able to address both full-volume and region-of-interest (ROI) imaging in the context of dual-rotation CT. By revisiting classical direct reconstruction methods, we also propose an alternative, dual-rotation direct reconstruction formula to accurately merge the information from both acquisitions (Reshef et al., 2017b; Reshef, Riddell, et al., 2018; Reshef, Nikoukhah, et al., 2018). Interestingly, this approach is also adapted to low-contrast imaging in the context of ROI imaging.

The works cited in the previous paragraph were published during this thesis. The list of publications, including supervised Master’s theses, can be found in Appendix B.

1.3.2 Thesis outline

We now provide a brief overview of the next chapters.

Chapter 2 reviews the fundamentals of X-ray imaging and provides the clues to

understand the approaches proposed in the following chapters. It describes the physical and mathematical concepts of tomographic image acquisition and reconstruction from interventional C-arm systems and raises awareness of the complex interactions of such systems on 3D image quality, more specifically on 3D low-contrast detection.

Chapter 3 focuses on the virtual bow-tie problem for C-arm CBCT. In this chapter, the problem of low-contrast detection is reduced to a problem of noise and scattered radiations. The concept of dual-rotation acquisition is proposed, where one un-truncated, low-exposure acquisition is complemented by truncated, high-exposure data. An iterative reconstruction framework is designed and experiments on real acquisitions of a quality assurance phantom and on a head phantom show improved images in terms of low-contrast detection.

Chapter 4 proposes a different, direct reconstruction method for dual-rotation acquisitions. From a semi-discrete framework, we derive a single formula connecting classical filtered backprojection (FBP) to Hilbert-transformed differentiated backprojection (DBP-HT) and backprojection-filtration (BPF) algorithms that uniquely exposes and addresses the issues of angular subsampling. It successfully merges data from dual-rotation acquisitions into a single image, as shown on experimental phantom acquisitions.

Chapter 5 further explores the potential of dual-rotation acquisitions, by highly subsampling the un-truncated acquisition, shifting the problem from full-volume imaging to region-of-interest (ROI) imaging. Interestingly, a small change in the method from Chapter 3 makes it still applicable to this new case. Thanks to its intrinsically view-based behavior, the method from Chapter 4 is particularly adapted to setups involving angular subsampling, thus providing an interesting alternative to the methods from the literature for ROI reconstruction.

Chapter 6 concludes on this work and proposes some industrial and theoretical perspectives based on this thesis.

Imaging with C-arm systems

C-arm systems play a key role in interventional procedures. They were primarily designed for two-dimensional, real-time X-ray imaging, and they were further adapted to three-dimensional imaging as well. This chapter reviews the fundamentals of X-ray imaging and provides the clues to understand the approaches proposed in the next chapters. It describes the physical and mathematical concepts of tomographic image acquisition and reconstruction from X-ray imaging systems and raises awareness of the complex interactions of interventional C-arm systems on 3D image quality, and more specifically on 3D low-contrast detection. In particular, we identify scattered intensities, sampling, and dose, as key factors for C-arm cone-beam CT (CBCT) low-contrast detection. We refer the interested reader to (Dowsett et al., 2006; Dendy, 2011; Dance et al., 2014) for a deeper insight into X-ray physics, and to (Kak & Slaney, 2001; Zeng, 2010) for more details about the mathematics of computed tomography.

Contents

2.1	2D X-ray imaging	18
2.1.1	System description	18
2.1.2	X-ray production	21
2.1.2.1	Bremsstrahlung	21
2.1.2.2	Characteristic radiations	22
2.1.2.3	Off-focal radiation, collimation	23
2.1.3	X-ray attenuation	24
2.1.3.1	Interactions with matter	24
2.1.3.2	Beer's law	25
2.1.3.3	Intensities, dose	25
2.1.3.4	Polychromaticity and beam hardening	26
2.1.4	Image formation	28
2.1.4.1	Primary intensities, scattered intensities	28
2.1.4.2	Flat-panel detector technology	28

2.1.5	Real-time image guidance	29
2.1.5.1	Imaging modes	29
2.1.5.2	Field of view and binned modes	30
2.1.5.3	Exposure management	30
2.1.6	Artifacts	31
2.1.6.1	Scattered intensities	31
2.1.6.2	Non-uniform pixel response	32
2.2	3D X-ray imaging	33
2.2.1	Principles of circular computed tomography	34
2.2.1.1	Geometries	34
2.2.1.2	Filtered backprojection	38
2.2.1.3	Semi-discrete formulation	39
2.2.1.4	Iterative reconstruction	40
2.2.2	Image quality assessment	42
2.2.2.1	The Catphan® 500 phantom	42
2.2.2.2	Spatial resolution	43
2.2.2.3	Contrast resolution	43
2.2.3	Factors impacting low-contrast detection in C-arm CBCT	45
2.2.3.1	Quantum noise	45
2.2.3.2	Detector non-idealities	45
2.2.3.3	X-ray beam	46
2.2.3.4	Scatter	47
2.2.3.5	Sampling	49
2.2.4	Discussion	50

2.1 2D X-ray imaging

2.1.1 System description

A C-arm system is an X-ray imaging system. An open, rigid arm, named C-arm after its shape, holds an X-ray tube on one side and a flat-panel detector on the other side. It leaves access to the patient lying on the bed table during the interventional procedure. The C-arm can be either mobile, hold by a multi-axis arm, ceiling-mounted or floor-mounted. In interventional neuroradiology, biplane systems combining a floor-mounted and a ceiling-mounted C-arm (the lateral and the frontal C-arms) are preferably used due to the complex anatomy of the vascular tree.

The geometry of C-arm systems used as two-dimensional real-time X-ray video cameras is the following (Figure 2.2). X-rays produced by the tube are assumed to originate from a single point and the tube is covered by a radio-opaque material (lead) that only leaves a small window allowing the emission of X-rays outside the tube within a cone. The cone axis intersects the isocenter (center of the 3D field-of-view) at a distance d from the X-ray source, called the *source-to-object distance* (SOD). In the ideal case, the flat-panel detector is orthogonal to the cone axis. It intersects the cone axis at a distance D from the source, called the *source-to-image distance* (SID). The *air gap* is the space left between the object and the detector.

The GE Healthcare IGS (Interventional Guided System) X-ray interventional system family is composed of a set of interventional X-ray C-arm systems. These



(a) GE Healthcare OEC Elite CFD mobile C-arm system (b) Siemens Artis zeego robotic C-arm system



(c) Philips Allura Xper ceiling-mounted C-arm system (d) GE Healthcare IGS 630 biplane C-arm system

Figure 2.1 – Photographs of commercially available C-arm systems.

systems are designed to perform monoplane (Figure 2.3) or biplane (Figure 2.1d) fluoroscopic X-ray examinations, in order to provide the imaging information needed to perform minimally invasive interventional imaging procedures. Additionally, in hybrid operating rooms, these systems allow for surgery and X-ray image-guided surgical procedures. IGS X-ray systems are stationary equipments (permanently installed equipments).

Functionally, the IGS system can be described as follows:

- An X-ray beam is generated (**X-ray production**) and directed to the region-of-interest (ROI) in the patient, who lies on a table. Multiple translational and rotational axes allow for flexible placement of the ROI.

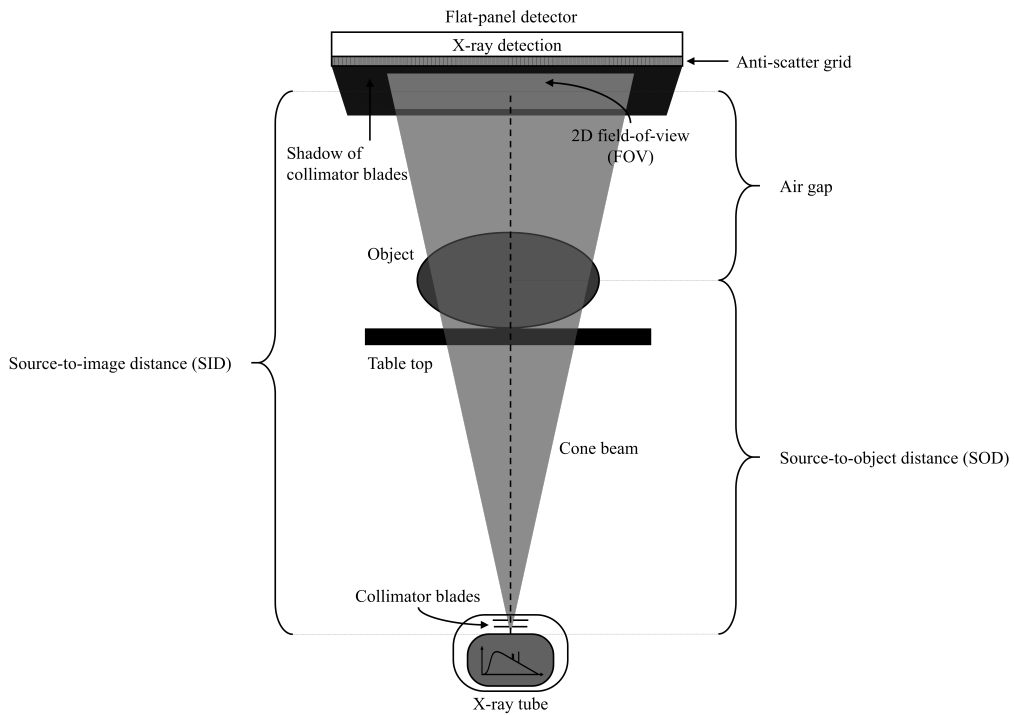


Figure 2.2 – Main components of a 2D X-ray imaging system.

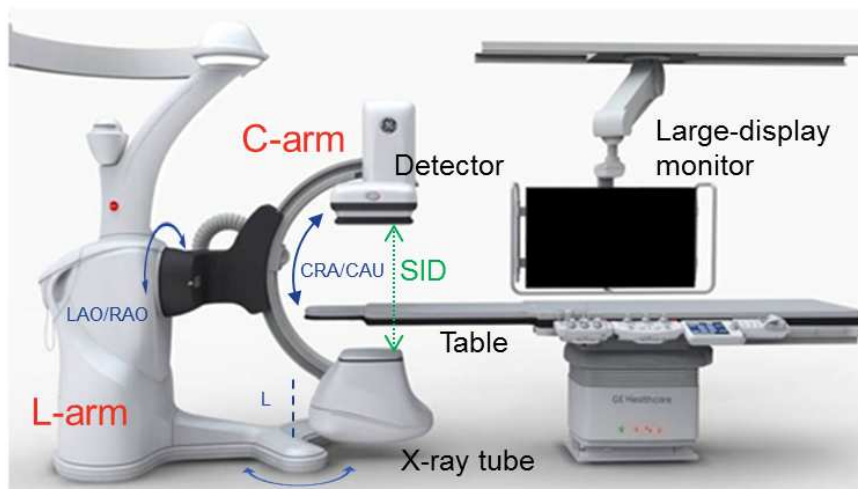


Figure 2.3 – Photograph of GE Healthcare IGS 730 monoplane system.

- The X-ray beam then interacts with matter (**X-ray attenuation**) as it crosses the ROI.
- The X-ray beam that crossed the ROI is finally captured and converted into a digital image data matrix (**image formation**), on which various digital treatments and enhancements are applied before the resulting image is sent

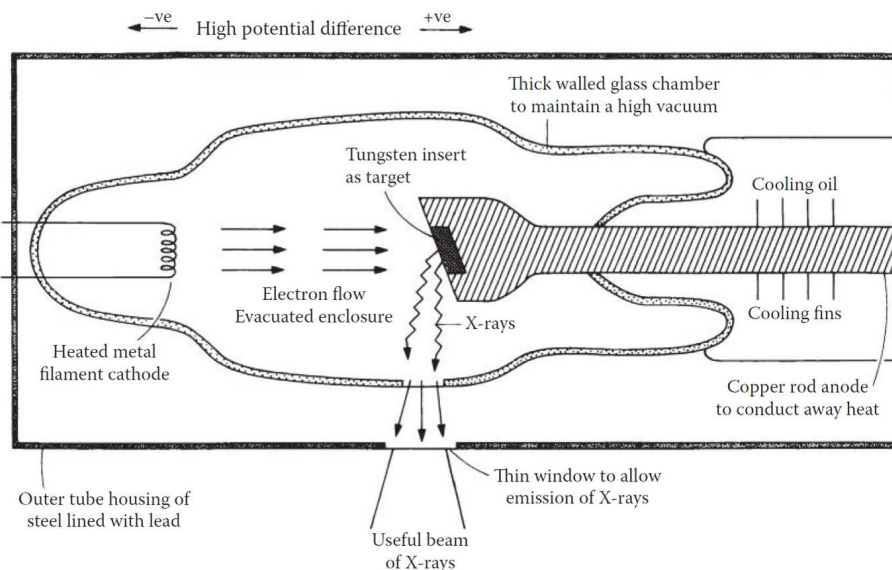


Figure 2.4 – Coolidge X-ray tube (Dendy, 2011).

out to a monitor for the physician to visualize the ROI in real time, and to perform image-guided procedures.

We describe the X-ray production, attenuation and the image formation steps in the next sections.

2.1.2 X-ray production

X-rays are electromagnetic waves with wavelength $\lambda \sim 1 \text{ \AA}$. Earth is constantly bombarded by cosmic radiation, which involves X-rays, but at such low levels that its effects are virtually unnoticed. X-rays were first observed in a laboratory by Wilhelm Röntgen in 1895, and were soon used for medical purposes. Medical X-rays are now produced by Coolidge X-ray tubes (Figure 2.4). X-ray production involves bombarding a small surface (called the focal spot) of a metal target anode with high-speed electrons that have been accelerated by tens to hundreds of kilovolts (kV) of electric potential difference between the anode and a heated filament cathode. The accelerated electron beam can be controlled by:

- the value of the potential difference, called the *peak kilovoltage* or kVp;
- the intensity of the filament tube current, expressed in milliamperes (mA).

The deceleration of fast electrons entering the anode is mostly converted into heat (99% of electron interactions). The rest of the electrons convert into X-rays in the following ways.

2.1.2.1 Bremsstrahlung

When hitting the metal anode, electrons are slowed down in matter by collisions and excitation interactions. If an energetic electron comes close to an atomic

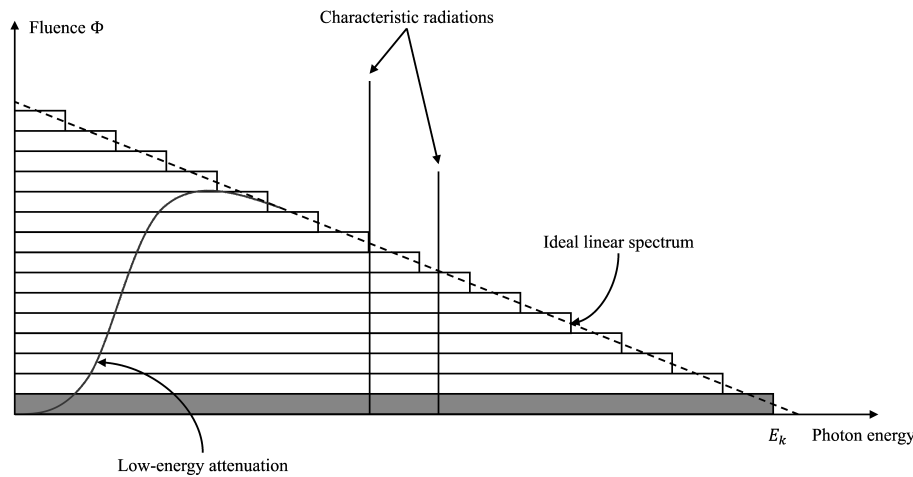


Figure 2.5 – Schematic of an X-ray spectrum produced by an X-ray tube.

nucleus, its trajectory changes due to the attractive Coulomb forces, and it emits X-ray radiation, called Bremsstrahlung radiation (or “braking radiation”). The energy of the emitted X-ray photon is subtracted from the kinetic energy of the electron.

The number of photons passing per unit area perpendicular to the direction of motion of the photons is called the fluence, denoted by Φ . Heuristically, one can deduce the ideal Bremsstrahlung-induced energy spectrum by considering the electron bombardment of an infinitesimally thin target, that yields a constant energy fluence from zero up to the initial electron kinetic energy (gray rectangle in Figure 2.5), given by the kVp value. The metal target anode can be decomposed as a superimposition of infinitesimally thin layers, each of them producing a rectangular distribution of energy fluence. Because the electron is slowed down in each layer, the maximum energy distribution decreases until its kinetic energy reaches zero. The ideal energy spectrum results from the superimposition of all the energy distributions from infinitesimally thin targets, thus the triangular shape of the energy distribution for a thick metal target (dashed line).

2.1.2.2 Characteristic radiations

Electrons can collide with electrons from inner shells of the atoms of the metal anode when their kinetic energies are higher than the binding energies of the electrons in these shells. Ejected primary electrons keep the difference of kinetic energies and binding energies, and the vacancies are filled when electrons drop down from higher energy levels and emit X-rays called “characteristic radiations”. The energies of the emitted X-rays correspond to the difference in binding energies of the shells involved. These radiations are characteristic of the metal anode element and appear as peaks in the X-ray spectrum (black impulses in Figure 2.5).

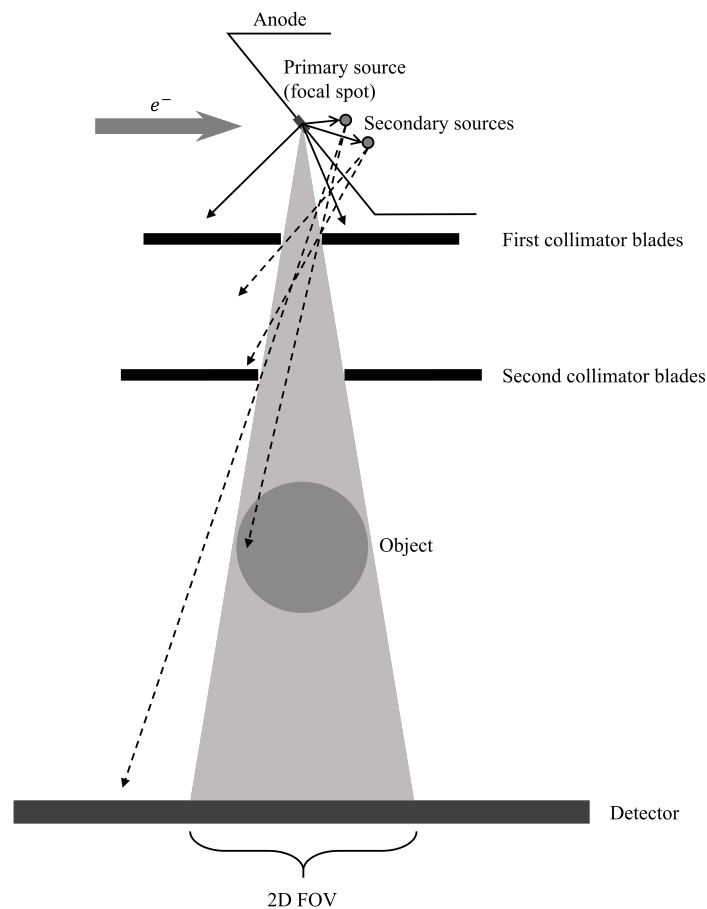


Figure 2.6 – Illustration of off-focal radiation. A second pair of collimator blades partly blocks off-focal X-rays (dashed arrows).

2.1.2.3 Off-focal radiation, collimation

The focal spot (the surface of the anode that is actually bombarded by the electron beam) is defined by an additional negatively charged focusing cup, and a bevel angle of the anode that further reduces the effective focal spot size. Electrons hitting the focal spot also emit secondary electrons, that interact deeper in the metal anode before they produce secondary X-ray radiations. Thus, secondary X-ray radiations are produced by a halo of lower-energy source points around the focal spot; they compose the so-called *off-focal radiation*.

Once X-rays are produced, they are further shaped into a rectangular cone beam using radio-opaque collimator blades, that define a rectangular exposed area on the detector called the *2D field of view* (2D FOV). Collimation ensures that the X-ray beam exposes at most the detector area or a smaller area corresponding to the object of interest. In order to remove most of the off-focal radiation, a second pair of collimator blades is used (Figure 2.6).

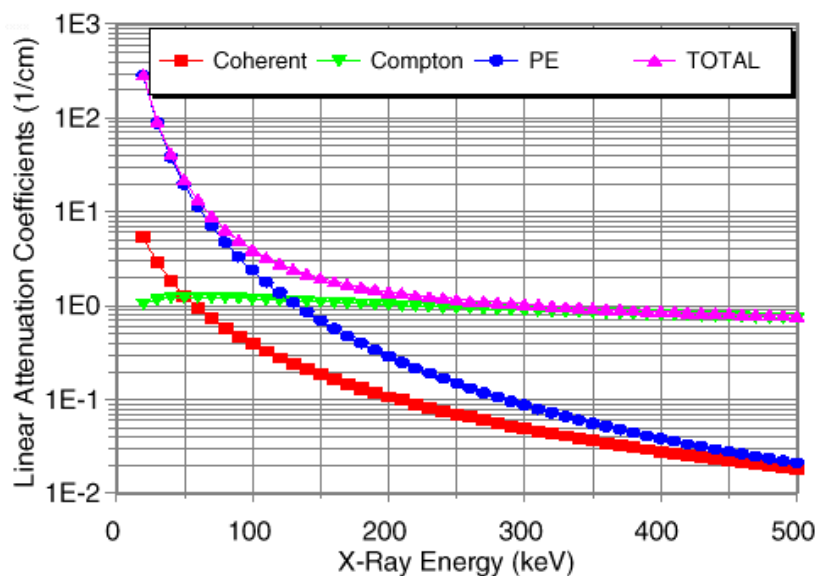


Figure 2.7 – Contribution of coherent scattering, Compton scattering and photo-electric effect to the total attenuation.

2.1.3 X-ray attenuation

2.1.3.1 Interactions with matter

X-rays interact with atoms in four different manners that we describe hereafter. These interactions are summed up by Beer's law, which is at the core of all X-ray imaging systems (Figure 2.7).

Rayleigh-Thomson scattering The Rayleigh-Thomson scattering event is an elastic scattering event during which the incoming X-ray is deviated from its original trajectory by an atom whose nucleus is small in diameter compared to the X-ray wavelength. The deviation occurs without energy transfer, meaning that the deviated X-ray has the same wavelength as the incoming X-ray. The elastic scattering effect occurs mainly at low energies; it stabilizes as the energy increases, so that other competing processes become dominant in the energy range of diagnostic and interventional radiology (it is involved in less than 1% of interactions with matter).

Compton scattering The Compton scattering event is an elastic scattering event: this time, the deviation of the incoming X-ray comes with an energy transfer to an electron, so that the scattered photon is at lower energy. Compton scattering is one of the dominant effects in diagnostic and interventional radiology, along with photoelectric absorption.

Photoelectric absorption During photoelectric absorption, the X-ray photon is completely absorbed and ejects an electron from an inner shell of the atom; such vacancy is refilled by an electron from the outer shell, which comes with the emission of a characteristic X-ray photon. The photoelec-

tric absorption is responsible for the characteristic rays that appear in the middle of the X-ray spectrum.

Pair production Pair production is an event that only occurs for very high energy photons (greater than 1 MeV). The high-energy photon can then be converted into a pair of one electron and one positron. This is not an interaction that happens in diagnostic and interventional radiology.

2.1.3.2 Beer's law

The interaction processes listed previously are statistically independent. When $N_0(\text{kV})$ monochromatic X-ray photons with energy E (in kilo-electronvolts) traverse an infinitesimally thin section of a mono-material, the number $N(\text{kV})$ of photons after all the interactions with the atoms of the mono-material is reduced. This reduction is characterized by a *linear attenuation coefficient* $\mu(\text{kV})$, defined as the attenuation of the mono-material per unit distance at energy kV. The number $N(\text{kV})$ can be seen as a random variable following a Poisson distribution; the probability of observing n such photons knowing the mean number of observed photons $\bar{N}(\text{kV})$ is given by:

$$\mathbb{P}(n, \bar{N}(\text{kV})) = \frac{\bar{N}(\text{kV})^n e^{-\bar{N}(\text{kV})}}{n!}. \quad (2.1)$$

The expected number of photons $\bar{N}(\text{kV})$ is given by Beer's law:

$$\bar{N}(\text{kV}) = N_0(\text{kV}) e^{-\mu(\text{kV})\delta x}, \quad (2.2)$$

where δx is the thickness of the material.

Equation (2.2) is local; when X-rays traverse a thick section of multiple materials, Beer's law can be applied in cascade to each layer localized by its coordinate x , and with linear attenuation coefficient $\mu(\text{kV}, x)$, resulting in:

$$\bar{N}(\text{kV}) = N_0(\text{kV}) e^{-\int \mu(\text{kV}, x) dx}. \quad (2.3)$$

2.1.3.3 Intensities, dose

Note that Beer's law can also be expressed in terms of energy fluences or *intensities*:

$$I(\text{kV}) = I_0(\text{kV}) e^{-\int \mu(\text{kV}, x) dx}, \quad (2.4)$$

where $I(\text{kV}) = \text{keV} \cdot \Phi(\text{kV})$ and $I_0(\text{kV}) = \text{keV} \cdot \Phi_0(\text{kV})$. When X-rays only traverse air, $\mu_{\text{air}}(\text{kV}) \approx 0$ and $I = I_0$ is the intensity of X-rays leaving the tube. By definition, the air intensity I_0 varies linearly with respect to the number of photons, which is directly proportional to the product of the tube current by the exposure time, expressed in milliamperere-seconds (mAs). However, I_0 varies non-linearly with respect to kV; it approximately follows a power law, whose power is also a function of the energy:

$$I_0(\text{kV}, \text{mAs}) \propto \text{mAs} \times \text{kV}^{\alpha(\text{kVp})}. \quad (2.5)$$

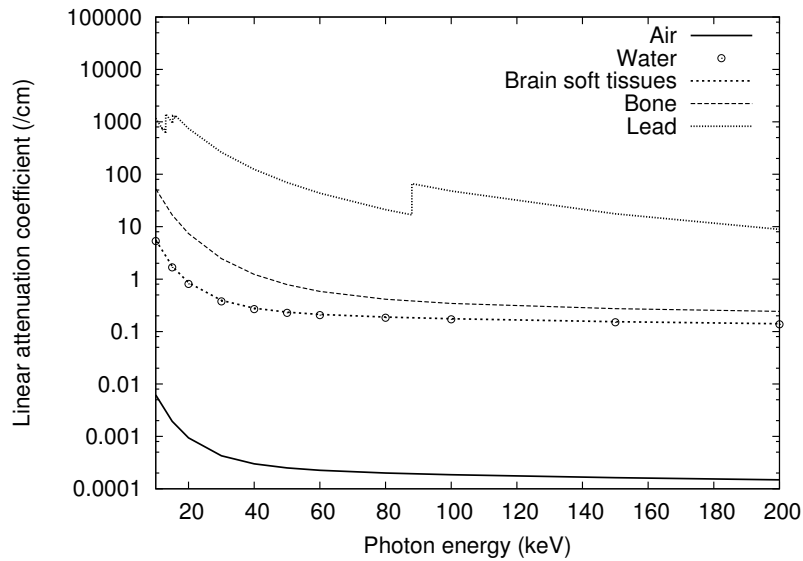


Figure 2.8 – Examples of linear attenuation coefficients as a function of the photon energy (Hubbell & Seltzer, 1995).

Values of $\alpha(\text{kVp})$ typically range between 2 and 6.

The dose is defined as the absorption of X-ray energy per unit mass of matter. The unit to measure dose is the Gray (Gy): $1 \text{ Gy} = 1 \text{ J/kg}$. Dose is approximately linear with respect to I_0 , so that the techniques (kVp, mAs) are used to monitor dose. Of course, the mAs cannot increase indefinitely, because of the maximal admissible tube current; this limitation is compensated by an increase of the kVp value if needed, despite a lower contrast resolution at higher kVp values.

2.1.3.4 Polychromaticity and beam hardening

Equation (2.4) only considers monochromatic X-rays. When X-ray energies are distributed according to a given spectrum, the mean attenuated intensity is given by:

$$\langle I \rangle = \int_0^{\text{kVp}} I(\text{kV}) d\text{kV} = \int_0^{\text{kVp}} I_0(\text{kV}) e^{-\int \mu(\text{kV}, x) dx} d\text{kV}. \quad (2.6)$$

When polychromatic radiation passes through matter, the lower-energy photons are preferentially absorbed (Figure 2.8), resulting in the fact that the remaining transmitted photons are higher-energy photons; hence, the mean kV value of the spectrum of $\langle I \rangle$ is higher than the mean kV of the spectrum of $\langle I_0 \rangle$: we say that the beam hardens during its passage, and we refer to this phenomenon as *beam hardening*.

Low-energy photons that are absorbed by the patient contribute to the patient dose, but are not useful to the X-ray beam detection: hence, it is desirable to cut low-energy X-rays before they reach the patient skin. This is achieved by inserting thin, flat copper sheets right after the anode of the X-ray tube. Copper filtration pre-hardens the beam so that less hardening happens within the patient.

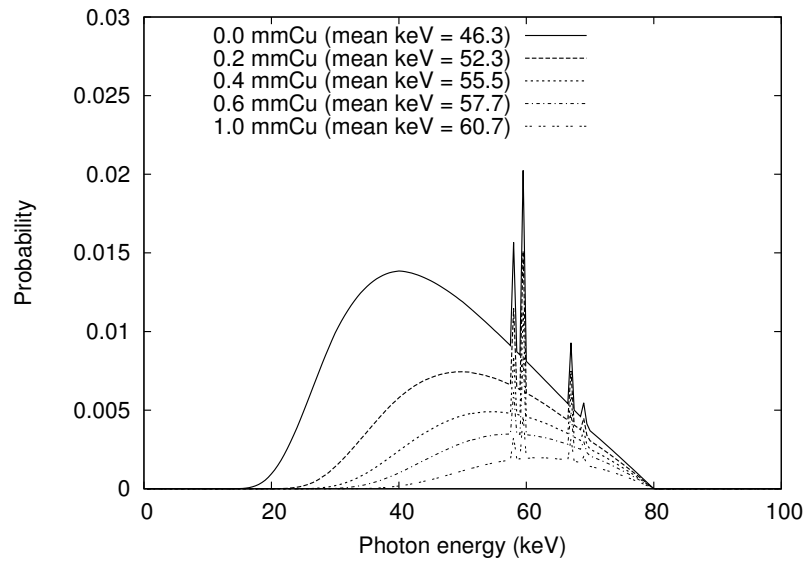


Figure 2.9 – Attenuation of an X-ray spectrum through different thicknesses of copper. Note that the mean energy of the attenuated spectrum increases with the copper thickness (beam hardening).

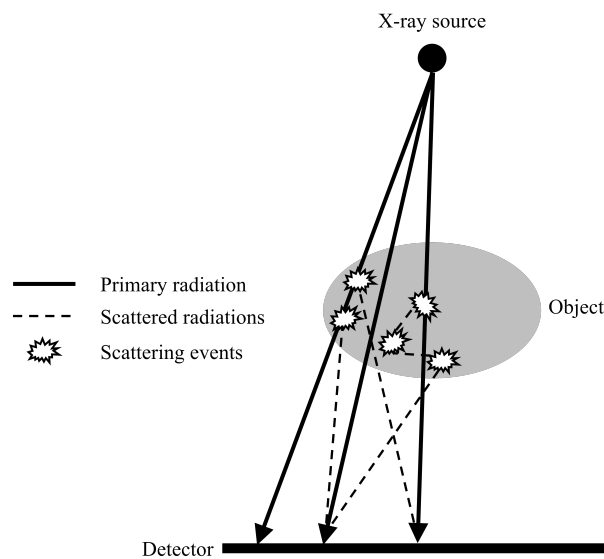


Figure 2.10 – Contribution of scattered radiations to the image formation. Scattered intensities (dashed lines) superimpose to the primary intensity (thick arrow).

Examples of attenuated spectrums through different thicknesses of copper are shown in Figure 2.9.

<i>Anatomy</i>	<i>Panel size</i>	<i>Number of pixels</i>
Heart	21 cm	1024
Head	31 cm	1536
Abdomen, extremities	41 cm	2048

Table 2.1 – Detector sizes for different clinical fields.

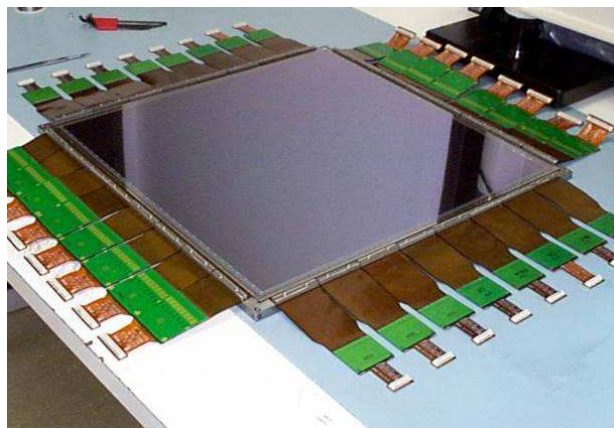


Figure 2.11 – Photograph of GE Innova 4100 flat-panel detector.

2.1.4 Image formation

2.1.4.1 Primary intensities, scattered intensities

Conventional X-ray detectors are energy-integrating detectors: they measure mean intensity values $\langle I \rangle$ with respect to the X-ray spectrum. When X-rays come directly from the source point, $\langle I \rangle$ is called the *primary intensity*. However, when interacting with matter, some photons are scattered due to elastic (Rayleigh-Thomson) and inelastic (Compton) scattering events. As a result, a detector point may be exposed to a superimposition of intensities due to X-rays coming from random directions and forming an additional intensity value that is not the projection of the X-ray source (Figure 2.10): this value is called the *scatter intensity*.

Scattered intensities lower contrast resolution in 2D X-ray imaging and are a source of artifacts in 3D X-ray imaging, as we will discuss in Section 2.2.3.4.

2.1.4.2 Flat-panel detector technology

GE Healthcare IGS C-arm system flat-panel detectors considered in this work are square matrices with square pixels of 0.2 mm (Figure 2.11). The size of flat-panel detectors depends on the clinical field (Table 2.1). For INR systems, the detectors used on GE Healthcare IGS 630 biplane systems are 30 cm wide.

These detectors are called indirect detectors (Granfors, 1999; Granfors & Aufrichtig, 2000; Granfors & Albagli, 2009). Contrary to direct X-ray detectors, which perform a direct conversion from X-ray photons to electronic charges, in-

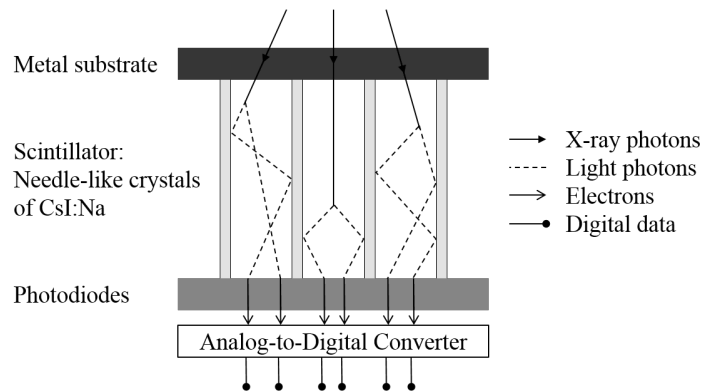


Figure 2.12 – Indirect conversion detector steps (adapted from (Dendy, 2011)).

direct X-ray detectors first convert X-rays into light photons, which are further converted into electronic charges by photodiodes. Conversion from X-rays to light photons is performed by a scintillator. A scintillator is a material that absorbs the incoming X-ray energy and re-emits it in the form of light photons. Scintillation generally occurs isotropically: hence, structured scintillators are preferred to better guide light photons to photodiodes, such as needle-like CsI polycrystals that limit lateral dispersion (Figure 2.12). Furthermore, a mirror is placed on the top of the scintillator to reflect light photons emitted opposite to the photodiodes.

Electronic charges are further sent to a readout electronics via thin-film transistors (Rowlands & Yorkston, 2000; W. Zhao & Siewerdsen, 2014) The analog-to-digital conversion (ADC) step, also known as quantization, defines a subdivision of the real line and assigns a finite digit to each interval, that encodes the analog signal whenever it falls within this interval. Quantization will be covered in more details in Section 3.1.1.

2.1.5 Real-time image guidance

2.1.5.1 Imaging modes

Besides single-frame acquisitions, flat-panel detectors are extensively used for real-time image guidance (Granfors & Albagli, 2009). Fluoroscopy is a temporary low dose X-ray exposure. It can represent more than 90% of the duration of an intervention. Fluoroscopy is used to localize vascular pathologies, position intravascular equipment, such as catheters, balloons, or stents, and perform vascular interventions in real time. In INR procedures, fluoroscopy is used at a few frames per second, and up to 30 Hz (or *frame per second*, denoted fps) to visualize the fastest arterial flows, resulting in a $20 \mu\text{s}$ readout time for each row of a 20 cm panel with 1000 rows of pixels. This constraint on readout times requires an efficient ADC step that allows high frame rates, as discussed in Section 3.1.1.

In addition to low-dose fluoroscopic imaging, C-arm systems also provide other 2D real-time imaging modes that are higher-dose and automatically recorded on the storing disk. Cardiac Record is a non-subtracted high-dose X-ray exposure which offers high image quality. It is usually employed, once the catheter is

<i>Field-of-view</i>	<i>Panel size</i>		
	41 cm	31 cm	21 cm
40 cm	$2 \times 2 - 4 \times 2$	NA	NA
32 cm	$2 \times 1 - 4 \times 2$	$2 \times 1 - 3 \times 2$	NA
20 cm	$1 \times 1 - 2 \times 1$	$1 \times 1 - 2 \times 1$	$1 \times 1 - 2 \times 1$
17 cm	NA	NA	$1 \times 1 - 2 \times 1$
16 cm	$1 \times 1 - 2 \times 1$	$1 \times 1 - 2 \times 1$	$1 \times 1 - 2 \times 1$
15 cm	NA	NA	$1 \times 1 - 2 \times 1$
12 cm	NA	$1 \times 1 - 2 \times 1$	$1 \times 1 - 2 \times 1$

Table 2.2 – Available binning modes for each FOV and each detector size, in pixel \times pixel.

in place, to document the pre-interventional region of interest, or for evidence of a completed interventional action. In INR procedures, Digital Subtraction Angiography (DSA) is often performed. DSA is used for any investigation in vessels (arteries, veins, lymphatic and bile ducts) that requires to keep a record from the examination: evidence of an interventional action, pre-interventional record of the region of interest with injection of contrast medium, diagnosis of a vessel disease with injection of contrast medium. Before injecting the contrast medium to illuminate the vessels, the first image of the sequence is log-subtracted from the next ones, so that only the injected vessels remain in the displayed image. Depending on the clinical application, DSA may be performed at 7.5 fps, 15 fps or 30 fps.

2.1.5.2 Field of view and binned modes

The flat-panel detectors support different field-of-views (denoted FOV). In order to limit bandwidth and reach acceptable frame rates, detector pixels are binned to matrices smaller than 1024×1024 . Hence, 40 cm flat-panel detectors are always read with a 0.4 mm pitch. In addition, anisotropic binning are also used in order to achieve higher frame rates.

The different binning modes with respect to detector sizes are summarized in Table 2.2. Note that for a given detector size, the binning modes differ depending on whether the FOV is higher than 20 cm, or lower than 20 cm. When the binning mode is 1×1 , the native pitch (0.2 mm) is used.

2.1.5.3 Exposure management

Fixed X-ray techniques (kVp, mAs) may not provide optimal image quality over the whole image sequence. Automatic exposure control (AEC) is thus the norm for C-arm systems. AEC fine-tunes the imaging parameters based on a real-time analysis of images, and a continuous estimation of delivered dose. The concept assumes that one can sufficiently pre-determine the optimal X-ray techniques to use for any application and patient size once technique information is known from a previous exposure.

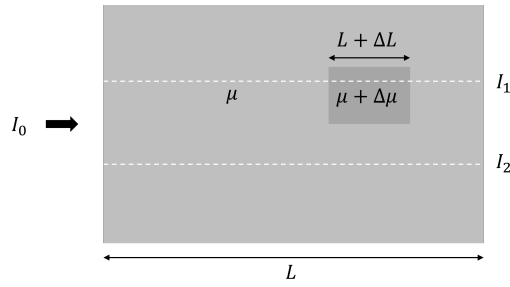


Figure 2.13 – Toy example of a uniform material with attenuation μ embedding a small object with attenuation $\mu + \Delta\mu$, exposed to a uniform, monochromatic intensity I_0 .

Current X-ray techniques, along with other acquisition parameters such as the focal spot, the spectral filtration and the pulse width, are used to alternatively estimate the patient dose and the equivalent patient thickness (EPT) in terms of PMMA¹ attenuation. The EPT is then used to adjust the new X-ray techniques by tuning the mAs, or, if necessary, by switching to a higher kVp value. Note that AEC never computes I_0 explicitly. In fact, most of the time, I_0 is *unknown*, as the 2D FOV is often too small to image the whole anatomy of interest.

2.1.6 Artifacts

2.1.6.1 Scattered intensities

As mentioned previously, flat-panel detectors measure at each pixel the sum of the primary intensity and the scatter intensity. The effect of scattered radiations on the 2D X-ray image quality is twofold. First, as an additional measured signal, they improve the signal-to-noise ratio (SNR) in the image; in particular, it is a relatively low-frequency phenomenon (Rührnschopf & Klingensbeck, 2011b). However, they also reduce the contrast resolution in the image. Indeed, let us consider the toy example from Figure 2.13. The relative contrast of the small rectangular object with respect to the uniform material it is embedded in is given by:

$$C = \frac{I_2 - I_1}{I_2}. \quad (2.7)$$

In absence of scatter, intensities I_1 and I_2 are given by $I_1 = I_0 e^{-\mu L} e^{-\Delta\mu\Delta L}$ and $I_2 = I_0 e^{-\mu L}$. Hence $C = 1 - e^{-\Delta\mu\Delta L}$. Moreover, the contrast-to-noise ratio is given by:

$$\text{CNR} = C \frac{I_2}{\sigma(I_2)} = C \sqrt{I_2}. \quad (2.8)$$

However, if measurements of I_1 and I_2 are corrupted by an additional constant scatter value S , the relative contrast becomes:

$$C_S = \left(1 - \frac{S}{I_2 + S}\right) C = \frac{1}{1 + \text{SPR}} C, \quad (2.9)$$

¹PMMA refers to poly(methyl methacrylate), also known as acrylic or Plexiglas. It is a water-equivalent material.

where $\text{SPR} = \frac{S}{I_2}$ is the *scatter-to-primary ratio*. Hence, the contrast is reduced due to scattered radiations. Assuming that the superimposition of the primary and scattered intensities approximately follows a Poisson statistics, the resulting contrast-to-noise ratio becomes:

$$\text{CNR}_S = C_S \frac{I_2 + S}{\sigma(I_2 + S)} = \frac{1}{\sqrt{1 + \text{SPR}}} \text{CNR}. \quad (2.10)$$

The contrast-to-noise ratio is also reduced by scattered radiations. Note that both in the case of contrast loss and CNR loss, the involved quantity is the SPR, which is insensitive to the mAs.

Scatter rejection methods consist in physically preventing scattered radiations from reaching the detector array cells (Altunbas, 2014). In 2D X-ray imaging, three basic hardware approaches are used (Altunbas, 2014; Fahrig et al., 2014):

- increase the air gap between the imaged object and the detector;
- reduce the field of view with the collimator blades;
- insert an anti-scatter grid on the top of the detector.

An anti-scatter grid consists of an array of (radio-opaque) lead strips, focused towards the X-ray source, that can be inserted on the top of the detector to reduce the amount of scattered radiations reaching the detector cells. In addition, lower kVp will be preferred to minimize the generation of scattered radiations.

2.1.6.2 Non-uniform pixel response

Detectors also need to be corrected for non-uniform pixel responses over the detector active matrix (Granfors & Albagli, 2009; W. Zhao & Siewerdsen, 2014). Pixel-wise affine corrections are performed in two steps. Because of variations in the electronics of the detector (charge retention, diode leakage, etc.), a pixel-wise offset correction is needed. The detector signal is read in absence of exposure and stored as a two-dimensional offset image, that will be subtracted from subsequent X-ray images. Since the offsets vary with the temperature, the frame rate and the detector radiation history, the offset map is permanently refreshed as a background task.

Flat field images (no object in the field of view) are not natively uniform but made uniform by gain calibration. The sources of variations are diverse: for example, they include differences in the pixel gains, or changes in thickness of the CsI crystal. The gain calibration also compensates for the variations of solid angle and accounts for imperfections of the anti-scatter grid. As for offsets, a gain map is generated and stored in the system during a specific pixel gain calibration procedure with flat-field images. Offset-corrected image pixels are then multiplied by their gain correction coefficients. Gain maps are collected periodically every few months.

Bad pixels (with abnormal offsets, gains or noise) are also masked and inpainted from the neighboring pixel values. The detector corrections are summarized in Figure 2.14. In addition, the detector also corrects for undesirable

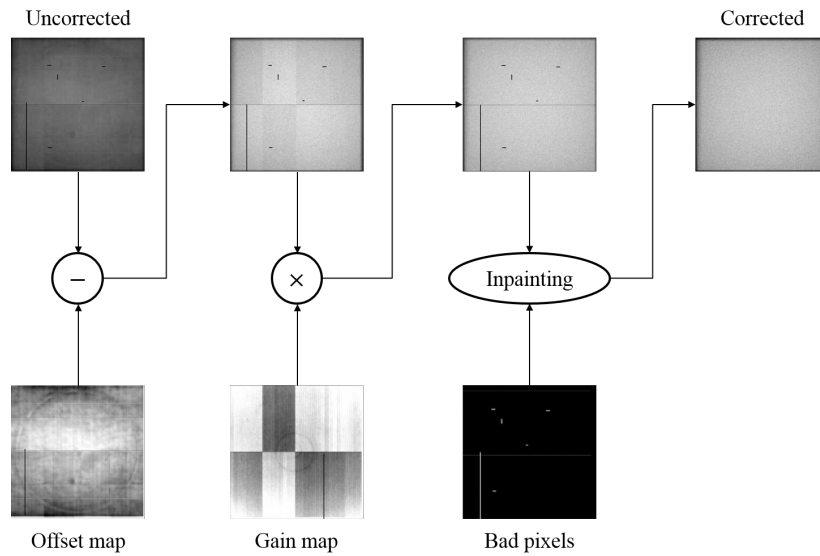


Figure 2.14 – Non-uniform flat-panel detector pixel response correction. An offset map is subtracted from the uncorrected image, that is further multiplied by a gain map. Remaining bad pixels are identified and inpainted to provide the corrected intensity image.

<i>Parameters</i>	<i>GE Healthcare IGS 7x</i>
Frame rate	50 fps
Rotation speed	16°/s - 28°/s - 40°/s
Acquisition time	12.5 s - 7 s - 5 s
Amount of views	600 - 350 - 250
Angular coverage	200°
SID (mm)	1295 (large) - 1180 (short)

Table 2.3 – Tomographic acquisition parameters of IGS 7x C-arm systems.

image retention from frame to frame, or lag artifact, typically coming from the trapping of electrons in the diodes of the readout electronics. In-house correction algorithms are performed after high-dose acquisitions between the offset and gain correction steps.

2.2 3D X-ray imaging

In addition to 2D real-time image guidance, C-arm systems can provide fully three-dimensional images of the patient anatomy. The C-arm rotates around the patient and acquires a series of 2D X-ray images over 200°, called a *spin* (Figure 2.15a). A reconstruction algorithm then reconstructs a 3D image of linear attenuation coefficients μ from the spin and the system parameters. Slices of the 3D image are usually displayed along one of the anatomical planes shown in Figure 2.15b. An example of such reconstructed image is shown in Figures 2.15c–

2.15e. The main parameters of GE Healthcare IGS 7x C-arm systems are given in Table 2.3.

The computed attenuation coefficient depends upon the X-ray energy spectrum of the imaging device. The values are converted to a device-independent unit, called Hounsfield unit, by normalizing them by the attenuation of water computed by the same device via²:

$$f(l) = 1000 \cdot \frac{\mu}{\mu_{\text{water}}}. \quad (2.11)$$

The principles of circular computed tomography are presented in the next subsection. The non-idealities of realistic C-arm systems are then discussed with respect to the mathematical theory of tomographic reconstruction.

2.2.1 Principles of circular computed tomography

2.2.1.1 Geometries

The mathematical basis of circular computed tomography is best understood in the parallel-beam geometry (Figure 2.16), which was the geometry of the first-generation CT scanners and is still used in single-photon emission computed tomography (SPECT) (Hsieh, 2009). The parallel-beam acquisition geometry assumes that incoming rays are parallel to each other and orthogonal to the detector. They are parametrized by angle θ with respect to the x -axis, so that the rays are oriented along vector $\boldsymbol{\theta} = (\cos \theta, \sin \theta)^T$. The detector axis is orthogonal to the incoming rays, hence it is oriented along vector $\boldsymbol{\theta}^\perp = (-\sin \theta, \cos \theta)^T$. We take the projection of the origin point O as the origin of the detector axis. Any point \boldsymbol{x} projects onto the detector axis at coordinate:

$$u_\theta(\boldsymbol{x}) = \boldsymbol{x} \cdot \boldsymbol{\theta}^\perp. \quad (2.12)$$

The *projection* view at angle θ of a two-dimensional image $f : \mathbb{R}^2 \rightarrow \mathbb{R}$ is denoted by $\mathcal{R}_\theta[f] = p_\theta$; it is defined at detector coordinate u as the sum of f over the ray orthogonal to the detector and passing by u :

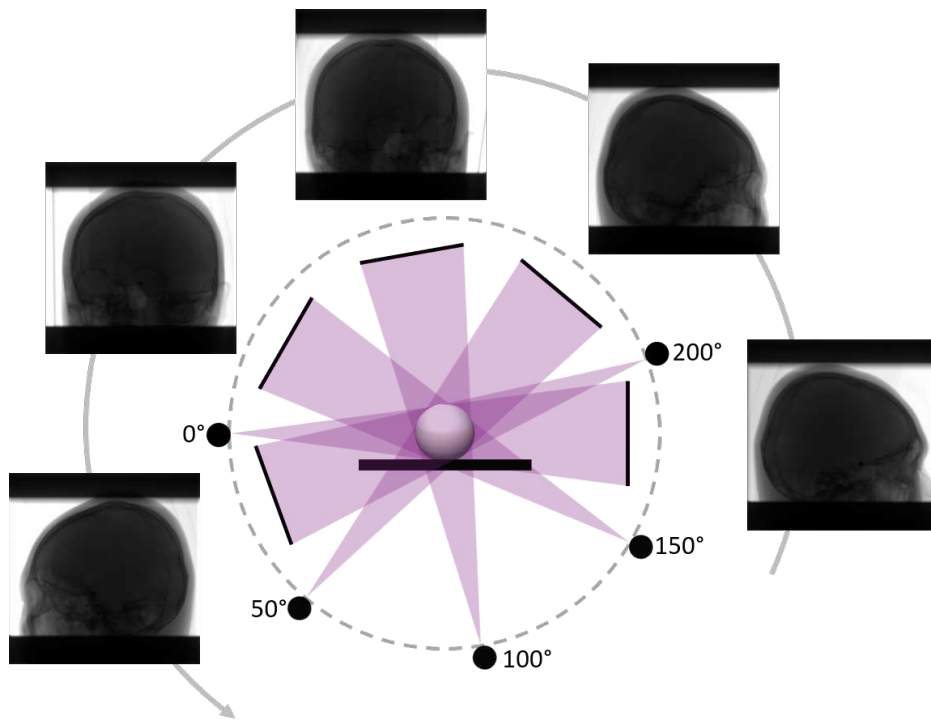
$$\forall u \in \mathbb{R}, \quad \mathcal{R}_\theta[f](u) = p_\theta(u) = \int_{-\infty}^{+\infty} f(t\boldsymbol{\theta} + u\boldsymbol{\theta}^\perp) dt. \quad (2.13)$$

Note that when f is compactly supported, p_θ is also compactly supported. Projection p_θ satisfies the symmetry property $p_{\theta+\pi}(-u) = p_\theta(u)$ and is 2π -periodic. The continuous parallel-beam circular tomographic acquisition is the collection³:

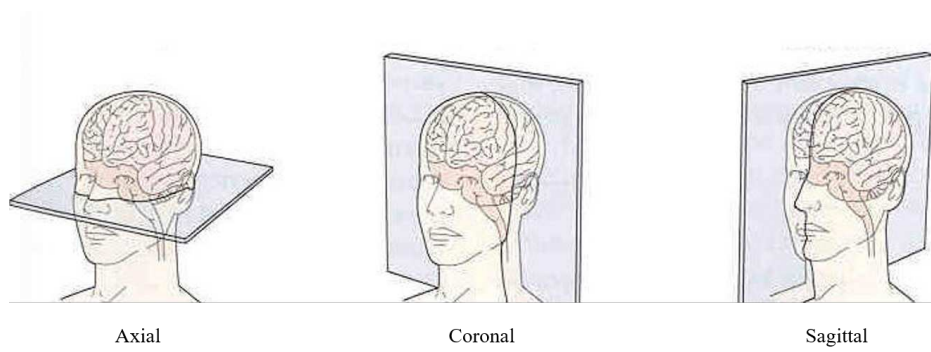
$$p = \{p_\theta \mid \theta \in [0, 2\pi]\}. \quad (2.14)$$

²Note that this is not the standard definition of Hounsfield units; however, since $\mu_{\text{air}} \ll \mu$ for typical values of μ , we set $\mu_{\text{air}} \approx 0$. We also shifted the scale by 1000, so that air is 0 HU and water is 1000 HU.

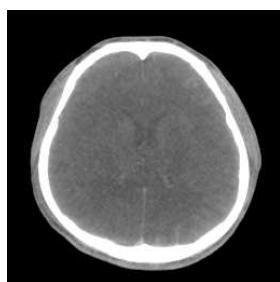
³Acquisitions over the half circle $[0, \pi]$ are enough to invert the problem; however, we define the parallel-beam tomographic acquisition over the full circle $[0, 2\pi]$ to make it more consistent with the divergent-beam case.



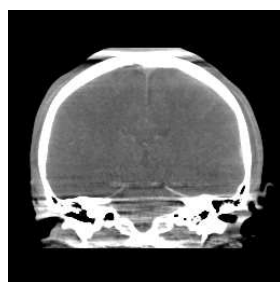
(a) Spin acquisition



(b) Anatomical planes



(c) Reconstructed image (axial view)



(d) Reconstructed image (coronal view)



(e) Reconstructed image (sagittal view)

Figure 2.15 – 3D cone-beam computed tomography on a C-arm system.

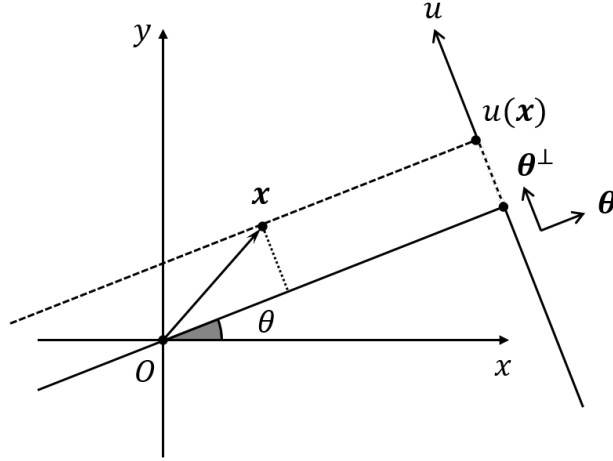


Figure 2.16 – Parallel-beam circular tomographic acquisition geometry.

The goal of circular tomographic reconstruction is to recover the 2D function f from the collection of 1D projections p . We will denote by \mathcal{B}_θ , the *backprojection* operator from angle θ :

$$\mathcal{B}_\theta : \begin{pmatrix} (\mathbb{R} \rightarrow \mathbb{R}) & \mapsto & (\mathbb{R}^2 \rightarrow \mathbb{R}) \\ \phi & \mapsto & \phi \circ u_\theta \end{pmatrix}. \quad (2.15)$$

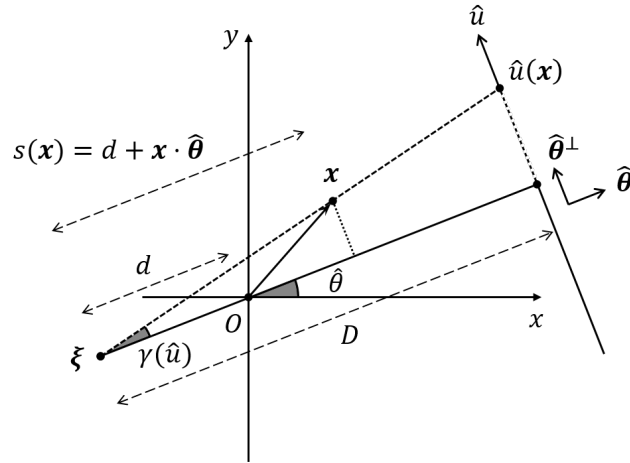
Note that \mathcal{B}_θ is actually the adjoint operator of \mathcal{R}_θ when using the classical L^2 inner product (Kak & Slaney, 2001).

In divergent-beam acquisition geometries with linear or planar detectors (Figure 2.17), the X-ray source is now located at point ξ , and we denote by $d = |\xi|$ the SOD. The orthogonal projection of the source over the detector defines an angle $\hat{\theta}$ with respect to the x -axis. In the fan-beam geometry, the detector axis is oriented along $\hat{\theta}^\perp$ (Figure 2.17a), while in the cone-beam geometry, the detector plane is orthogonal to $\hat{\theta}$ (Figure 2.17b). In any case, the detector is located at a distance D from the X-ray source, which is the SID. Again, the projection of O defines the origin of the detector axis. Note that in the ideal, circular (planar) source-detector trajectory, the fan-beam geometry corresponds to the plane $z = 0$ of the cone-beam geometry, which projects onto the line $\hat{v} = 0$ of the detector plane.

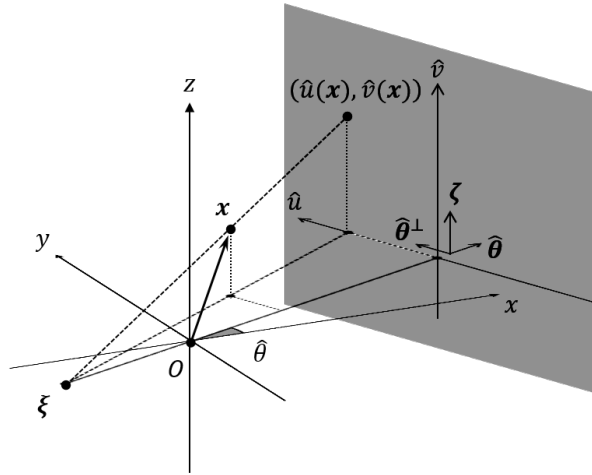
In the circular cone-beam geometry, a 3D point $\mathbf{x} = (x, y, z)^T$ projects onto the detector plane at coordinate $(\hat{u}_\theta(\mathbf{x}), \hat{v}_\theta(\mathbf{x}))$, where:

$$\begin{pmatrix} s_{\hat{\theta}}(\mathbf{x}) \hat{u}_\theta(\mathbf{x}) \\ s_{\hat{\theta}}(\mathbf{x}) \hat{v}_\theta(\mathbf{x}) \\ s_{\hat{\theta}}(\mathbf{x}) \end{pmatrix} = \underbrace{\begin{pmatrix} -D \sin \hat{\theta} & D \cos \hat{\theta} & 0 & 0 \\ 0 & 0 & D & 0 \\ \cos \hat{\theta} & \sin \hat{\theta} & 0 & d \end{pmatrix}}_{P_{\hat{\theta}}} \begin{pmatrix} x \\ y \\ z \\ 1 \end{pmatrix}. \quad (2.16)$$

Matrix $P_{\hat{\theta}}$ is called the *projection matrix* at view angle $\hat{\theta}$. Note that $P_{\hat{\theta}}$ is defined



(a) Fan-beam geometry



(b) Cone-beam geometry

Figure 2.17 – Divergent-beam circular tomographic acquisition geometries.

up to a constant scaling. Cone-beam projections are written:

$$\hat{p}_\theta(\hat{u}, \hat{v}) = \hat{\mathcal{R}}_\theta[f](\hat{u}, \hat{v}) = \int_0^{+\infty} f(\xi + t\mathbf{l}(\hat{u}, \hat{v})) dt, \quad (2.17)$$

where:

$$\mathbf{l}(\hat{u}, \hat{v}) = \frac{1}{\sqrt{D^2 + \hat{u}^2 + \hat{v}^2}} (D\boldsymbol{\theta} + \hat{u}\hat{\boldsymbol{\theta}}^\perp + \hat{v}\boldsymbol{\zeta}). \quad (2.18)$$

The cone-beam full-scan circular tomographic acquisition is the collection:

$$\hat{p} = \{ \hat{p}_\theta \mid \theta \in [0, 2\pi] \}, \quad (2.19)$$

and the cone-beam backprojection operator is defined as:

$$\hat{\mathcal{B}}_\theta : \left(\begin{array}{cc} (\mathbb{R}^2 \rightarrow \mathbb{R}) & \rightarrow & (\mathbb{R}^3 \rightarrow \mathbb{R}) \\ \phi & \mapsto & \phi(\hat{u}_\theta, \hat{v}_\theta) \end{array} \right). \quad (2.20)$$

All the notations above extend to the fan-beam geometry by letting $z = 0$ (hence $\hat{v}_{\hat{\theta}} = 0$), and $\hat{v} = 0$. In this geometry, we drop the fixed coordinates for sake of simplicity. Finally, note that when $(D, d) \rightarrow (+\infty, +\infty)$, the fan-beam geometry reduces to the parallel-beam geometry.

2.2.1.2 Filtered backprojection

The *projection-slice theorem* is at the core of computed tomography (Kak & Slaney, 2001). It states that:

$$\mathcal{F}_1 [p_\theta] (\rho) = \mathcal{F}_2 [f] (\rho\theta^\perp), \quad (2.21)$$

where \mathcal{F}_n is the n -dimensional Fourier transform operator. Hence, when $\theta \in [0, \pi]$, projection lines p_θ describe the whole 2D Fourier plane of f and the inversion of the Fourier transform of f yields the filtered backprojection (FBP) formula:

$$f = \frac{1}{2} \int_0^{2\pi} \mathcal{B}_\theta \mathcal{D} [p_\theta] d\theta = \frac{1}{2} \int_0^{2\pi} \mathcal{D} [p_\theta] (u_\theta) d\theta, \quad (2.22)$$

where \mathcal{D} denotes the linear *ramp* filtering operator, which amounts to a multiplication in the Fourier domain by the frequency module $|\rho|$. If one denotes by \mathcal{B} the cumulative backprojection operator:

$$\mathcal{B} [\phi] = \frac{1}{2} \int_0^{2\pi} \mathcal{B}_\theta [\phi] d\theta, \quad (2.23)$$

and if one still denotes by \mathcal{D} the operator ramp-filtering all projection lines in p , then FBP can be further written as:

$$f = \mathcal{B}\mathcal{D} [p]. \quad (2.24)$$

Note that since the true ramp filter has an infinite support in the Fourier space, it is actually weighted by an apodization window in practice.

Reconstruction from the fan-beam full-scan, circular tomographic acquisition can be derived from the parallel-beam FBP formula from Equation (2.22) by exploiting the relationship between fan-beam parameters $(\hat{\theta}, \hat{u})$ and the equivalent parallel-beam parameters (θ, u) for the same projection ray (Kak & Slaney, 2001):

$$\begin{cases} \theta &= \hat{\theta} + \gamma(\hat{u}) \\ u &= \frac{\hat{u}d}{\sqrt{\hat{u}^2 + D^2}} \end{cases}, \quad \text{where } \gamma(\hat{u}) = \arctan\left(\frac{\hat{u}}{D}\right). \quad (2.25)$$

There are two ways of exploiting this equivalence. The simplest approach is to perform a rebinning of the fan-beam data into the equivalent parallel-beam projections. Once rebinned, the data can be reconstructed using any parallel-beam reconstruction method, such as the parallel-beam FBP method. We can

also apply the change of variables from parallel-beam to fan-beam parameters from Equation (2.25), yielding the fan-beam FBP formula:

$$f = \frac{1}{2} \int_0^{2\pi} \frac{D^2}{s_{\hat{\theta}}^2} \hat{\mathcal{B}}_{\hat{\theta}} \mathcal{D} [\tilde{p}_{\hat{\theta}}] d\hat{\theta}, \quad (2.26)$$

where:

$$\tilde{p}_{\hat{\theta}}(\hat{u}) = \frac{d}{D} \cdot \cos \gamma(\hat{u}) \cdot \hat{p}_{\hat{\theta}}(\hat{u}) = \frac{d}{D} \cdot \frac{D}{\sqrt{\hat{u}^2 + D^2}} \cdot \hat{p}_{\hat{\theta}}(\hat{u}). \quad (2.27)$$

In parallel-beam and fan-beam geometries, the FBP formulas from Equations (2.22) and (2.26) are exact. In the cone-beam full-scan circular geometry, however, it is not possible to find an exact inversion formula: indeed, a circular source-detector trajectory does not completely determine the cone-beam transform. This is a consequence of Tuy's condition for exact reconstruction (Tuy, 1983), which states that every plane intersecting the object must contain a point from the source-detector trajectory. Despite its non-exactness, the Feldkamp-David-Kress (FDK) method (Feldkamp et al., 1984) remains the most used direct reconstruction method in cone-beam computed tomography (CBCT). FDK is a direct extension of the fan-beam FBP formula to the cone-beam case. The FDK reconstructed image is written as:

$$f_{\text{FDK}} = \frac{1}{2} \int_0^{2\pi} \frac{D^2}{s_{\hat{\theta}}^2} \hat{\mathcal{B}}_{\hat{\theta}} \mathcal{D} [\tilde{p}_{\hat{\theta}}(\cdot, \hat{v}_{\hat{\theta}})] d\hat{\theta}, \quad (2.28)$$

where:

$$\tilde{p}_{\hat{\theta}}(\hat{u}, \hat{v}) = \frac{d}{D} \cdot \frac{D}{\sqrt{\hat{u}^2 + \hat{v}^2 + D^2}} \hat{p}_{\hat{\theta}}(\hat{u}, \hat{v}). \quad (2.29)$$

Whenever $\hat{v} = 0$, FDK reduces to the fan-beam FBP formula. It is thus an exact reconstruction within the trajectory plane. Moreover, FDK is exact outside the trajectory plane when the object to be reconstructed is invariant in the z -direction (Feldkamp et al., 1984). FDK reduces to row-wise ramp filtering of cosine-weighted projections, followed by a weighted backprojection step.

2.2.1.3 Semi-discrete formulation

The FBP/FDK formulas have been proposed in a continuous formulation: FBP is an exact analytical inversion formula, from which FDK provides an approximate solution to the continuous reconstruction problem. In order to implement them in practice, they need to be further discretized. In particular, a discretization of the angular range is needed. Assuming a uniform angular sampling of N angular samples, we define the set:

$$\Theta = \left\{ \theta_i = \left(i - \frac{1}{2} \right) \Delta\theta, i = 1, \dots, N \right\}, \text{ where } \Delta\theta = \frac{2\pi}{N}. \quad (2.30)$$

Then, the semi-discrete formulation for the parallel-beam FBP is:

$$f_N = \frac{1}{2} \sum_{\theta \in \Theta} \mathcal{B}_{\theta} \mathcal{D} [p_{\theta}] \Delta\theta = \frac{\pi}{N} \sum_{\theta \in \Theta} \mathcal{B}_{\theta} \mathcal{D} [p_{\theta}]. \quad (2.31)$$

Similarly, the semi-discrete formulation for FDK (which reduces to the semi-discrete fan-beam FBP in the midplane) is:

$$f_{\text{FDK},N} = \frac{1}{2} \sum_{\hat{\theta} \in \Theta} \frac{D^2}{s_{\hat{\theta}}^2} \widehat{\mathcal{B}}_{\hat{\theta}} \mathcal{D} [\tilde{p}_{\hat{\theta}}(\cdot, \hat{v}_{\hat{\theta}})] \Delta\theta = \frac{\pi}{N} \sum_{\hat{\theta} \in \Theta} \frac{D^2}{s_{\hat{\theta}}^2} \widehat{\mathcal{B}}_{\hat{\theta}} \mathcal{D} [\tilde{p}_{\hat{\theta}}(\cdot, \hat{v}_{\hat{\theta}})]. \quad (2.32)$$

We call these formulations semi-discrete, as only angles are discretized here. They are closer to real cases, where obviously there is only a finite set of measurements. The semi-discrete setting also breaks the trivial equalities from the continuous case: for example, a continuous fan-beam FBP is equal to a continuous parallel-beam FBP, which is not the case with the semi-discrete formulations.

Semi-discrete formulations will be useful in Chapter 4 in order to derive direct reconstruction formulas that remain intrinsically view-based, in the sense that the reconstruction algorithm amounts to cumulating information from different projection views independently.

2.2.1.4 Iterative reconstruction

Instead of discretizing continuous formulas, or expressing the problem in the semi-discrete setting, one can also directly translate the tomographic problem into a discrete problem. In this case, f represents a vector, whose size is equal to the number of voxels in the finite 3D grid. Projections are concatenated into a single vector p of size N times the number of pixels of the detector array. The projection matrix \mathcal{R} is now a rectangular matrix such that $\mathcal{R}f = p$. The FDK solution, which can be written as $f_{\text{FDK}} = \text{FDK}(p) = \mathcal{R}^T \mathcal{D} p$ once the problem is discretized, is only an approximate solution to the cone-beam tomographic reconstruction problem. In particular, FDK does not handle cone-beam artifacts. Instead of the direct FDK reconstruction, iterative methods (Fessler, 2006; Langet et al., 2015) solve a minimization problem of the form:

$$\min_f \{ \mathcal{C}(f, p) + \chi(f) \}, \quad (2.33)$$

where $\mathcal{C}(f, p)$ is a data fidelity term ensuring that f is consistent with measured data p , and $\chi(f)$ is a regularization term based on *a priori* knowledge on the image structure. In particular, a least-squares criterion can be minimized (Langet et al., 2015):

$$f_{\text{iFDK}} = \underset{f}{\operatorname{argmin}} \frac{1}{2} (\mathcal{R}f - p)^T \mathcal{D} (\mathcal{R}f - p) \quad (2.34)$$

The ramp filter \mathcal{D} , which is diagonal in the Fourier space, is included in the quadratic form. A gradient descent scheme with fixed gradient step $\tau > 0$ yields the iterative FDK (iFDK) algorithm:

$$f^{(i+1)} = f^{(i)} - \tau \mathcal{R}^T \mathcal{D} (\mathcal{R}f^{(i)} - p) = f^{(i)} - \tau \cdot \text{FDK}(\mathcal{R}f^{(i)} - p). \quad (2.35)$$

iFDK is typically used to deal with non-uniform or redundant measurement as well as truncation. Fast convergence is also expected when sampling conditions are favorable, since the FDK reconstruction $f^{(1)}$ is already close to the desired solution.

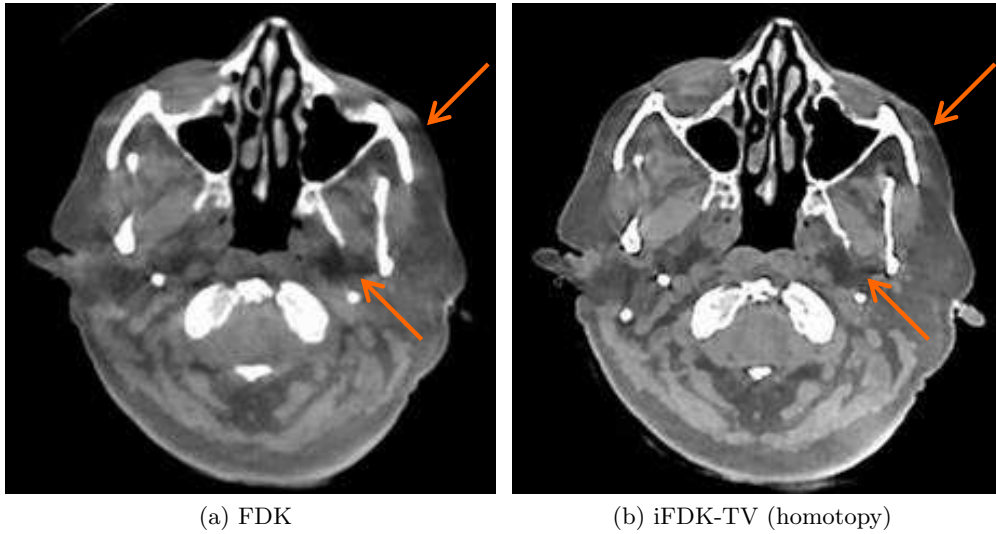


Figure 2.18 – FDK reconstruction of a head (a), and iFDK reconstructions with homotopy of the same dataset using total variation regularization (b). Isotropic voxel size: 0.78 mm^3 . Window level-width: 1100-1020. Source: (Langet et al., 2015).

Regularization can be added to Equation (2.34) via a convex, not necessarily differentiable penalty function $\chi(f)$ (Langet et al., 2015):

$$f_{\text{iFDK}} = \underset{f}{\operatorname{argmin}} \left\{ \frac{1}{2} (\mathcal{R}f - p)^T \mathcal{D}(\mathcal{R}f - p) + \chi(f) \right\}. \quad (2.36)$$

Such minimization problems can be solved iteratively using the forward-backward splitting algorithm, consisting in alternating one iFDK iteration (one gradient step) with a filtering step (proximity operator):

$$\begin{cases} f^{(i+1/2)} = f^{(i)} - \tau \cdot \text{FDK}(\mathcal{R}f^{(i)} - p) \\ f^{(i+1)} = \operatorname{prox}_{\tau\chi}(f^{(i+1/2)}) \end{cases}. \quad (2.37)$$

Here, we used the notation $\operatorname{prox}_{\tau\chi}(f^*)$ to denote the proximity operator of $\tau\chi$ at point f^* , defined as:

$$\operatorname{prox}_{\tau\chi}(f^*) = \underset{f}{\operatorname{argmin}} \left\{ \frac{1}{2} \|f - f^*\|^2 + \tau\chi(f) \right\}. \quad (2.38)$$

Proximity operator $\operatorname{prox}_{\tau\chi}(f^*)$ can be seen as a black box filtering step, depending on penalty $\chi(f)$. Often, we write $\chi(f) = \lambda \cdot \psi(f)$, and parameter λ may be decreased during the iterations (this approach is called homotopy or continuation). This reduces the bias induced by the penalty function, until λ reaches zero (un-biased solution).

Figure 2.18 compares two iFDK reconstructed images with the standard FDK reconstruction. The iFDK reconstructions used homotopy with 21 stages of either total variation or non-linear isotropic diffusion using Weickert's diffusivity

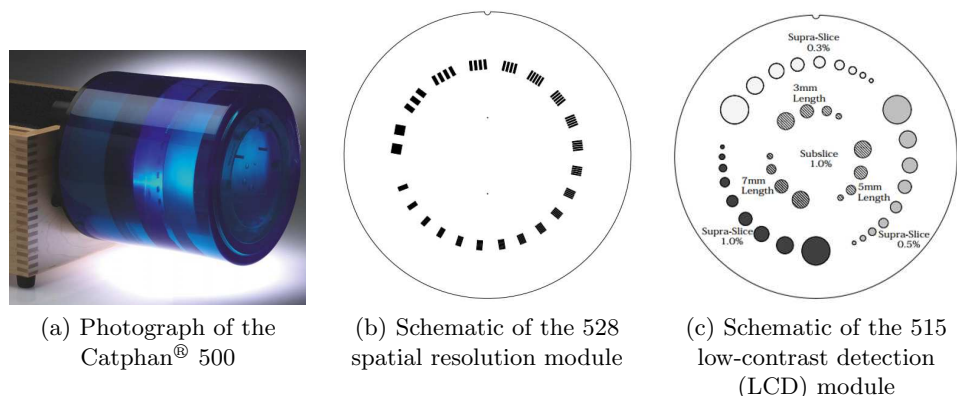


Figure 2.19 – The Catphan[®] 500 phantom (Goodenough, 2012).

map (Langet et al., 2015). The FDK image (Figure 2.18a) shows dark lines (highlighted by the arrows) that are cone-beam artifacts. These artifacts are removed by iFDK (Figures 2.18b, which yields much flatter images. Iterative reconstructions also display a higher resolution because it removes the smoothing effect of the apodization filter (Section 2.2.1.2).

2.2.2 Image quality assessment

C-arm CBCT image quality is assessed with respect to spatial resolution and contrast resolution (in particular, with respect to noise). Visual assessment of the impact of specific artifacts (motion streaks, geometric distortion, scatter-induced cupping artifact, etc.) may also be used. Evaluations are performed on quality assurance phantoms such as the Catphan[®] phantom, as well as on anthropomorphic phantoms.

2.2.2.1 The Catphan[®] 500 phantom

The Catphan[®] 500 phantom (Goodenough, 2012) is designed as a series of cylindrical modules, each of them testing a specific performance of the system (Figure 2.19). We focus on the performance of C-arm CBCT in terms of spatial resolution and low-contrast detection.

The Catphan[®] CTP 528 spatial resolution module (Figure 2.19b) is made of 21 groups of highly contrasted aluminium lines cast into epoxy. The lines are all oriented radially. The gap between two consecutive lines of one group is fixed, but it varies from one group to the other, resulting in different *line pairs per centimeter* (denoted lp/cm). Groups are ranged in increasing order from 1 lp/cm to 21 lp/cm. A visual assessment of the maximum number of differentiable line pairs per centimeter provides an information on the spatial resolution.

The Catphan[®] CTP 515 LCD module (Figure 2.19c) consists of a uniform water-equivalent cylinder with small cylindrical contrast inserts of various diameters. Relative contrasts of the inserts are 1%, 0.5% and 0.3%. Their diameters vary from 2 mm to 15 mm. The diameters of the central (subslice) inserts vary

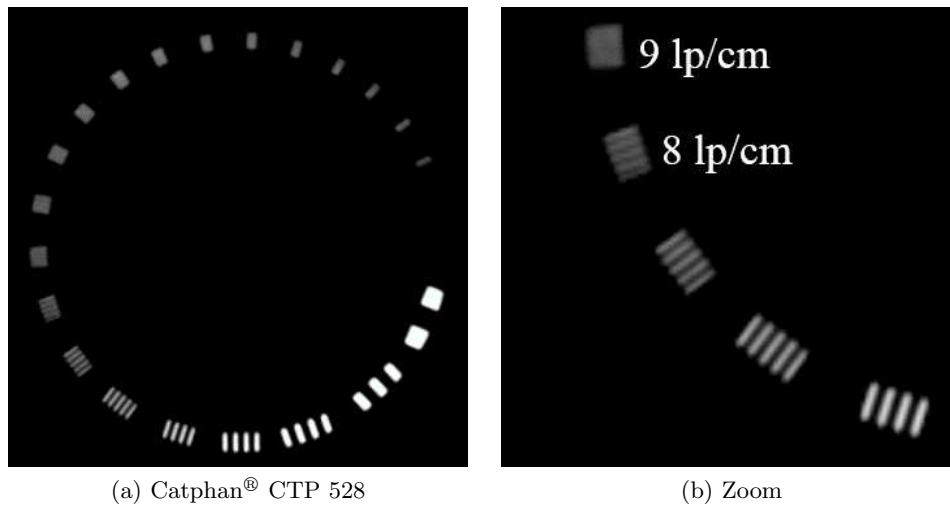


Figure 2.20 – IGS 740 C-arm CBCT of the Catphan[®] CTP 528 module. FDK reconstruction from 600 views covering 200° (Parker’s weights used), at SID = 1295 mm and SOD = 820 mm, on a 40 cm square FOV. Isotropic voxel size: 0.48 mm³. Window width: 1000 HU.

from 3 mm to 9 mm.

2.2.2.2 Spatial resolution

C-arm CBCT is known to achieve a very good spatial resolution. With a voxel size of 0.48 mm, the image of the Catphan[®] CTP 528 module reconstructed from a spin acquired on GE Healthcare IGS 740 at 16°/s, an SID of 1295 mm and an SOD of 820 mm, and on a 40 cm square FOV, achieves an 8 lp/cm spatial resolution (Figure 2.20). However, spatial resolution depends both on the voxel size and on the actual pixel size (which may be greater than 0.2 mm because of binning in large FOV sizes). With a voxel size of 0.96 mm, the resolution drops to 5 lp/cm. By contrast, with a voxel size of 0.48 mm and a spin acquired with the same parameters except that the FOV is now a 12 cm square, the resolution increases to 21 lp/cm. In comparison, diagnostic CT scanners achieve no more than 13 lp/cm.

2.2.2.3 Contrast resolution

In terms of low-contrast detection, however, C-arm CBCT underperforms diagnostic CT. This can be observed when reconstructing the Catphan[®] CTP 515 module, as shown in Figure 2.21. Figure 2.21a shows a 10 mm thick axial slice of the CT reconstruction of the CTP 515 module. The 1% contrast inserts are easily detectable, and 0.5% inserts can be visually detected from diameters 15 mm down to 7 mm. The 0.3% contrast inserts are more difficult to detect, but are still noticeable, in particular for the 15 mm and 9 mm inserts. Regarding subslice inserts, the axial averaging decreases their contrast values, but all the 9 mm inserts can be detected.

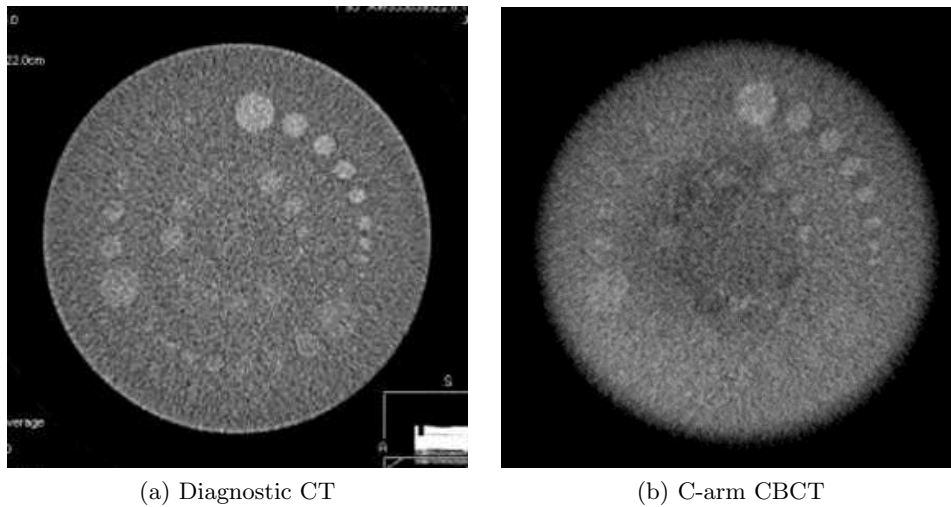


Figure 2.21 – Comparison between an IGS 740 C-arm CBCT and a diagnostic CT of the Catphan[®] CTP 515 module. (a) FBP reconstruction from a CT acquisition. Axial slices were averaged over 10 mm. Window width: 50 HU. (b) FDK reconstruction from 600 views covering 200° (Parker’s weights used), at SID = 1295 mm and SOD = 820 mm, on a 40 cm square FOV. Voxel size (mm³): 0.48 × 0.48 × 9.6. Window width: 50 HU.

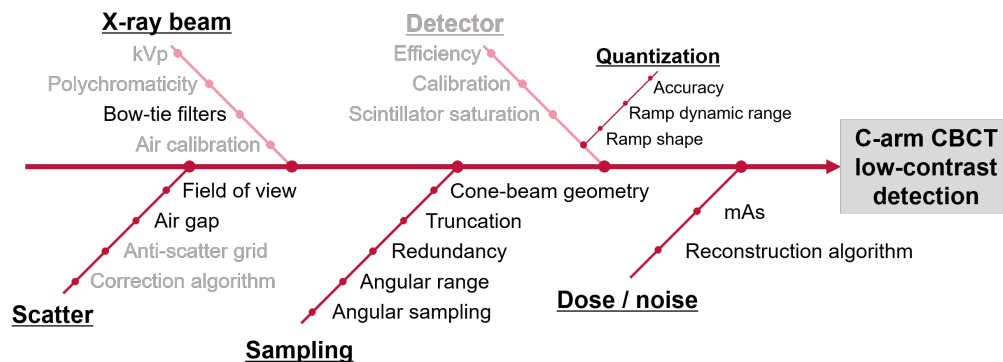


Figure 2.22 – Factors impacting low-contrast detection in C-arm CBCT. Factors that will not be covered by this thesis are shown in light gray.

On the other hand, the C-arm CBCT reconstruction of the same module (Figure 2.21b), averaged along the axial slice over 9.6 mm, does not perform well for contrasts lower than 1%. Of all the 0.5% contrast inserts, only the 15 mm and 9 mm inserts are visible, and the 0.3% inserts are almost lost. The background also appears less uniform than in the diagnostic CT image. The performance of C-arm CBCT, with respect to diagnostic CT, is even worse when looking at the central, subslice inserts, which are barely noticeable.

2.2.3 Factors impacting low-contrast detection in C-arm CBCT

Low-contrast detection in C-arm CBCT images depends on a number of factors all along the imaging chain. These factors are summarized in Figure 2.22. We describe them in the following paragraphs, and we highlight the key factors that will be the topic of this thesis: namely, scattered intensities, sampling issues, quantization, and dose (hence noise).

2.2.3.1 Quantum noise

Patient safety requires not to deliver unnecessary dose to the tissues. In particular, if a given dose achieves a good SNR on a particular area of the detector, it is not needed to increase dose on this area. Noise, however, is not uniform on the detector for a uniformly exposed patient. Because of the exponential decrease of Beer’s law, a small change in thickness yields a higher change in dose at the detector. The dose profile (hence the noise profile) may vary a lot on the detector. In particular, thin structures may be over-exposed to acquire thicker parts with enough SNR. Diagnostic CT scanners address this issue via the use of bow-tie filters (see Section 2.2.3.3), that flatten the dose profile with respect to the expected anatomy.

The influence of the reconstruction algorithm on the 3D noise behavior is also fundamental (Barrett et al., 1976; Fessler, 2000). FDK is not a statistical method: it does not handle the Poisson statistics of incoming photons. Instead, FDK images show a rather uniform noise distribution. The rationale behind this behavior is that FDK can be seen as the approximate solution to a Gaussian least-squares problem with constant variance model, as presented in Section 2.2.1.4.

Quantum noise is directly related to the amount of X-ray photons produced by the X-ray tube for a given spectrum (hence a given kVp value). The higher the tube current, the higher the number of photons, hence the lower the noise. C-arm systems do not address noise issues the same way as diagnostic CT scanners do, in particular because of the way the X-ray beam is pre-shaped in diagnostic CT (see Section 2.2.3.3). Therefore, we will need to investigate to which extent noise is responsible for poorer contrast resolution of C-arm systems with respect to diagnostic CT (see Chapter 3).

2.2.3.2 Detector non-idealities

The C-arm CBCT image quality also depends on the engineering design choices of the flat-panel detector. The detector efficiency, that is also related to 2D image noise, the scintillator properties, in particular in terms of X-ray saturation, may impact the overall low-contrast detection in the reconstructed images. However, the study of their actual influences is out of the scope of this work.

2D X-ray imaging with flat-panel detectors requires calibration procedures in order to account for defective pixels and for gain and offset deviations (Section 2.1.6.2). Each of these corrections needs to be done accurately, as a pixel with a deterministic bias backprojects this error as an arc of a circle in the axial slices of the reconstructed volume (“ring artifacts”). Note that since the recon-

struction step accumulates information from more than a hundred projections, ring artifacts may appear in the reconstructed volume even when the pixel bias does not impact the image quality of a single projection. The improvement of calibration steps to better handle pixel gain and offset biases is, again, a matter of engineering design choices, and is out of the scope of this work. Moreover, simple ring artifact post-correction methods (Prell et al., 2009), combined with current calibration procedures, are generally sufficient to remove most of the ring artifacts in the images.

Another factor impacting 3D low-contrast detection from the detector’s side is the analog-to-digital conversion (ADC) step, or quantization. Indeed, the aim of quantization is to represent X-ray intensities with a finite set of symbols. It is an irreversible process, and a source of information loss. In particular, saturation induced by the ADC step can be of much importance. IGS systems use a quantization step that significantly differs from the one used in diagnostic CT scanners. It is thus desirable to check whether this step is responsible for poorer contrast resolution of C-arm systems with respect to diagnostic CT (see Chapter 3).

2.2.3.3 X-ray beam

The X-ray beam quality also impacts C-arm CBCT low-contrast detection. For a given target entrance dose at the detector (thus a given noise level), it is desirable to keep the peak kilovoltage as low as possible (Nakayama et al., 2006). This means that the tube current should compensate for low kVp values, resulting in tube heating. By design, GE Healthcare in-house automatic exposure control (AEC) selects the best pair (kVp, mAs) for a target image quality metric. In this work, we do not intend to modify the AEC mechanism. When it is not used, we fix the kVp to a value such that for our target exposure levels, we are able to set the mAs accordingly.

As presented in Section 2.1.3.4, the X-ray beam is intrinsically polychromatic: the photon energies vary between 0 kV and the peak kilovoltage kVp. Hence, measured intensities are subject to the beam hardening effect. For a given intensity value on the detector, the line integrals are under-estimated, and this effect gets more dramatic as the path lengths increase. The result of this beam hardening effect is a low frequency cupping artifact in the reconstructed image (water beam hardening), as well as streaks along the paths where very dense objects (bone, iodine) are present. Although adequate beam filtration can already harden the incoming beam spectrum, additional processing steps are needed to correct for beam hardening artifacts.

Beam hardening is not specific to C-arm CBCT: diagnostic CT scanners also need to account for the polychromaticity of the X-ray beam. To do so, a water beam hardening pre-correction, along with a skull beam hardening post-correction, can be used (Joseph & Spital, 1978). These corrections rely on polychromatic corrections to recover a quasi-linear relationship between the log-transformed intensities and the true materials’ thicknesses, be it water or cortical bone. In practice, we observe that similar corrections in C-arm CBCT produce the same effects as in diagnostic CT, and we do not further explore the influence of polychromaticity on C-arm CBCT low-contrast detection.

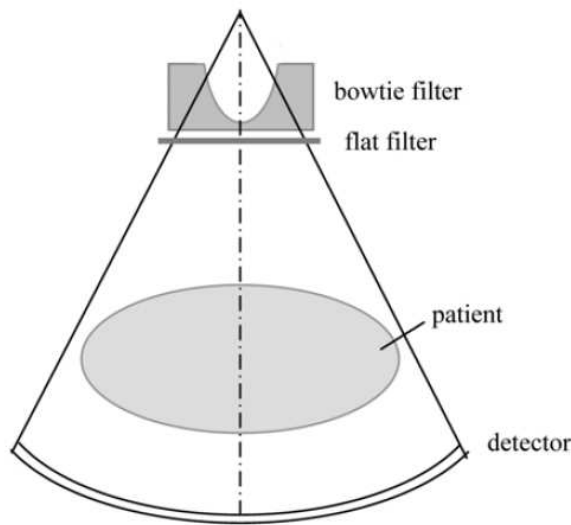


Figure 2.23 – Illustration of a bow-tie filter (Hsieh, 2009).

In order to reduce the dynamic range of the detector and improve the noise homogeneity, diagnostic CT scanners use additional physical beam shapers in front of the X-ray tube, called bow-tie filters (Figure 2.23). Their shapes are designed to compensate for the variable path lengths of the patient across the FOV: to this end, the filter thicknesses increase quickly from the center to the outer edge. In addition to providing flatter dynamic ranges and better dose profiles on the detector, bow-tie filters also significantly reduce the patient’s skin dose.

A major drawback of bow-tie filters is their dependency to a given patient shape. As a result, a single filter cannot be optimal for all anatomical scans, and multiple bow-tie filters should be available in order to use the more appropriate one depending on the patient’s size and anatomy. Moreover, bow-tie filters require an accurate centering of the patient anatomy: when the patient is off-centered with respect to the beam shapers, significant noise increase may result (Hsieh, 2009). The use of bow-tie filters with C-arm systems is still a research topic (Mail et al., 2009; Menser et al., 2010; G. Zhang et al., 2013). Lastly, we point out that bow-tie filters require an accurate, ray-dependent, open field intensity measurement or calibration. Although prior air calibration steps are able to transform open field intensities into a constant I_0 value on the detector, this value can only be estimated via in-house calibration models on C-arm systems.

We will build upon the concept of bow-tie filters to design a new acquisition and reconstruction framework in Chapter 3.

2.2.3.4 Scatter

Scattered intensities have a strong impact on C-arm CBCT low-contrast detection (Siewerdsen et al., 2014; Fahrig et al., 2014). Indeed, writing P the primary intensities given by Beer’s law and S the scatter intensities, the measured intensities

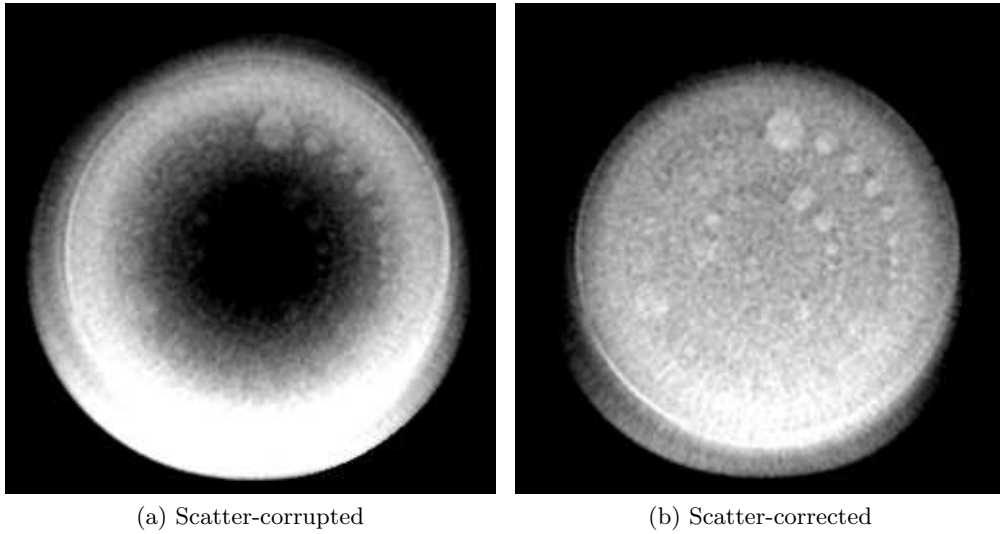


Figure 2.24 – Standard reconstruction from scatter-corrupted data of a Catphan[®] low-contrast detection module (a) and the same reconstruction (b) from scatter pre-corrected data (Siewerdsen et al., 2006). Window level-width: 1050-50 HU.

write $I = P + S$ and measured densities are given by:

$$p' = \log\left(\frac{I_0}{P+S}\right) = \log\left(\frac{I_0}{P(1+\text{SPR})}\right) = p - \log(1 + \text{SPR}), \quad (2.39)$$

where $p = \log(I_0/P)$ denotes the true line integrals. Equation (2.39) shows that measured line integrals are under-estimated, and that this under-estimation depends on the SPR. Typical values of SPR for head C-arm CBCT can be up to 1 or 2, where diagnostic CT scanners would show typical SPR values of 0.1 or 0.2. Image artifacts resulting from scattered radiations are of two forms: a low-frequency cupping strongly reducing contrast resolution (Figure 2.24a), and dark streaks between dense structures (Siewerdsen et al., 2014). Scatter rejection methods (Section 2.1.6.1) can still be used. However the air gap needs to be kept short in the case of head imaging (short SID) to prevent truncation artifacts in the reconstructed images (Section 2.2.3.5). The field of view also depends on the clinical application; reducing it is not always an option and may even generate truncation artifacts. Thus, most of scatter rejection is achieved by the anti-scatter grid. Because C-arm systems can easily change the SID, anti-scatter grids cannot be strongly focused on the X-ray source; moreover, the grid also partially attenuates the primary rays, thus limiting the performance of anti-scatter grids in terms of SPR. By contrast, diagnostic CT scanners have a fixed geometry, so that perfectly focused anti-scatter collimators can be used, in addition to bow-tie filters that reduce the SPR by up to 50% (Altunbas, 2014). Hence, scatter correction methods have been developed for C-arm CBCT. The scatter correction method used in IGS systems is based on the approach of (Siewerdsen et al., 2006). It is a measurement-based correction method (Rührnschopf & Klingensbeck, 2011a; Love & Kruger, 1987; Ning et al., 2004; Siewerdsen et al.,

2006; Liu et al., 2006; Rinkel et al., 2007). These methods make use of actual measurements of the phenomenon and are mathematically less demanding than system-theoretic approaches (Rührnschopf & Klingenberg, 2011a). Siewerdsen et al. (2006) make use of already embedded collimator blades to measure scatter at the borders of the field of view. The method relies on the assumption that the intensities measured in the shadow of the collimator blades are entirely due to scattered radiations. Samples of column-wise (in the case of vertical collimation) scatter intensity profiles are independently interpolated by polynomial functions, smoothed laterally and then smoothed again between consecutive views. Scatter estimates are then subtracted from measured intensities.

Scatter-induced artifacts are typical of C-arm CBCT. Diagnostic CT scanners, which have a fixed geometry, can use focused anti-scatter collimators, in addition to bow-tie filters that reduce the SPR by up to 50% (Altunbas, 2014). Alternative scatter correction methods have been proposed over the years (Rührnschopf & Klingenberg, 2011b, 2011a) and finding more precise scatter correction methods is still a research topic (Wiegert, 2007; Schörner, 2012; Bhatia, 2016). We thus keep in mind that reducing the contribution of scattered intensities is key for C-arm CBCT low-contrast detection. Although we do not intend to propose improved correction strategies in this thesis, we will design our solutions in such a way that they can be efficient in terms of scatter rejection, and in such a way that they may be further used to propose smarter scatter correction strategies, that are out of the scope of this work (see Chapter 6 for perspectives on scatter correction).

2.2.3.5 Sampling

The square shape of the detector defines a reconstruction cylinder of about 20 cm in height and diameter for a 30 cm flat-panel detector, which represents a small transaxial field of view: data truncation is thus the norm. Lateral truncation is forbidden by the FDK method, as the ramp filter needs complete row data. In head imaging, truncation is reduced by changing the magnification factor via a shorter SID, despite its bad influence on scatter. Interestingly, C-arm CBCT is often used to do region-of-interest (ROI) imaging, with limited contrast detection due to truncation artifacts. In diagnostic CT, truncation only occurs in case of wide anatomies and poor patient centering, typically in the case of abdominal imaging. In head imaging, however, CT scans never show truncation artifacts. This thesis will propose a way to handle truncated data both to enrich full-FOV projections for full-volume imaging and to perform ROI reconstruction.

As mentioned previously, C-arm systems do not perform a rotation of 360° around the anatomy of interest; instead, they cover an angular range of 200° , which corresponds to 180° plus the angular spread (fan angle) of the divergent beam in the source-detector plane. Even in this plane, which satisfies Tuy's conditions (Tuy, 1983), redundancy needs to be taken into account in the reconstruction. The simplest way of handling data redundancy is to apply Parker's weights prior to ramp filtering in the FDK method (Parker, 1982). Parker's weights create a smooth window that set to zero most of the redundant projection columns, do not alter most of non-redundant projection columns, and smoothly applies a

weight between 0 and 1 on a few projection columns. The smoothness is imposed by the fact that ramp filtering strongly enhances discontinuities. Note also that setting projection columns to zero is not optimal in terms of dose usage. Short-scan artifacts related to data redundancy, as well as cone-beam artifacts out of the midplane, will need to be handled by iterative reconstruction methods.

Angular sampling is also of much interest in C-arm CBCT. Indeed, in diagnostic CT, several hundreds of projections are acquired every 360° rotation of the X-ray tube, yielding a very fine angular sampling. In C-arm CBCT with IGS systems, for the same acquisition speed (frame rate) of 50 frames per second (fps) and the same angular coverage, three rotation speeds are available (Table 2.3), leading to spins of 250 to 600 views sampling a short-scan of 200° . For imaging the soft-tissue low contrasts, the rotation must be set to its lowest speed, leading to the highest number of views. However, it would be desirable to design reconstruction methods that could apply to coarser angular sampling as well.

2.2.4 Discussion

C-arm systems use a complex 2D X-ray imaging chain for real-time 2D image guidance. By letting the C-arm rotate around the patient, a tomographic acquisition can be performed and a fully three-dimensional image can be reconstructed.

Artifacts may corrupt the reconstructed image, either because the reconstruction algorithm did not account for all the aspects of the X-ray physics (polychromatic beam, scattered radiations), or because of system non-idealities (pixel biases, sampling). Most of these limitations disappear in diagnostic CT: excellent pixel calibration only leaves small residual ring artifacts in the image, that can be easily corrected; larger fields of view make it possible to perform head imaging without lateral truncation over 360° , and with excellent angular sampling. Bow-tie filters reduce the contribution of scattered intensities and flatten the dose profile, yielding narrower dynamic ranges on the detector, that are finely quantized. The residual scattered intensities are almost completely rejected by focused collimator blades.

From these observations, we conclude that the key factors in C-arm CBCT low-contrast detection are:

- scattered intensities, that need to be at least rejected as much as possible;
- sampling, as truncation needs to be accounted for, and angular sampling must be as fine as reasonably achievable;
- quantization, which seems much coarser on IGS systems than in diagnostic CT scanners;
- and dose (hence noise), since X-rays are not shaped with bow-tie filters on C-arm systems.

The next chapter will show that, although we listed four items here, quantization can be partially discarded as a key factor for low-contrast detection in C-arm CBCT. More precisely, we will show that saturation has a stronger impact on low-contrast detection than the actual number of quantization bins. The remaining

chapters will try to design optimal acquisition and reconstruction frameworks to increase low-contrast detection in C-arm CBCT, in such a way that they emulate bow-tie filters, reduce the contribution of scattered intensities in the reconstructed images, and account for the presence of truncated data, in particular for ROI imaging.

We end this chapter by a final remark. FDK was designed to reconstruct a static object from projections acquired over a circular source-detector trajectory. If the C-arm system vibrates during the spin, and if these vibrations are repeatable, geometric calibration procedures can be performed in order to better characterize projection matrices P_θ in Equation (2.16) with respect to system deformations. We will assume that all repeatable distortions have been taken into account in calibration procedures when performing our own acquisitions on C-arm systems. We also discard any additional object motion in our study. Perspectives on the applications of the results of this thesis to patients with head motion can be found in Chapter 6.

Virtual bow-tie C-arm CBCT

Chapter 2 described the fundamentals of 2D and 3D X-ray imaging with C-arm systems, as well as the factors impacting C-arm CBCT image quality. Scattered intensities, sampling, quantization and X-ray exposure (thus noise), were shown to be the key differences with respect to diagnostic CT. In this chapter, we show that, more than quantization, dose is a critical factor for low-contrast detection in C-arm CBCT. Building up on this observation, we investigate the capabilities of a dual-rotation C-arm CBCT framework to improve non-contrast-enhanced low-contrast detection for full volume brain imaging. The idea is to associate two spins: one over the full detector field of view (FOV) at low dose, and one collimated to deliver a higher dose to the central densest parts of the head. The method is intended to act as a virtual bow-tie. Full volume reconstruction of dual-rotation simulations and phantom acquisitions are shown to have increased low-contrast detection for less dose, with respect to a single-rotation acquisition.

Contents

3.1 A matter of noise	54
3.1.1 Impact of analog-to-digital conversion	54
3.1.1.1 Principle of analog-to-digital conversion	54
3.1.1.2 Ramp-based quantization	55
3.1.1.3 Actual ramp-based ADC	57
3.1.1.4 Quantization and low-contrast detection	58
3.1.2 Influence of dose increase	60
3.1.2.1 Experiments and results	60
3.1.2.2 Conclusion	60
3.2 Virtual bow-tie via the dual-rotation framework	62
3.2.1 Acquisition	62
3.2.1.1 Assumptions	62
3.2.1.2 Parameters	63
3.2.1.3 Virtual bow-tie	64

3.2.2	Reconstruction	64
3.2.2.1	Analytical reconstruction	64
3.2.2.2	Energy minimization	65
3.2.2.3	Ramp filtering operators	65
3.2.3	Experiments	66
3.2.3.1	Simulations	66
3.2.3.2	Acquisitions, reconstructions	66
3.2.3.3	Image quality measures	67
3.2.4	Results	69
3.2.4.1	Simulations	69
3.2.4.2	Real phantom data	69
3.3	Discussion and conclusion	75

3.1 A matter of noise

In this section, we reduce the key factors impacting low-contrast detection to quantization and noise, by focusing on a specific acquisition setting of the Catphan[®] CTP 515 LCD module. Firstly, for actual Catphan[®] 515 acquisitions, the 2D FOV height was set at its minimum, in order to reduce scattered radiations as much as possible. Lateral collimation was not applied in order to limit lateral truncation to its minimum as well. Moreover, we will focus on central slices, so that cone-beam artifacts are not expected to impact the observed image quality. Since the Catphan[®] 515 module is a uniform water-equivalent cylinder with small contrast inserts, the only beam hardening effect that can be observed is due to water: in this case, a water beam hardening pre-correction method is enough to account for the polychromaticity of X-rays. Lastly, acquisitions are performed at the slowest rotation speed, leading to the highest number of views for accurate tomographic reconstruction.

Hence, only quantization and noise remain as factors impacting low-contrast detection in the image. In the following, we describe the principles of analog-to-digital conversion (ADC) and how it is performed on IGS systems. We then simulate fan-beam acquisitions with and without quantization, in order to evaluate the impact of the ADC step on low-contrast detection. We then show that, more than quantization, dose is a critical factor for low-contrast detection in C-arm CBCT.

3.1.1 Impact of analog-to-digital conversion

3.1.1.1 Principle of analog-to-digital conversion

Once X-rays are converted into electronic charges, they are further converted into digital numbers through analog-to-digital conversion (ADC). The ADC step essentially defines a subdivision of the real line $-\infty = q_{-1} < q_0 < \dots < q_B < q_{B+1} = +\infty$, and assigns a constant quantized value Q_i to each interval $[q_{i-1}, q_i[$. The quantization step can thus be defined as a function \mathcal{Q} such that:

$$\mathcal{Q}(I) = \sum_{i=0}^{B+1} Q_i \mathbb{1}_{[q_{i-1}, q_i[}(I). \quad (3.1)$$

In the ideal case of noise-free measurements for the toy example of Figure 2.13, if $\mathcal{Q}(I_2)$ does not under- or over-saturate (namely, if $\mathcal{Q}(I_2) = Q_i \notin \{Q_0, Q_{B+1}\}$), then I_1 and I_2 are quantized on two different values if and only if:

$$I_2 - I_1 = I_2 \left(1 - e^{-\Delta\mu\Delta L}\right) > \delta_i = Q_i - q_{i-1}. \quad (3.2)$$

Hence, quantization limits contrast resolution, since Equation (3.2) yields:

$$\Delta\mu\Delta L > -\log\left(1 - \frac{\delta_i}{I_2}\right). \quad (3.3)$$

In practice, however, thank to the random nature of X-ray photon statistics, the lower detectable contrast can be lower than the one given by Equation (3.3) (see for example (Lipshitz et al., 1992) for an analysis of the impact of noisy samples on quantization).

Quantization also bounds the admissible dynamic range: if one needs to image a material with attenuation μ and with thicknesses L ranging from L_{\min} to L_{\max} , the incoming X-ray intensity I_0 should be such that:

$$I_0 e^{-\mu L_{\min}} \leq q_B \text{ and } I_0 e^{-\mu L_{\max}} > q_0, \quad (3.4)$$

hence:

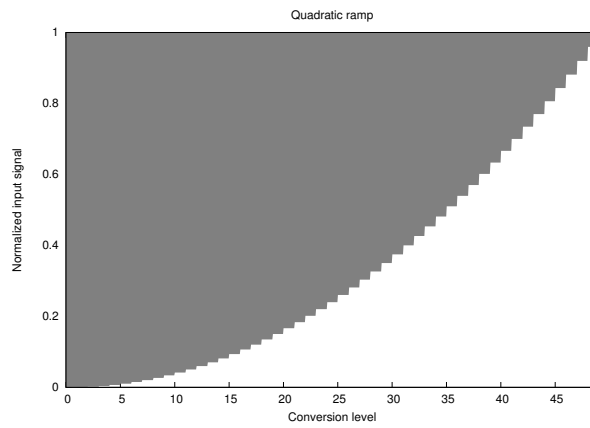
$$q_0 e^{\mu L_{\max}} < I_0 \leq q_B e^{-\mu L_{\min}}. \quad (3.5)$$

The choice of I_0 remains a compromise between high CNR values, admissible dose levels, and achievable detector dynamic ranges. If I_0 is too high, quantization will be blind to a range of small thicknesses μL between 0 and $\log(I_0) - \log(q_B)$, which may lead to heavy information loss.

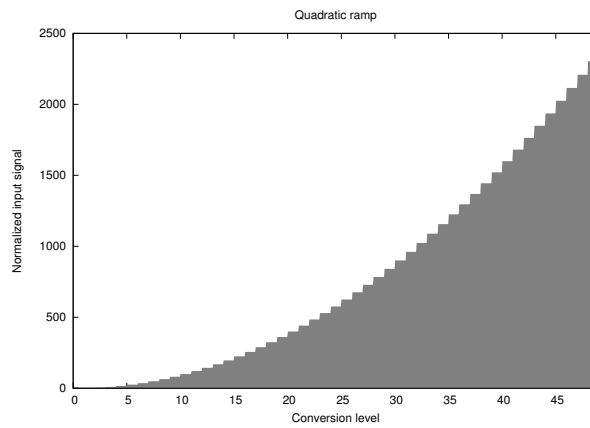
3.1.1.2 Ramp-based quantization

The definition of the ADC subdivision $\{q_i\}_i$ depends on the noise distribution of the input signal. Linear quantization corresponds to a uniform subdivision $q_i = q_0 + \frac{i}{B}(q_B - q_0)$ and to a uniform noise distribution. Quantization can also be performed via a non-linear transfer function, which means that the quantization step $\delta_i = q_i - q_{i-1}$ between two coded values is not constant. The rationale for non-linear quantization comes from the X-ray photon statistics. If I is the input signal then $\sigma \propto \sqrt{I}$, since the variance of a Poisson distribution is proportional to its mean (because of the blur induced by detector cells, σ^2 is not strictly equal to \sqrt{I} , typically $\sigma = c\sqrt{I}$ with $c \approx 0.6$).

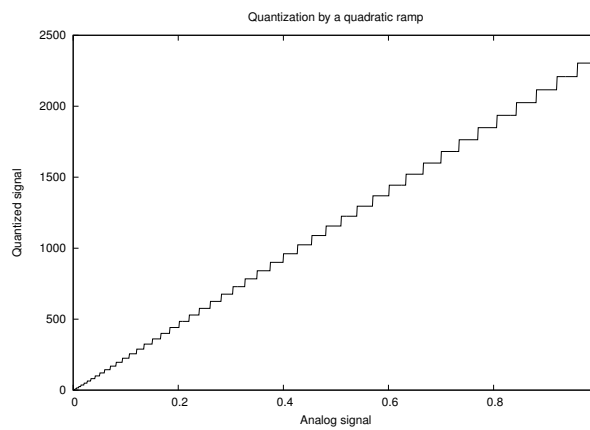
It is tempting to choose δ_i so that it does not quantize below quantum noise, *i.e.*, $\delta_i \propto \sqrt{I}$, which makes it possible to increase the signal range of the analog-to-digital converter, while keeping the number of bits to a minimum. An example of such a quantization is given in Figure 3.1. The x -axis represents the number of conversion levels. In Figure 3.1a, the gray bins assign values of the interval $[0, 1]$ to each conversion level according to a quadratic ramp function. The same ramp shape is used to re-map each of these 50 indexes to digits (gray bins in Figure 3.1b) varying linearly (up to the quantization error) with the analog input value (Figure 3.1c), with a quantization step proportional to the square root of the input analog signal. The quantized values range from 0 to 2401, so we need $\lceil \log_2(2401) \rceil = 12$ bits to store our 50 samples in this example.



(a) Input ramp

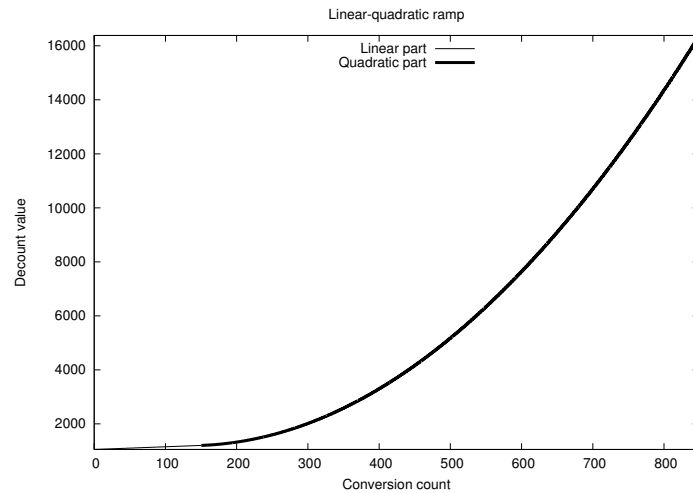
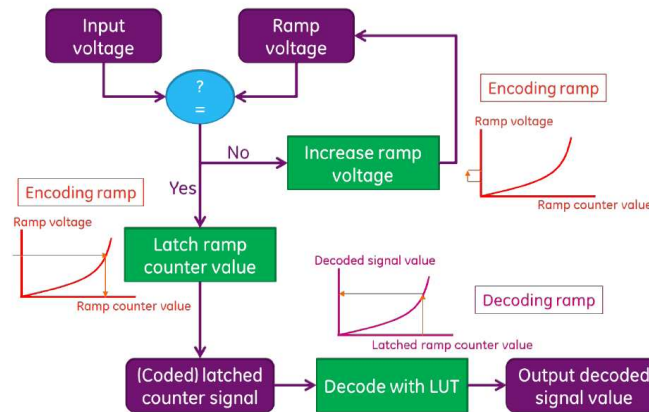


(b) Output ramp



(c) Transfer function

Figure 3.1 – Example of a quadratic input ramp (a) quantizing $[0, 1]$ on 50 levels and its corresponding output ramp (b) remapping these 50 levels to integer values. These integer values are the quantized input signal values. The quantized values vary linearly with the analog values (c), with a non-uniform quantization step.

(a) IGS 5X-6X Record 30 fps-high (2×2 binned).

(b) Actual ramp comparison process.

Figure 3.2 – Actual linear-quadratic output ramp (a) and two-step ramp comparison process (b) in Apollo Readout Chips.

3.1.1.3 Actual ramp-based ADC

Because the offset map needs to be stored with enough accuracy, a linear ramp is defined in a range corresponding to the offset zone, with a typical quantization step of 1 or 2. The rest of the ramp is quadratic, with a C^1 -continuity between both portions of this linear-quadratic ramp function (Garverick & Michon, 1994; Granfors, 1999; Granfors & Aufrichtig, 2000; Wrigley et al., 2014). It is expected that quantized X-ray photons hit the quadratic portion of the ramp, unless the entrance dose is very low. The ramps used for CBCT quantize on 850 conversion levels that spread over a 14-bit dynamic range (Table 3.1). An example of such ramps and of the actual ADC step is shown in Figure 3.2. Up to 47% of these conversion levels may be used for the linear part of the ramp. The 14-bit quantized signal is further compressed to a 12-bit image by applying a square-root shaped

<i>Parameters</i>	<i>Low-dose</i>	<i>Medium-dose</i>	<i>High-dose</i>
Lower bound	1053	1053	1053
Upper bound	16383	16383	16383
Total conversion levels	850	850	850
Saturating dose (nGy)	1900	4680	7590
Linear upper bound	1853	1653	1353
Linear conversion levels	400	300	300
Linear quantization step	2	2	1

Table 3.1 – Ramp specifications in IGS 540 (CBCT 2×2 binned modes).

function, that uniformizes noise in the image. This 12-bit square-root encoding is of course further decoded prior to reconstruction. Note that as compared to diagnostic CT scanners, that benefit from a full 24-bit linear quantization, C-arm systems seem to be limited by the lower dynamic range and the even smaller number of actual quantization bins.

3.1.1.4 Quantization and low-contrast detection

Studies of the influence of quantization on image quality have already been published (Knaup et al., 2012; J. Xu et al., 2016a) but they rely on a linear quantization over 2^q conversion levels, where q is the bit depth of the dynamic range. This is very different from sampling $N \ll 2^q$ quantization values non-uniformly spread over 2^q values.

In order to determine the effect of quantization on low-contrast detection, we performed a simulation study in the 2D fan-beam geometry with a linear detector. Analytical full-scan (1440 views sampling 360°) density sinograms of a 2D phantom similar to the CTP 515 were generated and converted into intensities using Beer’s law. The value of I_0 was set to an arbitrary value and at each detector bin an additional zero-mean Gaussian noise with variance proportional to the initial intensity value ($\sigma^2 = \kappa I_0 e^{-p}$, where $\kappa > 0$ and p is the density projection) was generated.

We simulated a quantization through a quadratic ramp with a slope of 1 at the origin and spreading 850 conversion levels between 0 and 16383. Hence, quantization is over 14 bits. The quantized, noisy intensity sinograms were further re-converted into density sinograms and reconstructed by the FBP method. Reconstructed images were compared to density sinograms obtained from the non-quantized, noisy intensity sinograms. The final images were also applied a Gaussian filter. The Gaussian standard deviation and the coefficient of proportionality κ were set empirically to match the noise level and the spatial resolution of standard reconstructed volumes from IGS C-arm tomographic acquisitions with fixed techniques (76 kVp, 3.4 mAs).

Results of the simulation are shown in Figure 3.3. We first simulated four acquisitions with $I_0 = 16383$, so that the full dynamic range fits in the quantization ramp (Figure 3.3a). Although it is difficult to identify contrast inserts with relative contrasts lower than 1%, they can be detected more easily when averaging

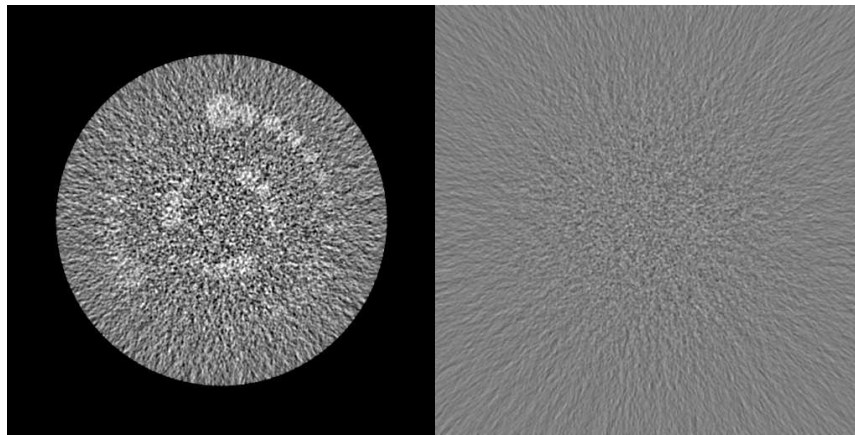
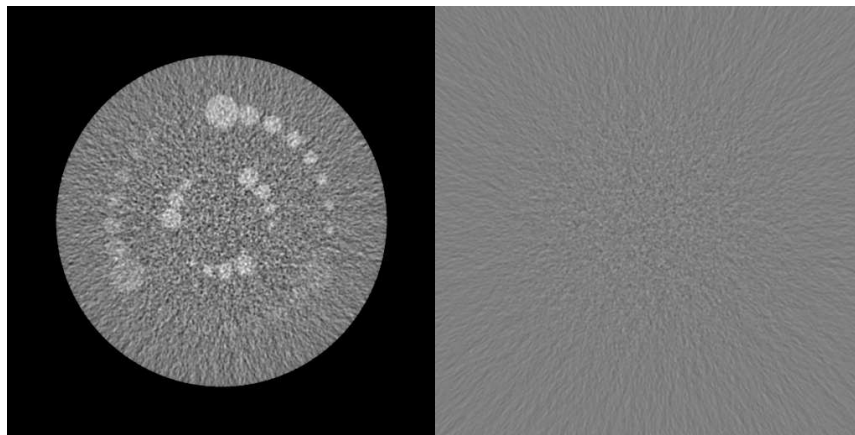
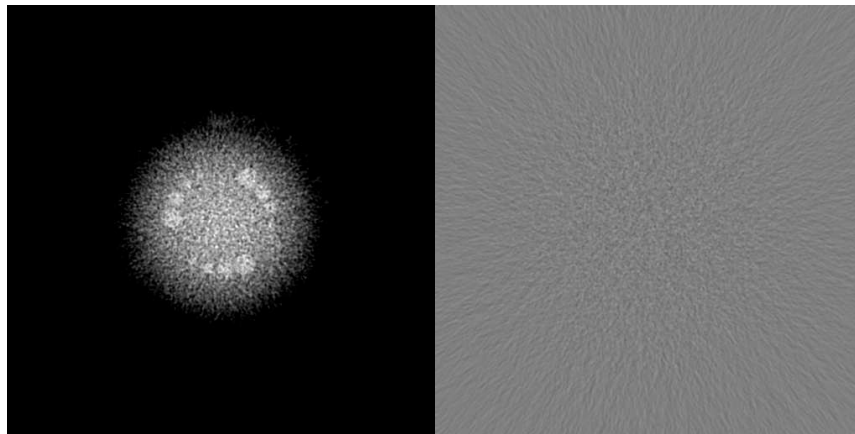
(a) $I_0 = 16383$ (b) Average of 4 acquisitions, $I_0 = 16383$ (c) $I_0 = 4 \times 16383$

Figure 3.3 – Effect of quantization on low-contrast detection. The quantization ramp is quadratic with slope 1 at the origin and spreads 850 conversion levels between 0 and 16383. Residual images on the right are the obtained by subtracting to the left columns the reconstructed images from non-quantized sinograms. Window level: 50 HU.

the images reconstructed from the four acquisitions (Figure 3.3b). Moreover, the difference between this averaged image and the averaging of the images reconstructed from the four non-quantized acquisitions does not show any structural information. However, both dose and quantization were increased by averaging four noisy reconstructed images. We thus simulate an additional acquisition at $I_0 = 4 \times 16383$, and we clip intensity values larger than 16383 to this value even in the non-quantized case (Figure 3.3c). The central contrast inserts become clearly visible, although saturation of intensities higher than 16383 yields a strong non-uniformity in the reconstructed image.

The simulation study tends to show that the current quantization design, despite the small number of quantization levels in comparison with diagnostic CT, is sufficient to reconstruct low-contrast inserts. Quantum noise, on the other hand, is of much importance if one wishes to detect low-contrast inserts.

3.1.2 Influence of dose increase

3.1.2.1 Experiments and results

Experiments We acquired four spins of the Catphan[®] CTP 515 at (76 kVp, 3.4 mAs) with 0.3 mm of copper filtration on an IGS 630 biplane system whose flat-panel detector is 30 cm wide. In order to increase the dose by a factor 4, a shifted spectrum at 120 kVp was used to acquire a fifth spin, all other parameters being equal. Note that the influence of X-ray spectrum is neglected here. We compare the FDK reconstructed images with Parker's weights from the high-dose spin with the image reconstructed from one regular-dose spin, and with the average of four images reconstructed from regular-dose spins.

Results FDK reconstructed Catphan[®] phantoms are shown in Figure 3.4. As in the simulated case, the regular-dose FDK reconstruction is too noisy to identify the central low-contrast inserts (Figure 3.4b), although they become visible if one averages four such reconstructed images (Figure 3.4d). Figure 3.4e shows an inverse cupping that is due to the ramp saturation on the detector, which yields a strong low-frequency non-uniformity in the reconstructed image. Despite this non-uniformity, the central low-contrast inserts are visible (Figure 3.4f).

3.1.2.2 Conclusion

The simulation study tends to show that the current quantization design, despite the small number of quantization levels in comparison with diagnostic CT, is sufficient to reconstruct low-contrast inserts. Quantum noise, on the other hand, and detector saturation, on the other hand, are of much importance if one wishes to detect low-contrast inserts.

Experiments on the Catphan[®] CTP 515 module confirm the simulation study: dose is definitely a critical factor, as we observe that low-contrast inserts are visible at high dose. Of course, multiplying the dose by a factor 4 is not possible in practice, as peripheral areas are over-exposed, yielding to saturation on the detector and non-uniformities in reconstructed images. If saturation is only due

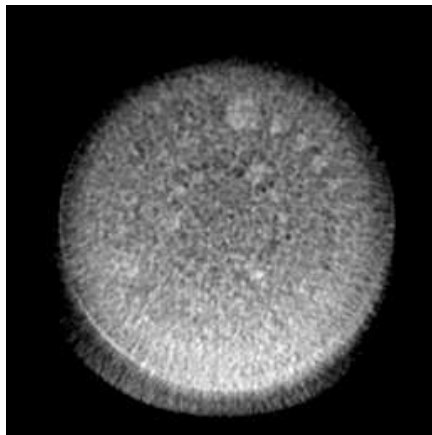
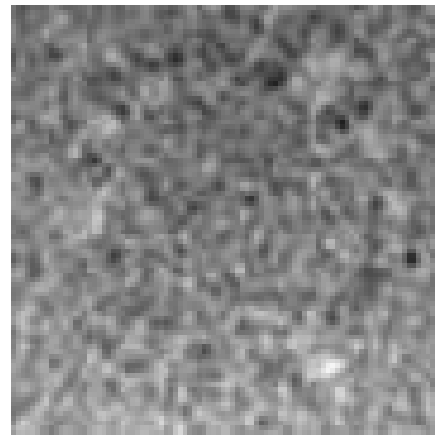
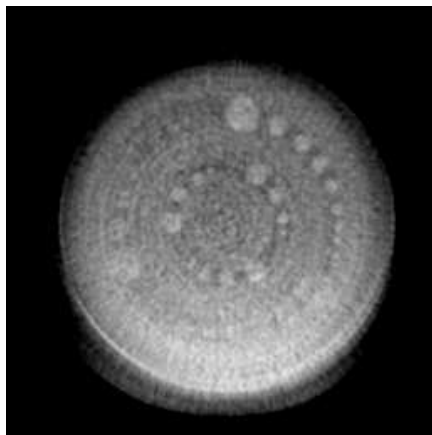
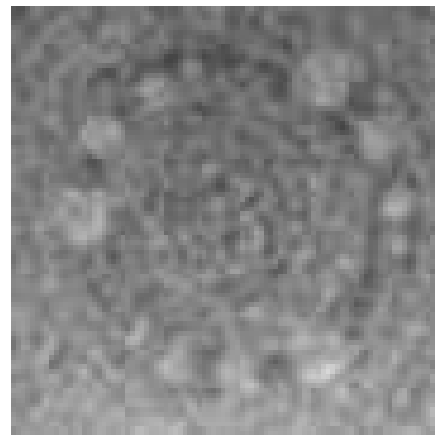
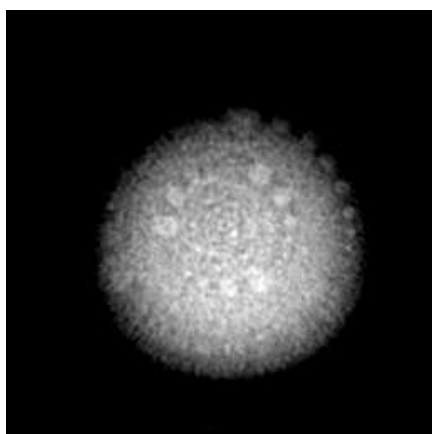
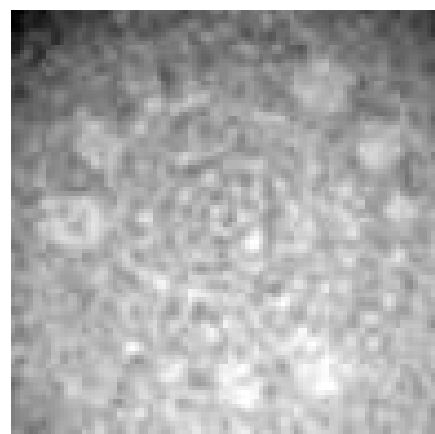
(a) 1 acquisition at dose $\times 1$ (b) 1 acquisition at dose $\times 1$ (c) 4 acquisition at dose $\times 1$ (d) 4 acquisition at dose $\times 1$ (e) 1 acquisition at dose $\times 4$ (f) 1 acquisition at dose $\times 4$

Figure 3.4 – Influence of dose on low-contrast detection of a Catphan[®] CTP 515. Image (b) (resp. (d), (f)) is a zoom of image (a) (resp. (c), (e)). Voxel size (mm³): $0.78 \times 0.78 \times 4.68$. Window level-width: 1070-50 HU (a), (b), (c), (d); 1085-50 HU (e), (f).

to the readout (and not to the scintillator), a dual-gain readout (Roos et al., 2004; Matsinos & Kaissl, 2006; Schmidgunst et al., 2007) providing a double reading of the input signal (one quantizing accurately low-signal values, one doing the same for high-signal values) may get rid of quantization artifacts. However, this solution does not address over-exposure. A physical bow-tie filter would help preventing saturation.

3.2 Virtual bow-tie via the dual-rotation framework

The mechanical flexibility provided by C-arm systems does not allow for efficient scatter rejection and the small number of C-arm CBCT acquisitions of brain soft tissues that need to be performed per day does not warrant the expensive integration of a bow-tie filter dedicated to this specific imaging task. Without a bow-tie filter, higher intensities must be recorded on the detector together with a wider dynamic range. This is a challenge for flat-panel detectors, that must be addressed by improved detector readout (Sukovic & Clinthorne, 2001; J. Xu et al., 2016b) or exposure (Sisniega et al., 2013; Ritschl et al., 2013). Higher scatter fraction must be corrected separately prior to reconstructing the image (Zellerhoff et al., 2005; Siewerdsen et al., 2006). There is thus an interest in designing an acquisition with a non-uniform exposure delivering better measurements with less dose to the patient.

We propose to study the capabilities of a dual rotation acquisition to improve low-contrast detection when imaging the full brain without administration of contrast agent in C-arm CBCT. The proposed dual rotation consists of two short-scan spins, one over the full detector FOV and the second with a detector FOV that is reduced by collimation. The second spin is truncated to bring more dose to the center of the patient’s anatomy. This acquisition can sample the brain with two degrees of freedom: (i) the aperture of the truncated spin, (ii) the dose ratio between both spins. They allow us to emulate a bow-tie filter to increase low-contrast detection. This work has been published in (Reshef et al., 2016, 2017a).

3.2.1 Acquisition

3.2.1.1 Assumptions

Ideal system measurements are intensity projections I related to density projections p via Beer’s law $I = I_0 e^{-p}$ where I_0 is the intensity of the X-ray beam measured in air. We assume that prior calibration steps transformed the open-field intensities into a constant I_0 value on the detector. Intensity projections are related to object density f through a linear projection operator \mathcal{R} such that $\mathcal{R}[f] + \log(I) = \log(I_0)$. Of course, real data are also corrupted by noise and scattered radiations.

We consider two sets of intensity projections (Figure 3.5): one set of full-FOV projections (indexed by F), and one set of truncated projections (indexed by T). In order to mimic a bow-tie filter for dose optimization, the full-FOV spin is acquired at low dose – this prevents unnecessary patient dose – while the

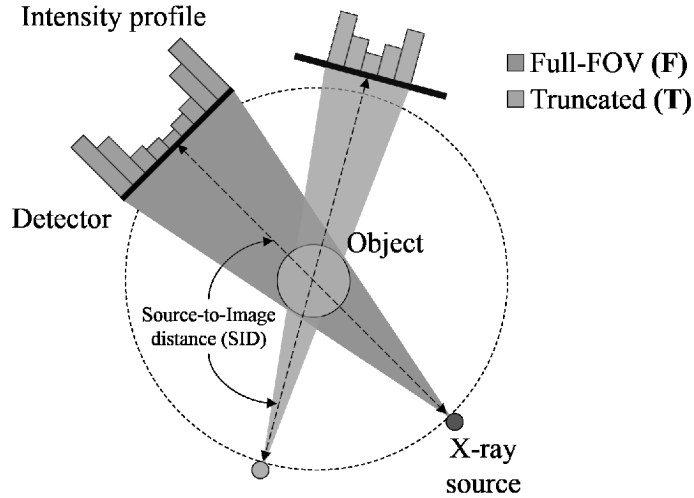


Figure 3.5 – Dual-rotation acquisition: a set of N_T truncated projections is acquired at the dose required by the central thickest areas and a set of N_F full-FOV projections is acquired at a lower dose, sufficient for the less dense, external areas.

truncated spin is acquired at a higher dose to achieve an exposure target at the center of the imaged object that is thicker. In the following, we assume that the number of views in each tomographic acquisition is approximately the same, and we denote by N this number.

We intend the dual-rotation acquisition to be as little restrictive as possible:

- we do not assume to know the exposure ratio between the full-FOV spin and the truncated spin, even though truncated data do not contain a reference air measurement of the incoming X-ray beam;
- we do not assume the geometry to be the same for each acquisition; in particular, the angular sampling may vary both in terms of angular positions; however, in this work, we assume that both acquisitions have the same number of projection views.

3.2.1.2 Parameters

The flexibility of the dual-rotation acquisition comes from two degrees of freedom.

- (i) First, although one acquisition is always assumed to be full-FOV, the opening of the truncated FOV is a free parameter; we denote by t , $0 < t \leq 1$, the level by which truncation reduces the exposed detector area as compared to the un-collimated case¹.
- (ii) Secondly, we do not impose any constraint on the intensity ratio that is used between the two acquisitions: if I_0^F denotes the air intensity corresponding

¹Parameter t is actually a ratio of 2D FOV areas; if the truncated (resp. full-FOV) 2D FOV height is h_T (resp. h_F) and its width is w_T (resp. w_F), then t is defined as: $t = \frac{h_T \cdot w_T}{h_F \cdot w_F}$. Since in general, $h_T = h_F$, the truncation ratio t becomes a ratio of 2D FOV widths.

to the exposure at the center of the object achieved with the full-FOV spin and I_0^T is the intensity of the truncated spin, we write $x = I_0^T/I_0^F$, so that the actual exposure at the center of the object is equal to $(1+x)I_0^F$ in the dual-rotation acquisition. Putting aside a dual-energy approach, x is simply the mAs ratio.

3.2.1.3 Virtual bow-tie

To emulate a bow-tie that increases low-contrast detection over the full volume, we choose $x \geq 1$. Truncation is controlled by t and depends on the targeted dose optimization.

We define the dose reduction factor d as how much dose to the object is saved with the dual-rotation acquisition as compared to an equivalent single-rotation, full-FOV acquisition achieving the same exposure level at the center of the object. This factor is thus equal to:

$$d = \frac{I_0^F + I_0^T}{I_0^F + t \cdot I_0^T} = \frac{1+x}{1+tx}. \quad (3.6)$$

3.2.2 Reconstruction

Given (t, x) , we define the contribution of the full-FOV acquisition to the overall dose as:

$$\alpha_F = \frac{I_0^F}{I_0^F + t \cdot I_0^T} = \frac{1}{1+tx}. \quad (3.7)$$

Reciprocally, we define the contribution of the truncated acquisition as $\alpha_T = 1 - \alpha_F$.

3.2.2.1 Analytical reconstruction

If intensity spins I_T and I_F were acquired at the very same angular positions, the data could be blended according to:

$$p = \begin{cases} \alpha_F \cdot p_F + \alpha_T \cdot p_T & \text{in the collimated area,} \\ p_F & \text{elsewhere.} \end{cases} \quad (3.8)$$

Equation (3.8) is sensitive to offset errors in p_F or p_T . In C-arm CBCT, projections are acquired with short-scan spins. They are reconstructed with the Feldkamp-Davis-Kress (FDK) algorithm (Feldkamp et al., 1984) using Parker's weights to account for data redundancy (Parker, 1982). We denote $f_{\text{FDK}} = \mathcal{B}\mathcal{D}[p_w]$ this analytical reconstruction, with p_w the Parker-weighted version of density projections p , \mathcal{D} the ramp filter and \mathcal{B} the backprojection operator. In the discrete case, $\mathcal{B} = \mathcal{R}^T$, the transpose of the projection operator \mathcal{R} .

If acquisition geometries are different, there is no standard solution and for each situation clever re-sampling or extrapolation of the truncated data must be derived. We instead propose a unique iterative algorithm to handle all dose and sampling configurations.

3.2.2.2 Energy minimization

We define two quadratic forms for $n \in \{\text{F}, \text{T}\}$:

$$\mathcal{Q}_n(f) = \frac{1}{2}(\mathcal{R}_n f + \log(I_n))^T \mathcal{D}_n(\mathcal{R}_n f + \log(I_n)), \quad (3.9)$$

where \mathcal{R}_F (resp. \mathcal{R}_T) is the projection operator for the untruncated (resp. truncated) geometry, and \mathcal{D}_F (resp. \mathcal{D}_T) is the ramp filtering operator for untruncated (resp. truncated) signals.

Since $\log(I_n)$ is known instead of the density projections p_n , we cannot reconstruct an image f such that $\mathcal{R}_n f + \log(I_n) = \log(I_0^n)$ but only such that:

$$\mathcal{D}_n(\mathcal{R}_n f + \log(I_n)) = \mathcal{D}_n(\log(I_0^n)) = 0. \quad (3.10)$$

Consequently, \mathcal{D}_n must remove any unknown offset $\log(I_0^n)$.

We minimize both data fidelity terms simultaneously through:

$$\operatorname{argmin}_f \left\{ \sum_{n \in \{\text{F}, \text{T}\}} \alpha_n \mathcal{Q}_n(f) + \chi(f) \right\}, \quad (3.11)$$

where $\chi(f)$ is a convex regularizing term. Quadratic forms like $\mathcal{Q}_n(f)$ have already been used (Langet et al., 2015) with sparsity-enforcing regularizers to correct for angular sub-sampling and cone-beam artifacts. Dual-rotation however is aimed at avoiding the need for a strong *a priori* like sparsity. Therefore, we use a small quadratic regularization $\chi(f) = \lambda \|\nabla f\|^2$ that is known to induce a Gaussian diffusion with full width at half maximum (FWHM) equal to $3.33\sqrt{\lambda}$ (Riddell et al., 2004). Following Langet et al. (2015), we solve Equation (5.3) using a forward-backward splitting scheme:

$$\begin{cases} f^{(i+1/2)} &= f^{(i)} - \tau \sum_{n \in \{\text{F}, \text{T}\}} \alpha_n \mathcal{R}_n^T \mathcal{D}_n(\mathcal{R}_n f^{(i)} - p_n) \\ f^{(i+1)} &= \operatorname{prox}_{\tau\chi}(f^{(i+1/2)}) \end{cases}. \quad (3.12)$$

3.2.2.3 Ramp filtering operators

Row-wise ramp filtering of the projection data is usually performed in the Fourier space. It has been reported (Zeng, 2015) that, for accurate FDK reconstruction, the discrete ramp filter should be computed as the Fourier transform of the finite spatial ramp kernel. Yet this results in a non-zero DC value, which does not satisfy $\mathcal{D}_n(\log(I_0^n)) = 0$.

Instead we take advantage of the decomposition of the ramp filter into a derivative operator ∂_u and a Fourier-based Hilbert transform \mathcal{H} . Applying ∂_u guarantees that $\mathcal{D}_n(\log(I_0^n)) = 0$. We write:

$$\mathcal{D}_\text{F} = \mathcal{H}\partial_u. \quad (3.13)$$

In the case of \mathcal{D}_T , ∂_u is local and applied within the truncated FOV. However, the Fourier-based Hilbert transform needs data extrapolation. The residual $\mathcal{R}_\text{T} f + \log(I_\text{T})$ is expected to converge to a constant that cannot be zero-padded.

Instead, extrapolation of $\partial_u(\mathcal{R}_T f + \log(I_T))$ with zeroes prior to computing the Fourier-based Hilbert transform makes perfect sense. However, non-idealities in the data may still introduce some undesirable discontinuities near the truncation boundaries. To ensure a smooth transition, a Hanning window is applied to the residual *after* it is differentiated. The minimization problem (5.3) thus actually uses two different operators \mathcal{D}_F and \mathcal{D}_T , where \mathcal{D}_F is defined in Equation (3.13) and:

$$\mathcal{D}_T = \mathcal{H}W\partial_u, \quad (3.14)$$

with W being the Hanning apodization operator.

3.2.3 Experiments

3.2.3.1 Simulations

We arbitrarily fixed $x = 4$, and determined through simulations which truncation width t would provide the best approximation to a true bow-tie to flatten the noise distribution in the reconstructed images. An analytical density sinogram p was computed and consisted of 600 profiles in parallel-beam geometry of a centered disk with diameter 15 cm and density $\mu = 0.376 \text{ cm}^{-1}$. The value of I_0^F was fixed to 10^5 to generate two intensity sinograms I_F and I_T corrupted by Gaussian approximations of Poisson noise, further transformed into noisy densities $p_F = \log(I_0^F) - \log(I_F)$ and $p_T = \log(I_0^T) - \log(I_T)$. Sinogram p_T was then digitally truncated by keeping a fraction t of the initial FOV (Figure 3.8a). Projections p_F and p_T were then blended according to Equation (3.8). The blended sinogram is equivalent to a single acquisition at high-dose, using an ideal beam filter that absorbs five times more energy at its peripheries. We generated 100 pairs of noisy sinograms at low and high dose, yielding 100 reconstructed images per value of t .

We also generated 100 sinograms using $I_0 = I_0^T + I_0^F$ and a simulated bow-tie filter perfectly compensating the shape of the disk, by computing a flat, noisy sinogram further divided by the gain map of the bow-tie filter. All reconstructions were performed using data blending and analytical (FBP) reconstruction. Maps of the pixel-wise standard deviation were computed using all replicate reconstructions. Since the simulated phantom is rotationally invariant, we computed a radial averaging to obtain radial profiles characteristic of the noise distribution.

3.2.3.2 Acquisitions, reconstructions

We tested the dual-rotation framework on the CTP 515 and on two anthropomorphic head phantoms. One head phantom contains a few brain soft-tissue-like structures, the other is a skull filled with a uniform tissue-equivalent material.

Acquisitions were performed on an IGS-740 C-arm system. The IGS-740 flat-panel detector has a size of 40 cm \times 40 cm, resulting in 500 \times 500 projection images with pixels of size 0.8 mm \times 0.8 mm.

The source-to-object distance (SOD) is 820 mm. The source-to-image-distance (SID) was set at 1295 mm, yielding a magnification factor of 1.58. The full-FOV width was always 40 cm. The FOV height was first set at 5.8 cm to minimize scattered radiation, leading to an anatomical coverage of 3.7 cm. Each spin was

<i>Nominal contrast</i>	<i>Diameter</i>	<i>Single</i>	<i>Dual</i>
1.0%	15 mm	1.5	2.8
0.5%	15 mm	1.0	2.0
0.3%	15 mm	0.5	1.0
1.0%	7 mm (length: 7 mm)	1.0	2.6
1.0%	7 mm (length: 5 mm)	0.8	1.8
1.0%	7 mm (length: 3 mm)	1.4	3.0

Table 3.2 – CNR of single- and dual-rotation reconstructions of the CTP 515 (Figure 3.9a and 3.9c).

acquired as a single acquisition, then dual-rotation spin pairs were formed associating one full-FOV spin with a truncated spin of same FOV height and same truncation $t = 0.6$. For each pair, both spins uniformly sampled the 194° short-scan circular orbit, and at least one spin had 607 views ($16^\circ/\text{s}$ rotation at 50 views per second). In order to test a larger anatomical coverage, one pair of spins was acquired with a FOV height of 15.6 cm, corresponding to a coverage of 9.9 cm. For this case, the truncated spin was acquired at a faster gantry rotation speed ($28^\circ/\text{s}$ at 50 views per second), yielding 347 projections.

For X-ray exposure techniques the system automatic exposure control (AEC) would use 80 kVp for the head. For the Catphan[®], we decided to use 120 kVp to generate intensities beyond the usual clinical practice in order to reach the higher dose levels needed for resolving lower contrast inserts. The current was set to 3.4 mAs for the high-dose, truncated projections and 0.85 mAs for the low-dose full FOV spins (hence $x = 4$). The readout is achieved via a single-gain mode and was not changed between acquisitions. Thus for the highest intensities ($120 \text{ kVp} \times 3.4 \text{ mAs}$) the detector readout would saturate for thicknesses lower than a few centimeters.

Reconstructed images have isotropic voxels of size 0.94 mm. We used 50 iterations with a gradient step of 0.9. The quadratic regularization strength was always set to an FWHM of 1 voxel. Using these settings, the reconstruction of the Catphan[®] 528 module resolved the 5 line pairs per cm target (Figure 3.6). For comparison purposes, single-rotation iterative reconstructions were obtained using $\alpha_F = 1$ for the full-FOV spin and $\alpha_T = 1$ for the truncated one.

3.2.3.3 Image quality measures

The CTP 515 was used to evaluate the performance of the dual-rotation framework in terms of contrast detection. The contrast was measured for the inserts listed in Table 3.2. The background region was defined as a hollow cylinder around the target contrast insert with mean μ_{bkg} , and the foreground region was defined as a plain cylinder with a smaller radius, completely included in the contrast insert, and whose mean value is denoted by μ_{fg} . Each average was computed over at least 36 voxels.

Noise was estimated from two volumes f_1 and f_2 reconstructed from two

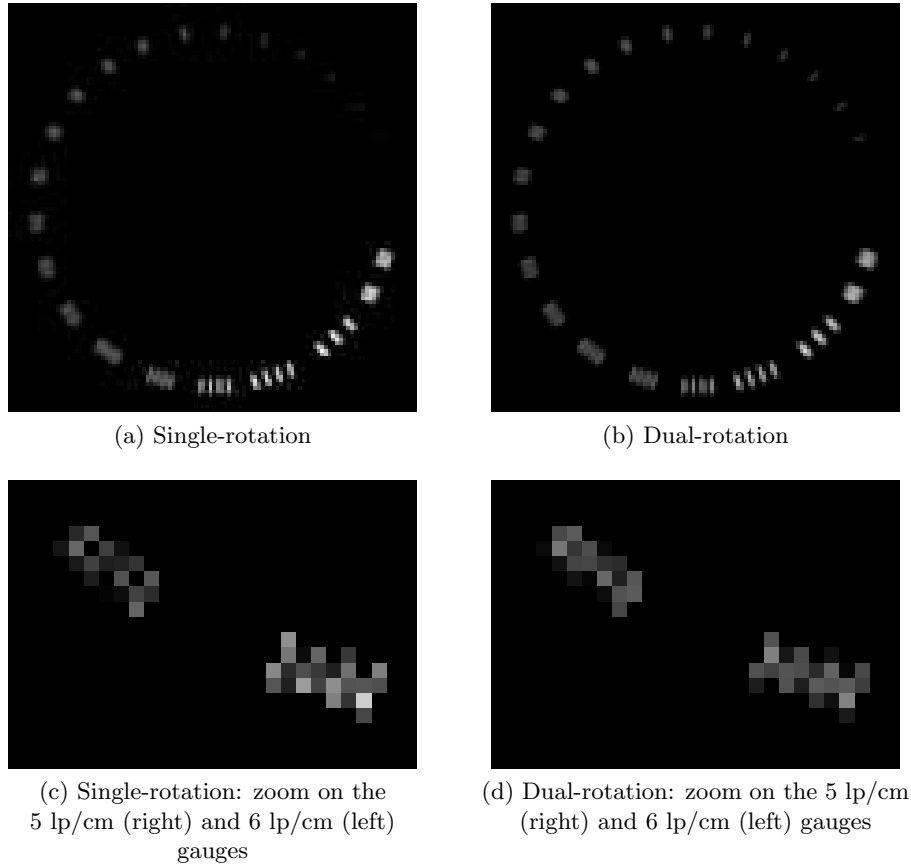


Figure 3.6 – Single- and dual-rotation reconstructions of the Catphan[®] 528 spatial resolution module.

replicated projection sets, each one being a statistical realization of the same acquisition protocol (either single-rotation or dual-rotation). By doing so, volume $\Delta = f_1 - f_2$ contained only noise. Since the Catphan[®] can be considered rotationally invariant, noise was estimated in K concentric hollow cylinders Ω_k containing all voxels of radius $r_{k-1} \leq r < r_k$. The radial sampling $\{r_1, \dots, r_K\}$ was non-uniform in order to keep the total number of voxels $|\Omega_k|$ approximately constant. With a cylinder height of 8 slices, this number was equal to 805. We thus computed the radial standard deviation as:

$$\sigma(\Omega_k) = \sqrt{\frac{1}{|\Omega_k|} \sum_{v \in \Omega_k} \frac{1}{2} \Delta^2(v)}. \quad (3.15)$$

The contrast-to-noise ratios (CNR) of insert i belonging to hollow cylinder Ω_j was then computed as:

$$\text{CNR}(i) = \frac{|\mu_{\text{fg}} - \mu_{\text{bkg}}|}{\sigma(\Omega_j)}. \quad (3.16)$$

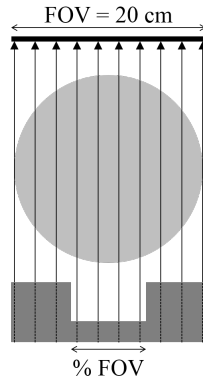


Figure 3.7 – Simulation setting in parallel-beam geometry.

3.2.4 Results

3.2.4.1 Simulations

The simulated noise distributions are shown in Figure 3.8a. The single-rotation case corresponds to the FBP reconstruction from p_F only, which means that the entrance dose profile is uniform. The noise is much higher at the center of the disk than at its periphery. By contrast, the noise distribution produced by the bow-tie filter shows a flat profile.

Dual-rotation shows an intermediate behavior. The tail of the noise standard deviation has globally the same shape as in the single-rotation case, and characterizes an unnecessary high dose in the peripheral areas. But at the center of the disk, the noise standard deviation matches the case of a bow-tie filter, as was targeted. A transition between the two FOV creates a bump that is stronger as t gets smaller. Figure 3.8b shows that when t gets higher, noise decreases significantly at the periphery of the disk and that when t is lower, the image is noisier. Using $t \approx 0.4$ – 0.6 provided the lowest variability of the radial profiles, while $t \approx 43\%$ matches the profile mean level of the bow-tie (black dot).

In these simulations, blended density sinograms were reconstructed with FBP, since air intensity measurements are perfectly known. We now show the results on real phantom data using our dedicated reconstruction method.

3.2.4.2 Real phantom data

The dose-area products (DAP) were the one reported by the system and corresponding to the system uniform exposure. They are summarized in Table 3.3. Summing the DAPs of the truncated, high-dose acquisition (first row) and of the full-FOV, low-dose acquisition (second row) yields the DAP of the dual-rotation acquisition (third row). The equivalent single-rotation acquisition corresponds to the case of a unique full-FOV rotation achieving the same dose level at the center of the object. The equivalent DAP is obtained by summing five times the DAP of the full-FOV, low-dose acquisition (fourth row). The empirical dose reduction factor is calculated by dividing the DAP of the single-rotation acquisition by the

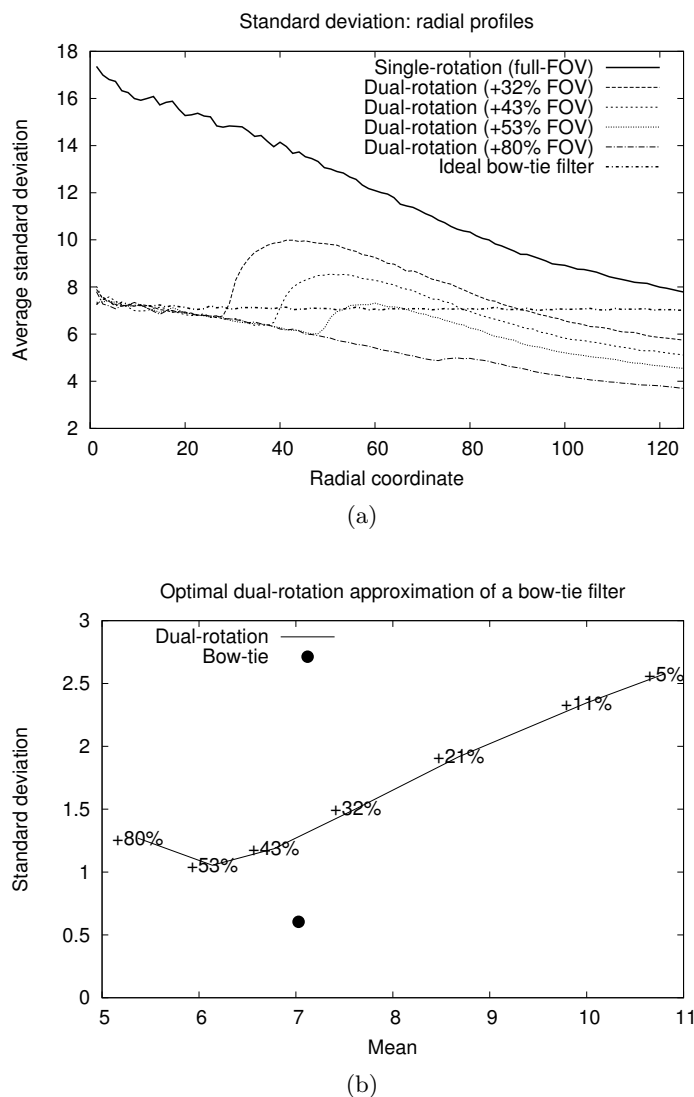


Figure 3.8 – Simulation of equivalent noise distribution in dual-rotation. (a) Radial profiles of the standard deviations of reconstructed images using FBP, with a single acquisition only and with different truncated FOV. (b) Noise uniformity, computed as the standard deviation of the noise radial profiles from (a) as a function of their mean values.

DAP of the dual-rotation acquisition, yielding $d_{\text{emp}} = 1.54 \approx d$.

Figure 3.9a shows an axial slice of the 515 low-contrast detection module. The image is flat, but the noise level prevents a good visualization of the inserts. Figure 3.9b is the dual-rotation reconstruction without smoothing the differentiated residual of the truncated data with a Hanning window. The image is already improved in terms of noise reduction and contrast detection; however, intense streaks are reconstructed as well. Figure 3.9c shows the dual-rotation reconstruction using the additional smoothing with a Hanning window. The image shows a uniform background with lower noise. The improvement extends beyond the

<i>Phantom</i>	<i>Catphan</i>	<i>Soft-tissue head</i>
<i>Truncated, 3.4 mAs</i>	60.0	13.3
<i>Full-FOV, 0.85 mAs</i>	26.8	7.7
Dual-rotation	86.8	21.0
Equivalent single-rotation	134.1	38.5

Table 3.3 – Dose-area products ($\text{dGy} \cdot \text{cm}^2$) for the dual-rotation acquisition and for the equivalent single-rotation acquisition achieving the same dose at the center of the phantom.

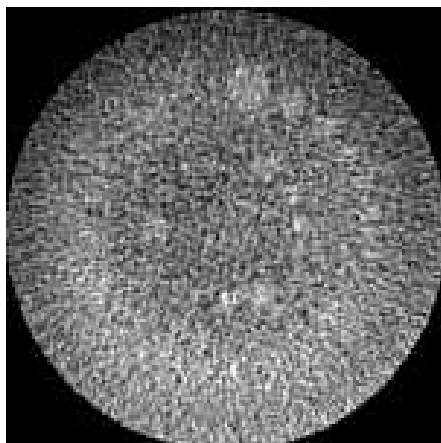
truncated FOV, as the backprojection operator redistributes density projections along the entire projection lines. Low-contrast inserts thus become visible and the truncated FOV introduces no artifact.

Noise radial standard deviations are shown in Figure 3.10. The noise in the single-rotation reconstruction from the full-FOV spin is almost uniform, and tends to be lower at the periphery of the Catphan[®]. The dual-rotation reconstructed image shows a similar behavior, with much less noise. One can observe that the ratio between both curves varies from 1.9 to 2.6, with an average gain of 2.4. The CNR values for a set of inserts are given in Table 3.2. If we set a detectability index as $\text{CNR} \geq 1$, all inserts of the Table 3.2 are detected with high confidence, except the less dense one of 0.3% at 15 mm that is borderline.

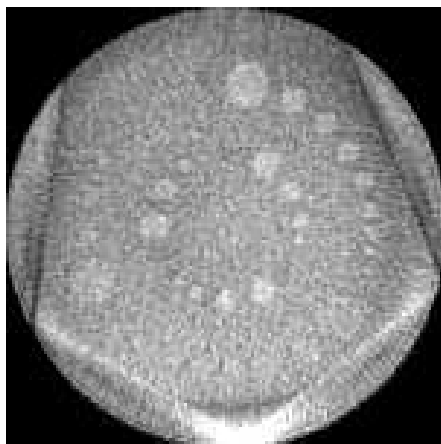
We further compare the reconstructed image of the CTP 515 using our approach with the image obtained on a conventional diagnostic multislice CT scanner (Figure 3.11). When averaged over 10 mm on the axial direction, the axial slice of the dual-rotation reconstructed image (Figure 3.11a) becomes less noisy and inserts with relative contrast of 0.3% start to appear. Despite low-frequency non-uniformity of the background and some oblique streaks due to the truncation of the bed table in C-arm acquisitions, the result is comparable to the CT reconstruction of the CTP 515 (Figure 3.11b).

Figure 3.12 shows an axial slice cutting the 515 module at the same position as in Figure 3.9 and a coronal slice cutting through the center of both the 515 and the 518 modules, that have different attenuations. The figure compares the iterative reconstruction from the full-FOV acquisition only and the dual-rotation reconstruction at a larger FOV height for the same truncation level $t = 0.6$. The reconstructed image from the low-dose, full-FOV spin is now both noisy and corrupted by scattered radiations, which results in a contrast loss. Associating this spin with the high-dose, truncated spin, which is less corrupted by scattered radiations, results in a visually more uniform and less noisy image, despite a residual cupping.

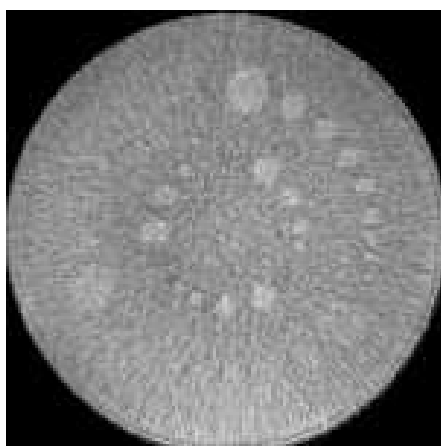
Figure 3.13a shows the reconstruction from the low-dose, full-FOV spin only. Again, the image is flat but noisy. Figure 3.13b shows the dual-rotation reconstruction. We observe no visible artifact coming from the fact that a truncated spin is involved in the reconstruction. Thus image quality fully benefits from the noise reduction.



(a)



(b)



(c)

Figure 3.9 – (a) Single-rotation reconstruction from the full-FOV, low-dose spin. (b) Dual-rotation reconstruction without using the Hanning window in Equation (3.14). (c) Dual-rotation reconstruction. Isotropic voxel size: 0.94 mm^3 . Window width: 50 HU.

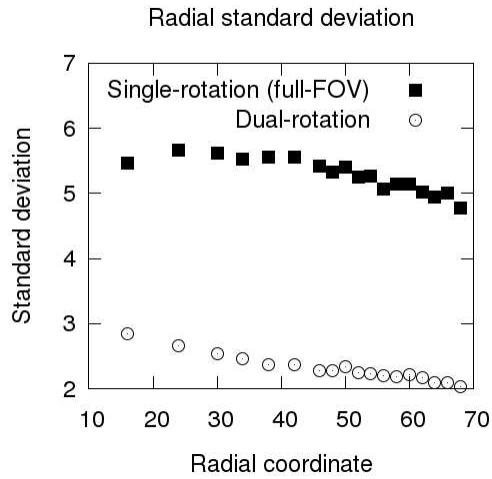


Figure 3.10 – Noise radial standard deviation for the single- and dual-rotation reconstructed images of the CTP 515.

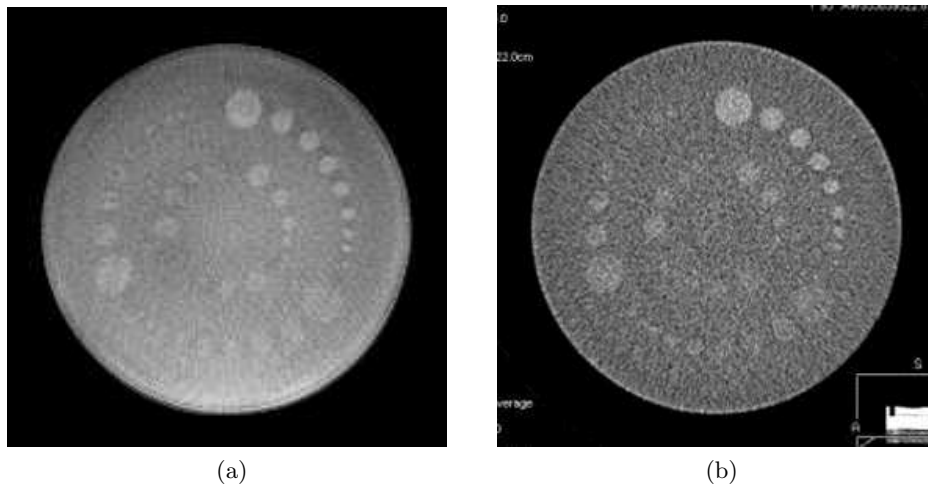


Figure 3.11 – Comparison between dual-rotation CBCT (a) and diagnostic multislice CT (b) reconstructions of the CTP 515. Slice thickness: 10 mm. Window width: 50 HU.

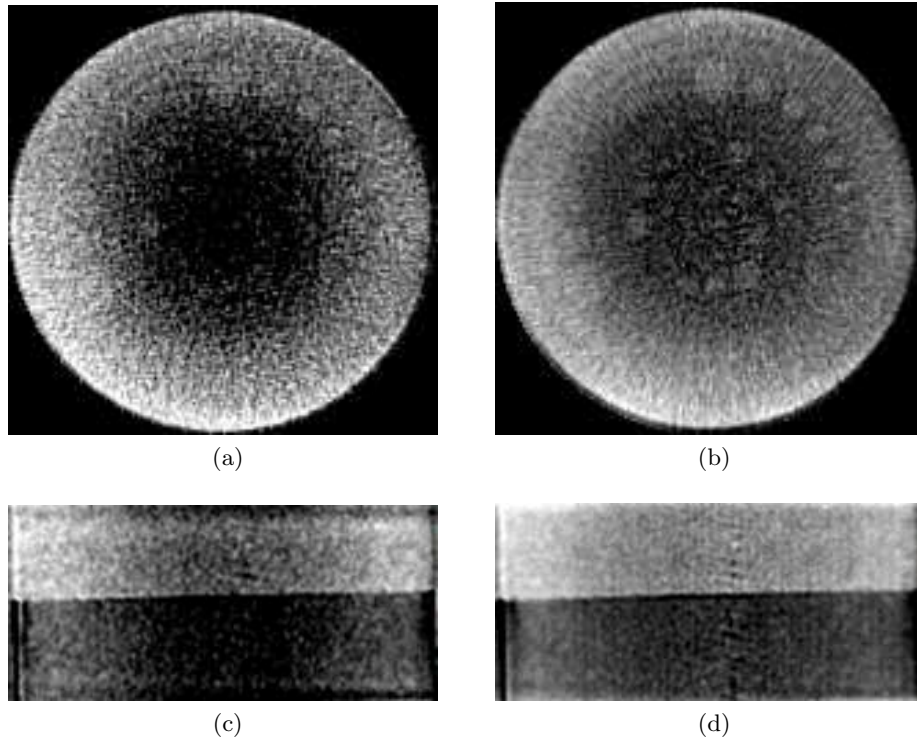


Figure 3.12 – Reconstructed images from acquisitions at a 3D FOV height of 9 cm. (a) Iterative reconstruction from the full-FOV acquisition only. (b) Dual-rotation reconstruction. (c) (resp. (d)) Coronal slice of (a) (resp. (b)). Isotropic voxel size: 0.94 mm^3 . Window width: 50 HU for (a),(b) and 75 HU for (c),(d).

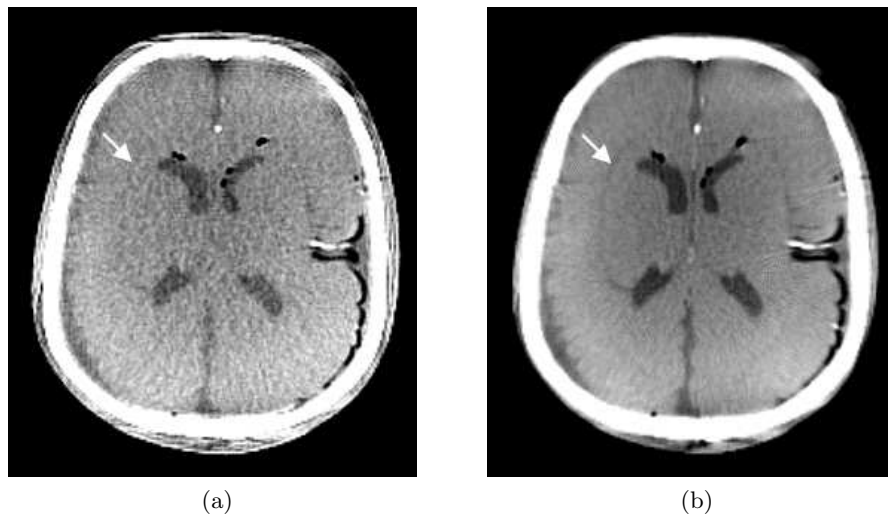


Figure 3.13 – Iterative reconstructions of the soft-tissue head phantom from (a) a single low-dose, full-FOV spin, (b) a dual-rotation acquisition. Isotropic voxel size: 0.94 mm^3 . Window width: 150 HU.

3.3 Discussion and conclusion

Dual-rotation CBCT routinely provides three-dimensional digital subtracted angiography (Anxionnat et al., 1998). Cardiac imaging is achieved via multiple sweeps of the C-arm gantry as well (Lauritsch et al., 2006). We here show that dual-rotation is also suitable for improved non-contrast-enhanced low-contrast detection in brain imaging. An iterative reconstruction algorithm was designed to handle the two degrees of freedom of the dual-rotation, namely, the truncation level t and the dose ratio x between spin intensities.

It simultaneously reconstructs two spins in a single volume, without merging measurements in the projection domain, in order not to require the knowledge of the incoming X-ray beam intensities in the truncated views, nor that measurements be taken at the exact same position twice. This thus puts no specific constraints on the mechanical design, but puts more weight on the computation infrastructure. As we mentioned, if the mechanical design is made precise enough to sample the exact same positions twice, analytical reconstruction is sufficient for full volume imaging. Let us emphasize that the proposed iterative reconstruction has more flexibility than a standard formulation. The optimization criterion directly handles the logarithm of the intensities $\log(I_n)$, not the density projections. Filtering with zero-padding of the difference between the reprojected image and the truncated data easily implements the extrapolation of the truncated data by the full-FOV acquisition through the image space (Cho et al., 2009). Most importantly, we found that an extra apodization is needed to get the desired uniformity in the solution. Note that this step formally makes the criterion non-symmetrical, but this seems minor as we never experienced any convergence issue. Finally, we designed our optimization criterion using only a small quadratic regularization term. Although our reconstruction framework would handle more sophisticated sparsity-enforcing penalties such as the image total variation (TV) (Bian, Han, et al., 2010), the reconstructed images using TV show modified textures in the soft-tissue contrast window, that are often undesirable in practice. However, we did not find the need to move from smooth regularization to TV.

On a quality assurance phantom and on an anthropomorphic head phantom, images showed superior low-contrast detection and no artifactual trace of being made of two separate spins. High CNR values in 0.94 mm thick slices with dose reduction were obtained at 120 kVp with fixed techniques, a dose ratio of 4, a truncation level of 0.6 and 607 views per spin. These values certainly are beyond the needs of the clinical practice. They primarily illustrate the capabilities of dual-rotation framework and should not be considered optimal.

To provide optimal parameters, we need to take into account all aspects of the system with respect to the targeted clinical task. Let us mention a few. Angular automatic exposure control (AEC) is the norm. Total acquisition time should be as short as possible, so that the truncated spin might be acquired with less views at a faster speed. The scatter contamination depends on the collimated aperture, and the signal read by the detector in the shadow of the collimation provides pure scatter measurement than can be used for scatter correction (Siewerdsen et al., 2006). Flat-panel detectors limited bit-depth with respect to CT degrades

the measured signal and thus the contrast resolution. Electronic noise degrades detection of very low intensities.

The proposed acquisition and reconstruction framework does not require to know nor to estimate the X-ray techniques used by the AEC. It allows one to vary the truncation (potentially dynamically) in order to better handle scatter. The increased number of measurements increases the overall bit-depth, but is more sensitive to electronic noise.

An obvious drawback of C-arm dual-rotation acquisition is that it takes twice as much time and is thus more sensitive to patient motion. Because C-arm detectors have low acquisition frame rates, several rotation speeds are available to yield more or less images for a given acquisition frame rate. Low-contrast resolution requires the maximum angular sampling, thus the lowest speed. In addition, the iterative reconstruction method increases the overall complexity of this framework.

Direct reconstruction for virtual bow-tie C-arm CBCT

The iterative reconstruction framework from Chapter 3 was designed in order to deal with truncated data, that could not be handled by simple direct methods like FBP. In this chapter, we show that, by switching from FBP to backprojection-filtration (BPF) methods, an alternative, direct reconstruction for dual-rotation acquisitions is possible. We revisit the standard direct reconstruction formulas in parallel-beam and fan-beam geometries with linear detectors, and derive a new semi-discrete BPF formula, that is well suited to coarse angular sampling of C-arm data. The formula, extended to C-arm cone-beam geometries, gives access to an unfiltered backprojection space, that is used to combine the data from the dual-rotation acquisition. Simulations on synthetic data, as well as experiments on the Catphan[®] CTP 515 and on the head phantom with soft-tissue-like structures confirm the potential of this new, direct reconstruction framework.

Contents

4.1	Filtered backprojection, backprojection-filtration . . .	78
4.1.1	Challenges of dual-rotation direct reconstruction	78
4.1.2	Backprojection-filtration methods: a literature review	78
4.2	K-pass Hilbert-transformed DBP (DBP-HT-K)	80
4.2.1	Parallel-beam case	80
4.2.1.1	Notations	80
4.2.1.2	Angular splitting	81
4.2.1.3	Differentiated backprojection	84
4.2.2	Divergent-beam case	85
4.2.2.1	Resampling formula for the fan-beam case	85
4.2.2.2	Semi-discrete fan-beam BPF formula	86
4.2.2.3	Extension to C-arm CBCT	88
4.2.3	Simulations	89

4.2.3.1	Planar geometries	89
4.2.3.2	CBCT reconstruction of a uniform cylinder	91
4.2.3.3	CBCT reconstruction of a head	93
4.3	Application to virtual bow-tie C-arm CBCT	96
4.3.1	Principle	96
4.3.2	Validation on phantom acquisitions	97
4.3.2.1	Experiments	97
4.3.2.2	Results	98
4.4	Discussion	103
4.5	Proofs of the theorems	104
4.5.1	Proof of Theorem 4.2.1	104
4.5.2	Proof of Theorem 4.2.3	104
4.5.3	Proof of Theorem 4.2.4	105
4.5.4	Proof of Theorem 4.2.6	108
4.5.5	Proof of Theorem 4.2.7	108

4.1 Filtered backprojection, backprojection-filtration

4.1.1 Challenges of dual-rotation direct reconstruction

In the previous chapter, an iterative reconstruction was designed because the dual-rotation acquisition cannot be pre-processed in the projection space prior to using a single-rotation, direct reconstruction method such as FDK. Indeed, as already discussed, we did not enforce any constraint on the repeatability of the actual positions of the acquired projection views in both spins.

A post-processing solution, that would blend images reconstructed separately from each spin of the dual-rotation acquisition, was not an option either. Indeed, this would imply reconstructing a region of interest (ROI) from the truncated acquisition only, which cannot be performed through direct reconstruction (Natterer, 2001). In particular, since the ramp filter \mathcal{D} is non-local, applying FDK to truncated data p_T would inevitably yield artifacted images when rows of the acquired projection views are not known over their whole supports.

In order to apply a direct reconstruction method to dual-rotation acquisitions, it seems necessary to blend data from p_F and p_T in the 3D image space, but *prior* to filtering. This observation makes us move from filtered backprojection methods to backprojection-filtration (BPF) methods, which apply the non-local filtering operator in the image space. In the following, we review the main state-of-the-art BPF methods.

4.1.2 Backprojection-filtration methods: a literature review

The standard parallel-beam FBP method first performs a one-dimensional ramp filter to each projection view and then backprojects the filtered projections in the image space. It is mathematically equivalent to swap the order of the steps, namely, to backproject unfiltered projections and to apply a two-dimensional ramp filter to the backprojected image (Kak & Slaney, 2001). However, this solution is not implementable in practice, since the backprojected image is infinitely supported but it is actually computed only over a bounded support.

In the context of diagnostic helical CT, a new type of BPF formula was proposed (Zou & Pan, 2004a, 2004b), that is based on the reconstruction of PI-lines. PI-lines are straight lines connecting two points of a helical source trajectory, that are separated by less than one helix turn. The proposed reconstruction method backprojects locally filtered projections over PI-lines, that are further filtered by a Hilbert transform: hence, the filtering step remains intrinsically one-dimensional. The local filtering step is a differentiation with respect to the source trajectory curvilinear abscissa.

These results were further extended to a broader class of source trajectories (Zhuang et al., 2004; Zou et al., 2005; Pack et al., 2005; Schöndube et al., 2007; Bian, Xia, et al., 2010). They were also reformulated in the circular parallel-beam and fan-beam geometries by Noo et al. (2004). The authors first define the differentiated backprojection (DBP) in the parallel-beam geometry as the back-projection of differentiated projections with respect to the detector coordinates; they relate it to the true image f via:

$$\text{DBP}(\mathbf{x}) = \int_0^\pi \mathcal{B}_\theta [p'_\theta](\mathbf{x})d\theta = -2\pi\mathcal{H}_{\frac{\pi}{2}} [f](\mathbf{x}), \quad (4.1)$$

where \mathcal{H}_α applies the one-dimensional Hilbert transform to all lines oriented along α^\perp . When f is derived through Equation (4.1), we call the method the Hilbert-transformed DBP, denoted DBP-HT. Only a local operation (the derivation) is applied to the projections. The authors further adapted this result to fan-beam projections by applying a change of variables from parallel-beam to fan-beam parameters in the integrals.

The previous results involve the inversion of the one-dimensional Hilbert transform. A simple multiplication by $-i \operatorname{sgn}(\rho)$ in the Fourier space is not an option in practice: again, the supports of backprojection lines are infinite, and only truncated lines are actually computed. To address this issue, alternative formulas to invert truncated Hilbert transforms have been proposed (Noo et al., 2004; Pack et al., 2005; You & Zeng, 2006; Ye et al., 2007; Zeng et al., 2007). Solutions rely on the assumption that the lines are truncated Hilbert transforms of a compactly supported function. If so, alternative inversion formulas can be derived. Let $\phi(t) = f(\mathbf{x} + t\alpha)$ for some point \mathbf{x} and $\alpha = \frac{\pi}{2}$. The inversion formulas look like:

$$\phi(t) = \frac{-1}{w(t)} \left(\mathcal{H} \left[w \cdot \left(\mathcal{H} [\phi] \cdot \mathbb{1}_{[-R,R]} \right) \right] (t) + C(p) \right), \quad (4.2)$$

where $\mathcal{H} [\phi] \cdot \mathbb{1}_{[-R,R]}$ is the truncated Hilbert line, known only over $[-R, R]$ such that $\operatorname{supp}(\phi) \subset [-R, R]$, $w(t) = \sqrt{(t+R)(R-t)}$ for $t \in [-R, R]$ and $w(t) = 0$ otherwise, and $C(p)$ is a constant value that depends on projection data $p = \{p_\theta\}_{\theta \in [0, \pi]}$. Note that since function:

$$t \mapsto w(t) \cdot \left(\mathcal{H} [\phi] (t) \cdot \mathbb{1}_{[-R,R]}(t) \right) \quad (4.3)$$

is zeroed outside $[-R, R]$, the application of the Hilbert transform to this function can be performed by simple multiplication by $-i \operatorname{sgn}(\rho)$ in the Fourier domain.

Alternative inversion methods for truncated Hilbert transforms have also been investigated; they either rely on a different computation of $\mathcal{H} \left[w \cdot \left(\mathcal{H} [\phi] \cdot \mathbb{1}_{[-R,R]} \right) \right]$ (Schöndube et al., 2010), on a least-squares fit of coefficients in a given basis expansion (Sidky & Pan, 2005), or on inversion approaches based on singular value decomposition (Katsevich, 2010).

Such BPF methods were originally designed for 2D geometries or for 3D helical geometries of diagnostic CT. They were further extended to cone-beam geometries (Pack et al., 2005; Ye et al., 2005; S. Zhao et al., 2005; L. Yu et al., 2006; Zhuang & Chen, 2006; D. Xia et al., 2007) and to a wider class of trajectory curves. Such extensions use differentiated projections with respect to the trajectory curve, thus this curve needs to be densely sampled, which is always the case in diagnostic CT. In C-arm CBCT, however, angular sampling is coarser. Noo et al. (2007) proposed a new differentiation scheme that is more robust to changes in the data acquisition geometry and to coarser angular sampling, but still needs about 200 views to sample a half circular trajectory.

In the following, we propose a semi-discrete BPF formula, that we call the K -pass Hilbert-transformed DBP formula, and that we denote DBP-HT- K , in the parallel-beam geometry. It is equivalent to the discretized DBP-HT when $K = 1$ and to the semi-discrete FBP when K is equal to the number of projections. In the context of C-arm CBCT, angular sampling can be an issue; we thus elaborated on the proposed parallel-beam formula to derive a divergent-beam extension of it, such that it performs as good as FBP whatever the number of projections. Parts of this work has been published in (Reshef et al., 2017b; Reshef, Nikoukhah, et al., 2018; Reshef, Riddell, et al., 2018).

4.2 K -pass Hilbert-transformed DBP (DBP-HT- K)

We start by some mathematical notations. A linear filtering operator \mathcal{O} , typically defined over the Schwartz space $\mathcal{S}(\mathbb{R}^n)$ of rapidly decreasing functions of $\mathcal{C}^\infty(\mathbb{R}^n, \mathbb{R})$ such that all their derivatives are also rapidly decreasing, applies a linear filter through the convolution by a kernel function $h \in \mathcal{S}(\mathbb{R}^n)$:

$$\mathcal{O} : \begin{pmatrix} \mathcal{S}(\mathbb{R}^n) & \rightarrow & \mathcal{S}(\mathbb{R}^n) \\ \phi & \mapsto & \phi \star h \end{pmatrix}. \quad (4.4)$$

We use the notations $\mathcal{F}_n[\mathcal{O}]$ and $\mathcal{F}_n[h]$ interchangeably and we use the term ‘‘Fourier transform of \mathcal{O} ’’ to denote the n -dimensional Fourier transform of filter kernel h used by operator \mathcal{O} .

4.2.1 Parallel-beam case

4.2.1.1 Notations

The FBP reconstructed image f is obtained by summing up elementary contributions from different view angles sampling the interval $[0, 2\pi]$ (we intentionally place ourselves over the full circle already, as in the divergent-beam case). In the

semi-discrete setting, we denote the finite set of N uniformly sampled angles:

$$\Theta = \left\{ \theta_i = \left(i - \frac{1}{2} \right) \Delta\theta, i = 1, \dots, N \right\}, \text{ where } \Delta\theta = \frac{2\pi}{N}. \quad (4.5)$$

We define a subdivision of Θ as a collection of subsets $\{\Theta_k\}_{k=1, \dots, K}$ such that:

$$\bigcup_{k=1}^K \Theta_k = \Theta \text{ and } \forall k \neq l, \Theta_k \cap \Theta_l = \emptyset. \quad (4.6)$$

Then, our semi-discrete FBP reconstruction is:

$$f_N = \frac{\pi}{N} \sum_{\theta \in \Theta} \mathcal{B}_\theta \mathcal{D} [p_\theta] = \frac{\pi}{N} \sum_{k=1}^K g_{\Theta_k}, \quad (4.7)$$

where:

$$g_{\Theta_k} = \sum_{\theta \in \Theta_k} \mathcal{B}_\theta \mathcal{D} [p_\theta]. \quad (4.8)$$

Note that when $K = 1$, $\Theta_K = [0, 2\pi]$ and we have $\frac{\pi}{N} g_{\Theta_K} = f_N$. On the other hand, if $K = N$, $\Theta_k = \{\theta_k\}$ is reduced to a single view angle, g_{Θ_k} is the back-projection along lines colinear to θ_k of the ramp-filtered projection at angle θ_k , $\mathcal{D} [p_{\theta_k}]$. In this case, we write $g_{\Theta_k} = g_{\{\theta_k\}} = \mathcal{B}_{\theta_k} \mathcal{D} [p_{\theta_k}]$. In between these two extreme cases, a natural subdivision of $[0, 2\pi]$ is $\Theta_{\text{FRT}} = \left[\frac{\pi}{4}, \frac{3\pi}{4} \right] \cup \left[\frac{5\pi}{4}, \frac{7\pi}{4} \right]$, the subset of frontal views, and $\Theta_{\text{LAT}} = \Theta \setminus \Theta_{\text{FRT}}$, the subset of lateral views.

4.2.1.2 Angular splitting

We now have a closer look at elementary contribution g_θ . Note that more generally, the ramp filter operator can be decomposed into an order- n derivative operator and a residual operator:

$$\mathcal{D} [p_\theta] = F^{(n)} \left[p_\theta^{(n)} \right], \quad (4.9)$$

where $F^{(n)}$ writes in the Fourier space as:

$$\mathcal{F}_1 \left[F^{(n)} \right] (\rho) = \frac{|\rho|}{(2i\pi\rho)^n}. \quad (4.10)$$

Typically, $n \in \{0, 1\}$. We also denote by $F_\alpha^{(n)}$, the two-dimensional filter that amounts to filtering each line $\mathcal{L}_\alpha(t) = \{t\boldsymbol{\alpha} + u\boldsymbol{\alpha}^\perp \mid u \in \mathbb{R}\}$ with $F^{(n)}$ (Table 4.1). The first result of this section is Theorem 4.2.1. The proof is given in Section 4.5.1.

Theorem 4.2.1. *Let $\alpha \in \mathbb{R}$ such that $\boldsymbol{\theta} \cdot \boldsymbol{\alpha} \neq 0$. Then the following holds:*

$$g_\theta = F_\alpha^{(n)} \left[b_\theta^{(n)}(\alpha; \cdot) \right], \quad (4.11)$$

where:

$$b_\theta^{(n)}(\alpha, \cdot) = \mathcal{B}_\theta \left[\sigma_\theta^\alpha (\boldsymbol{\theta} \cdot \boldsymbol{\alpha})^{n-1} p_\theta^{(n)} \right], \text{ and } \sigma_\theta^\alpha = \text{sgn}(\boldsymbol{\alpha} \cdot \boldsymbol{\theta}). \quad (4.12)$$

	$n = 0$	$n = 1$
	Ramp \mathcal{D}	Hilbert \mathcal{H}
$(-2\pi)^n \mathcal{F}_1 [F^{(n)}] (\rho)$	$ \rho $	$-i \operatorname{sgn}(\rho)$
$(-2\pi)^n \mathcal{F}_2 [F_\alpha^{(n)}] (\boldsymbol{\nu})$	$ \boldsymbol{\nu} \cdot \boldsymbol{\alpha}^\perp $	$-i \operatorname{sgn}(\boldsymbol{\nu} \cdot \boldsymbol{\alpha}^\perp)$

Table 4.1 – Operator $F^{(n)}$ of Equation (4.10) for $n \in \{0, 1\}$, and the corresponding formulation of the 2D mono-directional filter $F_\alpha^{(n)}$.

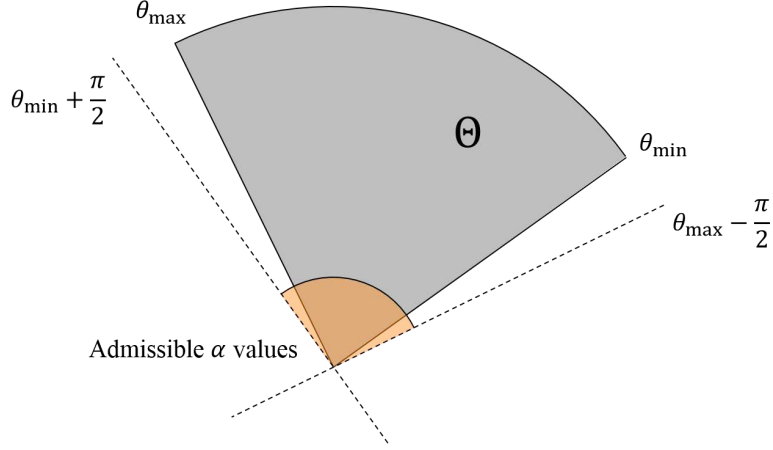


Figure 4.1 – Backprojection-filtration over an angular subset

We now discuss the consequences of Theorem 4.2.1. First, by showing that it is possible to swap the filtering and the backprojection steps, it provides a BPF formula for an elementary FBP image g_θ . The trivial case is $\alpha = \theta$, which means that backprojecting a filtered projection oriented along $\boldsymbol{\theta}^\perp$ is equivalent to backprojecting first the unfiltered projection (that is, copying translated versions of the original projection in the image space), and then filtering each line colinear to $\boldsymbol{\theta}^\perp$. Of course, this is not preferred to conventional FBP.

The interesting result is that α can be arbitrarily selected as long as $\boldsymbol{\theta} \cdot \boldsymbol{\alpha} \neq 0$. In particular, let $\Theta_k = [\theta_{\min}, \theta_{\max}] \subsetneq [0, \pi]$. Then α can be chosen fixed for all $\theta \in \Theta_k$. More specifically, any $\alpha \in]\theta_{\max} - \frac{\pi}{2}, \theta_{\min} + \frac{\pi}{2}[$ is an admissible angle such that Equation (4.11) holds for all $\theta \in \Theta_k$ (Figure 4.1). Hence:

$$g_{\Theta_k} = F_\alpha^{(n)} [b_{\Theta_k}^{(n)}(\alpha; \cdot)], \quad b_{\Theta_k}^{(n)}(\alpha; \cdot) = \sum_{\theta \in \Theta_k} b_\theta^{(n)}(\alpha; \cdot). \quad (4.13)$$

Equation (4.13) is the backprojection-filtration counterpart of Equation (4.8). It tells that projections can be applied a local operator first (namely, an order- n derivative operator), weighted, then backprojected in the image space; the filtering step is applied along lines \mathcal{L}_α of the image space; it thus reduces to a collection of one-dimensional filtering operations.

We are now able to propose our K -pass BPF formula for reconstructing f

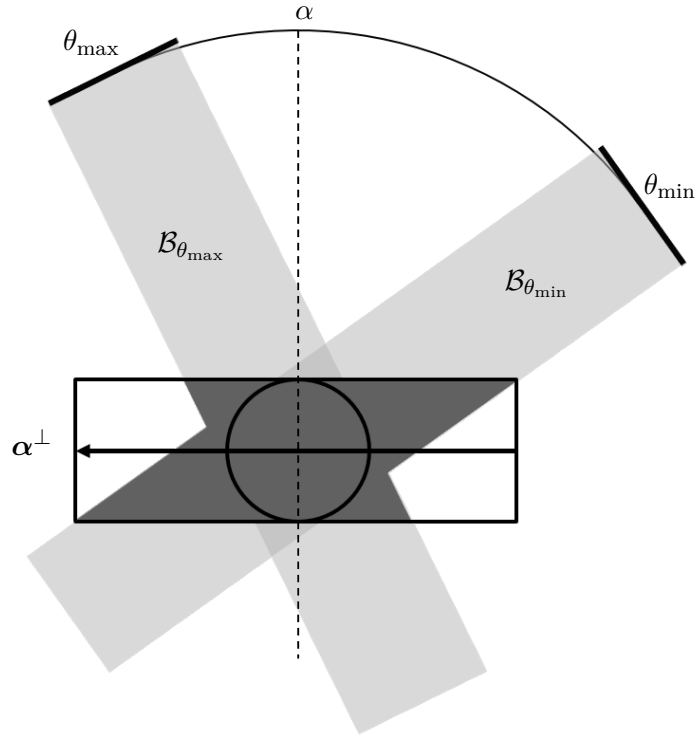


Figure 4.2 – Extended support for filtering a backprojection over an angular subset. Lines that cross the circular field of view (black circle) have a finite intersection with the support of the backprojection (dark area). It is thus sufficient to compute the backprojection over a rectangular extended support (black rectangle) to perform Fourier-based filtering along direction α^\perp (arrow).

from the set $p = \{p_\theta\}_{\theta \in \Theta}$ of projections, using the splitting approach from Equation (4.7) and the backprojection-filtration formula from Equation (4.13).

Theorem 4.2.2. *If for each angular subset Θ_k there exists an appropriate α_k satisfying Equation (4.13), then:*

$$f_N = \frac{\pi}{N} \sum_{k=1}^K F_{\alpha_k}^{(n)} \left[b_{\Theta_k}^{(n)}(\alpha_k; \cdot) \right]. \quad (4.14)$$

Let us have a closer look at the filtering step. As already mentioned, it reduces to one-dimensional filtering along lines \mathcal{L}_α . We take advantage of the fact that if $\Theta_k = [\theta_{\min}, \theta_{\max}] \subsetneq [0, \pi]$, and if $\alpha \in]\theta_{\max} - \frac{\pi}{2}, \theta_{\min} + \frac{\pi}{2}[$, then the intersection between the support of the backprojection over Θ_k and any line \mathcal{L}_α is *finite* (Figure 4.2). In other words, provided that the bounded support, over which the backprojection is actually computed, is large enough (namely, if it extends in the direction α^\perp from $2R$ to $2R(1 + \max(|\theta_{\min} \cdot \alpha|^{-1}, |\theta_{\max} \cdot \alpha|^{-1}))$), where R is the radius of the circular field of view), all lines \mathcal{L}_α that are needed to reconstruct f_N are known over their entire supports, and can thus be filtered in the Fourier domain directly instead of using the finite inverse Hilbert transform, just like in FBP. Note that this observation remains valid whatever the angular sampling

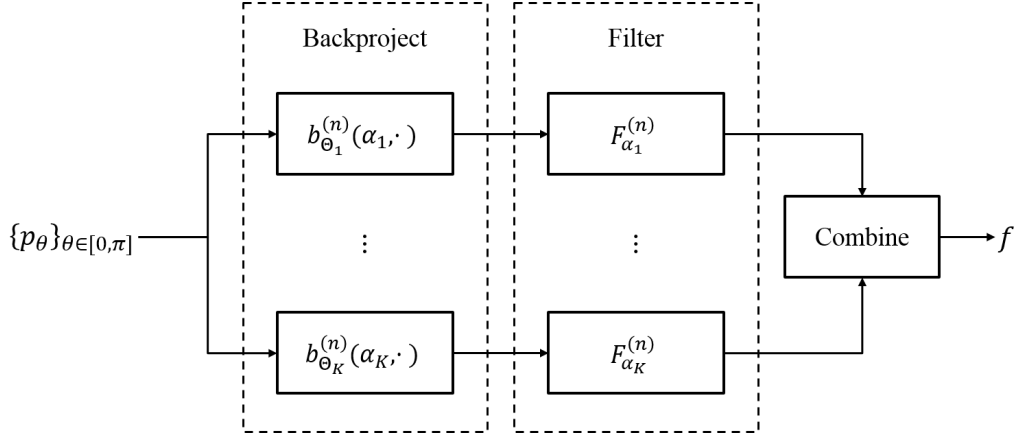


Figure 4.3 – General reconstruction flowchart for the splitting BPF method.

N : there is an equivalence between the semi-discrete FBP and the proposed semi-discrete BPF formula.

When $n = 1$, we call our formula the K -pass Hilbert-transformed DBP formula, denoted DBP-HT- K . As a special case of the general flowchart of Figure 4.3, we suggest to use $K = 2$ and to divide projection views into lateral and frontal views (Figure 4.4). For frontal views, we choose $\alpha_{\text{FRONT}} = \frac{\pi}{2}$, leading to horizontal filtering of the backprojected lines. The support of the backprojected lines does not exceed $(1 + \sqrt{2})$ times the reconstructed FOV diameter along the x -axis. For lateral views, we choose $\alpha_{\text{LAT}} = 0$, leading to vertical filtering of the backprojected columns. Again, the support of the backprojected columns does not exceed $(1 + \sqrt{2})$ times the reconstructed FOV diameter along the y -axis.

4.2.1.3 Differentiated backprojection

We set $n = 1$ and $K = 1$. Then, using $\alpha_1 = \frac{\pi}{2}$, we get:

$$f_N = \frac{\pi}{N} g_{\Theta_1} = \frac{1}{2\pi} \mathcal{H}_{\frac{\pi}{2}} \left[\frac{\pi}{N} \sum_{\theta \in \Theta} \mathcal{B}_{\theta} [p'_{\theta}] \right]. \quad (4.15)$$

Equation (4.15) is our DBP-HT-1 reconstruction formula. It is nothing but the discretized formulation of the DBP-HT formula from (Noo et al., 2004), which is easily recovered by letting $N \rightarrow +\infty$. Let us make two observations at this point:

- (i) When $K = 1$, the support of the backprojected image $b_{\Theta}^{(1)}(\frac{\pi}{2}, \cdot)$ may spread far in the direction of the x -axis; more precisely, the size of the original square grid is increased by a factor $\left(1 + \cos\left(\frac{\pi - \Delta\theta}{2}\right)^{-1}\right)$, where $\Delta\theta = \frac{2\pi}{N}$ along the x -axis. Although it is still theoretically possible to perform the Hilbert filtering step in the Fourier domain, it becomes intractable in practice, as it would require to compute the backprojection over a very large support. Hence, the shift from “traditional” Hilbert filtering to alternative inversion methods when the Hilbert line is only known over a bounded support.

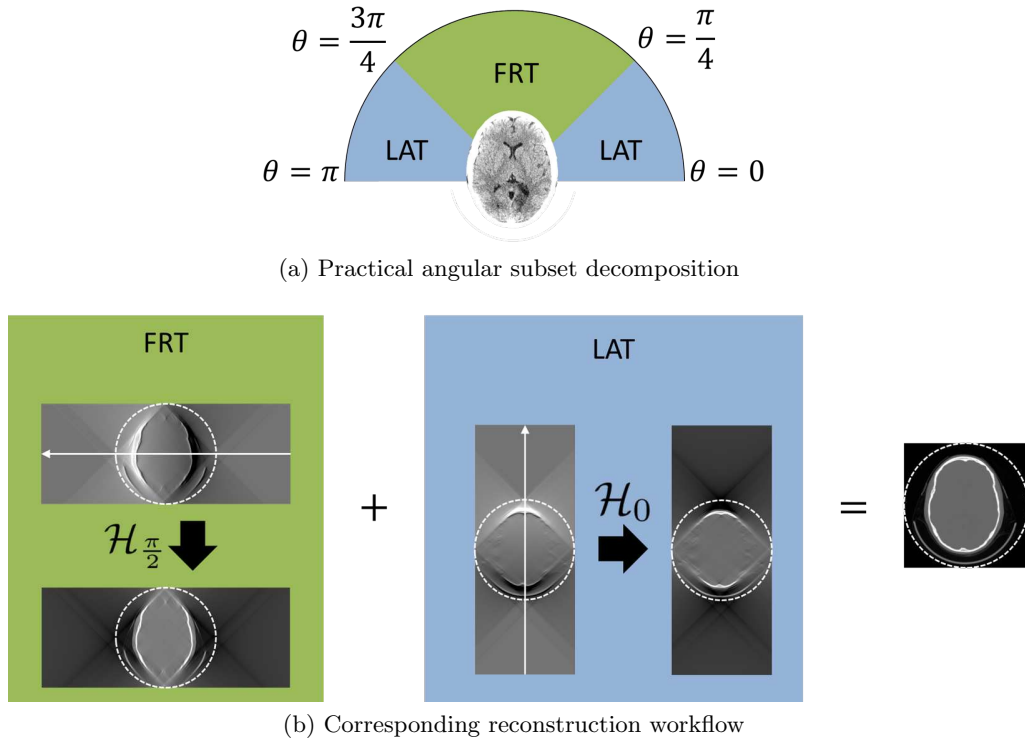


Figure 4.4 – Practical parallel-beam BPF reconstruction.

- (ii) These alternative inversion methods are defined in the context of analytical reconstruction; they are not adapted to semi-discrete settings where N gets smaller. This will be investigated in Chapter 5.

4.2.2 Divergent-beam case

We now study the translation of our method from the parallel-beam to the fan-beam geometry. A first resampling method is derived in a similar way as for the fan-beam FBP method, which was also used in (Noo et al., 2004) for the fan-beam Hilbert-transformed differentiated backprojection method. Limits of this approach are discussed and a new, intrinsically fan-beam method is then proposed.

4.2.2.1 Resampling formula for the fan-beam case

We place ourselves in the continuous domain, by letting $N \rightarrow +\infty$ and replacing the Riemann sums by integrals over $[0, 2\pi]$. The resampling formula first rewrites integrals involved in Theorem 4.2.1 in order to use parallel-beam parameters (θ, u) , and then performs the change of variables provided in Equation (2.25). We first write $b_\theta^{(n)}(\alpha; \mathbf{x})$ as (Kak & Slaney, 2001; Noo et al., 2004):

$$b_\theta^{(n)}(\alpha, \mathbf{x}) = \int_0^{2\pi} \int_{-\infty}^{+\infty} \text{sgn}(\boldsymbol{\theta}' \cdot \boldsymbol{\alpha}) (\boldsymbol{\theta}' \cdot \boldsymbol{\alpha})^{n-1} \delta^{(n)}(\mathbf{x} \cdot \boldsymbol{\theta}'^\perp - u) p_{\theta'}(u) \delta(\theta' - \theta) du d\theta', \quad (4.16)$$

where we denoted by $\delta^{(n)}$ the convolution kernel associated with the order- n derivative, which is $(-n - 1)$ -homogeneous¹, and δ is the Dirac delta function. Fan-beam parameters are related to parallel-beam parameters via the formulas given in Equation (2.25). The corresponding Jacobian determinant writes:

$$J = \frac{D^2 d}{\sqrt{\hat{u}^2 + D^2}^3}. \quad (4.17)$$

We end up with the following result. The proof is given in Section 4.5.2.

Theorem 4.2.3. *The un-filtered backprojection $b_\theta^{(n)}(\alpha, \cdot)$ can be expressed using fan-beam projections via:*

$$b_\theta^{(n)}(\alpha, \cdot) = \int_0^{2\pi} \frac{D^2}{s_{\hat{\theta}}^{n+1}} \hat{\mathcal{B}}_{\hat{\theta}} \left[\frac{d^n}{d\hat{u}^n} \left\{ \tilde{p}_{\hat{\theta}}(\hat{u}) \operatorname{sgn}(\boldsymbol{\omega} \cdot \boldsymbol{\alpha}) (\boldsymbol{\omega} \cdot \boldsymbol{\alpha})^{n-1} \right. \right. \\ \left. \left. \times \delta \left(\hat{\theta} + \arctan \left(\frac{\hat{u}}{D} \right) - \theta \right) \right\} \right] d\hat{\theta}, \quad (4.18)$$

where $\boldsymbol{\omega} = D\hat{\boldsymbol{\theta}} + \hat{u}\hat{\boldsymbol{\theta}}^\perp$, and:

$$\tilde{p}_{\hat{\theta}}(\hat{u}) = \frac{d}{D} \cdot \frac{D}{\sqrt{\hat{u}^2 + D^2}} \hat{p}_{\hat{\theta}}(\hat{u}). \quad (4.19)$$

Again, Equation (4.18) can be seen as an extension of the fan-beam Hilbert-transformed differentiated backprojection formula, whose proof is left in Appendix A. Of course, chain rules should be further applied to put the discontinuities induced by the Dirac delta function out of the derivative operator (Noo et al., 2004). However, this approach needed to get back to a continuous formulation, from which discretization should be applied. Here, moving from the continuous domain to a finite number of projections is not straightforward: indeed, since the integrals use resampling of the fan-beam data, they must be densely sampled both spatially and angularly around view θ , in order to find a pair $(\hat{\theta}, \hat{u})$ that satisfies the equation $\hat{\theta} + \arctan \left(\frac{\hat{u}}{D} \right) = \theta$. Although this can be the case in diagnostic CT, this will not be the case for C-arm CBCT, nor, *a fortiori*, for an arbitrarily small number N of views.

4.2.2.2 Semi-discrete fan-beam BPF formula

Instead of computing the same quantities as in the parallel-beam case using fan-beam projections and the change of variables from Equation (2.25), we compute different quantities that are intrinsically related to the fan-beam geometry. The new method derives directly from what was done in parallel-beam geometry using the parallel-beam FBP formula; here, we start from the fan-beam FBP from Equation (2.26). We can still write:

$$f_N = \frac{\pi}{N} \sum_{k=1}^K g_{\Theta_k}, \quad (4.20)$$

¹Recall that h is β -homogeneous if $h(\lambda x) = |\lambda|^\beta h(x)$ for any x and any λ

and:

$$g_{\Theta_k} = \sum_{\hat{\theta} \in \Theta_k} \frac{D^2}{s_{\hat{\theta}}^2} \hat{\mathcal{B}}_{\hat{\theta}} \mathcal{D} [\tilde{p}_{\hat{\theta}}]. \quad (4.21)$$

We write $g_{\hat{\theta}} = g_{\{\hat{\theta}\}}$ and we derive an elementary BPF formula for $g_{\hat{\theta}}$, that relies on the decomposition of the ramp filter \mathcal{D} into a spatial derivative operator and a Hilbert transform. We further observe that, for a given 2D point $\mathbf{x} = (\mathbf{x} \cdot \boldsymbol{\alpha})\boldsymbol{\alpha} + (\mathbf{x} \cdot \boldsymbol{\alpha}^\perp)\boldsymbol{\alpha}^\perp$, the corresponding detector coordinate $\hat{u}_{\hat{\theta}}$ is written as:

$$\begin{pmatrix} s_{\hat{\theta}}(\mathbf{x}) \hat{u}_{\hat{\theta}}(\mathbf{x}) \\ s_{\hat{\theta}}(\mathbf{x}) \end{pmatrix} = H_{\hat{\theta}}^\alpha(\mathbf{x} \cdot \boldsymbol{\alpha}) \begin{pmatrix} \mathbf{x} \cdot \boldsymbol{\alpha}^\perp \\ 1 \end{pmatrix}, \quad (4.22)$$

where $H_{\hat{\theta}}^\alpha(\mathbf{x} \cdot \boldsymbol{\alpha}) \in \mathbb{R}^{2 \times 2}$ is a homography matrix, whose inverse is also a homography matrix. Hence, projection and backprojection can be seen as a collection of homographic transformations applied from/to lines colinear to $\boldsymbol{\alpha}^\perp$. The proof of Theorem 4.2.4 is given in Section 4.5.3.

Theorem 4.2.4. *Let $\alpha \in [0, 2\pi]$ such that $\boldsymbol{\alpha}^\perp$ is not colinear to an acquired ray at view angle $\hat{\theta}$, which means (Figure 2.17a):*

$$\det \left(H_{\hat{\theta}}^\alpha(\mathbf{x} \cdot \boldsymbol{\alpha}) \right) \neq 0. \quad (4.23)$$

We further define $\sigma_{\hat{\theta}}^\alpha(\mathbf{x}) = \text{sgn} \left(\det \left(H_{\hat{\theta}}^\alpha(\mathbf{x} \cdot \boldsymbol{\alpha}) \right) \right)$. The following holds:

$$g_{\hat{\theta}} = \frac{1}{2\pi} \mathcal{H}_\alpha \left[b_{\hat{\theta}}^{(1)}(\alpha; \cdot) \right], \quad (4.24)$$

where:

$$\hat{b}_{\hat{\theta}}^{(1)}(\alpha, \cdot) = \sigma_{\hat{\theta}}^\alpha \frac{D^2}{s_{\hat{\theta}}^2} \hat{\mathcal{B}}_{\hat{\theta}} \left[\tilde{p}'_{\hat{\theta}} \right]. \quad (4.25)$$

Theorem 4.2.4 states that the weighted backprojection of Hilbert-transformed projections $\tilde{p}'_{\hat{\theta}}$ is equal to the Hilbert-filtering along direction $\boldsymbol{\alpha}^\perp$ of the weighted backprojection (with the same geometrical weights) of $\tilde{p}_{\hat{\theta}}$. In other words, the weighted backprojection operator commutes with the Hilbert transform operator, which can be taken in 2D as a collection of mono-directional Hilbert operators along an arbitrary direction $\boldsymbol{\alpha}^\perp$.

As for the parallel-beam case, the same result yields for an angular subset Θ_k :

$$g_{\Theta_k}(\mathbf{x}) = \frac{1}{2\pi} \mathcal{H}_\alpha \left[\hat{b}_{\Theta_k}^{(1)}(\alpha, \cdot) \right](\mathbf{x}), \quad \hat{b}_{\Theta_k}^{(1)}(\alpha, \mathbf{x}) = \sum_{\theta \in \Theta_k} \hat{b}_{\hat{\theta}}^{(1)}(\alpha, \mathbf{x}). \quad (4.26)$$

We again obtain a semi-discrete reconstruction formula in the fan-beam geometry by cumulating partial reconstructions over all subsets.

Theorem 4.2.5 (Semi-discrete fan-beam DBP-HT- K). *If one can choose a value of α_k such that Equation (4.26) holds for each subset Θ_k , then image f_N can be recovered as:*

$$f_N = \frac{\pi}{N} \sum_{k=1}^K \frac{1}{2\pi} \mathcal{H}_{\alpha_k} \left[\hat{b}_{\Theta_k}^{(1)}(\alpha_k, \cdot) \right]. \quad (4.27)$$

Until now, the local derivative operator was kept in the projection space, and only the Hilbert transform was applied in the image space. In the following, we also show that the derivative operator can be moved out of the backprojection step, so that the full ramp filtering can be applied after backprojection. The proof is given in Section 4.5.4.

Theorem 4.2.6. *Let $\alpha \in [0, 2\pi]$ such that $(\mathbf{x} + d\hat{\boldsymbol{\theta}}) \cdot \boldsymbol{\alpha} \neq 0$. The following holds wherever $\hat{u}_{\hat{\boldsymbol{\theta}}}(\mathbf{x})$ is non-degenerate (that is, wherever \mathbf{x} is not the source point):*

$$g_{\hat{\boldsymbol{\theta}}}(\mathbf{x}) = \mathcal{D}_{\alpha} \left[\hat{b}_{\hat{\boldsymbol{\theta}}}^{(0)}(\alpha, \cdot) \right] (\mathbf{x}), \quad (4.28)$$

where:

$$\hat{b}_{\hat{\boldsymbol{\theta}}}^{(0)}(\alpha, \mathbf{x}) = \sigma_{\hat{\boldsymbol{\theta}}}^{\alpha}(\mathbf{x}) \frac{D^2}{\det(H_{\hat{\boldsymbol{\theta}}}^{\alpha}(\mathbf{x} \cdot \boldsymbol{\alpha}))} \hat{\mathcal{B}}_{\hat{\boldsymbol{\theta}}} [\tilde{p}_{\hat{\boldsymbol{\theta}}}] (\mathbf{x}). \quad (4.29)$$

The corresponding splitting reconstruction formula is given by:

$$f_N = \frac{\pi}{N} \sum_{k=1}^K \mathcal{D}_{\alpha_k} \left[\hat{b}_{\Theta_k}^{(0)}(\alpha_k, \cdot) \right], \quad \hat{b}_{\Theta_k}^{(0)}(\alpha, \cdot) \sum_{\theta \in \Theta_k} \hat{b}_{\hat{\boldsymbol{\theta}}}^{(0)}(\alpha, \cdot). \quad (4.30)$$

Note that Equations (4.27) and (4.30) not only coincide with the fan-beam FBP formula when $N \rightarrow +\infty$: indeed, they yield the same semi-discrete reconstruction as the semi-discrete fan-beam FBP formula from Equation (2.26). The general reconstruction flowchart from Figure 4.3 can thus be used with $n = 0$ and $n = 1$ using $\hat{b}_{\Theta_k}^{(n)}$ as backprojected images.

4.2.2.3 Extension to C-arm CBCT

As already pointed out, the Tuy conditions are not satisfied by the circular cone-beam geometry. Hence, only approximate direct reconstruction methods exist, such as the FDK method. FDK is a direct extension of the fan-beam FBP method to circular cone-beam geometries (Feldkamp et al., 1984). Following the same approach, we propose an immediate extension of our method to cone-beam data. We define this time

$$\hat{b}_{\hat{\boldsymbol{\theta}}}^{(0)}(\alpha, \mathbf{x}) = \sigma_{\hat{\boldsymbol{\theta}}}^{\alpha}(\mathbf{x}) \frac{D^2}{\det(H_{\hat{\boldsymbol{\theta}}}^{\alpha}(\mathbf{x} \cdot \boldsymbol{\alpha}))} \hat{\mathcal{B}}_{\hat{\boldsymbol{\theta}}} [\tilde{p}_{\hat{\boldsymbol{\theta}}}] (\mathbf{x}). \quad (4.31)$$

$$\hat{b}_{\hat{\boldsymbol{\theta}}}^{(1)}(\alpha, \mathbf{x}) = \sigma_{\hat{\boldsymbol{\theta}}}^{\alpha}(\mathbf{x}) \frac{D^2}{s_{\hat{\boldsymbol{\theta}}}(\mathbf{x})^2} \hat{\mathcal{B}}_{\hat{\boldsymbol{\theta}}} \left[\frac{\partial \tilde{p}_{\hat{\boldsymbol{\theta}}}}{\partial \hat{u}} \right] (\mathbf{x}), \quad (4.32)$$

where $\boldsymbol{\alpha}$ is orthogonal to the z -axis. This time, the homography matrix $H_{\hat{\boldsymbol{\theta}}}^{\alpha}(\mathbf{x} \cdot \boldsymbol{\alpha}) \in \mathbb{R}^{3 \times 3}$ is defined by:

$$\begin{pmatrix} s_{\hat{\boldsymbol{\theta}}} \hat{u}_{\hat{\boldsymbol{\theta}}} \\ s_{\hat{\boldsymbol{\theta}}} \hat{v}_{\hat{\boldsymbol{\theta}}} \\ s_{\hat{\boldsymbol{\theta}}} \end{pmatrix} = H_{\hat{\boldsymbol{\theta}}}^{\alpha}(\mathbf{x} \cdot \boldsymbol{\alpha}) \begin{pmatrix} \mathbf{x} \cdot \boldsymbol{\alpha}^{\perp} \\ z \\ 1 \end{pmatrix}. \quad (4.33)$$

The approximate splitting BPF methods for circular cone-beam data are:

$$\hat{f}_{N,0} = \frac{\pi}{N} \sum_{k=1}^K \mathcal{D}_{\alpha_k} \left[\hat{b}_{\hat{\Theta}_k}^{(0)}(\alpha_k, \cdot) \right] (\mathbf{x}), \quad (4.34)$$

$$\hat{f}_{N,1} = \frac{\pi}{N} \sum_{k=1}^K \frac{1}{2\pi} \mathcal{H}_{\alpha_k} \left[\hat{b}_{\hat{\Theta}_k}^{(1)}(\alpha_k, \cdot) \right] (\mathbf{x}). \quad (4.35)$$

Note that if the object is invariant along the z -axis, the reconstruction formulas are exact, in the sense that they correspond to the semi-discrete slice-by-slice fan-beam FBP formula, which leads to the exact fan-beam FBP when $N \rightarrow +\infty$. The proof is given in Section 4.5.5.

Theorem 4.2.7. *Assume that f is invariant along the z -axis. Then the reconstruction formulas from Equation (4.34) are equal to the semi-discrete slice-by-slice fan-beam FBP formula: $\hat{f}_{N,0} = \hat{f}_{N,1} = f_N$.*

As for FDK, these formulas would yield cone-beam artifacts in practice, since anatomies of interest are not invariant along the z -axis. Equation (4.34) also amounts to a slice-by-slice parallel-beam reconstruction when $(D, d) \rightarrow (+\infty, +\infty)$. An interesting property of formulas from Equation (4.34) is that they involve quantities such as $\det(H_{\hat{\theta}}^{\alpha})$ or $s_{\hat{\theta}}$, which are intrinsically related to projection matrices. Hence, these formulas are well adapted to non-ideal orbits, which may differ from a pure circular orbit, but whose differences are encoded into projection matrices.

Again, in practice, a two-pass reconstruction using frontal and lateral views is used, yielding, for $n = 1$:

$$f_{\text{BPF}} = \frac{\pi}{N} \frac{1}{2\pi} \left(\mathcal{H}_{\frac{\pi}{2}} \left[\hat{b}_{\Theta_{\text{FRT}}}^{(1)} \left(\frac{\pi}{2}; \cdot \right) \right] + \mathcal{H}_0 \left[\hat{b}_{\Theta_{\text{LAT}}}^{(1)}(0; \cdot) \right] \right). \quad (4.36)$$

4.2.3 Simulations

4.2.3.1 Planar geometries

In this section, we compare reconstructions from non-truncated projections using our approach with either $n = 0$ or $n = 1$ to standard FBP. Ideal parallel-beam projections of a uniform centered unit disk were analytically generated (Figure 4.5a); we computed a geometry of 720 view angles uniformly distributed over 180° . Images are reconstructed over a square grid of size 512^2 . Three cases were investigated:

- (i) the noise-free, fully sampled case (Figure 4.5b);
- (ii) the noise-free, under-sampled case, where only 22 views out of 720, uniformly distributed over 180° , were used (Figure 4.5c);
- (iii) the noisy, fully sampled case, where projection lines p were corrupted by noise according to the Poisson statistics of $I_0 e^{-p}$ with parameter $I_0 e^{-p}$ (Figure 4.5d).

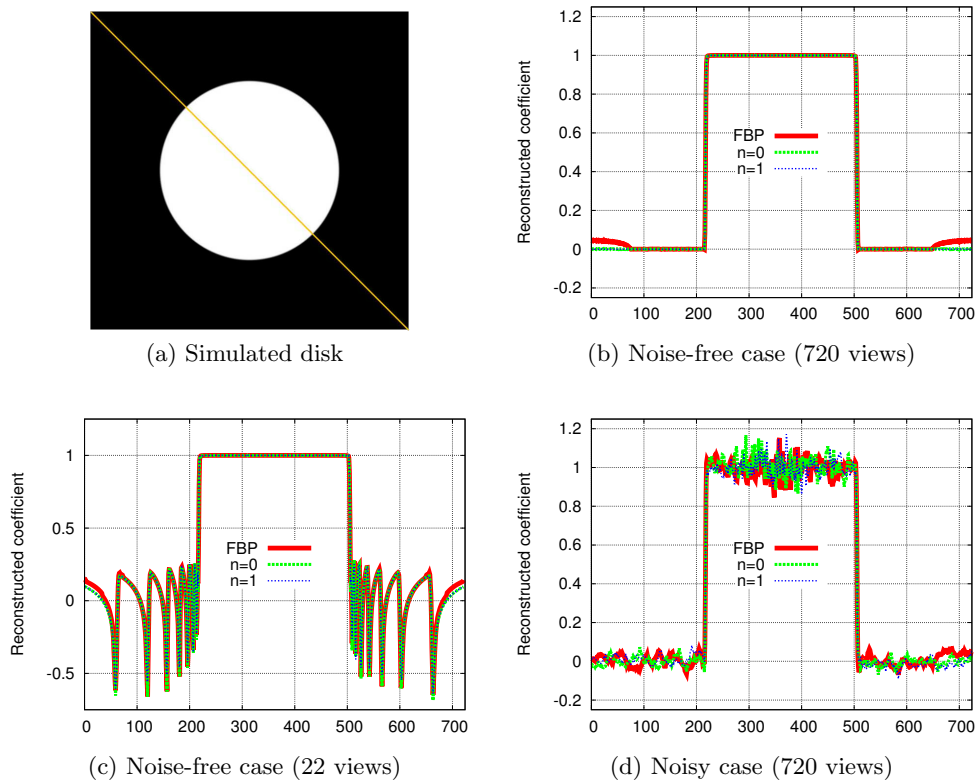


Figure 4.5 – Parallel-beam reconstructions of a uniform disk. Profiles are taken along the orange line shown in (a).

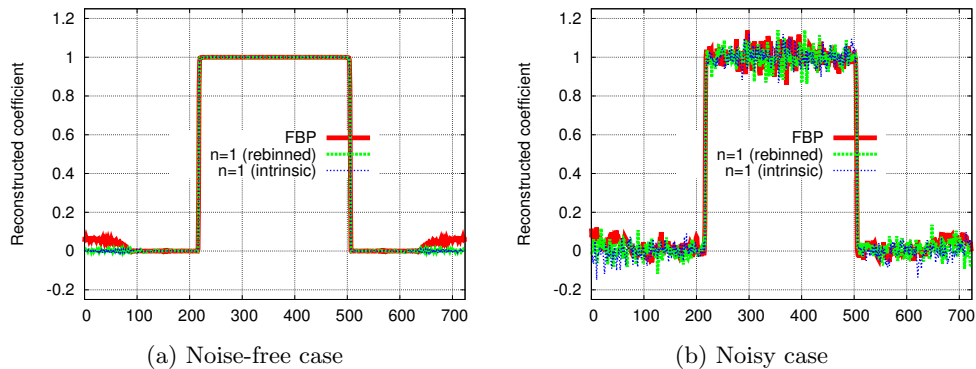
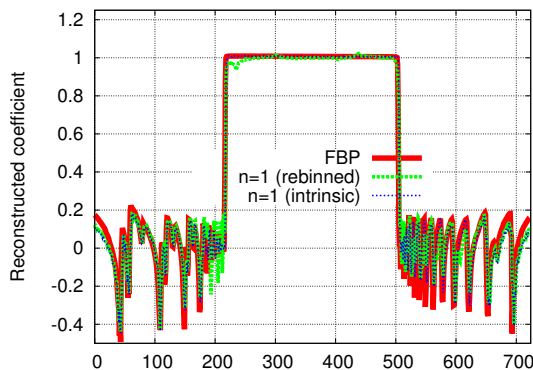


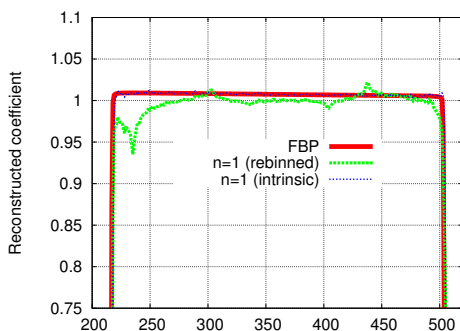
Figure 4.6 – Fan-beam reconstructions of a uniform disk from 1440 views uniformly spread over 360° . Profiles are taken along the orange line shown in Figure 4.5a.

The value of I_0 was set to $3 \cdot 10^5$. In all cases, the line profiles show a very good agreement between all three methods.

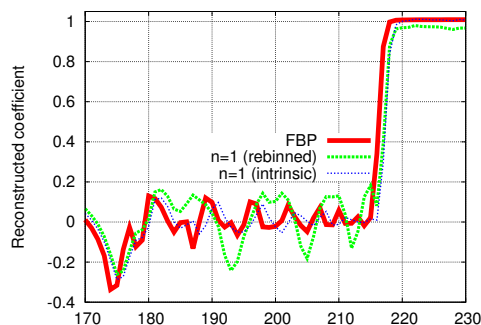
We now set $n = 1$. Ideal fan-beam projections of the same disk were analytically generated for 1440 views uniformly distributed over 360° . We set $D = 1195$ and $d = 720$ in this experiment. Noise-free simulations include fully sampled



(a) Noise-free case



(b) Zoom from (a)



(c) Zoom from (a)

Figure 4.7 – Fan-beam reconstructions of a uniform disk from 45 views uniformly spread over 360° . Profiles are taken along the orange line shown in Figure 4.5a.

(1440 view) and under-sampled (45 views) data; our fan-beam reconstructions using the rebinning method or the intrinsically fan-beam method are compared to standard FBP. Results are shown in Figures 4.6 and 4.7. Line profiles are taken along the same orange line depicted in Figure 4.5a. All three methods show a similar behavior when the angular sampling is dense (Figure 4.6a and Figure 4.6b). However, in the under-sampled case (Figure 4.7a), the rebinned method lacks reconstruction accuracy, compared to the intrinsically fan-beam approach: the flat area of the line profile is corrupted by oscillatory patterns (Figure 4.7b), and under-sampling streak patterns near the object differ from the patterns given by FBP (Figure 4.7c).

4.2.3.2 CBCT reconstruction of a uniform cylinder

In this section, we still fix $n = 1$ and we keep the angular sampling to 1440 projection views uniformly distributed over 360° . Density projections were analytically generated for a uniform cylinder centered at the z -axis. This time, $D = 1295$ and $d = 820$. We compare our reconstruction method to FDK. Results are shown in Figure 4.8.

We can make two interesting observations from this result. First, the axial

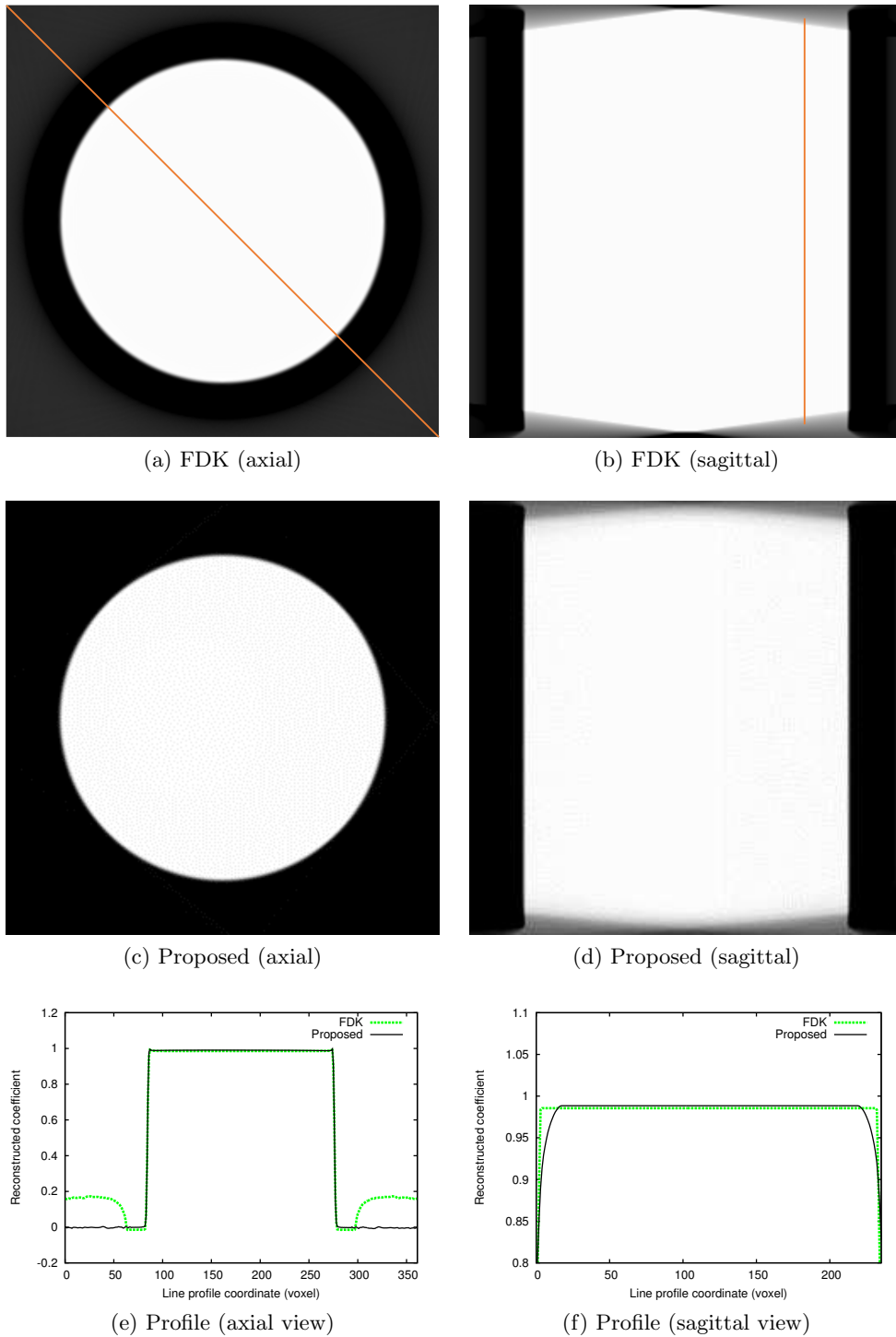


Figure 4.8 – CBCT direct reconstruction of a uniform cylinder with FDK (a),(b) and with the proposed method (c),(d). Line profiles in axial (e) and sagittal (f) views are shown for both methods.

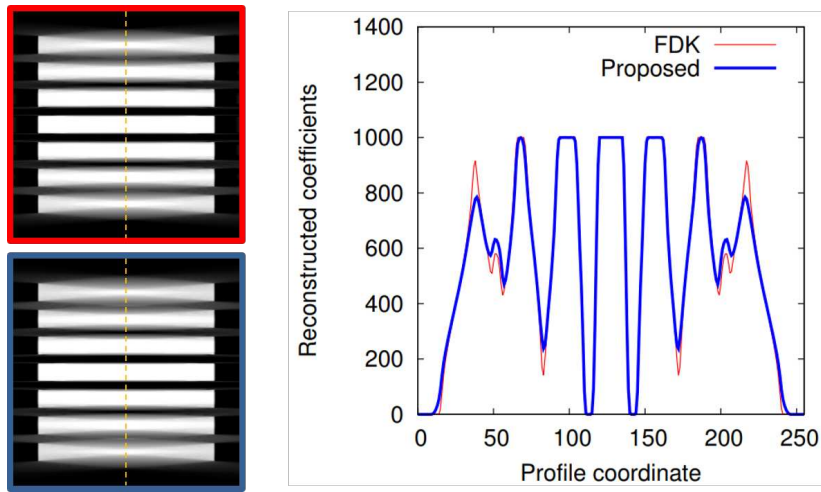


Figure 4.9 – CBCT direct reconstruction of a numerical Defrise phantom with FDK (red) and with the proposed method (blue). The line profile is taken over a vertical line at the center of the sagittal slice.

slice of the FDK reconstructed image (Figure 4.8a) shows an accurate reconstruction within the reconstructed FOV, but values outside the FOV become nonzero. This is due to the fact that FDK backprojects filtered 2D projections, whose rows have been ramp-filtered. Ramp-filtered signals of compactly supported signals are infinitely supported; in the particular case of a uniform cylinder, the filtered rows tend to zero asymptotically from negative values. In practice, however, only truncated versions of the filtered rows are computed and backprojected: this explains why positive values outside the FOV cannot be compensated by missing negative tails of the filtered projections. By contrast, the axial slice of the reconstructed image using our approach shows a flat background even outside the FOV (Figure 4.8c). The difference between both reconstructed images can be observed over a line profile in Figure 4.8e. Of course, this makes no difference in practice, as it is assumed that only the 3D FOV needs to be reconstructed accurately.

The second observation regards the boundary effects on the sagittal slices. These boundary effects are visually similar in both FDK and our method (Figures 4.8b and 4.8d), but it seems that FDK achieves a more uniform reconstruction over a larger number of axial slices, as suggested on the plotted line profile in Figure 4.8f. This is confirmed by the reconstruction of a numerical Defrise phantom using the same parameters (Figure 4.9), which shows more accurate reconstruction with FDK than with the proposed method. However, for small cone angles, both methods are equivalent.

4.2.3.3 CBCT reconstruction of a head

A diagnostic CT scan of a head was forward-projected over an ideal circular orbit using $D = d = 1180$ mm. A total of 1440 projections sampling Θ was generated. The projections were reconstructed using FDK (yielding image f_{FDK}) and Equation (4.36) (yielding image f_{BPF}). We computed the relative error image

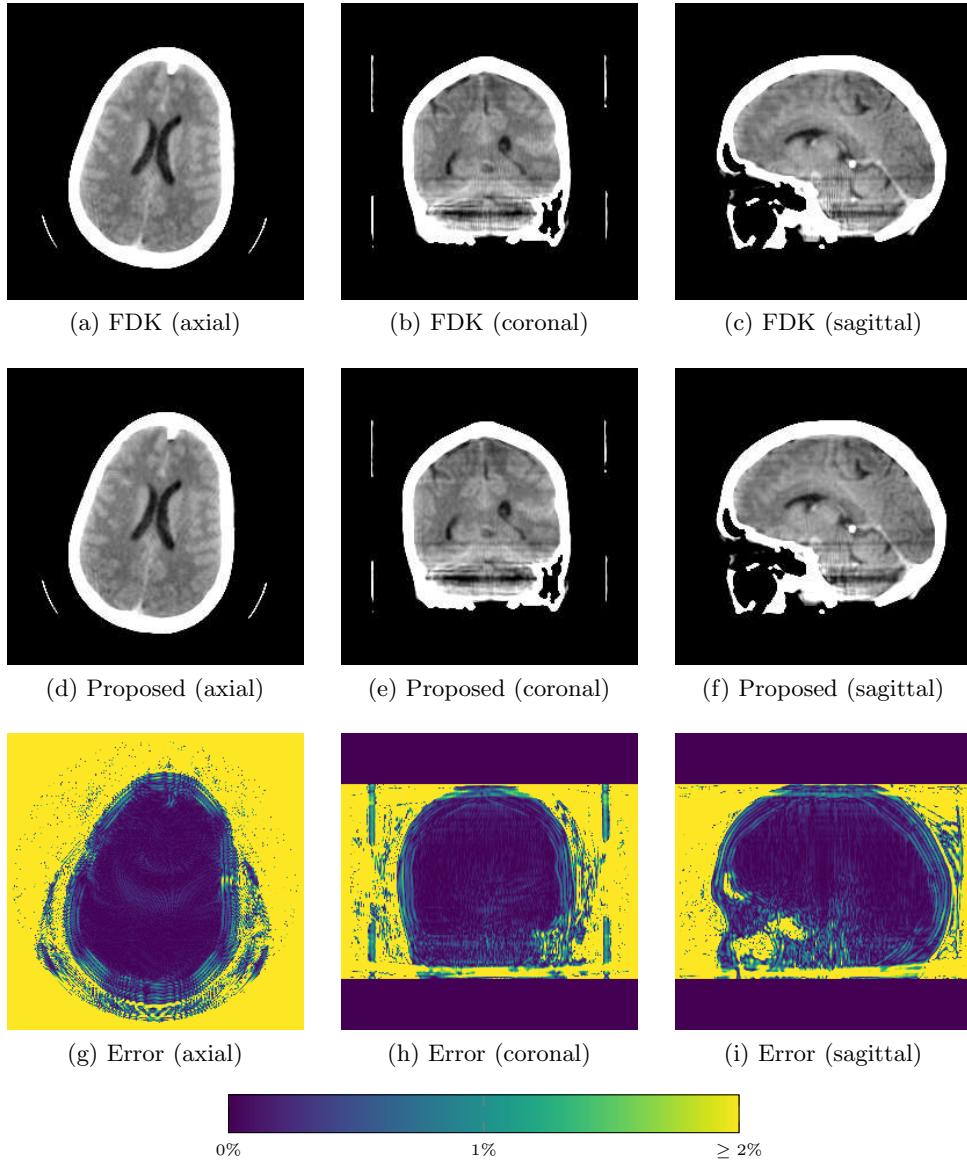


Figure 4.10 – Noise-free CBCT direct reconstruction of a head using FDK (a),(b),(c), and the proposed method (d),(e),(f). Pointwise relative error with respect to FDK are shown in (g),(h),(i). Window width: 50 HU.

of f_{BPF} with respect to f_{FDK} , and we computed the mean relative error (MRE) over a mask Ω_0 , denoted $\Delta_{\Omega_0}(f_{\text{BPF}}, f_{\text{FDK}})$, using the formula:

$$\Delta_{\Omega}(f, f^*) = \frac{1}{\text{Card}(\Omega)} \sum_{\mathbf{x} \in \Omega} \frac{|f(\mathbf{x}) - f^*(\mathbf{x})|}{|f^*(\mathbf{x})|} \quad (4.37)$$

Mask Ω_0 was defined in order to keep only the voxels higher than 750 HU. Images were reconstructed on a $256 \times 256 \times 256$ grid with isotropic voxels of size 1.17 mm^3 .

We repeated the experiment using modified projection data corresponding to

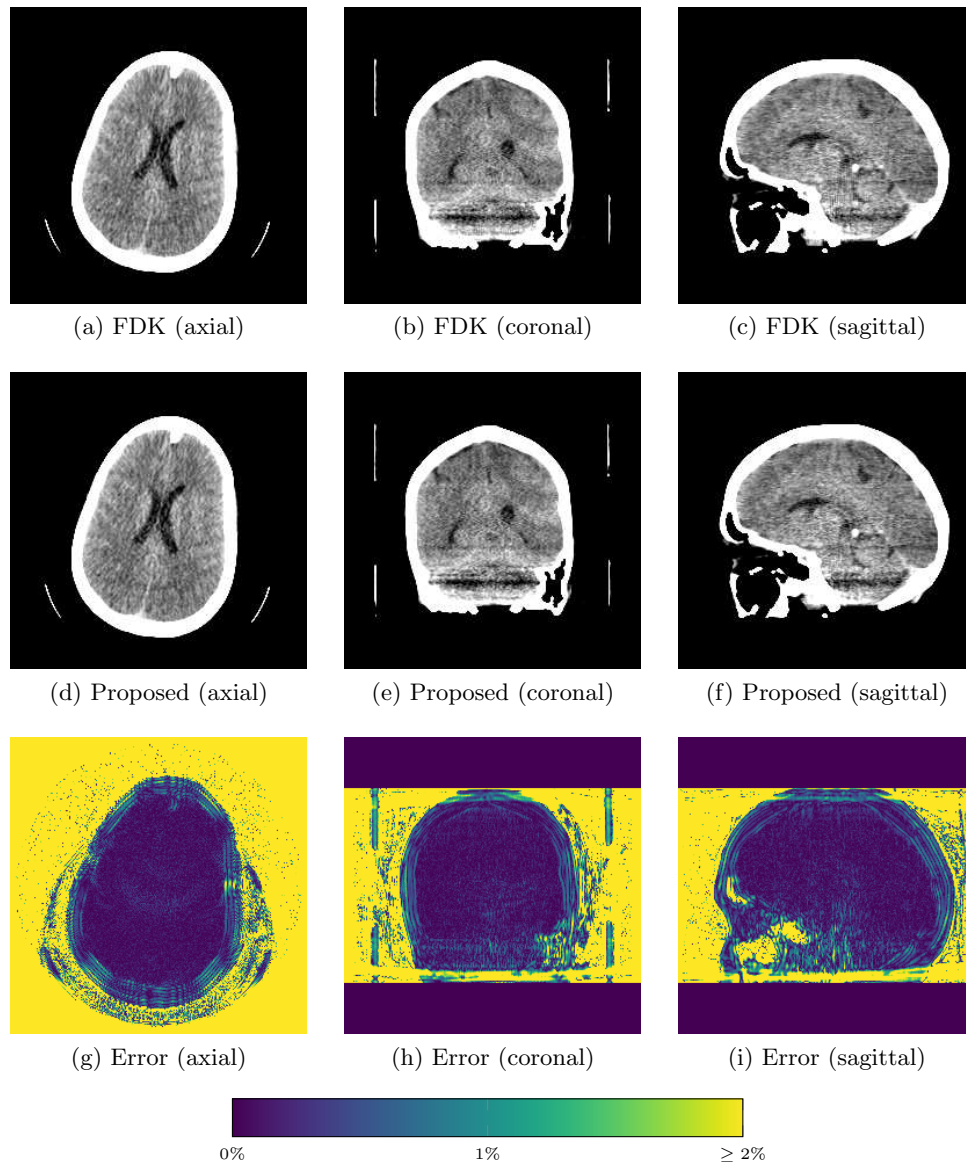


Figure 4.11 – Noisy CBCT direct reconstruction of a head using FDK (a),(b),(c), and the proposed method (d),(e),(f). Pointwise relative error with respect to FDK are shown in (g),(h),(i). Window width: 50 HU.

$1.6 \cdot 10^6$ photons per ray emitted from the X-ray source, in order to check the stability of the method with respect to noise, yielding images $f_{\text{FDK}}^{\text{noisy}}$ and $f_{\text{BPF}}^{\text{noisy}}$.

Noise-free reconstructed images are shown in Figure 4.10. The images f_{FDK} and f_{BPF} are visually very similar. Both reconstructions are exact and identical in the fan-beam geometry of the midplane. However, f_{BPF} is more sensitive to the cone-beam incomplete sampling over a circular orbit (see the dark streaks near the temporal bones in the coronal and sagittal slices), which was expected by the reconstruction of the Defrise phantom in the previous experiment. Similar noise

behavior occurs for both methods when reconstructing from noisy projections (Figure 4.11).

On average, the MRE inside Ω_0 is equal to 0.42% in the noise-free case and to 0.43% in the noisy case, the higher errors being located towards points with high cone angles, as shown in Figures 4.10g–4.10i and in Figures 4.11g–4.11i.

We have provided a new BPF reconstruction method that extends to C-arm CBCT. In contrast to previous BPF approaches, it is an intrinsically view-based method, that is well suited to C-arm CBCT acquisitions. We now take advantage of this new reconstruction method to address the problem of dual-rotation direct reconstruction for virtual bow-tie C-arm CBCT.

4.3 Application to virtual bow-tie C-arm CBCT

4.3.1 Principle

Recall that two acquisitions are available: one acquisition is a collection p_T of N truncated projections acquired at high dose; the second acquisition is a collection p_F of N non truncated views acquired at low dose. As stated in the beginning of this chapter, merging the data in the projection space is not relevant, nor is a simple post-processing step after reconstructing both p_F and p_T independently.

The key for a good dual-rotation direct reconstruction is to handle data truncation from p_T prior to any non-local filtering step. With FBP-like methods, filtering applies directly to the projections, so that truncation needs to be handled in the projection space, *e.g.* by ad hoc data extrapolation (Ohnesorge et al., 1999), with a risk that such empirical solutions leave a residual low-frequency error in the reconstructed image. In BPF approaches, however, filtering applies to the backprojected image of locally filtered projections, so that truncation may be handled either in the projection space or in the unfiltered backprojection space.

We choose the latter as our merging space (Figure 4.12). Since local operations are applied to projections p_T , they correctly sample the unfiltered backprojected image b_T within the truncated 3D FOV. Outside this FOV, however, each backprojected point is observed over a limited angular range, which differs from one point to the other. We thus merge the truncated 3D FOV of b_T with the unfiltered backprojected image b_F obtained from p_F , yielding image $\mathcal{M}(b_F, b_T)$ such that:

$$\mathcal{M}(b_F, b_T) = \begin{cases} w_F \cdot b_F + w_T \cdot b_T & \text{inside the truncated 3D FOV;} \\ b_F & \text{outside the truncated 3D FOV.} \end{cases} \quad (4.38)$$

Weighting functions w_F and w_T are such that $w_F + w_T = 1$. Function $w_F : \mathbb{R}^3 \rightarrow [0, 1]$ can be either a constant or a smooth function ensuring a continuous transition from b_F to b_T at the boundaries of the truncated 3D FOV. In the framework of our proposed BPF method, merging is performed separately for the frontal views and the lateral views.

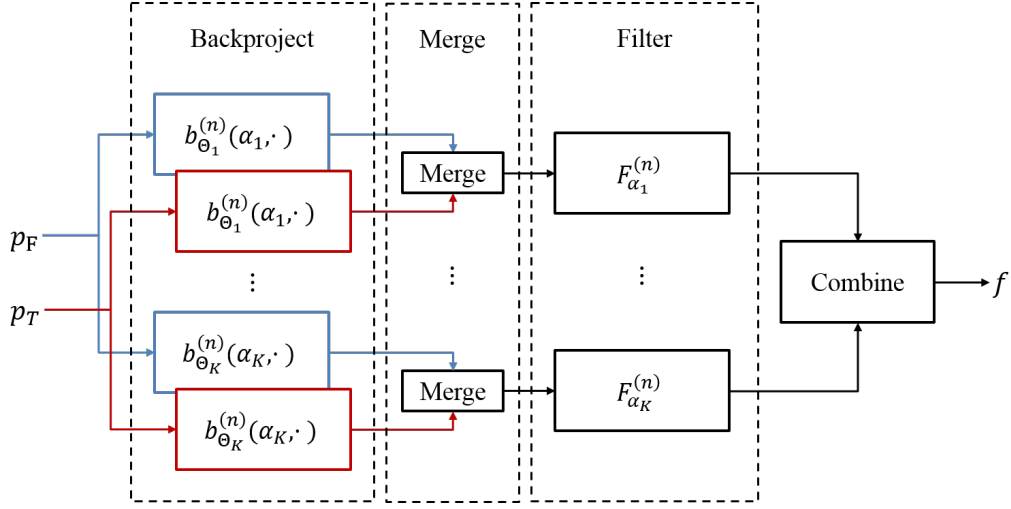


Figure 4.12 – General dual-rotation direct reconstruction flowchart.

4.3.2 Validation on phantom acquisitions

4.3.2.1 Experiments

We first consider the spin obtained by forward-projecting a diagnostic CT scan of a head as in Section 4.2.3.3. The truncated projections p_T were simulated by applying a digital transaxial truncation to the previous set of 1440 noisy projections, corresponding to a cylindrical, centered field of view Ω' whose edges cross the head skull. For the un-truncated projections p_F , we simulated an acquisition of 1440 projections corresponding to 10^5 photons per ray emitted from the X-ray source (hence the dose ratio between the un-truncated and the truncated acquisitions is fixed to 1/16). The BPF reconstruction from p_F is denoted f_{BPF}^F . The merging step was performed using the following weighting function:

$$w_F(\mathbf{x}) = \frac{1}{2} \left(1 - \cos \left(\pi \cdot \frac{|\mathbf{x}| - r_{\Omega'}}{\Delta r} \right) \right), \quad (4.39)$$

where $r_{\Omega'}$ denotes the radius of the cylindrical ROI Ω' , and Δr is the transition zone radial width. In the following, Δr was arbitrarily set to 5 voxels. The dual-rotation BPF reconstructed image is denoted $f_{\text{BPF}}^{F\&T}$. The MRE over the intersection set $\Omega = \Omega' \cap \Omega_0$ was computed with respect to the un-truncated FDK reconstruction $f_{\text{FDK}}^{\text{noisy}}$ (see Figures 4.11a–4.11c). We also show the relative error images with respect to f_{BPF}^F and to $f_{\text{BPF}}^{\text{noisy}}$ (see Figures 4.11d–4.11f).

Experiments on real data were performed on the Catphan[®] CTP 515 LCD module and on the head phantom with soft-tissue-like structures. The acquisition parameters were the same as in the previous chapter: spins were acquired on an IGS 740 C-arm system, with SOD = 820 mm and SID = 1295 mm. The full-FOV width is the detector width, which is 40 cm. The FOV height was 5 cm for the CTP 515 module and 17.5 cm for the head phantom. For the truncated, high dose acquisitions, parameter t was set to 0.5 for the CTP 515 module and to 0.3 for the head phantom. Fixed techniques were used at 0.85 mAs (respectively 3.4 mAs)

for the full-FOV (respectively truncated) acquisitions. A 120 kVp spectrum was used for the CTP 515 module, while the head phantom was acquired at 80 kVp. The short-scan circular orbit was sampled with 607 projections.

Because the reconstruction method is not iterative anymore, the computational complexity of the method is reduced. Hence, we reconstruct higher resolution images with isotropic voxel size 0.48 mm. Single-rotation reconstructions use $w_F = 1$ in Equation (4.38). They are compared to dual-rotation reconstructions, which use the weighting function w_F defined as a radial function of \mathbf{x} :

$$w_F(\mathbf{x}) = \frac{1}{2} \left(1 - \cos \left(\pi \cdot \frac{|\mathbf{x}| - r'}{r_T - r'} \right) \right), \quad (4.40)$$

where r_T denotes the radius of the truncated 3D FOV, and $r' = r_T - \Delta r < r_T$. In the following, Δr was arbitrarily set to 7.5 mm. Hence, the defined weights select image b_T in the 3D FOV with radius r' and image b_T whenever $|\mathbf{x}| > r_T$, with a smooth blending in the hollow cylinder defined by $r' < |\mathbf{x}| \leq r_T$. Reconstructions used $n = 1$: hence, the filtering step was reduced to a Fourier-based Hilbert transform.

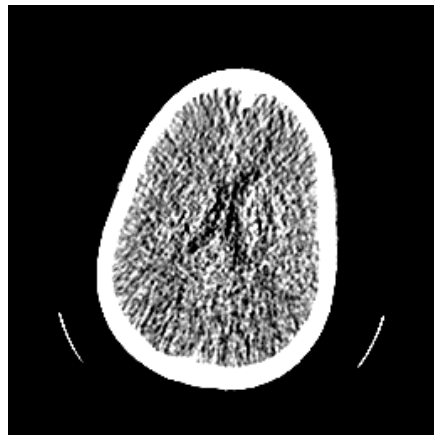
4.3.2.2 Results

Results of the single-rotation reconstruction from the low-dose spin p_F and the dual-rotation reconstruction are shown in Figure 4.13. The single-rotation reconstruction f_{BPF}^F (first column) is very noisy and a narrow display window cannot clearly show the difference between gray and white matters in the brain.

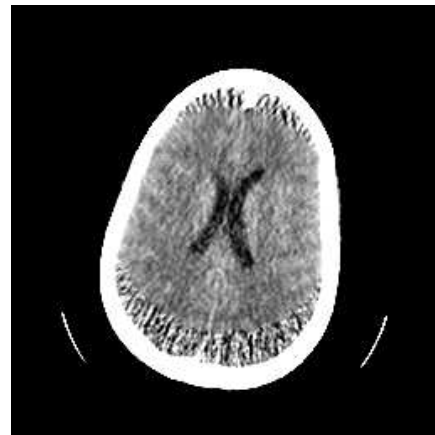
The dual-rotation reconstruction $f_{\text{BPF}}^{F\&T}$ (second column) is visually similar to the reference FDK reconstruction $f_{\text{FDK}}^{\text{noisy}}$ inside the ROI Ω' . Outside the ROI, image $f_{\text{BPF}}^{F\&T}$ shows a very noisy reconstruction of the head. However, the high noise contained in p_F does not seem to propagate inside Ω' . The value of the MRE inside region $\Omega = \Omega' \cap \Omega_0$ with respect to $f_{\text{FDK}}^{\text{noisy}}$ is 0.44%, which is very similar to the MRE value between the untruncated FDK and BPF reconstructed images of Section 4.2.3.3.

The relative errors of $f_{\text{BPF}}^{F\&T}$ with respect to $f_{\text{BPF}}^{\text{noisy}}$ and f_{BPF}^F are shown in the first and second columns of Figure 4.14, respectively. The error with respect to $f_{\text{BPF}}^{\text{noisy}}$ (first column) shows a very good agreement between $f_{\text{BPF}}^{F\&T}$ and $f_{\text{BPF}}^{\text{noisy}}$ inside Ω' . On the axial slice (Figure 4.14a), vertical and horizontal patterns are visible: they correspond to the proposed two-pass split between frontal and lateral views. The error with respect to f_{BPF}^F (second column) is also interesting. Indeed, it shows that $f_{\text{BPF}}^{F\&T}$ remains very close to f_{BPF}^F in the regions of the head that are not in Ω' . This confirms our observation, that the noise patterns contained in the un-filtered backprojected images do not spread over the whole image after filtering. Again, the vertical and horizontal bands crossing the axial slice in Figure 4.14b are characteristic of the two-pass algorithm.

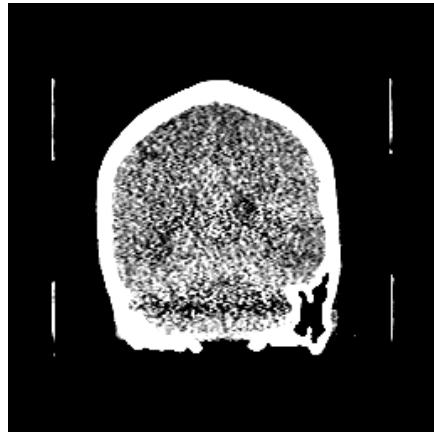
Results on real C-arm CBCT acquisitions are shown in Figures 4.15 and 4.16. Figure 4.15 shows the results on the CTP 515 module. Figure 4.15a shows a native thin slice of the BPF reconstructed image from the full-FOV spin only. Contrast inserts with relative contrasts lower than 1% are barely visible due to the noise



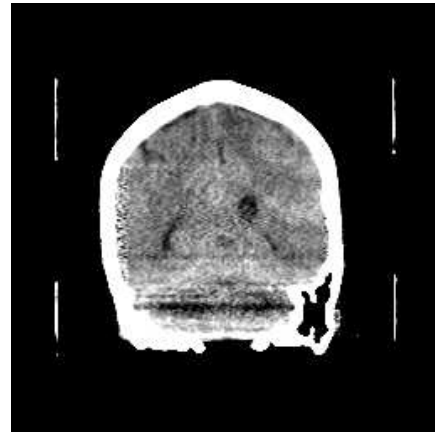
(a) Single-rotation (axial)



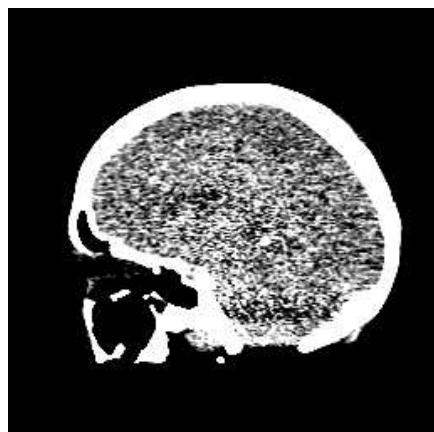
(b) Dual-rotation (axial)



(c) Single-rotation (coronal)



(d) Dual-rotation (coronal)

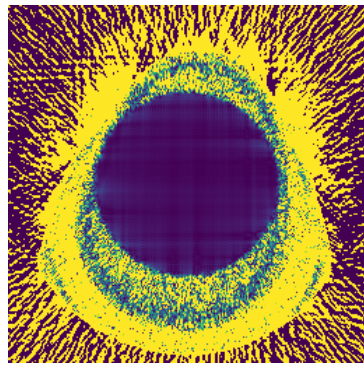


(e) Single-rotation (sagittal)

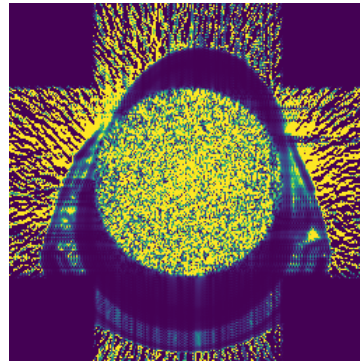


(f) Dual-rotation (sagittal)

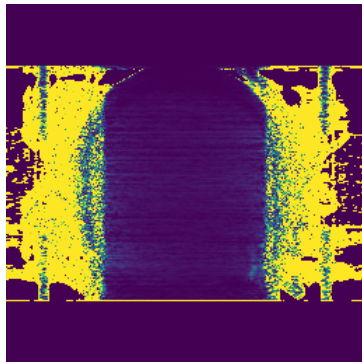
Figure 4.13 – Dual-rotation direct reconstruction of a head (right column). In comparison, the single-rotation, FDK reconstruction from the noisy, un-truncated spin is also shown (left column). Window width: 50 HU.



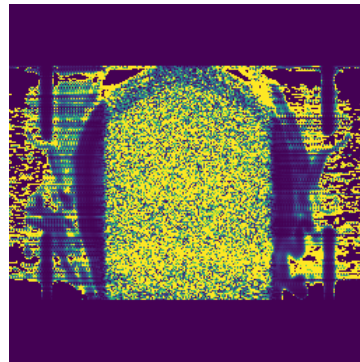
(a) Target: low-noise BPF (axial)



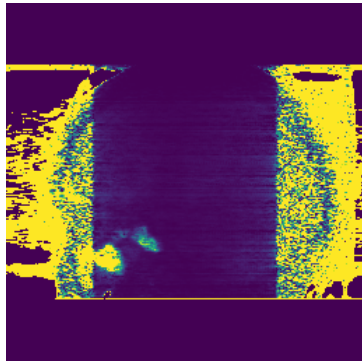
(b) Target: high-noise BPF (axial)



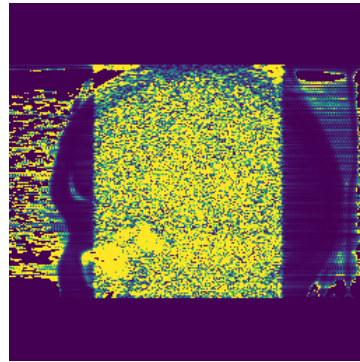
(c) Target: low-noise BPF (coronal)



(d) Target: high-noise BPF (coronal)



(e) Target: low-noise BPF (sagittal)



(f) Target: high-noise BPF (sagittal)

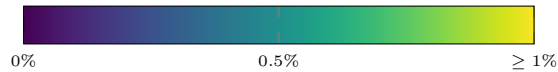
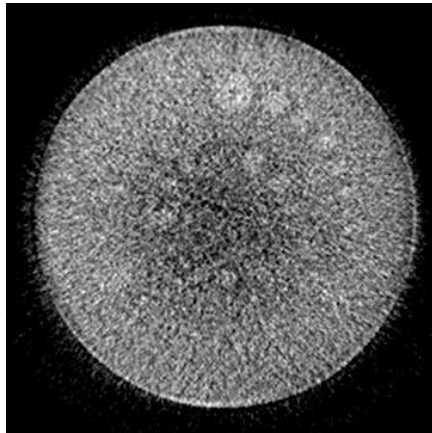
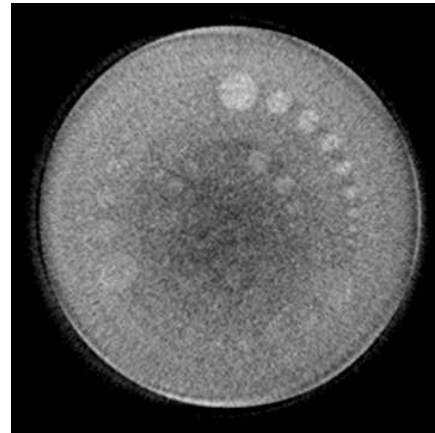


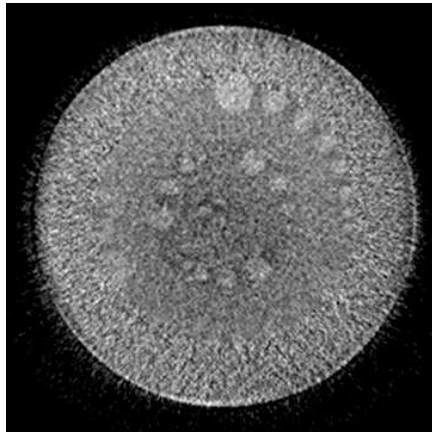
Figure 4.14 – Dual-rotation direct reconstruction of a head: relative errors (left column) with respect to the FDK reconstruction from the less noisy, un-truncated acquisition (Figure 4.11, first row) and (right column) with respect to the FDK reconstruction from the noisy, un-truncated acquisition (Figure 4.13, left column).



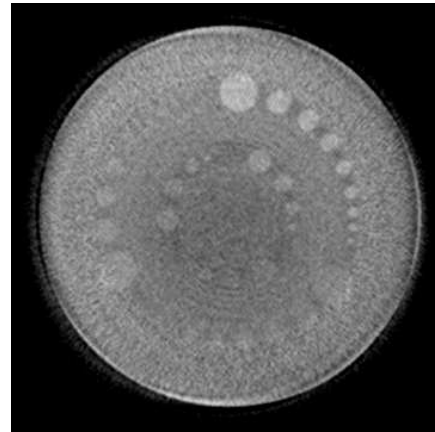
(a) Single-rotation, 0.48 mm thin slice



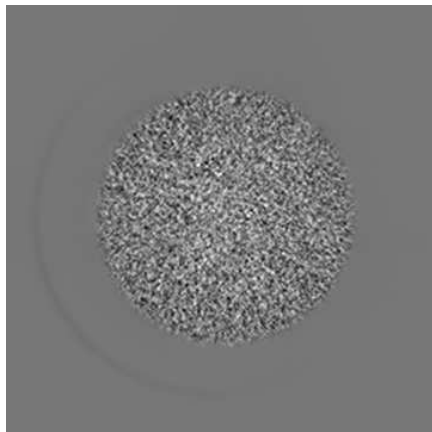
(b) Single-rotation, 10 mm thick slice



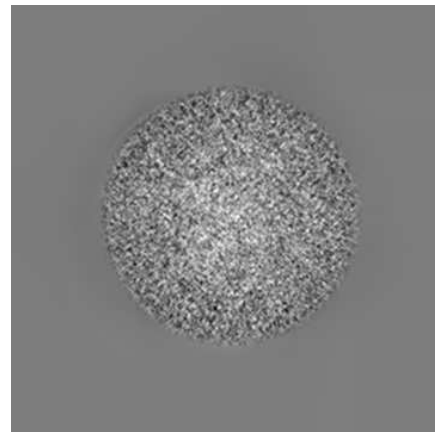
(c) Dual-rotation, 0.48 mm thin slice



(d) Dual-rotation, 10 mm thick slice



(e) Difference, 0.48 mm thin slice

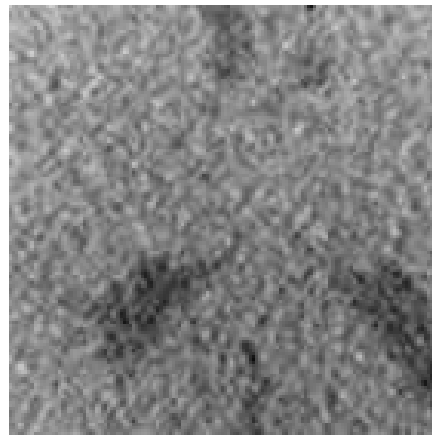


(f) Difference, 10 mm thick slice

Figure 4.15 – Dual-rotation direct reconstruction of the CTP 515 LCD module. Window width: 50 HU.



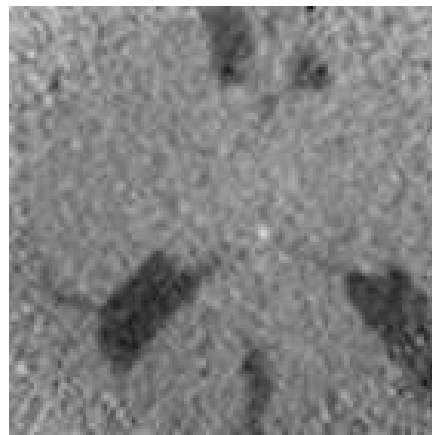
(a) Single-rotation



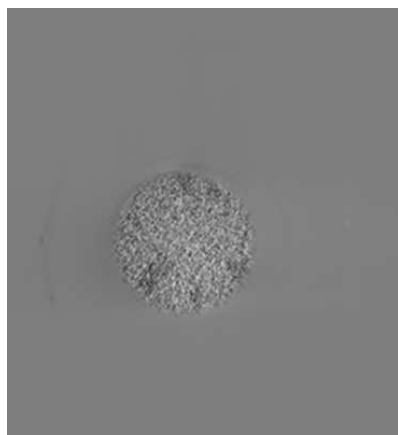
(b) Single-rotation (zoom)



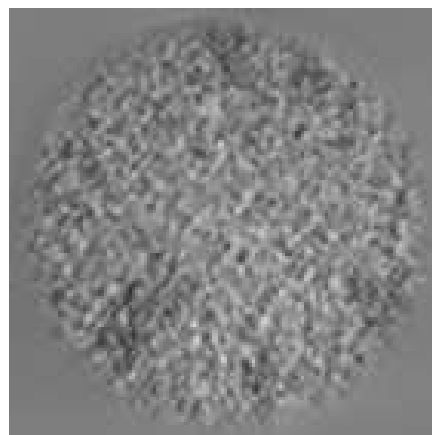
(c) Dual-rotation



(d) Dual-rotation (zoom)



(e) Difference



(f) Difference (zoom)

Figure 4.16 – Dual-rotation direct reconstruction of the head phantom. Window width: 150 HU.

level in the image. Averaging the axial slices over 10 mm (Figure 4.15b) increases the detectability of peripheral inserts, but does not help to recover sublice central inserts. Both images are still corrupted by a small residual cupping artifact due to scattered radiations.

Dual-rotation reconstruction (Figure 4.15c) both reduces the cupping artifact and increases low-contrast detection of the central contrast inserts. In particular, one can note that more 0.3% contrast inserts are visible in the 10 mm averaged thick slice of Figure 4.15d than in Figure 4.15c. From the subtraction of the single-rotation reconstructed image from the dual-rotation reconstructed image (Figures 4.15e and 4.15f), one immediately observes that changes only regard the truncated 3D FOV, where blending actually occurred. In this area, the difference image only shows noise and a low-frequency capping, confirming that noise and scatter-induced cupping were reduced with dual-rotation reconstruction.

All these observations are confirmed in the more realistic case of the head phantom with soft-tissue-like structures (Figure 4.16). Noise is reduced with dual-rotation reconstruction within the truncated 3D FOV (Figures 4.16c and 4.16d) as compared to the single-rotation case (Figures 4.16a and 4.16b). The scatter-induced cupping is also reduced in the truncated FOV. Outside this FOV, however, the difference remains negligible (Figures 4.16e and 4.16f).

4.4 Discussion

A new BPF method was designed in both planar and C-arm CBCT geometries, that can perform as well as FBP-like methods whatever the number of projection views, even in divergent-beam geometries: hence, this method is particularly adapted to the angular sampling of C-arm systems, which is coarser than in diagnostic CT. We took advantage of the BPF approach to blend dual-rotation acquisitions in the unfiltered backprojection space. The backprojected image b_T is only well sampled within the truncated 3D FOV, so that blending can only occur in this area; the full-FOV backprojected image b_F is used as a means to handle data truncation by extrapolating the truncated 3D FOV in the image space. Filtering is performed by Fourier-based multiplication along lines or columns of the image space.

As in the iterative reconstruction framework, the insertion of truncated data acquired at smaller FOV and (potentially) higher air gap reduces the impact of the scatter-induced cupping artifact in the reconstructed images. In terms of noise distribution, however, the direct reconstruction framework differs from the previous approach. The ramp filter and the Hilbert transforms are high-pass filters that localize high frequency contents, despite being non-local filtering operators. This property explains why peripheral noise does not corrupt low-noise data in the truncated 3D FOV of image $\mathcal{M}(b_F, b_T)$. Conversely, the peripheral noise is not mitigated by the insertion of b_T at the center of the image.

Hence, the direct reconstruction method for dual-rotation acquisitions intrinsically reconstructs regions of interest (ROI). In the context of virtual bow-tie imaging, ROI reconstruction should be understood in terms of dual resolution: our method reconstructs an image that is noisy outside the ROI and with reduced

noise inside the ROI. Although we believe that the proposed merging strategy within an iterative framework would improve both the final result and the convergence of the iterations, we propose to study the behavior of our two dual-rotation reconstruction methods (namely, the iterative and the direct methods) for ROI imaging in the next chapter.

4.5 Proofs of the theorems

4.5.1 Proof of Theorem 4.2.1

Let $\theta \in [0, 2\pi]$ and $b_\theta^{(n)}(\alpha; \cdot) = \mathcal{B}_\theta \left[\sigma_\theta^\alpha (\boldsymbol{\theta} \cdot \boldsymbol{\alpha})^{n-1} p_\theta^{(n)} \right]$, where $\sigma_\theta^\alpha = \text{sgn}(\boldsymbol{\alpha} \cdot \boldsymbol{\theta})$. Let $\mathbf{x} \in \mathbb{R}^2$. Then one can write:

$$b_\theta^{(n)}(\alpha; \mathbf{x}) = \sigma_\theta^\alpha (\boldsymbol{\theta} \cdot \boldsymbol{\alpha})^{n-1} p_\theta^{(n)}(\mathbf{x} \cdot \boldsymbol{\theta}^\perp) \quad (4.41)$$

$$= \text{sgn}(A) A^{n-1} p_\theta^{(n)}(A\mathbf{x} \cdot \boldsymbol{\alpha}^\perp + B), \quad (4.42)$$

where $A = \boldsymbol{\theta} \cdot \boldsymbol{\alpha}$ and $B = (-\mathbf{x} \cdot \boldsymbol{\alpha}) \boldsymbol{\theta} \cdot \boldsymbol{\alpha}^\perp$. The Fourier transform of $\mathcal{A}_{A,B}[p_\theta'] : u \mapsto p_\theta^{(n)}(Au + B)$ is related to the Fourier transform of $p_\theta^{(n)}$ through:

$$\mathcal{F} \left[\mathcal{A}_{A,B}[p_\theta^{(n)}] \right] (\rho) = \frac{1}{|A|} \mathcal{F} \left[p_\theta^{(n)} \right] \left(\frac{\rho}{A} \right) e^{2i\pi \frac{\rho}{A} B}. \quad (4.43)$$

Hence, applying $F_\alpha^{(n)}$ to $\bar{b}_\theta(\alpha; \cdot)$ is equivalent to multiplying the right-hand side of Equation (4.43) by $\frac{\text{sgn}(\rho)}{(2i\pi)^n \rho^{n-1}}$, prior to taking the inverse Fourier transform:

$$F_\alpha^{(n)} \left[b_\theta^{(n)}(\alpha; \cdot) \right] (\mathbf{x}) = \frac{1}{|A|} \int_{-\infty}^{+\infty} \text{sgn}\left(\frac{\rho}{A}\right) \frac{A^{n-1}}{(2i\pi)^n \rho^{n-1}} \mathcal{F}_1 \left[p_\theta^{(n)} \right] \left(\frac{\rho}{A} \right) e^{2i\pi \frac{\rho}{A} (A\mathbf{x} \cdot \boldsymbol{\alpha}^\perp + B)} d\rho. \quad (4.44)$$

Taking the change of variables $\rho' = \frac{\rho}{A}$ yields:

$$F_\alpha^{(n)} \left[b_\theta^{(n)}(\alpha; \cdot) \right] (\mathbf{x}) = \int_{-\infty}^{+\infty} \frac{\text{sgn}(\rho')}{(2i\pi)^n (\rho')^{n-1}} \mathcal{F}_1 \left[p_\theta^{(n)} \right] (\rho') e^{2i\pi \rho' \mathbf{x} \cdot \boldsymbol{\theta}^\perp} d\rho'. \quad (4.45)$$

The right-hand side of Equation (4.45) is equal to $\mathcal{B}_\theta F^{(n)} \left[p_\theta^{(n)} \right] = \mathcal{B}_\theta \mathcal{D} [p_\theta]$, which concludes the proof. \square

4.5.2 Proof of Theorem 4.2.3

The proof of Theorem 4.2.3 relies on some ingredients from the proof of the fan-beam DBP-HT formula of (Noo et al., 2004), which is given in Appendix A. We start from the formulation given in Equation (4.16), and we perform the change from parallel-beam to fan-beam variables in the integrals. First, note that, since $\delta^{(n)}$ is $(-n-1)$ -homogeneous:

$$\delta^{(n)}(\mathbf{x} \cdot \boldsymbol{\theta}^\perp - u) = \frac{\sqrt{\hat{u}^2 + D^2}}{s_\theta(\mathbf{x})^{n+1}} \delta^{(n)}(\hat{u}_\theta(\mathbf{x}) - \hat{u}). \quad (4.46)$$

Moreover:

$$(\boldsymbol{\theta} \cdot \boldsymbol{\alpha}) = \cos(\theta - \alpha) = \cos(\hat{\theta} + \gamma - \alpha) = \cos \gamma \cdot (\hat{\boldsymbol{\theta}} \cdot \boldsymbol{\alpha}) + \sin \gamma \cdot (\hat{\boldsymbol{\theta}}^\perp \cdot \boldsymbol{\alpha}), \quad (4.47)$$

where $\gamma = \arctan\left(\frac{\hat{u}}{D}\right)$. Hence:

$$(\boldsymbol{\theta} \cdot \boldsymbol{\alpha}) = \frac{D}{\sqrt{\hat{u}^2 + D^2}} (\hat{\boldsymbol{\theta}} \cdot \boldsymbol{\alpha}) + \frac{\hat{u}}{\sqrt{\hat{u}^2 + D^2}} (\hat{\boldsymbol{\theta}}^\perp \cdot \boldsymbol{\alpha}), \quad (4.48)$$

and:

$$(\boldsymbol{\theta} \cdot \boldsymbol{\alpha})^{n-1} = \frac{1}{\sqrt{\hat{u}^2 + D^2}^{n-1}} \left((D\hat{\boldsymbol{\theta}} + \hat{u}\hat{\boldsymbol{\theta}}^\perp) \cdot \boldsymbol{\alpha} \right)^{n-1}, \quad (4.49)$$

which can be rewritten as:

$$(\boldsymbol{\theta} \cdot \boldsymbol{\alpha})^{n-1} = \frac{1}{\sqrt{\hat{u}^2 + D^2}^{n-1}} (\boldsymbol{\omega} \cdot \boldsymbol{\alpha})^{n-1}, \quad (4.50)$$

where $\boldsymbol{\omega} = (D\hat{\boldsymbol{\theta}} + \hat{u}\hat{\boldsymbol{\theta}}^\perp)$. Hence, the change of variables in Equation (4.16) yields:

$$\begin{aligned} b_\theta^{(n)}(\boldsymbol{\alpha}; \mathbf{x}) &= \int_0^{2\pi} \int_{-\infty}^{\infty} \operatorname{sgn}(\boldsymbol{\omega} \cdot \boldsymbol{\alpha}) \frac{1}{\sqrt{\hat{u}^2 + D^2}^{n-1}} (\boldsymbol{\omega} \cdot \boldsymbol{\alpha})^{n-1} \hat{p}_\theta(\hat{u}) \frac{\sqrt{\hat{u}^2 + D^2}}{s_\theta(\mathbf{x})^{n+1}} \\ &\quad \times \delta^{(n)}(\hat{u}_\theta(\mathbf{x}) - \hat{u}) \delta\left(\hat{\theta} + \arctan\left(\frac{\hat{u}}{D}\right) - \theta\right) \frac{D^2 d}{\sqrt{\hat{u}^2 + D^2}^3} d\hat{u} d\hat{\theta}, \end{aligned} \quad (4.51)$$

which further simplifies into:

$$\begin{aligned} b_\theta^{(n)}(\boldsymbol{\alpha}, \mathbf{x}) &= \int_0^{2\pi} \frac{D^2}{s_\theta(\mathbf{x})^{n+1}} \hat{\mathcal{B}}_\theta \left[\frac{d^n}{d\hat{u}^n} \left\{ \hat{p}_\theta(\hat{u}) \operatorname{sgn}(\boldsymbol{\omega} \cdot \boldsymbol{\alpha}) (\boldsymbol{\omega} \cdot \boldsymbol{\alpha})^{n-1} \right. \right. \\ &\quad \left. \left. \times \delta\left(\hat{\theta} + \arctan\left(\frac{\hat{u}}{D}\right) - \theta\right) \right\} (\mathbf{x}) d\hat{\theta} \right] \end{aligned} \quad (4.52)$$

which concludes the proof. \square

4.5.3 Proof of Theorem 4.2.4

The proof of Theorem 4.2.4 relies on Lemma 4.5.1 that we prove below.

Lemma 4.5.1. *For a matrix $\bar{H} = \begin{pmatrix} \bar{h}_{11} & \bar{h}_{12} \\ \bar{h}_{21} & \bar{h}_{22} \end{pmatrix} \in \mathbb{R}^{2 \times 2}$ such that $\det \bar{H} = \pm 1$, define operator:*

$$U_{\bar{H}} : \quad \phi \mapsto \left(y \mapsto \frac{1}{\bar{h}_{21}y + \bar{h}_{22}} \phi \left(\frac{\bar{h}_{11}y + \bar{h}_{12}}{\bar{h}_{21}y + \bar{h}_{22}} \right) \right). \quad (4.53)$$

The Hilbert transform commutes with operator $U_{\bar{H}}$ up to a sign:

$$\mathcal{H}U_{\bar{H}} = \operatorname{sgn}(\det \bar{H}) \cdot U_{\bar{H}}\mathcal{H}. \quad (4.54)$$

Proof. Define $\phi_1 = U_{\bar{H}} \mathcal{H}[f]$ and $\phi_2 = \mathcal{H}U_{\bar{H}}[f]$. Then:

$$\phi_1(y) = \frac{1}{\bar{h}_{21}y + \bar{h}_{22}} \mathcal{H}[f] \left(\frac{\bar{h}_{11}y + \bar{h}_{12}}{\bar{h}_{21}y + \bar{h}_{22}} \right) \quad (4.55)$$

$$= \frac{1}{\pi} \int_{-\infty}^{+\infty} \frac{f(y') dy'}{\bar{h}_{11}y + \bar{h}_{12} - y' (\bar{h}_{21}y + \bar{h}_{22})}. \quad (4.56)$$

Moreover:

$$\phi_2(y) = \frac{1}{\pi} \int_{-\infty}^{+\infty} \frac{U_{\bar{H}}[f](y') dy'}{y - y'} = \frac{1}{\pi} \int_{-\infty}^{+\infty} \frac{(\bar{h}_{21}y' + \bar{h}_{22})^{-1} f\left(\frac{\bar{h}_{11}y' + \bar{h}_{12}}{\bar{h}_{21}y' + \bar{h}_{22}}\right)}{y - y'} dy'. \quad (4.57)$$

Define the change of variables $y'' = \frac{\bar{h}_{11}y' + \bar{h}_{12}}{\bar{h}_{21}y' + \bar{h}_{22}}$; since $\det \bar{H} = \pm 1$, we end up with $dy'' = \text{sgn}(\det \bar{H})(\bar{h}_{21}y' + \bar{h}_{22})^{-2} dy' = \text{sgn}(\det \bar{H})(-\bar{h}_{21}y'' + \bar{h}_{11})^2 dy'$. Hence, ϕ_2 becomes:

$$\phi_2(y) = \frac{\text{sgn}(\det \bar{H})}{\pi} \int_{-\infty}^{+\infty} \frac{f(y'') dy''}{\bar{h}_{11}y + \bar{h}_{12} - y'' (\bar{h}_{21}y + \bar{h}_{22})} = \text{sgn}(\det \bar{H}) \phi_1(y), \quad (4.58)$$

which concludes the proof. \square

We are now ready to prove Theorem 4.2.4. Let $\mathbf{x} = (x, y)^T$. Let $\alpha \in [0, 2\pi]$, we write $\mathbf{x} = x_\alpha \boldsymbol{\alpha} + x_{\alpha^\perp} \boldsymbol{\alpha}^\perp$; we keep x_α fixed, and we write:

$$\Phi(x_{\alpha^\perp}) = \frac{1}{s_{\hat{\theta}}(x_{\alpha^\perp})^2} \widehat{\mathcal{B}}_{\hat{\theta}} \left[\mathcal{H} \left[\tilde{p}'_{\hat{\theta}} \right] \right] (x_{\alpha^\perp}). \quad (4.59)$$

The relationship between the detector coordinate and x_α is given by:

$$\begin{pmatrix} s_{\hat{\theta}}(x_{\alpha^\perp}) \hat{u}(x_{\alpha^\perp}) \\ s_{\hat{\theta}}(x_{\alpha^\perp}) \end{pmatrix} = H_\alpha \begin{pmatrix} x_{\alpha^\perp} \\ 1 \end{pmatrix} \quad (4.60)$$

where $H_\alpha \in \mathbb{R}^{2 \times 2}$ is a homography matrix. In the ideal circular source-detector trajectory, H_α is equal to:

$$H_\alpha = \begin{pmatrix} D\hat{\boldsymbol{\theta}} \cdot \boldsymbol{\alpha} & -x_\alpha D\hat{\boldsymbol{\theta}} \cdot \boldsymbol{\alpha}^\perp \\ \hat{\boldsymbol{\theta}} \cdot \boldsymbol{\alpha}^\perp & d + x_\alpha \hat{\boldsymbol{\theta}} \cdot \boldsymbol{\alpha} \end{pmatrix}. \quad (4.61)$$

Define $\bar{H}_\alpha = |\det H_\alpha|^{-1/2} H_\alpha$: then the determinant of \bar{H}_α is equal to ± 1 ; in other words: $\bar{H}_\alpha \in \text{SL}(2, \mathbb{R})$, and from Lemma 4.5.1:

$$\Phi(x_{\alpha^\perp}) = \frac{1}{s_{\hat{\theta}}(x_{\alpha^\perp}) \det H_\alpha} U_{\bar{H}_\alpha} \mathcal{H} \left[\tilde{p}'_{\hat{\theta}} \right] (x_{\alpha^\perp}) \quad (4.62)$$

$$= \frac{\sigma_{\hat{\theta}}^\alpha}{s_{\hat{\theta}}(x_{\alpha^\perp}) \det H_\alpha} \mathcal{H} \left[U_{\bar{H}_\alpha} \tilde{p}'_{\hat{\theta}} \right] (x_{\alpha^\perp}) \quad (4.63)$$

$$= \frac{\sigma_{\hat{\theta}}^\alpha}{s_{\hat{\theta}}(x_{\alpha^\perp})} \mathcal{H} \left[\frac{1}{s_{\hat{\theta}}(x_{\alpha^\perp})} \widehat{\mathcal{B}}_{\hat{\theta}} \left[\tilde{p}'_{\hat{\theta}} \right] \right] (x_{\alpha^\perp}). \quad (4.64)$$

We now take advantage of the affine behavior of $s_{\hat{\theta}}$ with respect to $x_{\alpha\perp}$; indeed $s_{\hat{\theta}}(x_{\alpha\perp})$ can be written as:

$$s_{\hat{\theta}}(x_{\alpha\perp}) = Ax_{\alpha\perp} + B, \quad (4.65)$$

where A and B are constant. We then use the following property of the Hilbert transform: given a function ϕ , if one defines $\psi : y \mapsto y\phi(y)$, then:

$$\mathcal{H}[\psi](y) = -\frac{1}{\pi} \int_{-\infty}^{+\infty} \phi(y') dy' + y\mathcal{H}[\phi](y). \quad (4.66)$$

Hence, we end up with :

$$\mathcal{H}[s_{\hat{\theta}}\Phi](x_{\alpha\perp}) = s_{\hat{\theta}}(x_{\alpha\perp})\mathcal{H}[\Phi](x_{\alpha\perp}) - \frac{A}{\pi} \int_{-\infty}^{+\infty} \Phi(x') dx'. \quad (4.67)$$

But from Equation (4.64) we also have:

$$\mathcal{H}[s_{\hat{\theta}}\Phi](x_{\alpha\perp}) = -\frac{\sigma_{\hat{\theta}}^{\alpha}}{s_{\hat{\theta}}(x_{\alpha\perp})} \widehat{\mathcal{B}}_{\hat{\theta}}[\tilde{p}'_{\hat{\theta}}](x_{\alpha\perp}). \quad (4.68)$$

Combining Equation (4.67) and (4.68) yields:

$$\mathcal{H}[\Phi](x_{\alpha\perp}) = \frac{1}{s_{\hat{\theta}}(x_{\alpha\perp})} \left(-\frac{\sigma_{\hat{\theta}}^{\alpha}}{s_{\hat{\theta}}(x_{\alpha\perp})} \widehat{\mathcal{B}}_{\hat{\theta}}[\tilde{p}'_{\hat{\theta}}](x_{\alpha\perp}) + \frac{A}{\pi} \int_{-\infty}^{+\infty} \Phi(x') dx' \right), \quad (4.69)$$

so that applying $-\mathcal{H}$ one more time to each side of the previous equation leads to:

$$\Phi(x_{\alpha\perp}) = \mathcal{H} \left[\frac{\sigma_{\hat{\theta}}^{\alpha}}{s_{\hat{\theta}}^2} \widehat{\mathcal{B}}_{\hat{\theta}}[\tilde{p}'_{\hat{\theta}}] \right] (x_{\alpha\perp}) - \kappa \mathcal{H} \left[\frac{1}{s_{\hat{\theta}}} \right] (x_{\alpha\perp}), \quad (4.70)$$

where $\kappa = A\pi^{-1} \int_{-\infty}^{+\infty} \Phi(x') dx'$ is constant. We now use a last result on Hilbert transforms: the Hilbert transform of the Dirac Delta function δ is given by:

$$\mathcal{H}[\delta](y) = \eta(y), \text{ where } \eta(y) = \frac{1}{\pi y}. \quad (4.71)$$

Since:

$$\frac{1}{s_{\hat{\theta}}(x_{\alpha\perp})} = \frac{1}{Ax_{\alpha\perp} + B} = A^{-1} \tau_{-\frac{B}{A}} \eta(x_{\alpha\perp}), \quad (4.72)$$

where $\tau_a g(x) = g(x - a)$, we conclude that:

$$\Phi(x_{\alpha\perp}) = \mathcal{H} \left[\frac{\sigma_{\hat{\theta}}^{\alpha}}{s_{\hat{\theta}}^2} \widehat{\mathcal{B}}_{\hat{\theta}}[\tilde{p}'_{\hat{\theta}}] \right] (x_{\alpha\perp}) - \kappa \delta \left(x_{\alpha\perp} + \frac{B}{A} \right). \quad (4.73)$$

Hence, whenever $\widehat{u}(\mathbf{x})$ is non-degenerate, the Dirac function is equal to zero and:

$$\Phi(x_{\alpha\perp}) = \mathcal{H} \left[\frac{\sigma_{\hat{\theta}}^{\alpha}}{s_{\hat{\theta}}^2} \widehat{\mathcal{B}}_{\hat{\theta}}[\tilde{p}'_{\hat{\theta}}] \right] (x_{\alpha\perp}), \quad (4.74)$$

which concludes the proof. \square

4.5.4 Proof of Theorem 4.2.6

From Theorem 4.2.4, the following holds:

$$g_{\hat{\theta}}(\mathbf{x}) = \frac{1}{2\pi} \mathcal{H}_{\alpha} \left[\widehat{b}_{\hat{\theta}}^{(1)}(\alpha, \cdot) \right] (\mathbf{x}), \quad (4.75)$$

where:

$$\widehat{b}_{\hat{\theta}}^{(1)}(\alpha, \mathbf{x}) = \sigma_{\hat{\theta}}^{\alpha} \frac{D^2}{s_{\hat{\theta}}^2} \widehat{\mathcal{B}}_{\hat{\theta}} \left[\widetilde{p}_{\hat{\theta}}' \right] (\mathbf{x}). \quad (4.76)$$

Let $\mathbf{x} = (x, y)^T$. Let $\alpha \in [0, 2\pi]$ such that $\det H_{\alpha} \neq 0$, where H_{α} was defined in Equation (4.60). We write $\mathbf{x} = x_{\alpha} \boldsymbol{\alpha} + x_{\alpha^{\perp}} \boldsymbol{\alpha}^{\perp}$; we keep x_{α} fixed, and we define:

$$\Psi(x_{\alpha^{\perp}}) = \frac{1}{s_{\hat{\theta}}(x_{\alpha^{\perp}})^2} \widehat{\mathcal{B}}_{\hat{\theta}} \left[\widetilde{p}_{\hat{\theta}}' \right] (x_{\alpha^{\perp}}) = \frac{1}{s_{\hat{\theta}}(x_{\alpha^{\perp}})^2} \widetilde{p}_{\hat{\theta}}' \left(\frac{h_{11}x_{\alpha^{\perp}} + h_{12}}{h_{21}x_{\alpha^{\perp}} + h_{22}} \right), \quad (4.77)$$

where:

$$H_{\alpha} = \begin{pmatrix} h_{11} & h_{12} \\ h_{21} & h_{22} \end{pmatrix} = \begin{pmatrix} D\widehat{\boldsymbol{\theta}} \cdot \boldsymbol{\alpha} & -x_{\alpha} D\widehat{\boldsymbol{\theta}} \cdot \boldsymbol{\alpha}^{\perp} \\ \widehat{\boldsymbol{\theta}} \cdot \boldsymbol{\alpha}^{\perp} & d + x_{\alpha} \widehat{\boldsymbol{\theta}} \cdot \boldsymbol{\alpha} \end{pmatrix}. \quad (4.78)$$

We observe that:

$$\frac{\partial \widehat{\mathcal{B}}_{\hat{\theta}} \left[\widetilde{p}_{\hat{\theta}}' \right]}{\partial x_{\alpha^{\perp}}} (x_{\alpha^{\perp}}) = \frac{\det(H_{\alpha})}{s_{\hat{\theta}}(x_{\alpha^{\perp}})^2} \widetilde{p}_{\hat{\theta}}' \left(\frac{h_{11}x_{\alpha^{\perp}} + h_{12}}{h_{21}x_{\alpha^{\perp}} + h_{22}} \right) = \frac{\det(H_{\alpha})}{s_{\hat{\theta}}(x_{\alpha^{\perp}})^2} \widehat{\mathcal{B}}_{\hat{\theta}} \left[\widetilde{p}_{\hat{\theta}}' \right] (x_{\alpha^{\perp}}). \quad (4.79)$$

Hence:

$$\Psi(x_{\alpha^{\perp}}) = \frac{1}{\det(H_{\alpha})} \frac{\partial \widehat{\mathcal{B}}_{\hat{\theta}} \left[\widetilde{p}_{\hat{\theta}}' \right]}{\partial x_{\alpha^{\perp}}} (x_{\alpha^{\perp}}). \quad (4.80)$$

Finally:

$$\widehat{b}_{\hat{\theta}}^{(1)}(\alpha, \mathbf{x}) = \sigma_{\hat{\theta}}^{\alpha} \frac{D^2}{\det(H_{\alpha})} \frac{\partial \widehat{\mathcal{B}}_{\hat{\theta}} \left[\widetilde{p}_{\hat{\theta}}' \right]}{\partial x_{\alpha^{\perp}}} (x_{\alpha^{\perp}}), \quad (4.81)$$

and:

$$g_{\hat{\theta}}(\mathbf{x}) = \frac{1}{2\pi} \mathcal{H}_{\alpha} \left[\widehat{b}_{\hat{\theta}}^{(1)}(\alpha, \cdot) \right] (\mathbf{x}) = \mathcal{D}_{\alpha} \left[\widehat{b}_{\hat{\theta}}^{(0)}(\alpha, \cdot) \right] (\mathbf{x}), \quad (4.82)$$

where:

$$\widehat{b}_{\hat{\theta}}^{(0)}(\alpha, \mathbf{x}) = \sigma_{\hat{\theta}}^{\alpha} \frac{D^2}{\det H_{\alpha}} \widehat{\mathcal{B}}_{\hat{\theta}} \left[\widetilde{p}_{\hat{\theta}} \right] (\mathbf{x}), \quad (4.83)$$

which concludes the proof. \square

Note that in the case of a circular trajectory, we have $\det H_{\alpha} = D(\mathbf{x} + d\widehat{\boldsymbol{\theta}}) \cdot \boldsymbol{\alpha}$, and:

$$\widehat{b}_{\hat{\theta}}^{(0)}(\alpha, \mathbf{x}) = \sigma_{\hat{\theta}}^{\alpha} \frac{D}{(\mathbf{x} + d\widehat{\boldsymbol{\theta}}) \cdot \boldsymbol{\alpha}} \widehat{\mathcal{B}}_{\hat{\theta}} \left[\widetilde{p}_{\hat{\theta}} \right] (\mathbf{x}). \quad (4.84)$$

4.5.5 Proof of Theorem 4.2.7

The proof follows the remarks of [Feldkamp et al. \(1984\)](#), which we recall below for $n = 1$. The case $n = 0$ is derived in a similar way. Note that if f is invariant

along the z -axis, then a projection along a given ray is equal to its projected ray onto the midplane axis ($z = 0$), up to a geometrical factor. More specifically:

$$\widehat{p}_\theta(\widehat{u}, \widehat{v}) = \frac{\sqrt{D^2 + \widehat{u}^2 + \widehat{v}^2}}{\sqrt{D^2 + \widehat{u}^2}} \widehat{p}_\theta(\widehat{u}, 0). \quad (4.85)$$

Hence, the cosine-weighted projections \widetilde{p}_θ satisfy:

$$\widetilde{p}_\theta(\widehat{u}, \widehat{v}) = \frac{D}{\sqrt{D^2 + \widehat{u}^2}} \widehat{p}_\theta(\widehat{u}, 0) = \widetilde{p}_\theta(\widehat{u}, 0). \quad (4.86)$$

Consequently, derivatives with respect to \widehat{u} are such that:

$$\frac{\partial \widetilde{p}_\theta}{\partial \widehat{u}}(\widehat{u}, \widehat{v}) = \frac{\partial \widetilde{p}_\theta}{\partial \widehat{u}}(\widehat{u}, 0) \quad (4.87)$$

and:

$$b_\theta^{(1)}(\alpha; \mathbf{x}) = \sigma_\theta^\alpha \frac{D^2}{s_\theta(\mathbf{x})^2} \frac{\partial \widetilde{p}_\theta}{\partial \widehat{u}}(\widehat{u}(\mathbf{x}), 0). \quad (4.88)$$

Since $s_\theta(\mathbf{x})$ and $\widehat{u}(\mathbf{x})$ do not depend on the z -coordinate, $b_\theta(\alpha; \mathbf{x})$ is invariant along the z -axis, and so are the $b_{\Theta_k}^{(1)}(\alpha; \mathbf{x})$ for all subsets Θ_k . Since Equation (4.34) is exact in the midplane, it is exact everywhere, which concludes the proof. \square

From virtual bow-tie to region-of-interest C-arm CBCT

Although we used it to emulate a virtual bow-tie, our dual-rotation framework is intrinsically related to region-of-interest (ROI) imaging through its truncated acquisition. In this chapter, we shift from full-volume imaging to ROI imaging, given a dual-rotation acquisition, that has now a third degree of freedom, namely, the angular sampling ratio between both acquisitions. The previous iterative reconstruction framework is shown to successfully reconstruct regions of interest with only a few additional full-FOV projections, provided that the weights of the minimization problem are adapted to account for different angular sampling ratios. In the context of direct reconstruction, we highlight the issue of angular sampling in the well known Hilbert-transformed differentiated backprojection method of [Noo et al. \(2004\)](#), and we show that, with no change in the reconstruction framework, our direct method also works for ROI imaging. A multi-resolution strategy can further accelerate the computation time. Simulations in planar geometries and experiments on actual C-arm data demonstrate the feasibility of dual-rotation direct reconstruction for ROI imaging.

Contents

5.1 Challenges of ROI imaging	112
5.1.1 ROI imaging: a literature review	112
5.1.1.1 <i>A priori</i> knowledge	113
5.1.1.2 Knowledge from additional data	116
5.1.2 Proposed dual-rotation acquisition	117
5.2 Iterative reconstruction	118
5.2.1 Adapting the virtual bow-tie framework	118
5.2.2 Experiments and results	118
5.2.2.1 Catphan [®] CTP 515	118
5.2.2.2 Uniform head phantom	120

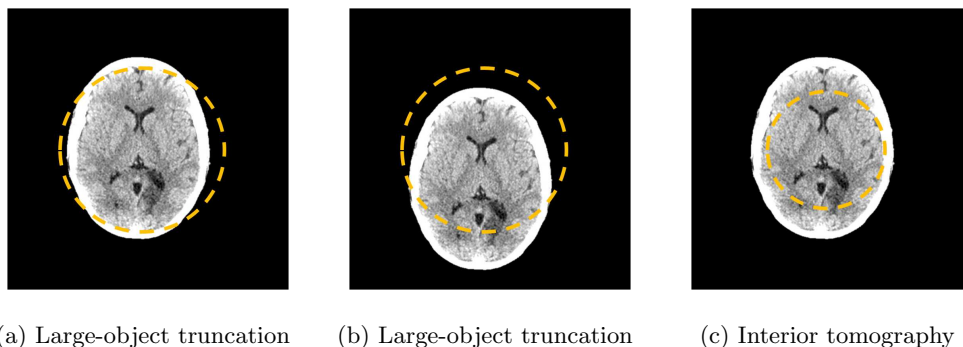


Figure 5.1 – Truncation in ROI imaging. The FOV is indicated as a dashed circle. (a),(b) Large-object truncations. (c) Interior tomography problem.

5.2.3	Discussion	122
5.3	Direct reconstruction	122
5.3.1	Adapting the Hilbert-transformed DBP	122
5.3.1.1	Hilbert-transformed DBP and angular sampling	122
5.3.1.2	Experiments	125
5.3.1.3	Results	126
5.3.1.4	Discussion	127
5.3.2	View-wise BPF solution	129
5.3.2.1	Standard scheme	129
5.3.2.2	Sped-up reconstruction through a dual-resolution strategy	130
5.3.2.3	Experiments	131
5.3.2.4	Results	132
5.4	Discussion	140

5.1 Challenges of ROI imaging

5.1.1 ROI imaging: a literature review

Region-of-interest (ROI) imaging consists in reconstructing the image FOV defined by transversally truncated projection data. Data truncation may originate from the limited detector size, or from the use of collimator blades to reduce the patient exposure to X-rays. ROI imaging arises in many medical applications including image-guided radiotherapy, three-dimensional angiography, breast CT, micro-CT, and C-arm CBCT. We differentiate large-object truncation cases (Figures 5.1a and 5.1b), where projections acquired along the source-detector trajectory are truncated only over subsets of this trajectory, from the case of interior tomography (Figure 5.1c), where the 3D FOV is completely inside the imaged object. We refer to (Wang & Yu, 2013; Y. Xia, 2016) for a deeper insight into ROI imaging. We hereafter provide an overview of existing methods in this topic.

When density projections $p = \{p_\theta = \mathcal{R}_\theta[f] \mid \theta \in \Theta\}$ are truncated, FBP fails at reconstructing the true object f from p . In the case of interior tomography (Figure 5.1c), it is known that image reconstruction within the ROI cannot be

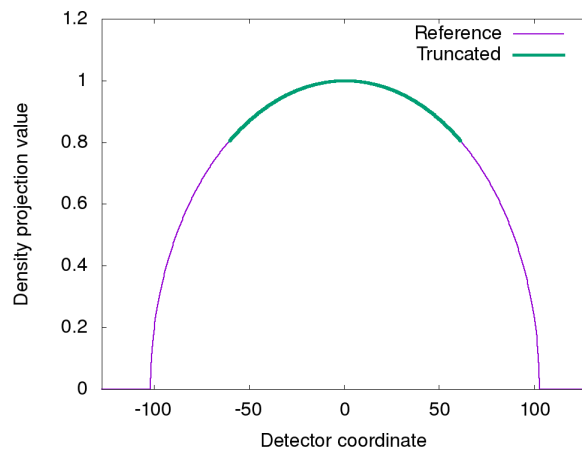
obtained exactly (Natterer, 2001). Truncation, however, is a low-frequency problem (Bilgot et al., 2012). In the context of FBP, the challenge of reconstructing an image from truncated projections is related to the non-local property of the ramp filtering operator \mathcal{D} (Hsieh, 2009). Hence, truncation must be handled prior to filtering. Ramp filtering is performed in the Fourier domain, thus padding is required. Zero-padding truncated data artificially create strong signal discontinuities, that are enhanced by the high-frequency ramp filter. Instead, different padding schemes can be used, that do not create such discontinuities, such as data mirroring or anti-mirroring, and affine padding. An illustration of these options is shown in Figure 5.2. The reference signal is the parallel-beam projection of a uniform disk. The truncated 1D signal is the central portion of this projection (Figure 5.2a). The padding schemes are shown in Figure 5.2b. The original data are located in the shaded region. When ramp-filtering the zero-padded full projection signal, we almost get a constant line over the truncated region (black horizontal line in Figure 5.2c). However, ramp-filtering the zero-padded truncated projection signal yields a much different signal, that suffers from a strong non-uniformity. This phenomenon is reduced when using continuous padding schemes, although the signal still suffers from a low-frequency non-uniformity and a DC shift (Figure 5.2c).

One solution consists in using other additional information to extrapolate the truncated data. This information may either come from *a priori* knowledge, or from additional measurements. We hereafter discuss these two options.

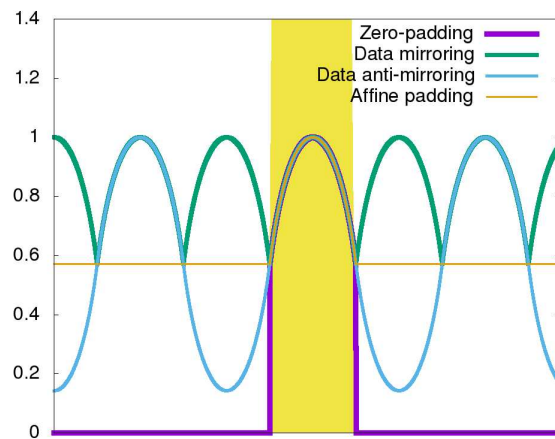
5.1.1.1 *A priori* knowledge

Empirical data extrapolation (or de-truncation) methods were proposed, for example in (Ohnesorge et al., 1999; Hsieh, Chao, et al., 2004; Sourbelle et al., 2005; Zellerhoff et al., 2005; Zamyatin et al., 2006; Maltz et al., 2007; Kolditz, Meyer, et al., 2010). These methods provide empirical means to estimate the missing data. They rely on the assumption that the truncated 3D FOV is most probably embedded into a medium that is not far from a water-equivalent shape (often a cylinder or an ellipsoid). By fitting the shape parameters to the data, one can extrapolate the truncated projections. Alternatively, Maier et al. (2012) optimize the extrapolated density values to reduce some known symptomatic artifacts in the reconstructed image. Bier et al. (2013) suggest to take advantage of the scattered radiations measured in the shadow of collimator blades to estimate a reasonable extrapolation of missing projection data. All these methods are routinely used in commercial C-arm CBCT systems; they are used in diagnostic CT only in the rarer cases where the patients do not fit the image FOV (*e.g.*, when imaging obese patients with out-of-FOV arms down). However, although the image quality of the reconstructed images is good enough for the examination of highly contrasted structures, it is still not enough when using narrow window widths that are necessary in soft-tissue imaging (Maier et al., 2012).

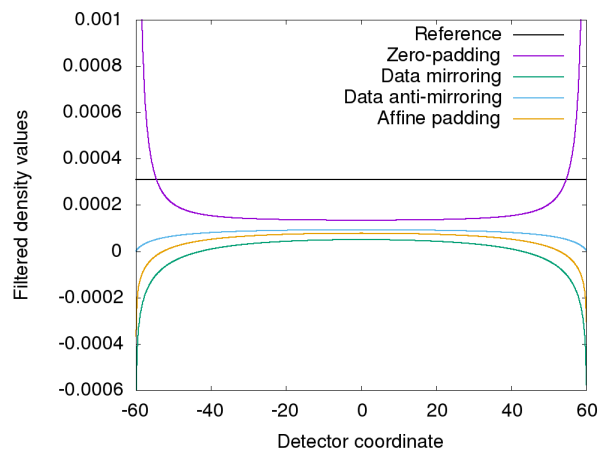
Instead of finding empirical data extrapolation prior to FBP-like reconstruction, BPF-based reconstruction methods rely on *a priori* knowledge about the support of the imaged object f (Noo et al., 2004; Pan et al., 2005; L. Yu et al., 2006; Defrise et al., 2006; Zhuang et al., 2004; Cho et al., 2007; Courdurier et



(a) 1D signals



(b) Padding (original truncated signal in the shaded area)



(c) Ramp-filtered 1D signals

Figure 5.2 – Padding, truncation and Fourier-based filtering.

al., 2008; Hoskovec et al., 2016; Clackdoyle et al., 2017). They decompose the ramp filter into a derivative operator and a Hilbert transform. The latter, which is non-local, is applied to the backprojected lines of the differentiated projections. In (Noo et al., 2004), such lines correspond to truncated Hilbert lines of the differentiated backprojection (DBP). They can be inverted using inversion formulas for the truncated Hilbert transform, provided that the support of image f is included in the computed truncated Hilbert lines. In case of large-object truncation (Figures 5.1a and 5.1b), some lines within the 3D FOV can still be recovered exactly using the Hilbert-transformed DBP approach. Defrise et al. (2006) further relaxed the conditions on the reconstructible Hilbert lines and showed that f could be inverted wherever one end-point of the truncated Hilbert transform lies outside the support of f . However, the interior tomography problem is still not solvable with these methods.

Building on these approaches, several works tried to extend the area of the truncated image FOV that could be recovered from Hilbert lines (Ye et al., 2007; Courdurier et al., 2008; Kudo et al., 2008; Lauzier et al., 2010; Taguchi et al., 2011; Tang et al., 2012; Ueda et al., 2017). These approaches assume the existence of a “tiny *a priori* knowledge”, in the sense that they assume that f is known over a given subregion (Ye et al., 2007; Courdurier et al., 2008; Kudo et al., 2008; Lauzier et al., 2010). Under some conditions on the subregion, the authors show that this additional information is enough to solve the interior tomography problem. However, the choice of the known subregion is still an open issue. Taguchi et al. (2011) suggest to manually select a region from an artifacted, FBP-like ROI reconstruction, and to estimate the true attenuation coefficients within this subregion through the minimization of a regularized reconstruction problem using total variation (TV). Ueda et al. (2017) constrain the ROI reconstruction by imposing a TV regularization over a band shape near the ROI boundaries. Such methods demonstrate that, although the interior tomography problem can be solved theoretically, the issue of actually knowing f over a subregion is not straightforward and often needs an intermediate iterative reconstruction loop using sparsity-enforcing penalties.

Other authors suggested to embed such sparsity-enforcing priors in the reconstruction problem (B. Zhang & Zeng, 2007; Ziegler et al., 2008; H. Yu & Wang, 2009; Q. Xu et al., 2011; Maier et al., 2012; Lee et al., 2014; Sidky et al., 2014; Z. Zhang et al., 2015; Ward et al., 2015; Y. Xia, 2016; Hu et al., 2016; H. Zhang et al., 2016; Arcadu et al., 2017; D. Xia et al., 2018). These compressed-sensing-based iterative reconstruction methods, however, introduce a bias in the reconstruction problem, and the resulting images often lack texture information, that is essential when looking at the low-contrast structures of soft-tissues in the brain.

Recently, Y. Xia et al. (2014) propose to decompose the ramp filtering operator into an order-2 Laplace filtering operator and its residual, non-local filter. This filter was shown to be more robust to data truncation. The authors show good reconstruction results for high-contrast imaging; however, they still need empirical artifact reduction techniques, and their method is not robust to the presence of highly contrasted objects at the boundary of the image FOV. Hence,

the method is not adapted to soft-tissue imaging.

5.1.1.2 Knowledge from additional data

Alternatively, additional information may directly come from additional measurements. One way to acquire missing data points, while severely reducing the patient dose outside the ROI, is to use physical beam shapers that pre-attenuate X-rays passing outside the ROI (R. N. Chityala et al., 2004; R. Chityala et al., 2005; Létourneau et al., 2005; Moore et al., 2006; Patel et al., 2008; Chen et al., 2008; Cho et al., 2009; Schafer et al., 2010; Lück et al., 2013). Once the projections are converted into densities, direct reconstruction methods are used. However, this conversion to densities requires accurate air intensity estimates, which are not constant over the 2D FOV. This would require additional calibration steps on C-arm systems. Similar to beam shapers, bow-tie filters may also be used (Yoo & Yin, 2006; Mail et al., 2009; Menser et al., 2010; G. Zhang et al., 2013), but their fixed shapes lack flexibility for ROI imaging.

Full-FOV data may be also obtained from prior low-dose, possibly undersampled or low-resolution acquisitions (H. Yu et al., 2006; Chen et al., 2009; Maaß et al., 2011; Shen et al., 2011; Kolditz et al., 2012; Sen Sharma et al., 2013), which are used to extrapolate the truncated data prior to a direct FBP-like reconstruction. When acquisition geometries are different, a first image reconstructed from the full-FOV projections is reprojected in the acquisition geometry of the truncated projections, and used to extrapolate the missing data (Chen et al., 2009; Maaß et al., 2011; Kolditz et al., 2012). When only a few full-FOV projections are available (Sen Sharma et al., 2013), the first reconstructed image can be iteratively improved, *e.g.*, by including a total variation (TV) penalty in the minimization problem, prior to reprojection in the geometry of the truncated projections. When the acquisition geometries are the same, data can be merged in the projection space and a direct FBP or BPF method can be applied to the merged projection data (H. Yu et al., 2006; Shen et al., 2011). This puts more mechanical constraints on the imaging system. It would also require, in the context of C-arm CBCT, two acquisitions with the same number of projections, where the full-FOV data are acquired at much lower dose than the truncated data. This case falls into our virtual bow-tie imaging framework, which was already explored in Chapters 3 and 4 with more general acquisition settings. Moreover, in contrast to our proposed approach for virtual bow-tie imaging C-arm CBCT, these methods only use the full-FOV data as a pre-processing step. We showed previously the interest of considering the full dual-rotation acquisition as a whole and to combine the data within a single reconstruction framework.

Interestingly, wavelet-based reconstruction methods using a few additional full-FOV projections were proposed in (Olson & DeStefano, 1994; Olson, 1995; Delaney & Bresler, 1995; Langer & Peyrin, 2010). They take advantage of the localization of wavelet bases to compute part of the wavelet expansion of the truncated projections, and complement them with coarser wavelet coefficients estimated from the full-FOV projections. Reconstruction is obtained by backprojecting filtered wavelets. Wavelet-based approaches have not been investigated in this work.

S. B. Jin et al. (2014) also suggest to use a few additional full-FOV projections and to solve simultaneously two TV minimization problems, resulting in a dual-resolution image reconstruction. By doing so, they succeed in extrapolating the image outside the ROI, even at a coarser resolution. By contrast, Lu et al. (2014) propose to acquire a dense set of low-dose projections, and to use a few additional high-dose, truncated projections to improve the image quality within the truncated FOV, via a compressed-sensing-based iterative reconstruction framework. The resulting image, however, lacks low-contrast texture information in the ROI. A hybrid solution was proposed in (Y. Xia et al., 2015a) in the context of interventional neuroradiology. The authors relied on two orthogonal fluoroscopic images acquired on a biplane C-arm system in order to estimate a 3D shape model of the head. This model was then used as a prior on the support of empirically extrapolated rows. This method was shown to perform as good as the work of (Kolditz, Meyer, et al., 2010), but still lacks low-contrast resolution for soft-tissue imaging.

5.1.2 Proposed dual-rotation acquisition

Direct FBP-like reconstruction methods require a non-local, Fourier-based filtering. In ROI imaging, data extrapolation is needed prior to filtering. Data extrapolation methods may either rely on *a priori* knowledge or from additional full-FOV measurements. Previous works showed that with a little spatial *a priori* knowledge, the interior tomography problem could be solved. However, finding this known subregion is still an open issue. It is likely that this information would not be available in the clinical practice. Model-based iterative reconstruction based on sparsity-enforcing regularizers is an alternative to these methods, but it still introduces a bias in the image, and it is more demanding in terms of computational complexity.

Instead, acquiring a few additional full-FOV data on a C-arm system seems to be more feasible than guessing an *a priori* information on the image content. We thus consider a dual-rotation acquisition in which the full-FOV projections are angularly subsampled. Hence, we add a third free parameter to the pair (t, x) characterizing respectively the amount of truncation of p_T with respect to p_F , and the mAs ratio between the two acquisitions. In the following, we always assume that projection views are uniformly sampled over the source trajectory, and we further write:

$$s = \frac{N_T}{N_F}, \quad (5.1)$$

where N_T is the number of truncated projections and N_F is the number of full-FOV projections. Typically, $N_F \ll N_T$ in ROI imaging (see Figure 3.5).

In the following, we focus on the reconstruction of such dual-rotation acquisitions, when increasing the sampling ratio s . We rely on our previous reconstruction methods developed for virtual bow-tie C-arm CBCT, and we investigate their application to interior tomography. As mentioned previously, we believe that it is beneficial to simultaneously use the truncated and un-truncated data in the reconstruction problem. We show that, provided a small modification in the cost function, the same iterative reconstruction framework as in Chapter 3

can be used for ROI imaging as well; in particular, it does not require a more demanding compressed-sensing-based reconstruction framework. We also revisit the Hilbert-transformed DBP method in the context of dual-rotation acquisitions. We highlight the limits of this approach with respect to angular sampling, and we propose a dual-resolution workaround in parallel-beam geometry. More generally, we revisit our direct BPF method from Chapter 4 and we show that it can accurately solve the interior problem. A dual-resolution variant is proposed only to speed-up the reconstruction.

5.2 Iterative reconstruction

5.2.1 Adapting the virtual bow-tie framework

We adapt the definition of weights α_F and $\alpha_T = 1 - \alpha_F$ in order to account for different angular sampling ratios s . The contribution of the full-FOV acquisition to the overall dose is now (Reshef et al., 2017a):

$$\alpha_F = \frac{N_F I_0^F}{N_F I_0^F + t \cdot N_T I_0^T} = \frac{1}{1 + t s}. \quad (5.2)$$

Note that when $N_T = N_F$, then $s = 1$ and we recover the previous formulation of Chapter 3. Since $s > 1$ in ROI imaging, no projection-based blending strategy can be used as a pre-processing step prior to direct reconstruction. However, using the new weights defined above, the same iterative reconstruction strategy as proposed for full-volume imaging can still be used for ROI reconstruction. In particular, we still minimize the following energy:

$$\operatorname{argmin}_f \left\{ \sum_{n \in \{F, T\}} \alpha_n \mathcal{Q}_n(f) + \chi(f) \right\}, \quad (5.3)$$

where the regularizing term is kept smooth $\chi(f) = \lambda \|\nabla f\|^2$. The definition of the ramp filtering operators remains the same as in the full-FOV imaging case. Note that $\chi(f)$ only acts as a stabilizer of the iterative reconstruction loop. Since it is smooth, we do not expect to extrapolate the image outside the ROI.

5.2.2 Experiments and results

Acquisitions were done with the same parameters as described in Section 3.2.3. For ROI imaging, spins with less views were obtained by digital uniform down-sampling by varying s from 8 to 128, yielding sets of 4 to 75 full-FOV projections. On a separate experiment, truncation was applied digitally.

5.2.2.1 Catphan[®] CTP 515

When no full-FOV view is available (Figure 5.3a), the quadratic criterion does not bring in any *a priori* information and performs no better than what would be obtained with an analytical reconstruction with extrapolation, which was expected. The association with 9 low-dose full-FOV projections yields an image

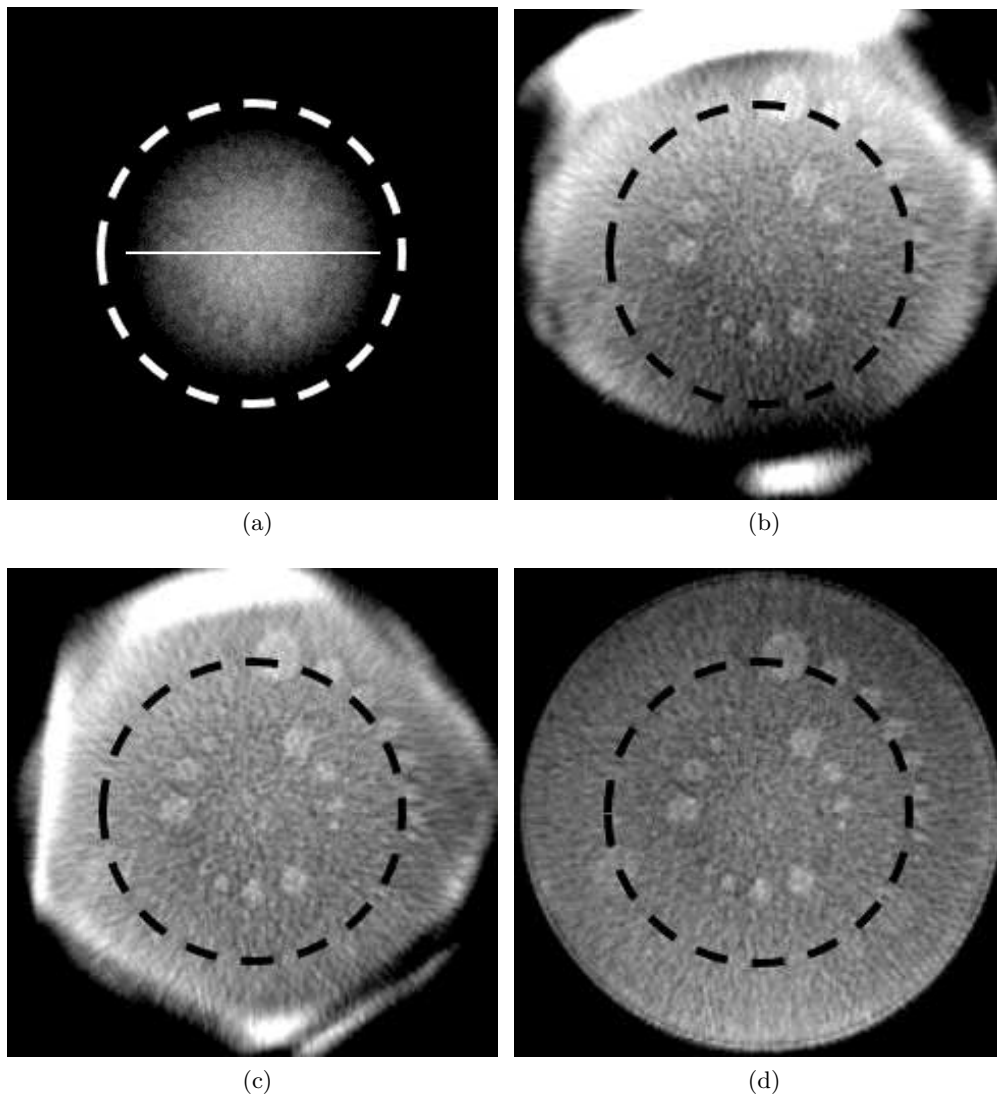


Figure 5.3 – Dual-rotation ROI imaging of the Catphan[®] 515 module. (a) Single-rotation iterative reconstruction. (b), (c) Dual-rotation reconstructions using (b) 9 projections and (c) 18 projections. (d) Dual-rotation reconstruction using the fully sampled full-FOV spin. The truncated FOV is shown as a dashed circle.

with severe distortions outside the ROI, but provides a much better uniformity inside, as shown in Figure 5.3b. At 19 projections (Figure 5.3c), the cupping within the ROI is entirely removed and all inserts can be seen as well as in Figure 5.3d where all full-FOV views have been used for the reconstruction. The plot of Figure 5.4 shows the central profiles through the ROI, after subtracting each profile with its mean value to remove DC-shifts that also affect the reconstruction of truncated data. It confirms how a small number of full-FOV projections flattens the profiles.

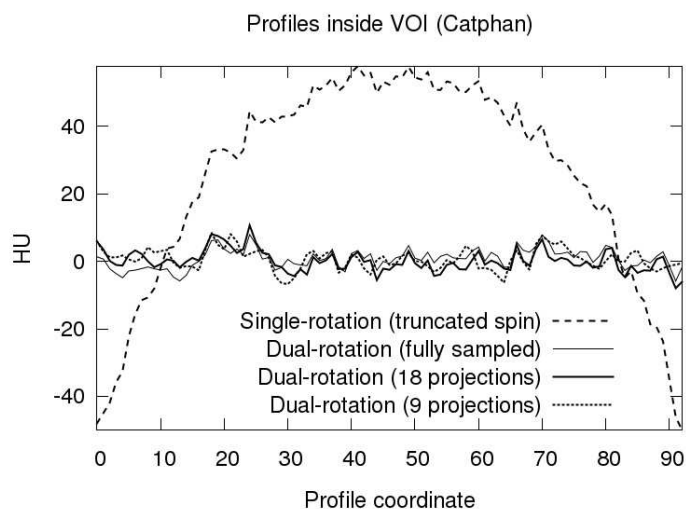


Figure 5.4 – Dual-rotation ROI imaging: deviations from the mean line profiles values. The line profile is the one drawn in Figure 5.3a.

5.2.2.2 Uniform head phantom

Figure 5.5 shows the reconstructions of the uniform head phantom acquisition for $s = 16$ to 128, after it has been digitally truncated right through the skull bones, a case that no simple extrapolation can compensate. Again, when no full-FOV view is available, the quadratic criterion does not perform any better than an analytical reconstruction. The skull outside the ROI is not even visible in the windowing of Figure 5.5a, but appears heavily distorted with the first subset of four full-FOV views (Figure 5.5b). As the number of full-FOV views is increased, the distortions disappear progressively outside the ROI and, most interestingly, much more quickly within the ROI (Figure 5.5b–5.5f). The profiles taken through the line shown in Figure 5.5a were similar and flat as soon as full-FOV views were introduced. However, they differed by DC shifts of 20% maximum for $s = 128$ (graph not shown). Once corrected for these offsets, absolute values of the errors with respect to the profile of the reference image (Figure 5.5f) are shown as histograms in Figure 5.6.

This measurement singles out the truncated case as much worse than when even 4 views only are introduced in the reconstruction criterion. The bar chart, however, does not show a consistent error reduction with respect to the increasing number of views: the case $s = 128$ has less voxels with errors greater than 3% than cases $s = 64$ and $s = 32$. This is possible due to the fact that it only captures part of the error, as it does not take into account the DC shift. We find that the DC shift is consistently reduced by increasing the number of views. The fact that the entire skull had been truncated did not change the behavior of the dual-rotation framework with respect to the Catphan[®] case: what appears as distortions outside the ROI is a sufficiently good depiction of the missing low frequencies to correct for truncation artifacts within the ROI.

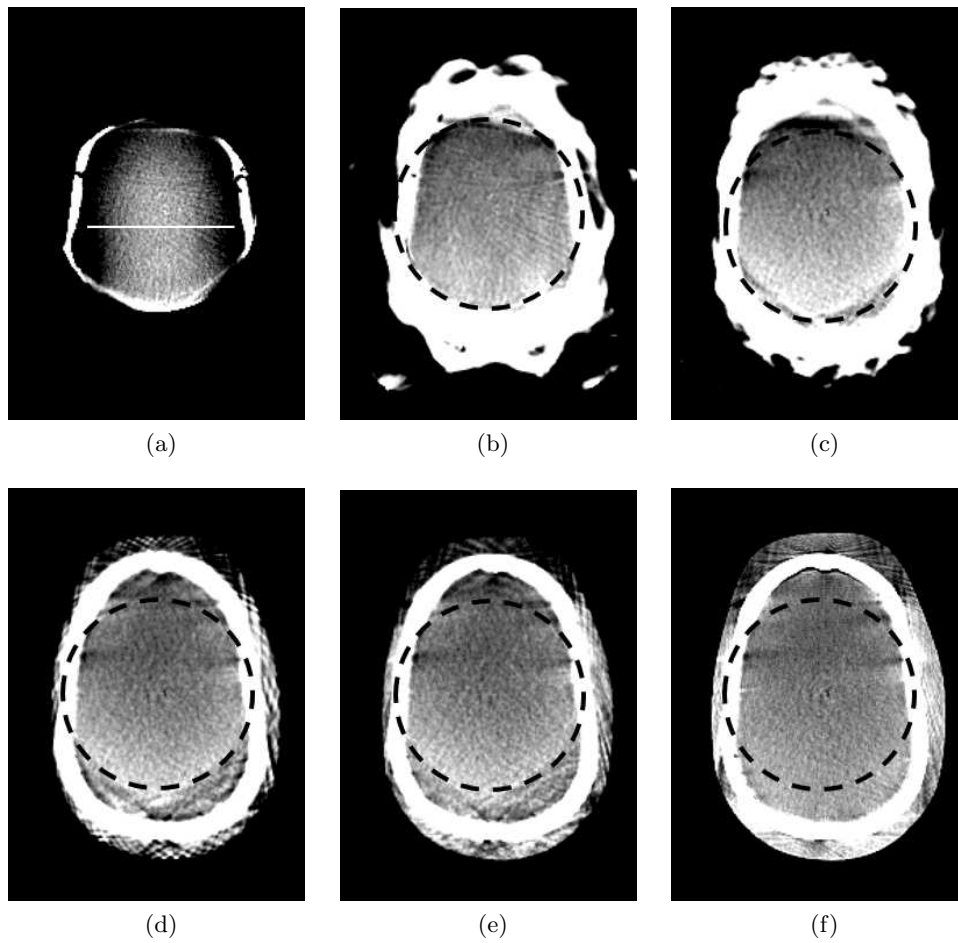


Figure 5.5 – Dual-rotation ROI imaging of a head phantom consisting of a skull with uniform soft tissues. (a) Iterative reconstruction from the truncated spin only. (b)–(e) Dual-rotation ROI reconstructions using respectively 4, 9, 37 and 75 additional full-FOV projections. (f) Iterative reconstruction from the full-FOV spin only. Isotropic voxel size: 0.94 mm^3 . Window width: 150 HU.

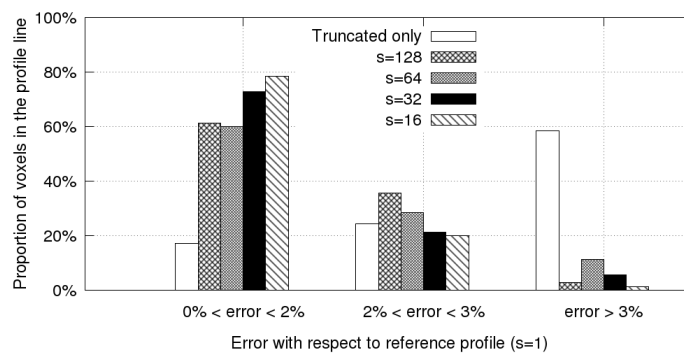


Figure 5.6 – Deviations from mean profile values along the line profile from Figure 5.5.

5.2.3 Discussion

Dual-rotation CBCT was shown to successfully emulate a virtual bow-tie in Chapters 3 and 4. We here show that it is also adapted to ROI imaging. The same iterative reconstruction algorithm was used for both virtual bow-tie and ROI imaging. A minor adaptation of weights α_F and α_T made it handle not only the truncation level t and the dose ratio x between spins, but also the ratio of views per spins s . The algorithm reconstructed the entire FOV with severe distortion outside the ROI, but it was quite accurate inside when using less than 10 additional views, that is 1/60th of additional views. This is better than what we anticipated when analyzing the literature on ROI imaging with two acquisitions. Our understanding of prior art is that authors searched for a low-dose low-frequency image of the outer field of view to extrapolate the missing low-frequencies. When they rely on angular undersampling, they used a sparsity prior to compensate the undersampling (Kolditz, Kyriakou, & Kalender, 2010; Kästner et al., 2015). On the other hand, authors working on interior tomography succeeded using “tiny” *a priori* information (Kudo et al., 2008, 2013; Wang & Yu, 2013). Our setup shows that what is a distorted image of the object outside the field of view still is a faithful-enough depiction of the low frequencies whose truncation causes artifacts in the ROI. The polar sampling of the tomographic acquisition does not need many angles to sample those central frequencies; therefore a least-square criterion does not need extra sparsity *a priori* to reconstruct the ROI well. The “tiny” *a priori* can thus be replaced by a “tiny” amount of full-FOV views.

5.3 Direct reconstruction

We now explore the feasibility of a dual-rotation direct reconstruction method for ROI imaging, including the interior tomography problem. We first adapt the Hilbert-transformed DBP approach of Noo et al. (2004) to dual-rotation acquisitions in the parallel-beam geometry. We highlight the important issue of angular sampling in the Hilbert-transformed DBP method, that will be handled by a dual-resolution reconstruction. We then move to our BPF-based dual-rotation direct reconstruction method and show that it is suited for ROI imaging as well. A dual-resolution variant of the proposed method is also proposed to further speed up the reconstruction.

5.3.1 Adapting the Hilbert-transformed DBP

5.3.1.1 Hilbert-transformed DBP and angular sampling

In the parallel-beam geometry, the Hilbert-transformed DBP method (Noo et al., 2004) relies on Equation (4.1), that we rewrite below:

$$\text{DBP}(\mathbf{x}) = \int_0^\pi \mathcal{B}_\theta [p'_\theta] (\mathbf{x}) d\theta = -2\pi \mathcal{H}_{\frac{\pi}{2}} [f] (\mathbf{x}). \quad (5.4)$$

The inversion of operator $\mathcal{H}_{\frac{\pi}{2}}$ is carried out by using inversion formulas for the truncated Hilbert transform like Equation (4.2), assuming that each line of image

DBP is the truncated Hilbert transform of a compactly supported function f .

This equality was derived in the continuous domain; when N finite projection views $p = \{p_{\theta_k}\}_{k=0\dots N-1}$ are available and uniformly distributed over $[0, \pi]$, the integral becomes:

$$\text{DBP}_N(\mathbf{x}) = \frac{\pi}{N} \sum_{k=0}^{N-1} \mathcal{B}_{\theta_k} [p'_{\theta_k}] (\mathbf{x}) \approx -2\pi \mathcal{H}_{\frac{\pi}{2}} [f] (\mathbf{x}). \quad (5.5)$$

More specifically, one can show that DBP_N is equal to $-2\pi \mathcal{H}_{\frac{\pi}{2}} [f_N]$, where f_N is the semi-discrete FBP reconstruction from p .

Theorem 5.3.1. *Let f_N be the FBP reconstruction from $p = \{p_{\theta_k}\}_{k=0\dots N-1}$:*

$$f_N(\mathbf{x}) = \frac{\pi}{N} \sum_{k=0}^{N-1} \mathcal{B}_{\theta_k} \mathcal{D} [p_{\theta_k}] (\mathbf{x}). \quad (5.6)$$

Then the following holds:

$$\text{DBP}_N(\mathbf{x}) = -2\pi \mathcal{H}_{\frac{\pi}{2}} [f_N] (\mathbf{x}). \quad (5.7)$$

Proof. Rewrite $f_N(\mathbf{x})$ with an integral over $[0, \pi]$ using Dirac functions:

$$f_N(\mathbf{x}) = \int_0^\pi \left(\mathcal{D} [p_\theta] (\mathbf{x} \cdot \boldsymbol{\theta}^\perp) \cdot \frac{\pi}{N} \sum_{k=0}^{N-1} \delta(\theta - \theta_k) \right) d\theta. \quad (5.8)$$

Write the ramp filtering step in the Fourier space and use the projection-slice theorem and the change of variables from polar to Cartesian coordinates to obtain:

$$f_N(\mathbf{x}) = \int_{-\infty}^{+\infty} \int_{-\infty}^{+\infty} \mathcal{F}_2 [f] (\boldsymbol{\nu}) \cdot \frac{\pi}{N} \sum_{k=0}^{N-1} \delta(\angle \boldsymbol{\nu} - \theta_k) e^{2i\pi \boldsymbol{\nu} \cdot \mathbf{x}} d\boldsymbol{\nu}, \quad (5.9)$$

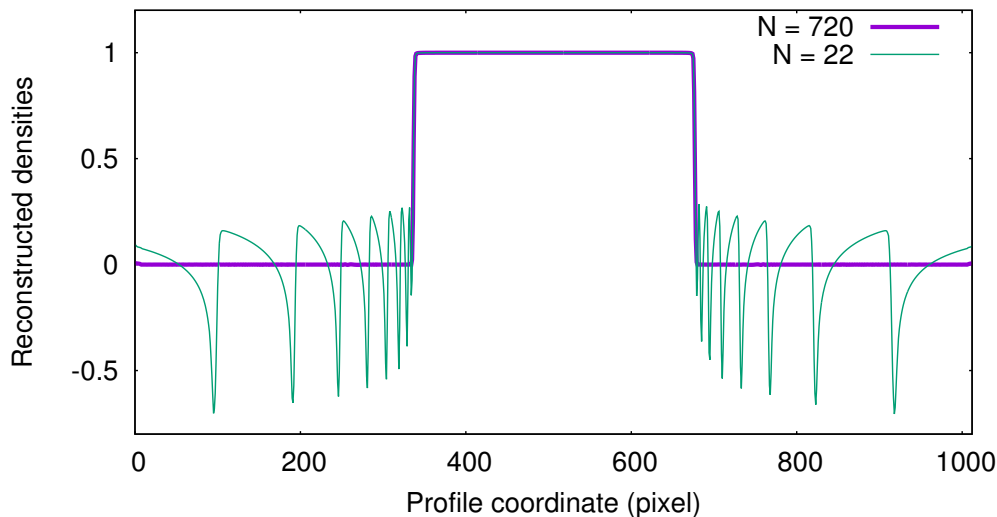
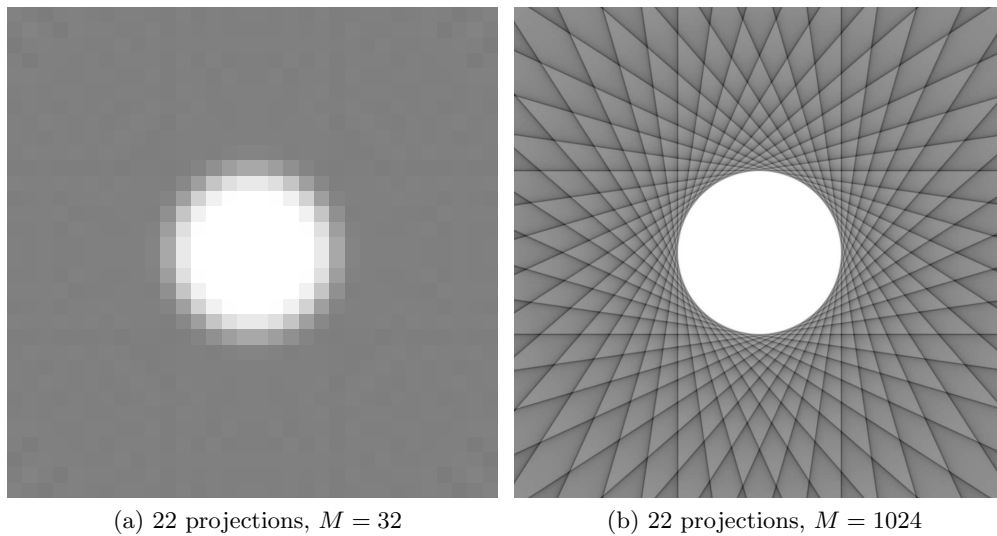
with $\angle \boldsymbol{\nu}$ denoting the polar angle of Cartesian coordinate $\boldsymbol{\nu}$ ($\angle \boldsymbol{\nu} = \theta$ if $\boldsymbol{\nu} = \rho \boldsymbol{\theta}^\perp$). Hence, the Fourier transform of f_N is:

$$\mathcal{F}_2 [f_N] (\boldsymbol{\nu}) = \mathcal{F}_2 [f] (\boldsymbol{\nu}) \cdot \frac{\pi}{N} \sum_{k=0}^{N-1} \delta(\angle \boldsymbol{\nu} - \theta_k). \quad (5.10)$$

As expected, $\mathcal{F}_2 [f_N]$ is nothing but a radial sampling of lines of $\mathcal{F}_2 [f]$. Similarly, one can write $\text{DBP}_N(\mathbf{x})$ using Dirac functions, and as in (Noo et al., 2004), express the derivative operator as a multiplication in the Fourier domain, and use again the projection-slice theorem and the change of variables from polar to Cartesian coordinates to obtain:

$$\begin{aligned} \text{DBP}_N(\mathbf{x}) &= -2\pi \int_{-\infty}^{+\infty} \int_{-\infty}^{+\infty} (-i \operatorname{sgn}(\boldsymbol{\nu} \cdot \boldsymbol{\alpha})) \mathcal{F}_2 [f] (\boldsymbol{\nu}) \cdot \frac{\pi}{N} \sum_{k=0}^{N-1} \delta(\angle \boldsymbol{\nu} - \theta_k) e^{2i\pi \boldsymbol{\nu} \cdot \mathbf{x}} d\boldsymbol{\nu} \\ &= -2\pi \mathcal{H}_\alpha [f_N] (\mathbf{x}), \end{aligned} \quad (5.11)$$

where $\alpha = \frac{\pi}{2}$. This concludes the proof. \square



(c) Horizontal line profile passing through the center of the disk ($M = 1024$)

Figure 5.7 – Angular sampling, resolution and image support.

When $N \rightarrow +\infty$, then $f_N \rightarrow f$, and the support of f_N gets closer to the support of f , which is compact. Hence, in the context of diagnostic CT, where the source trajectory is finely sampled, one can apply the finite Hilbert transform formula of Equation (4.2) to the lines of DBP_N . Recall that the issue of fine or coarse angular sampling depends on the resolution of the reconstruction grid (hence of the detector sampling) (Kak & Slaney, 2001). In theory, for an image of size $M \times M$ corresponding to a sampling of the detector axis into M bins, a natural choice is to ensure that all samples in the 2D Fourier plane are separated by no more than 1, yielding $N = \frac{\pi}{2}M$. In practice, satisfying this equality is not necessary, but N is still chosen approximately equal to M . Angular subsampling occurs when N is significantly lower than M .

An illustration of this observation is shown in Figure 5.7. A uniform disk is reconstructed from $N = 22$ projections on a grid of size $M = 32 \times 32$ (Figure 5.7a) and $M = 1024 \times 1024$ (Figure 5.7b). Although blurred, the low-resolution image shows a compactly supported disk with an approximately flat background equal to zero. By contrast, the high-resolution image shows many subsampling streaks in the background. When plotting a horizontal line profile passing through the center of the disk (Figure 5.7), the reconstructed image suffers from subsampling streaks. These streaks create oscillating bumps outside of the support of the object, so that the support of the line profile depicted in Figure 5.7c is not compact anymore.

Hence, the approximation of f by image f_N is valid at a given spatial resolution. Heuristically, one can find a low-pass filter L , such that $L[f_N]$ is close enough to $L[f]$. Indeed, projections p provide a radial sampling of the 2D Fourier transform of f : hence, the lower N , the lower the frequencies that are well sampled by p . As a low-pass filter, we consider an isotropic Gaussian filter G_σ with standard deviation σ . We thus obtain:

$$G_\sigma[\text{DBP}_N] = -2\pi G_\sigma \mathcal{H}_{\frac{\pi}{2}}[f_N] = -2\pi \mathcal{H}_{\frac{\pi}{2}} G_\sigma[f_N] \approx -2\pi \mathcal{H}_{\frac{\pi}{2}} G_\sigma[f], \quad (5.12)$$

and the inversion of Equation (4.2) can now be applied to $G_\sigma[\text{DBP}_N]$.

In the context of dual-rotation direct reconstruction, we merge the DBP images DBP_F and DBP_T , obtained respectively from projections p_F and p_T , using the following operator:

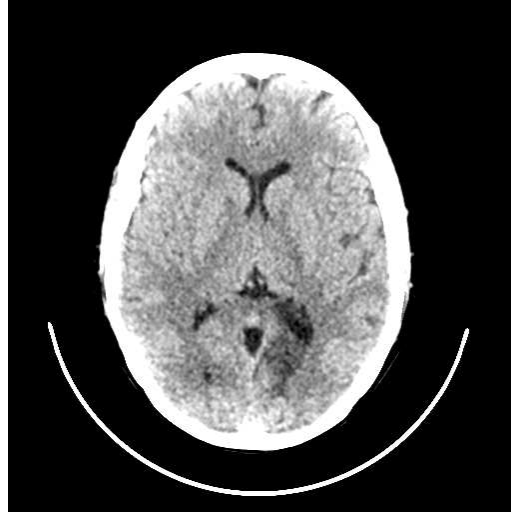
$$\mathcal{M}_{\text{ROI}}(\text{DBP}_F, \text{DBP}_T) = \begin{cases} w_F \cdot G_\sigma[\text{DBP}_F] + w_T \cdot \text{DBP}_T & \text{inside the ROI;} \\ G_\sigma[\text{DBP}_F] & \text{outside the ROI.} \end{cases} \quad (5.13)$$

The weighting functions w_F and $w_T = 1 - w_F$ are the same as in Chapter 4. The finite inverse Hilbert transform formula from Equation (4.2) is then applied to each line of image $\mathcal{M}_{\text{ROI}}(\text{DBP}_F, \text{DBP}_T)$.

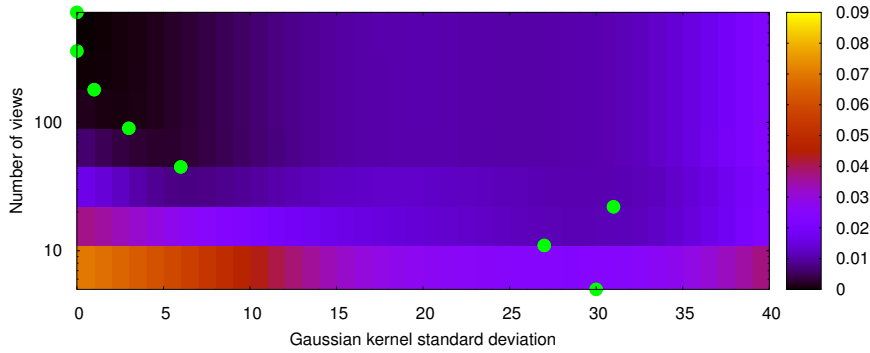
5.3.1.2 Experiments

We used a diagnostic CT slice of a brain (Figure 5.8a) and forward-projected it to simulate parallel-beam acquisitions. 720 parallel-beam projections of 576 bins were generated, sampling uniformly 180° . Truncated data p_T consisted of the 720 projections with a digital truncation keeping the detector bins corresponding to a centered, circular 2D FOV of 256 in diameter. Non-truncated data p_F were samples of the 720 original projections, that are uniformly distributed over 180° . Images were reconstructed on a square grid of size 512^2 . No noise was added to the data in this experiment, so that only the angular sampling of the non-truncated data was varied. The Hilbert-transformed DBP image obtained from the full set of 720 non-truncated projections was used as our reference image f_{ref} . The weighting function w_F was the same as in Equation (4.39), with $\Delta r = 15$ pixels. The inversion of the Hilbert transform was handled by the finite inverse transform formula of You and Zeng (2006).

In order to study the influence of the Gaussian kernel standard deviation σ , we varied it from 0 (no smoothing) to 40 with steps of 5, for each sampling ratio



(a) Reference image



(b) Mean relative error inside the ROI as a function of angular sampling and of the Gaussian smoothing filter

Figure 5.8 – Hilbert-transformed DBP-based dual-rotation reconstruction for ROI imaging. Window width: 50 HU.

s . In the simulations, we set $s = 2^q$, with q varying from 0 ($s = 1$) to 7 ($s = 128$). For each reconstructed image $f_{\sigma,s}$, the mean relative error (MRE) with respect to the reference image was computed over the ROI as:

$$\text{MRE}_{\sigma,s} = \frac{1}{|\text{ROI}|} \sum_{\mathbf{x} \in \text{ROI}} \frac{|f_{\sigma,s}(\mathbf{x}) - f_{\text{ref}}(\mathbf{x})|}{|f_{\text{ref}}(\mathbf{x})|}, \quad (5.14)$$

where $|\text{ROI}|$ denotes the total number of pixels within the ROI.

5.3.1.3 Results

The mean relative errors are shown in Figure 5.8b. For each value of s , the minimum MRE is indicated with a green dot. These values are also recalled in Table 5.1. Although for $N_F \geq 90$ ($s \leq 16$), the minimum MRE values seem

s	N_F	σ	$\text{MRE}_{\sigma,s}$ (%)
1	720	0	0.00
2	360	0	$8 \cdot 10^{-3}$
4	180	1	0.04
8	90	3	0.97
16	45	6	0.30
32	22	31	1.10
64	11	27	1.11
128	5	30	3.72

Table 5.1 – Optimal smoothing parameter σ and corresponding MRE for each angular subsampling ratio s .

to follow a smooth curve on the plane (σ, s) , they are significantly higher and towards much higher σ values when N_F drops to as few as 22 ($s \geq 32$). This change of behavior suggests that the proposed approach may fail when s is too high.

Reconstructed images with the optimal value of σ according to the MRE criterion are shown in Figure 5.9. For each case, the dual-rotation reconstruction without Gaussian smoothing of DBP_F is also shown. In all cases, when no Gaussian smoothing is applied to DBP_F (Figures 5.9a, 5.9c, 5.9e), the reconstructed ROI suffers from horizontal streaks due to the invalid inversions of the Hilbert lines, even with 90 full-FOV projections (Figure 5.9e). For $s < 32$, the optimal smoothing of DBP_F strongly reduces the impact of horizontal streaks in the ROI, resulting in values of the MRE of 0.003 for $s = 16$ (Figure 5.9d) and 0.001 for $s = 8$ (Figure 5.9f). As observed previously in Figure 5.8b, when $s = 32$, the strong Gaussian smoothing applied on DBP_F reduced the effect of the horizontal streaks, but the reconstructed image suffers from residual low-frequency non-uniformities (Figure 5.9b).

5.3.1.4 Discussion

In this study in the parallel-beam geometry, we adapted the Hilbert-transformed DBP method to dual-rotation acquisitions for ROI imaging, when only a few full-FOV projections are available. The case of angularly subsampled acquisitions was not investigated by the previous works on Hilbert-transformed DBP (Noo et al., 2004). Our study confirms that inversion formulas for the finite Hilbert transform are not appropriate when dealing with angular subsampling.

To overcome this limitation, a dual-resolution approach was proposed, and the hybrid DBP image $\mathcal{M}_{\text{ROI}}(\text{DBP}_F, \text{DBP}_T)$ merges the truncated DBP image at the native spatial resolution with the full-FOV DBP image, convolved with a Gaussian kernel with standard deviation σ . In our simulations, an exhaustive search was performed in order to find an optimal σ value for each sampling ratio s . However, automatizing this selection is still an open issue: the choice of the smoothing parameter should result from a compromise between a reduction of subsampling streaks and a preservation of the true high-frequency structures

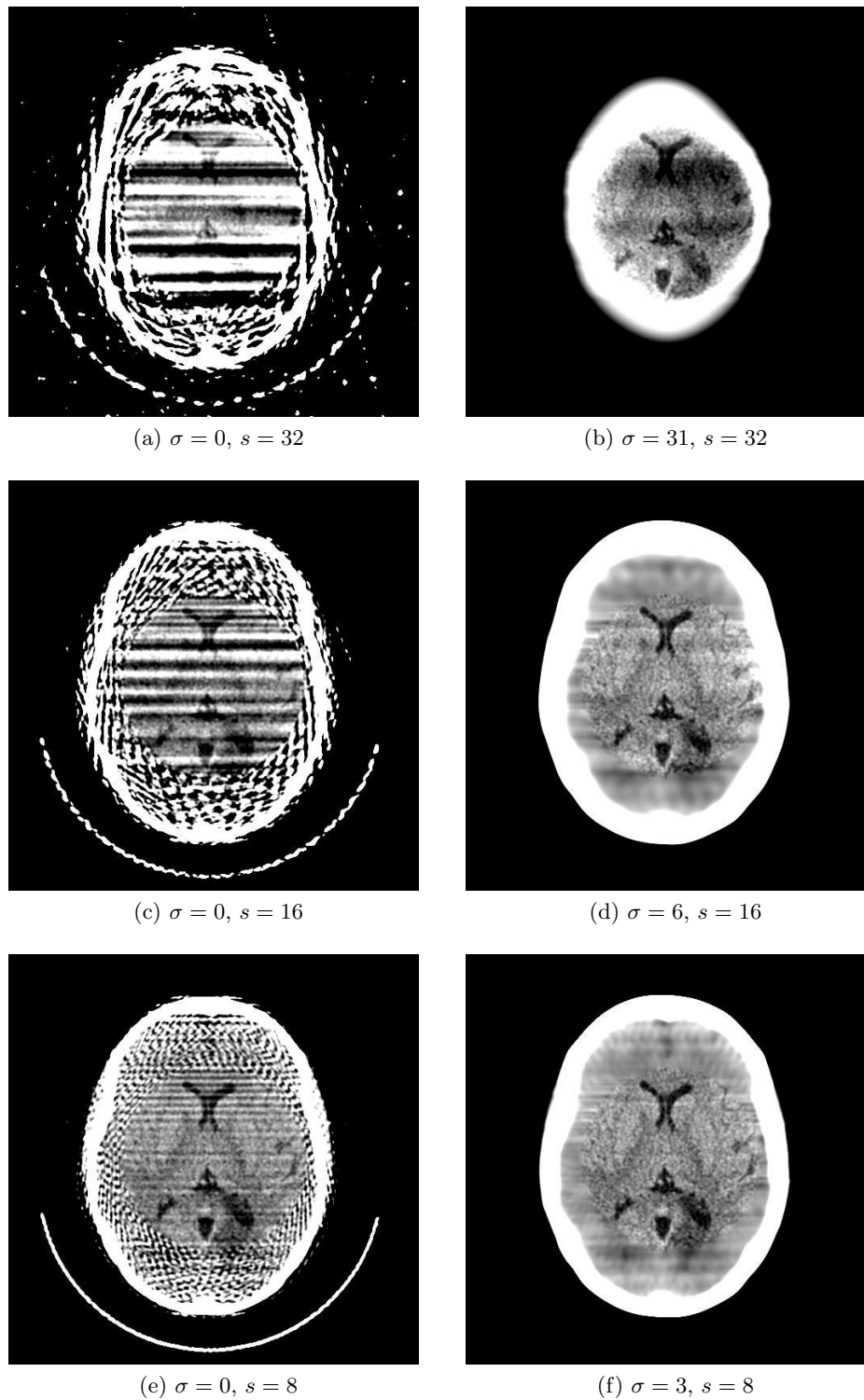


Figure 5.9 – Dual-rotation reconstruction via the Hilbert-transformed DBP method without and with optimal smoothing of DBP_F . Window width: 50 HU.

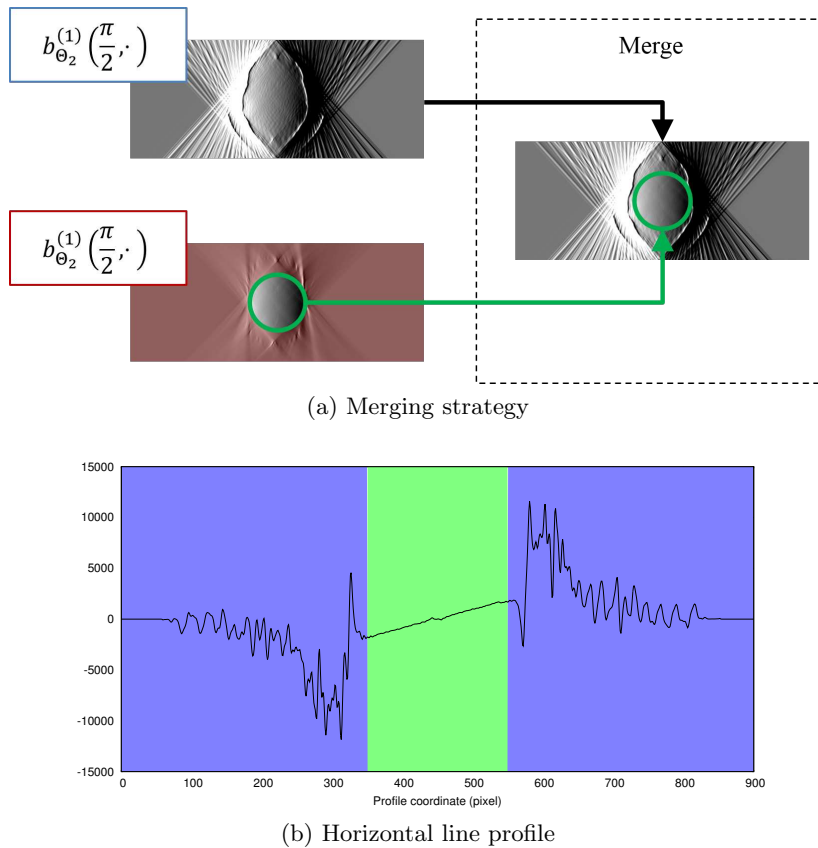


Figure 5.10 – Merging step in dual-rotation ROI direct reconstruction.

that are needed to extrapolate the Hilbert lines of DBP_T .

Our method successfully reconstructed the ROI when s is not too high. When using the optimal values of σ , the MRE was kept lower than 1% when $s < 32$. However, when s gets higher than 32, no good compromise between streak removal and structure preservation could be found for the value of σ , resulting in low-frequency non-uniformities in the reconstructed ROI.

One may wonder whether this approach is adapted to fan-beam geometries. In (Noo et al., 2004), the authors applied a change of variables from parallel-beam parameters (u, θ) to fan-beam parameters $(\hat{u}, \hat{\theta})$ in the integral definition of DBP. As a result, relevant fan-beam rays are picked up from the densely sampled projection data to reconstruct the same DBP as in the parallel-beam geometry. Unfortunately, this method cannot be used when the full-FOV acquisition is angularly subsampled. Instead, we take advantage of our proposed splitting BPF method (Chapter 4).

5.3.2 View-wise BPF solution

5.3.2.1 Standard scheme

The proposed dual-rotation direct reconstruction from Chapter 4 can be used without any modification in the context of ROI imaging. We recall how the

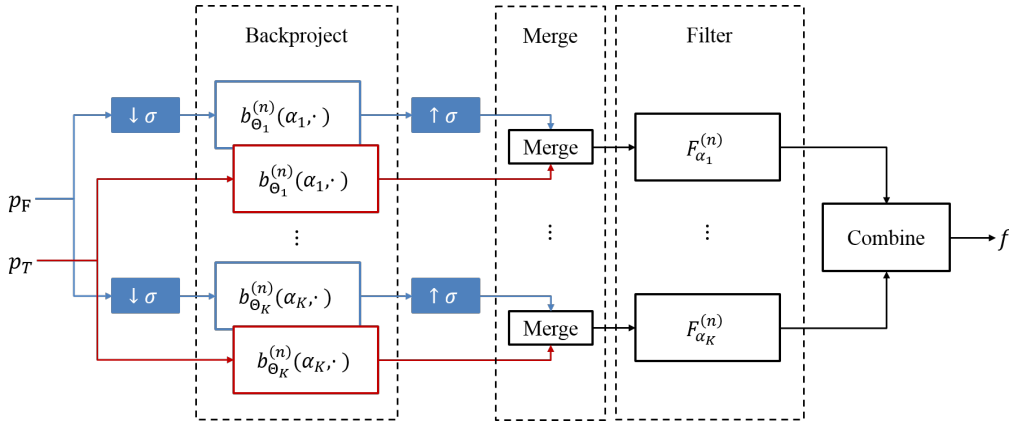


Figure 5.11 – Flowchart of the multiresolution dual-rotation direct reconstruction. Symbol $\downarrow \sigma$ denotes a downsampling of factor σ , and $\uparrow \sigma$ denotes an upsampling of factor σ .

merging step is carried out in Figure 5.10a. This example is in parallel-beam geometry, for $n = 1$ and for $\Theta_2 = \left[\frac{\pi}{4}, \frac{3\pi}{4}\right]$. Each line of the merged image is then filtered by a Hilbert transform computed as a multiplication in the Fourier transform.

One example of such hybrid line profiles is shown in Figure 5.10b. In Chapter 4, the tails of this line (blue areas) were as finely estimated as the central part of the line (green area), coming from the truncated projection data. The only difference was the amount of statistical noise corrupting the data at a higher level in the blue areas with respect to the green area. Here, the tails of the line are estimated from only a few full-FOV views, resulting in strong spikes along the line in the blue areas. However, these spikes oscillate around the true lower-frequency line, so that on average, the shape of the Hilbert line is still well estimated. Moreover, as in the previous chapter, the filtering operators, whether the ramp filter or the Hilbert transform, are expected not to propagate the zero-mean, high-frequency content of these spikes too far from their original locations.

As already shown in Chapter 4, this approach can be extended to C-arm CBCT via a Feldkamp-like extension of the fan-beam case.

5.3.2.2 Sped-up reconstruction through a dual-resolution strategy

Note that the support of the reconstructed image exceeds the support of the ROI. However, data outside the ROI are not of much interest here. Hence, it is not necessary to reconstruct areas outside the ROI at the native spatial resolution.

We thus propose to backproject unfiltered, non-truncated views into a lower-resolution grid (Figure 5.11). This solution speeds up the reconstruction process, since backprojection is a step that is computationally expensive, especially for C-arm cone-beam data; it also mitigates the subsampling streak artifacts in case of highly subsampled data. Of course, the choice of the subsampling factor depends on the content of the image: the higher the frequencies of the image, the less a low-resolution backprojected image will be able to extrapolate the data missing in the truncated projections.

Once the low-resolution backprojection step is done, the low-resolution image is further upsampled to the correct resolution, and merging of the unfiltered backprojection images can be performed as already mentioned previously.

5.3.2.3 Experiments

We first looked at the standard scheme in a simulated circular, full-scan, fan-beam geometry with a linear detector. We used the same diagnostic CT slice of a head as before. We set $d = 720$ and $D = 1195$. Since the source trajectory samples the full circle, 1440 density projections were generated, that uniformly sample 360° . Again, truncation was set digitally such that the ROI is centered, circular, with a diameter of 256 pixels. The reference image is the single-rotation BPF reconstruction from the 1440 full-FOV projections, and the actual full-FOV projections used in our dual-rotation reconstruction were uniformly sampled from these 1440 projections. For each value of s that was tested, the MRE was computed.

We then used again our ideal, circular cone-beam projections of a head CT scan. The truncated projections p_T were the same as in Section 4.3.2.1: they were obtained by applying a digital transaxial truncation to the previous set of 1440 noisy projections, corresponding to a cylindrical, centered field of view Ω' whose edges cross the head skull. It is thus expected that empirical projection extrapolation methods would not perform as well. Such a reconstruction was computed using (Hsieh, Chao, et al., 2004; Hsieh, Armstrong, et al., 2004), yielding image $f_{\text{FDK}}^{\text{ROI}}$. For the un-truncated projections p_F , we simulated an acquisition of 90 projections corresponding to $1.6 \cdot 10^6$ photons per ray, yielding image $f_{\text{BPF}}^{\text{ROI}}$. As in Section 4.3.2.1, the dose ratio between the un-truncated and the truncated acquisitions is fixed to 1/16. The merging step was performed using the same weighting function as in Equation (4.39).

Experiments were also performed on the Catphan[®] CTP 515 LCD module as in Section 4.3.2.1, with the same weighting function w_F . A uniform angular subsampling was applied to the full-FOV projections. The size of the reconstructed isotropic voxels is 0.48 mm, so that images consist of cubes of 512^3 voxels. For the dual-resolution strategy, the full-FOV projections were backprojected on coarser grids with voxel sizes varying from 0.48 mm (native resolution, $\sigma = 1$, grid of size 512^3) to 7.68 mm (coarsest resolution, $\sigma = 16$, grid of size 32^3). Coarse backprojected images were upsampled to the full resolution using trilinear interpolation. We used the dual-rotation direct reconstruction with the full set of full-FOV projections ($s = 1$) at the native resolution ($\sigma = 1$) as our reference image and we used the mean relative error (MRE) as our quality measure. Parker's weights were used to handle redundancy in the short-scan acquisition trajectory (Parker, 1982).

We then keep $\sigma = 1$ (single-resolution case) and we used a clinical non-injected acquisition of 600 projections of the head acquired over a short-scan trajectory. The truncated projections p_T were simulated by applying a digital transaxial truncation of $t = 0.52$. Additional vertical collimation was digitally applied. Full-FOV spins with less views were obtained by digital uniform downsampling. We first studied the limit case $N_F = 2$, when the full-FOV projections only

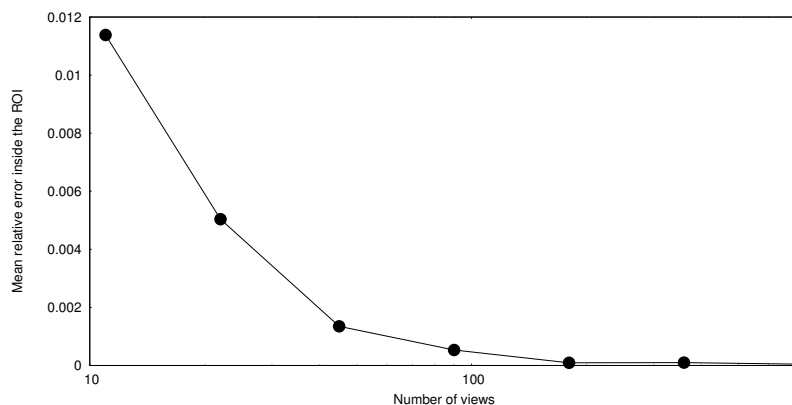


Figure 5.12 – Mean relative error as a function of the number of full-FOV projections.

consist of two orthogonal views. In this case, the reconstructed image has an isotropic voxel size of 0.48 mm. We then set $s = 16$, yielding a set of 37 full-FOV projections, and we reconstructed an image with isotropic voxel size 0.96 mm in order to mitigate the image noise and better visualize the brain soft-tissues. Because it is a real clinical acquisition, the auto-exposure control (AEC) loop was used to adapt the tube techniques with respect to the patient’s radio-opacity at each view angle.

5.3.2.4 Results

The results in the fan-beam geometry are shown in Figure 5.12. The MRE decreases quickly when increasing the number of full-FOV projections. We observe that the MRE drops below 0.2% when $N_F \geq 45$ ($s = 32$).

Reconstructed images in the fan-beam geometry are shown in Figure 5.13. As expected, a single-rotation reconstruction from the truncated projections (Figure 5.13a) induces a strong capping artifact, that forbids the use of short window widths for visualization. The reconstructed ROI is much flatter when using as few as 22 full-FOV projections ($s = 64$, Figure 5.13b), despite some residual non-uniformities localized near the boundaries of the ROI. When s gets lower, the reconstructed images are visually equivalent to the reference image in the ROI (Figures 5.13c and 5.13d); they achieve MRE values of 0.13% and 0.05%, respectively.

Results of ROI reconstruction in the ideal circular cone-beam geometry are shown in Figure 5.14. The left column shows the FDK reconstruction from the truncated projections only using empirical projection extrapolation. As expected, such extrapolation cannot perform well when highly contrasted structures such as bones lie at the edge of the field of view. The image $f_{\text{FDK}}^{\text{ROI}}$ suffers from a shift in gray values and from low-frequency non-uniformities that prevent from using a narrow window display. Our reconstruction method is shown in the right column. It yields an image that is visually similar to the reference FDK reconstruction $f_{\text{FDK}}^{\text{noisy}}$ (Figure 4.11, first row) inside the ROI Ω' . Outside the ROI, image $f_{\text{BPF}}^{\text{ROI}}$ shows streaks characteristic of angular subsampling. However, they do not seem

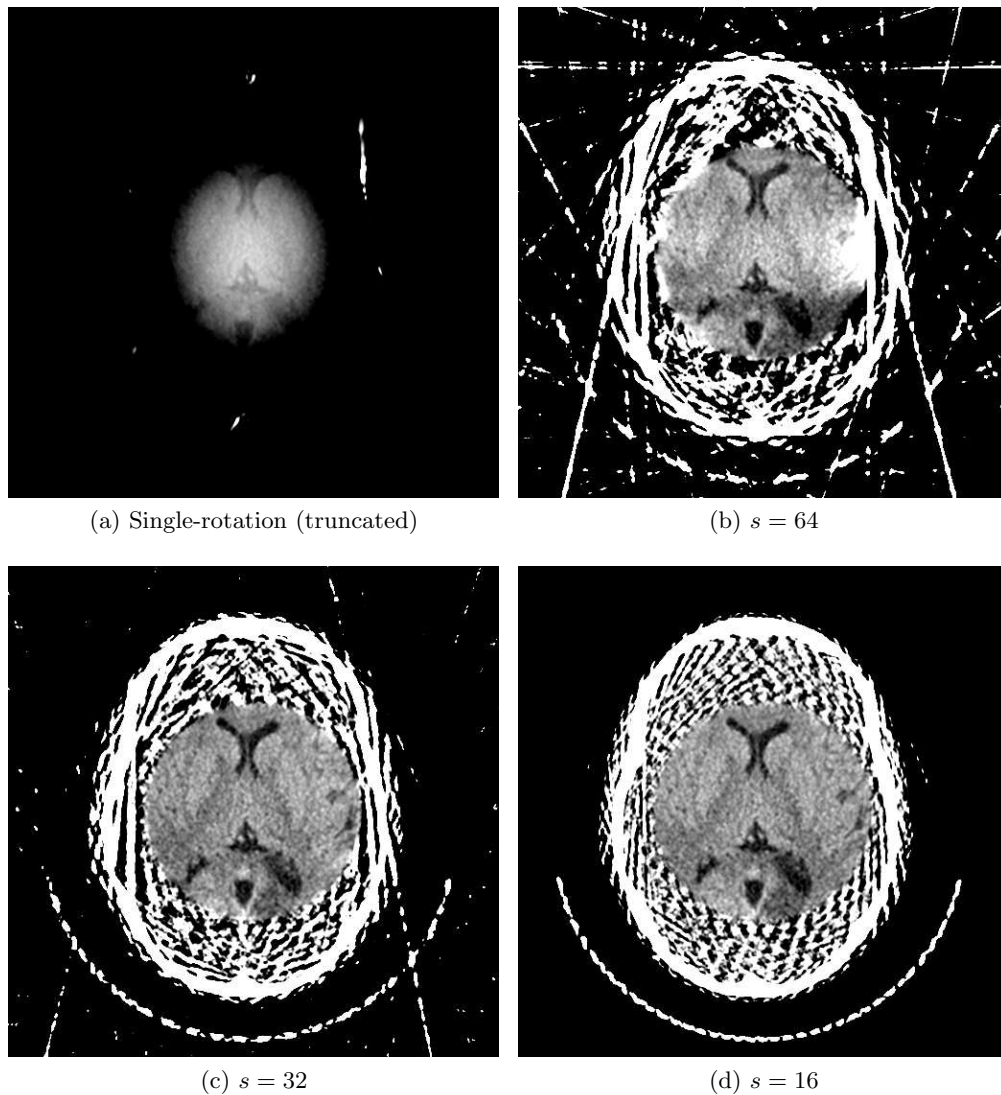


Figure 5.13 – Dual-rotation direct reconstruction for ROI imaging: circular, full-scan, fan-beam geometry with linear detector. Window width: (a) 150 HU (b)–(c)–(d) 50 HU.

to propagate much inside Ω' . The values of the MRE inside region $\Omega = \Omega' \cap \Omega_0$ with respect to $f_{\text{FDK}}^{\text{noisy}}$ remain below 1%, at 0.50% for $f_{\text{BPF}}^{\text{ROI}}$.

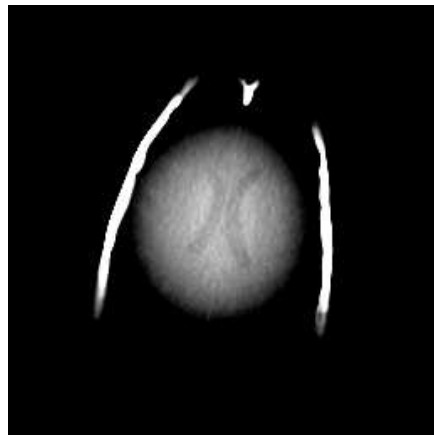
As in the case of virtual bow-tie direct reconstruction, it is interesting to look at the pointwise relative error images shown in Figure 5.15. The left column shows axial, coronal and sagittal slices of the relative error image with respect to the FDK reconstruction from low-noise, un-truncated, subsampled acquisitions. This column shows a very good agreement between the reference image and the proposed reconstruction inside the head and *outside* the ROI. As in Figure 5.15, the vertical and horizontal bands in Figure 5.15a reveal the processing steps of the two-pass approach. The same patterns can be seen in Figure 5.15b, but this time, the image and all the right column represent the relative error image with

respect to the FDK reconstruction from un-truncated, low-noise, fully sampled acquisitions (see Figure 4.11, first row). This time, the error is minimal within the ROI, with vertical and horizontal patterns that can be observed in the error image but are visually unidentifiable in the proposed dual-rotation reconstruction from Figure 5.14.

Results on the CTP 515 module are summarized in Figure 5.16. The MRE is minimal at full resolution with the finest angular sampling of the full-FOV data (top right corner), and increases when either the angular sampling or the resolution of the full-FOV backprojection gets coarser. We observe that the MRE remains below 1% when $s \geq 32$ ($N_F \geq 18$) and the coarse voxel size does not exceed 3.84 mm (reconstruction grid of size 64^3). Examples of reconstructed CTP 515 modules are shown in Figure 5.17 for $s = 16$ ($N_F = 37$) and various dual-resolution settings. The reconstructed image that is closest to the reference image (Figure 5.17a) according to the MRE uses the native resolution ($\sigma = 1$, Figure 5.17b). Using a resolution that is four times coarser for the full-FOV backprojection ($\sigma = 4$, Figure 5.17c) only increases the MRE by 0.03 points, from 0.15% to 0.18%, with visually no effect on the reconstructed ROI. However, when the resolution of the full-FOV backprojection gets too coarse ($\sigma = 16$, Figure 5.17d), it fails at reconstructing the ROI, which suffers from streaks and non-uniformities, and shifted gray values, a behavior that is similar to the one observed on simulations in parallel-beam geometry in Section 5.3.1.3. Despite this effect, the central contrast inserts with relative contrasts of 1% are visually detectable in all cases.

Results on the clinical head case are shown in Figure 5.18 in the limit case where using only two full-FOV projections. Visually, the reconstructed ROI (Figure 5.18a) looks very much like the image reconstructed from the full-FOV, fully sampled projections (Figure 5.18b). In particular, the structures of the temporal bones are correctly reconstructed. A profile taken along the yellow line in Figure 5.18a is shown in Figure 5.18c. The profile from the reconstructed ROI matches the profile from the reference image. The residual error (black curve) is negligible with respect to the reconstructed coefficients. However, this error still lies between -300 HU and 100 HU: hence, as expected by our previous simulation studies, using only two full-FOV views is not enough for soft-tissue imaging (note the large window width used for visualization of the bone structures).

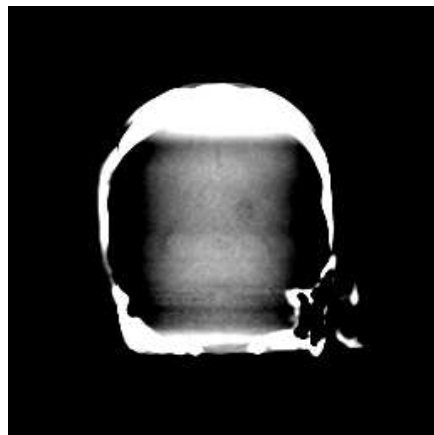
Results on the clinical head case using 37 full-FOV projections are shown in Figure 5.19. The MRE with respect to the image reconstructed from the full-FOV, fully sampled projections (left column) and taken within the ROI was 0.88%. A window width of 100 HU was used to display the results, with no visual difference in the ROI between the two reconstructions. This experiment is in very good agreement with the simulated full-scan cone-beam acquisition of the CT head scan, despite a small lateral truncation even in theoretically un-truncated data p_F .



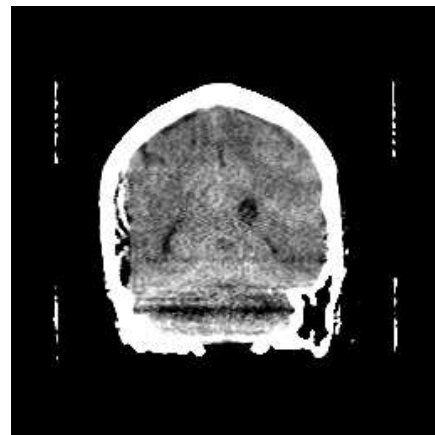
(a) FDK (axial)



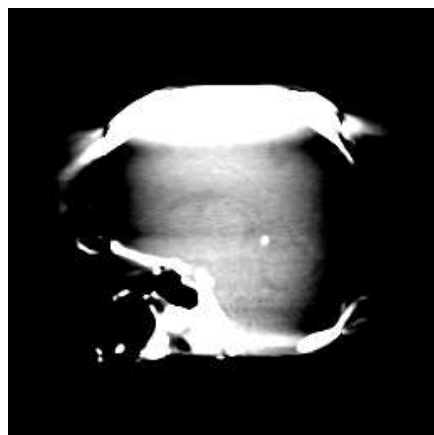
(b) Proposed (axial)



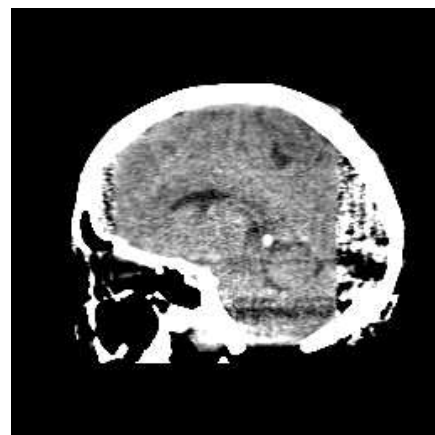
(c) FDK (coronal)



(d) Proposed (coronal)



(e) FDK (sagittal)



(f) Proposed (sagittal)

Figure 5.14 – Dual-rotation direct reconstruction for ROI imaging: circular, full-scan, cone-beam geometry with flat-panel detector. Window width: 200 HU (left column), 50 HU (right column).

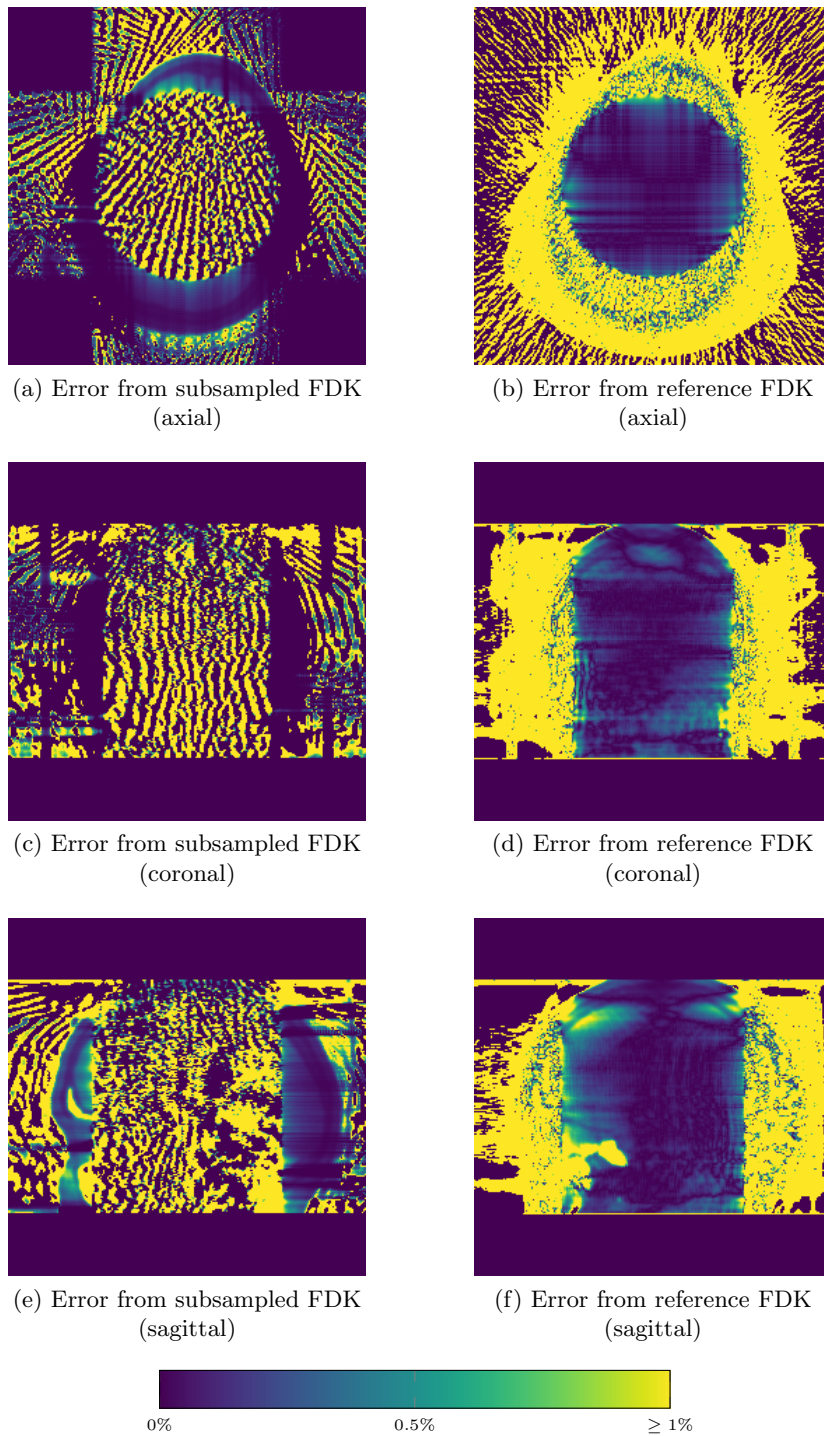


Figure 5.15 – Dual-rotation direct reconstruction for ROI imaging (see Figure 5.14): relative errors (left column) with respect to the FDK reconstruction from the subsampled, un-truncated acquisition (reconstruction not show) and (right column) with respect to the FDK reconstruction from the noisy, un-truncated acquisition (Figure 4.13, left column).

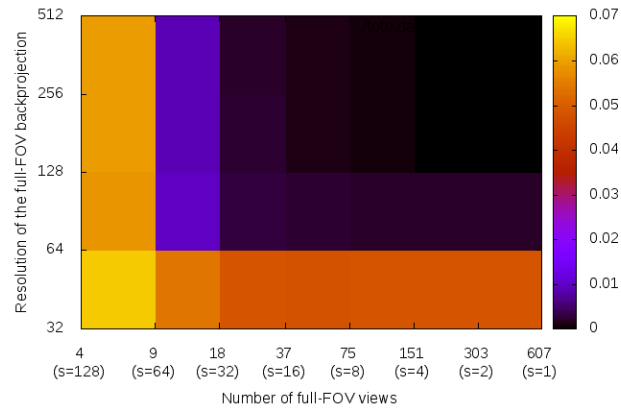
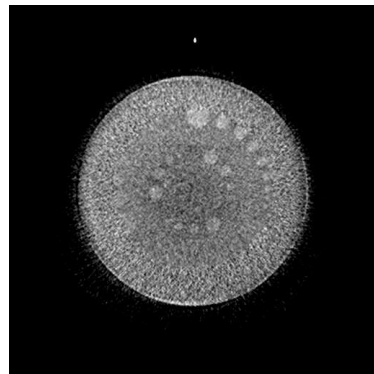
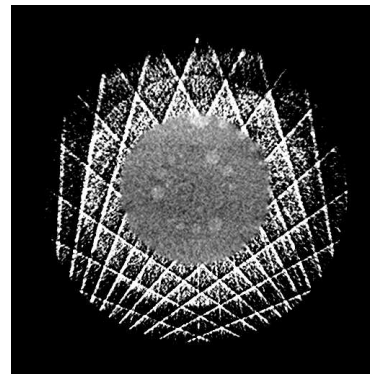


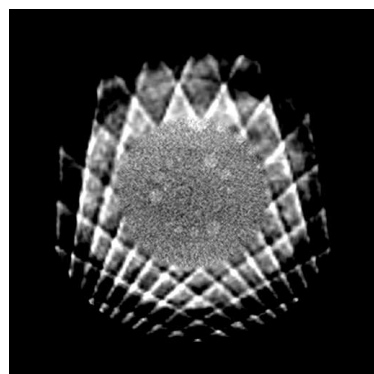
Figure 5.16 – Mean relative error as a function of the angular sampling and the resolution of the backprojection of the full-FOV projections.



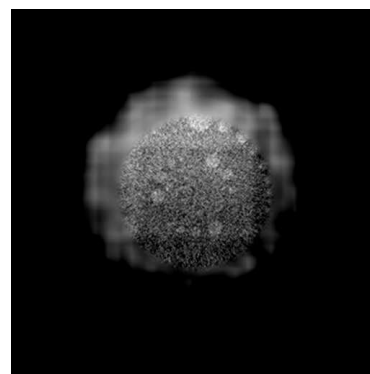
(a) Reference image, MRE = 0.00%



(b) $\sigma = 1$, MRE = 0.15%

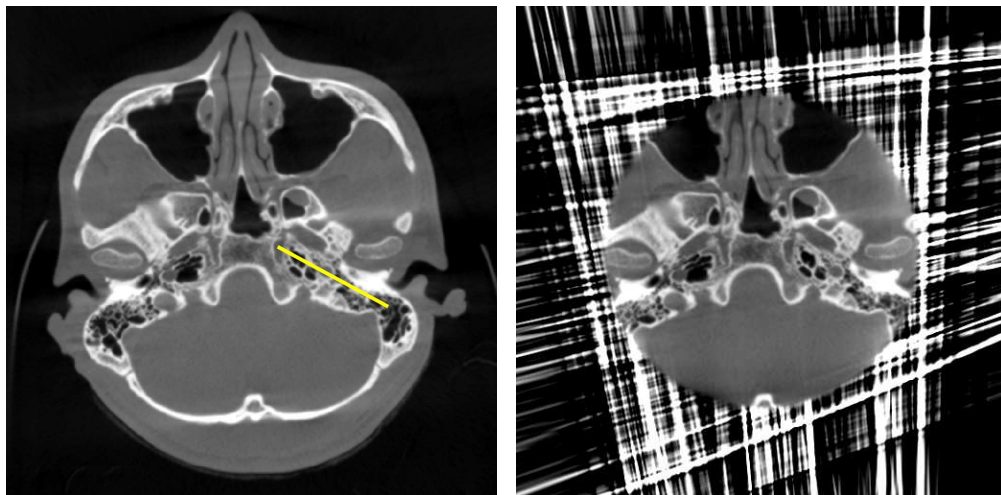


(c) $\sigma = 4$, MRE = 0.18%



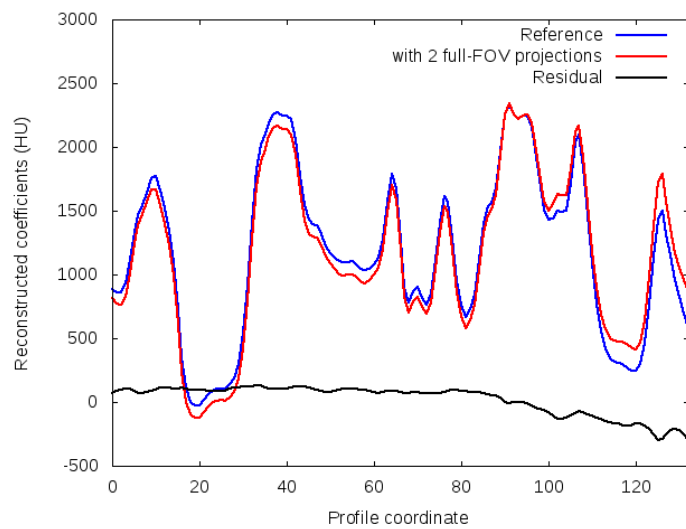
(d) $\sigma = 16$, MRE = 9.27%

Figure 5.17 – ROI direct reconstruction of the Catphan[®] 515 LCD module using different resolution factors for the full-FOV, subsampled spin. The MRE is computed within the ROI, with respect to the reference image (a), which is reproduced from Figure 4.15b. Window width: 50 HU.



(a) Full-FOV reconstruction

(b) ROI reconstruction



(c) Line profiles

Figure 5.18 – ROI reconstruction of a digitally truncated clinical C-arm CBCT acquisition of a head, using two additional full-FOV projections. The line profiles are taken along the yellow line displayed in (a). Window width: 2800 HU.

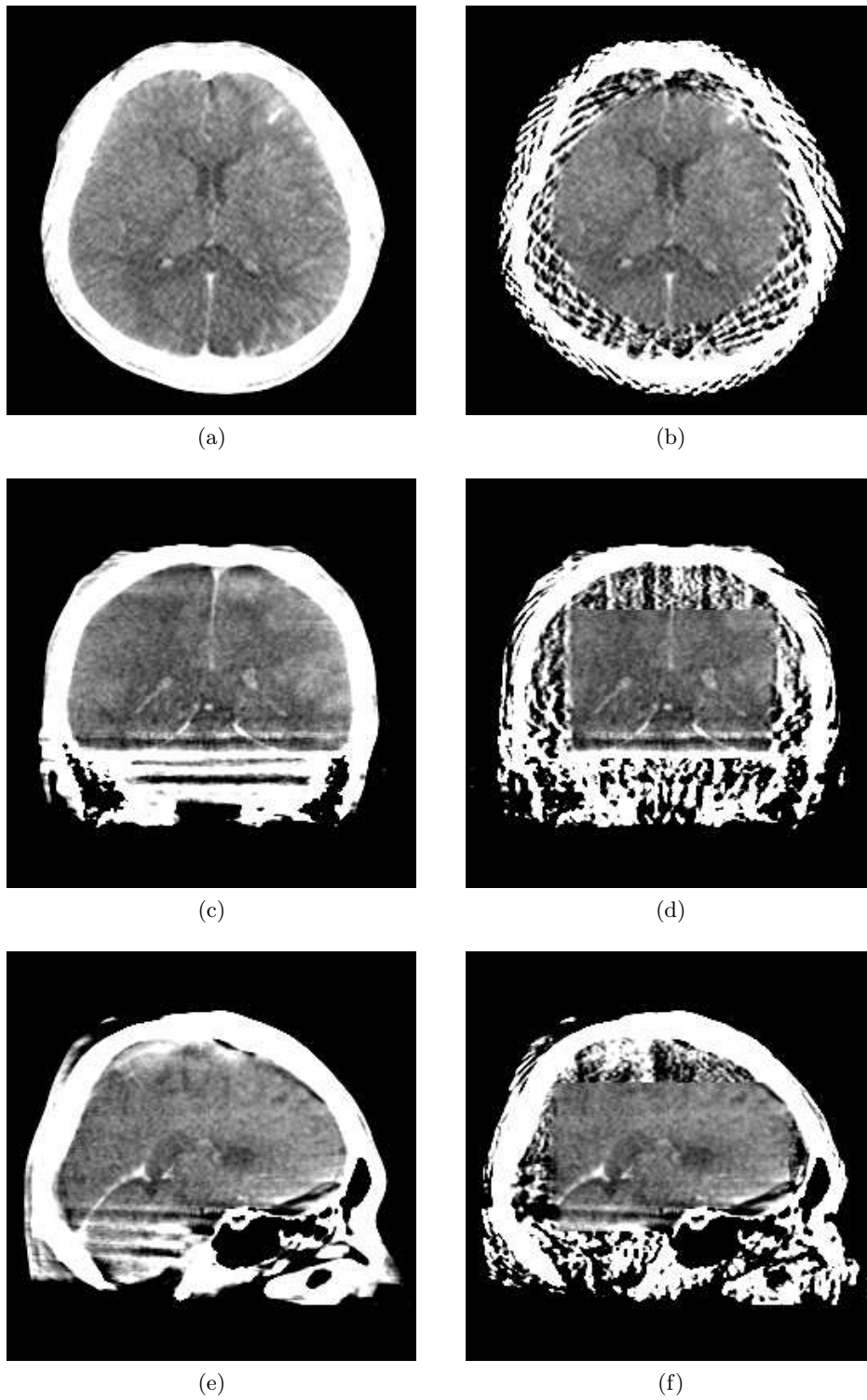


Figure 5.19 – ROI reconstruction of a digitally truncated clinical C-arm CBCT acquisition of a head, using 37 additional full-FOV projections (right column). The same reconstruction from the fully sampled full-FOV spin is also shown (left column) for comparison. Window width: 100 HU.

5.4 Discussion

In this chapter, we switched our viewpoint from full-volume imaging to ROI imaging using dual-rotation acquisitions. In this context, by contrast to the virtual bow-tie case, we did not look at the lowest possible dose per view but rather at vastly undersampling the full-FOV spin. By introducing an additional weight s defined as the ratio of views per spins, we successfully used the same iterative algorithm as in Chapter 3. Interestingly, the DBP-HT- K formula, that was used to propose an alternative, direct virtual bow-tie reconstruction in Chapter 4, could be used “as is” with undersampled full-FOV spins for ROI imaging, with almost no visible artifact in the reconstructed ROI when using as few as 1/32th of additional views. Heuristically, this can be understood from the fundamental property of the Hilbert transform, which localizes high frequency contents such as noise in the virtual bow-tie case, or more structured patterns such as subsampling streaks in the case of ROI imaging. Hence, neither the noise in the previous chapter, nor the streaks in this chapter, seem to propagate much inside the ROI.

Since reconstructed points outside the truncated 3D FOV are not of interest, a dual-resolution reconstruction could also be used, where a coarser reconstruction grid is selected when backprojecting the undersampled, full-FOV projections. Little image distortion was observed when using voxels four times larger outside the truncated FOV, showing the robustness of the approach to coarser reconstruction grids. Of course, at some point, the grid becomes too coarse to capture a reasonable extrapolation of the data, leading to low-frequency non-uniformities in the reconstructed ROI. The same phenomenon was observed in the special case of dual-rotation ROI imaging using DBP-HT-1 in parallel-beam geometry. This special case requires careful Hilbert transform inversion, since Fourier-based filtering is not an option anymore. Using $K = 1$, the formula DBP-HT- K also becomes intrinsically mono-directional, since only a single pass in one direction is required: it is thus the only case that may open the gates to diagnostic CT reconstruction methods based on pi-lines (Zou et al., 2005).

Although the main focus of this work has been low-contrast detection, it is instructive to see that a two-view extrapolation can yield a good ROI reconstruction for high-contrast imaging. This proof of concept demonstrates the feasibility of arbitrary high-contrast ROI reconstruction using only two additional, orthogonal full-FOV views, for example from fluoroscopic images acquired on a biplane C-arm system (Y. Xia et al., 2015b). Of course, this reconstruction would fail at recovering lower contrasts, which suggests that a more complex workflow would be needed to actually acquire a full-FOV spin, although undersampled.

Conclusion

Contents

6.1	Outcomes of this work	141
6.2	Perspectives	143
6.2.1	Engineering perspectives	143
6.2.2	Theoretical perspectives	144
6.2.2.1	Improved scatter correction	144
6.2.2.2	Applications of DBP-HT- <i>K</i>	145

6.1 Outcomes of this work

In the context of interventional neuroradiology, 3D X-ray imaging with C-arm systems is of much interest to reduce the time needed to treat patients and improve the clinical outcomes. In terms of soft-tissue imaging, however, C-arm systems still show inferior performance as compared to diagnostic CT scanners.

This work proposed to investigate the challenges of low-contrast detection with a commercial C-arm system. The CBCT imaging chain is complex: the X-ray tube, the mechanical deformations of the gantry, the non-idealities of the X-ray detector, the reconstruction algorithm, can all impact the 3D image quality. Through specific setups and simulations, we managed to isolate scattered radiations, dose, and sampling, as key factors to improve C-arm CBCT low-contrast detection. In particular, we discarded the quantization step as a key factor, despite the relatively low number of quantization bins that are used on IGS systems as compared to diagnostic CT.

As a proof of concept, we aimed at designing adapted acquisition and reconstruction frameworks to improve low-contrast detection, without the need to change the imaging system itself. To this end, we proposed a dual-rotation acquisition strategy, that associates one spin over the full detector field of view (FOV)

at low dose, with a spin that is collimated to deliver a higher dose to the central densest parts of the head. The method acts as a virtual bow-tie, and full volume reconstruction of dual-rotation simulations and phantom acquisitions have increased low-contrast detection for less dose, with respect to a single-rotation acquisition. An iterative reconstruction scheme was used, that is based on iterative FBP (iFBP) with smooth regularization. It simultaneously reconstructs two spins in a single volume, without merging measurements in the projection domain, in order not to require the knowledge of the incoming X-ray beam intensities in the truncated views, nor that measurements be taken at the exact same position twice. This thus puts no specific constraints on the mechanical design, but puts more weight on the computation infrastructure. In particular, we found that an extra apodization is needed to get the desired uniformity in the solution.

By switching from FBP to BPF approaches, an alternative, direct reconstruction for dual-rotation acquisitions was made possible. We revisited the standard direct reconstruction formulas in parallel-beam and fan-beam geometries with linear detectors, and derived a new BPF method in a semi-discrete formulation, called the K -pass Hilbert-transformed differentiated backprojection (DBP-HT- K), which performs as good as FBP with arbitrarily coarse angular sampling. The method, extended to the C-arm cone-beam geometry, gives access to an unfiltered backprojection space, that was used to combine the data from the dual-rotation acquisition. Simulations on synthetic data, as well as experiments on the Catphan[®] CTP 515 and on the head phantom with soft-tissue-like structures, confirmed the potential of this new, direct reconstruction framework for virtual bow-tie C-arm CBCT.

Although we used it to emulate a virtual bow-tie, our dual-rotation acquisition framework is intrinsically related to region-of-interest (ROI) imaging through the truncated acquisition. Hence, we shifted from full-volume imaging to ROI imaging, given a dual-rotation acquisition, that has now a third degree of freedom, namely, the angular sampling ratio between both acquisitions. Interestingly, both reconstruction frameworks could successfully reconstruct regions of interest with only a few additional full-FOV projections. In particular, our iterative reconstruction framework could reconstruct the ROI without the need for sparsity criteria in the optimization problem. In the context of direct reconstruction, we highlighted the issue of angular sampling in the well known Hilbert-transformed differentiated backprojection method of [Noo et al. \(2004\)](#), and we showed that our direct method also works for ROI imaging, with almost no visible artifact in the reconstructed ROI when using as few as 1/32th of additional views. Heuristically, this can be understood from the fundamental property of the Hilbert transform, which localizes high frequency contents such as noise in the virtual bow-tie case, or more structured patterns such as subsampling streaks in the case of ROI imaging. A multi-resolution strategy further accelerated the computation time. Simulations in planar geometries and experiments on actual C-arm data demonstrated the feasibility of dual-rotation direct reconstruction for ROI imaging, without any a priori information (neither through spatial a priori, nor through sparsity-enforcing regularization).

6.2 Perspectives

6.2.1 Engineering perspectives

In this work, we proposed dedicated acquisition and reconstruction frameworks to increase low-contrast detection in C-arm CBCT images. Now that the results showed that good image quality could be achieved on current C-arm systems using dual-rotation acquisitions, alternative engineering design solutions may be searched in order to better match the clinical constraints of INR procedures. In particular, we highlight that our proposed solutions are applicable in absence of patient motion, which would introduce inconsistencies both within a single spin and between the two acquisitions of the dual-rotation framework. This may become a limiting factor for clinical applications. For example, it is quite common to observe head motion in ischemic stroke patients (Fahmi et al., 2013). Hence, the current system design, that we used as a starting point for our study, may need further adjustments in order to reduce the acquisition time.

One solution may be to get back to traditional single-rotation acquisitions. In this case, as discussed in Chapter 3, it would be necessary to adjust either the beam shape using bow-tie filters, or to increase the detector readout and thus its dynamic range. The latter case, however, is not optimal in terms of patient skin dose, since this design does not include a spatial modulation of X-ray exposure. On the other side, bow-tie filters are intrinsically related to exposure modulation, and we expect them to achieve similar results as the ones from Chapter 3, including reduced scatter contribution (Altunbas, 2014). Unfortunately, this design choice would not be very attractive due to the lack of flexibility and the limited clinical applications (brain soft-tissue imaging).

Acquiring two sets of projections, as proposed in this thesis, may also be achieved in a single-rotation acquisition. In this case, it would be necessary to perform fast, dynamic collimation to acquire interleaved sets in one rotation. Although this seems feasible for ROI imaging (Kästner et al., 2015), it would still double the angular sampling per rotation in the context of virtual bow-tie acquisitions, thus doubling the acquisition time anyways. Hence, faster acquisitions, either with one rotation and ultra-fast dynamic collimation, or with the proposed dual-rotation strategy, would require increased rotation speeds, and thus higher numbers of frames per second as well.

Fortunately, in the context of high-contrast imaging, three-dimensional digital subtracted angiography (Anxionnat et al., 1998), also obtained through dual-rotation acquisitions, would benefit from system improvements in terms of rotation speed and frame rate, that would reduce both sampling streaks and motion artifacts during the injection of contrast media in the arteries. It is thus reasonable to expect further improvements in these directions in a near future, that would help improve clinical outcomes in a larger number of use cases.

In any case, the next engineering design choices will be able to benchmark with respect to motion-free, dual-rotation acquisition and reconstruction frameworks proposed in this thesis.

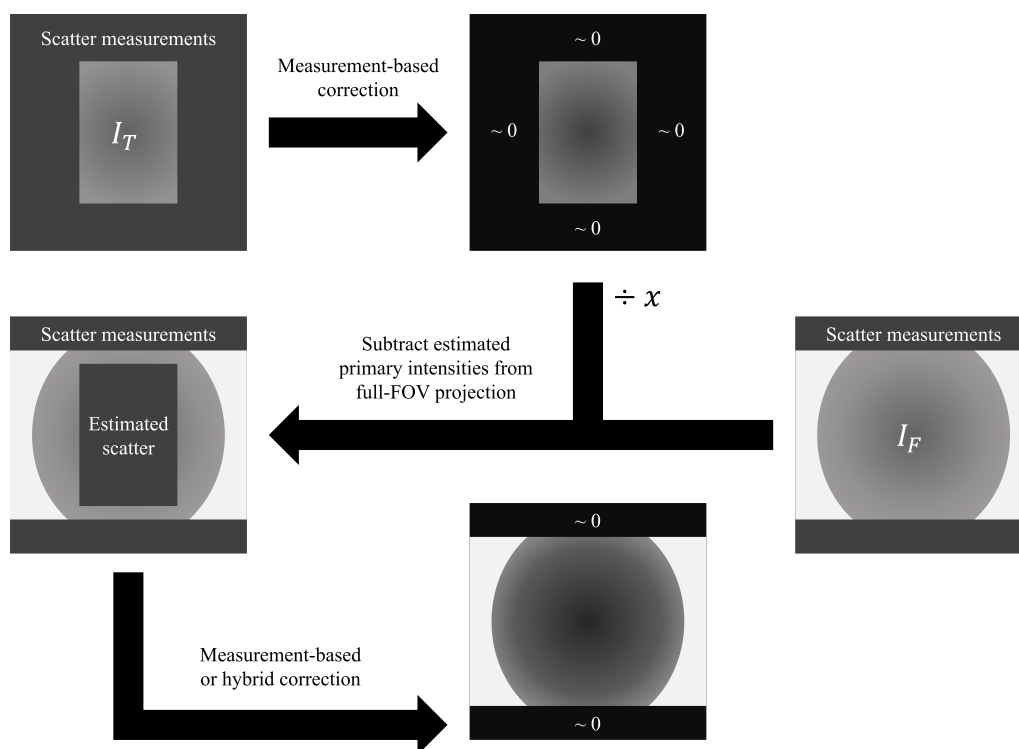


Figure 6.1 – Improved scatter correction using dual-rotation acquisitions.

6.2.2 Theoretical perspectives

6.2.2.1 Improved scatter correction

Scattered intensities have been identified as a key factor impacting low-contrast detection in C-arm CBCT (Chapter 2). However, the proposed dual-rotation approaches did not include any scatter correction method in their pipelines: indeed, we either worked with simulated, scatter-free data, or we designed experimental setups that were the most favorable in terms of scattered radiations. In clinical practice, however, larger FOV sizes may be used.

Our dual-rotation frameworks take advantage of the truncated acquisition, which, by design, rejects more scatter than the un-truncated acquisition. Hence, reconstructed images are less impacted by scatter-induced cupping artifacts. It may be possible to bring scatter reduction one step further in the context of dual-rotation, by estimating the scatter contribution in the two spins. For truncated acquisitions, a wide area of the flat-panel detector is covered by the shadow of the collimator blades. Hence, measurement-based scatter correction, such as the one proposed by [Siewerdsen et al. \(2006\)](#), may be quite efficient at providing a reasonable estimation of the scatter contribution in the truncated 2D FOV.

The same scatter reduction method may be used on full-FOV projections, by reading under the shadow of top and bottom collimator blades. However, additional constraints may be derived from the scatter correction in the truncated acquisition (Figure 6.1). Indeed, the subtraction of the scatter-corrected, truncated projections (rescaled with respect to the exposure ratio x , as defined

in Chapter 3) from the full-FOV projections provides an additional scatter estimation in the central area of the detector. This information is generally not available, unless beam stoppers are used (Ning et al., 2004; Liu et al., 2006). Note that the acquisition angles of both spins need not be exactly the same, due to the low-frequency behavior of scattered radiations. Finally, this additional scatter estimate, along with measurements in the shadow of collimator blades in the full-FOV projections, may be used in a similar, measurement-based scatter correction algorithm; it may also be used to fit parameters of model-based scatter estimation methods, which may lead to more precise, hybrid scatter correction methods.

6.2.2.2 Applications of DBP-HT- K

From a theoretical perspective, the main contribution of this work was built on our K -pass Hilbert-transformed DBP formula (Chapter 4). Contrary to analytical reconstruction formulas, which are further discretized for implementation purposes, DBP-HT- K directly takes into account the finite number of projections available through its semi-discrete formulation. A natural research axis would be to investigate the use of DBP-HT- K in an iterative framework to further reduce cone-beam artifacts (Langet et al., 2015). In addition, comparing the behavior of DBP-HT- K and FBP with respect to small lateral truncation and out-of-FOV structures, such as a bed table in C-arm CBCT acquisitions, is under investigation. It seems that performing the backprojection as a first step averages the missing information in the backprojection space, while filtering empirically extrapolated projections (Hsieh, Armstrong, et al., 2004) localizes the error near out-of-FOV structures (Figure 6.2). However, although the error due to table truncation seems stronger with FDK in the examples from Figure 6.2, the reconstructed images using DBP-HT-2 show a shift in the Hounsfield units. Yet, these first experiments tend to show the potential of DBP-HT- K to mitigate bed table artifacts in C-arm CBCT.

The applications of DBP-HT- K to ROI imaging illustrate the flexibility of the proposed approach. The framework is not limited to dual-rotation acquisitions: instead, it is general enough to handle multiple-rotation acquisitions. It is also well adapted to multiple-resolution tomography (Maaß et al., 2011). It also provides a third research axis between reconstruction methods aiming at reconstructing specific families of ROI without any additional information (namely, DBP-based methods (Noo et al., 2004) reconstructing some lines of the FOV in the case of large-object truncation), and reconstruction methods aiming at reconstructing any type of ROI using additional a priori knowledge (which include the interior tomography problem, by either using spatial a priori knowledge (Kudo et al., 2008) or sparsity-enforcing regularization terms in iterative reconstruction (Kolditz, Kyriakou, & Kalender, 2010; J.-Y. Jin et al., 2010; Lu et al., 2014)). Here, our method based on DBP-HT- K aims at reconstructing any type of ROI using a few additional full-FOV measurements with little extra cost in terms of patient dose, and without any other a priori of any kind. We believe this is an interesting alternative research axis, since a priori information may be questionable in practice.

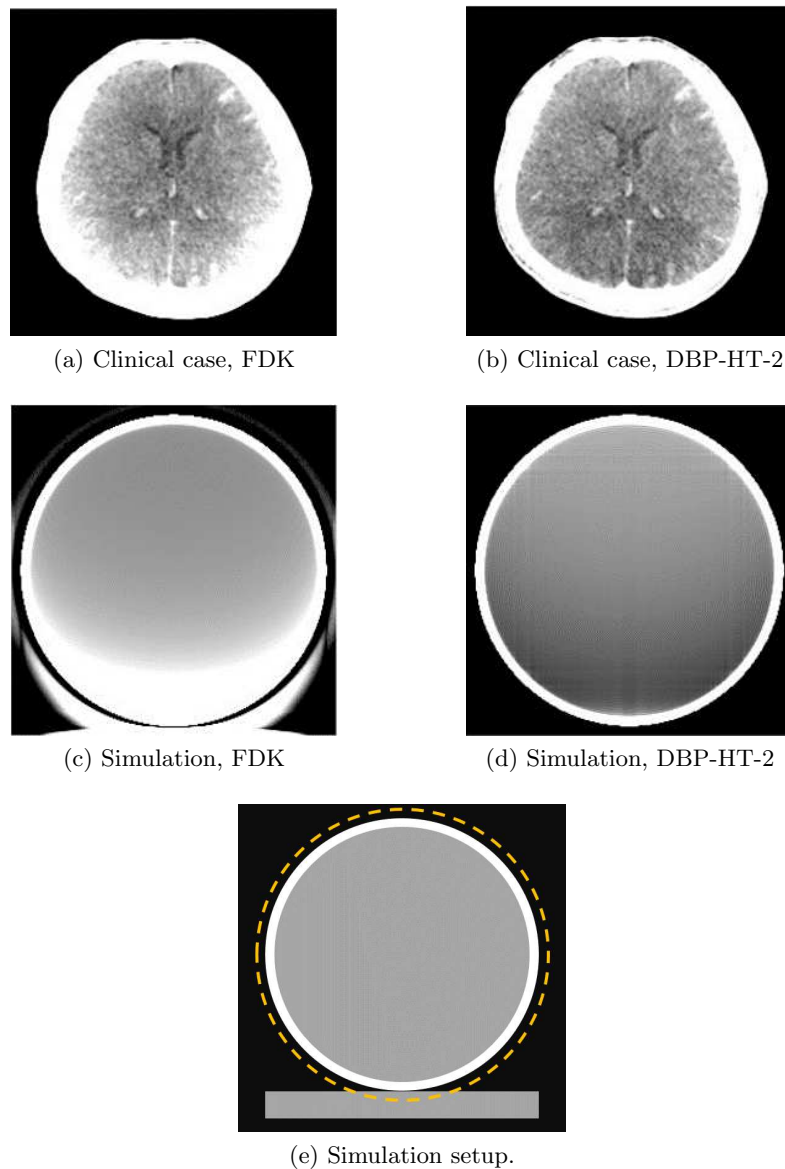


Figure 6.2 – Influence of out-of-FOV structures on FDK and DBP-HT-2. In the simulation setup (e), the FOV is shown as a dashed circle, and the bed table is partially truncated. Window width: 100 HU.

As mentioned in Section 5.1.1.2, we did not investigate wavelet-based reconstruction methods (Olson & DeStefano, 1994). However, there seems to be some connections between these approaches and our dual-rotation ROI direct reconstruction. Both use a few additional full-FOV projections to extrapolate low frequencies. On one side, coarse wavelet coefficients are estimated from full-FOV projections; on the other side, they are used to extrapolate the tails of Hilbert transforms. However, the relationships between both methods have not been explored yet; they could be the object of further works.

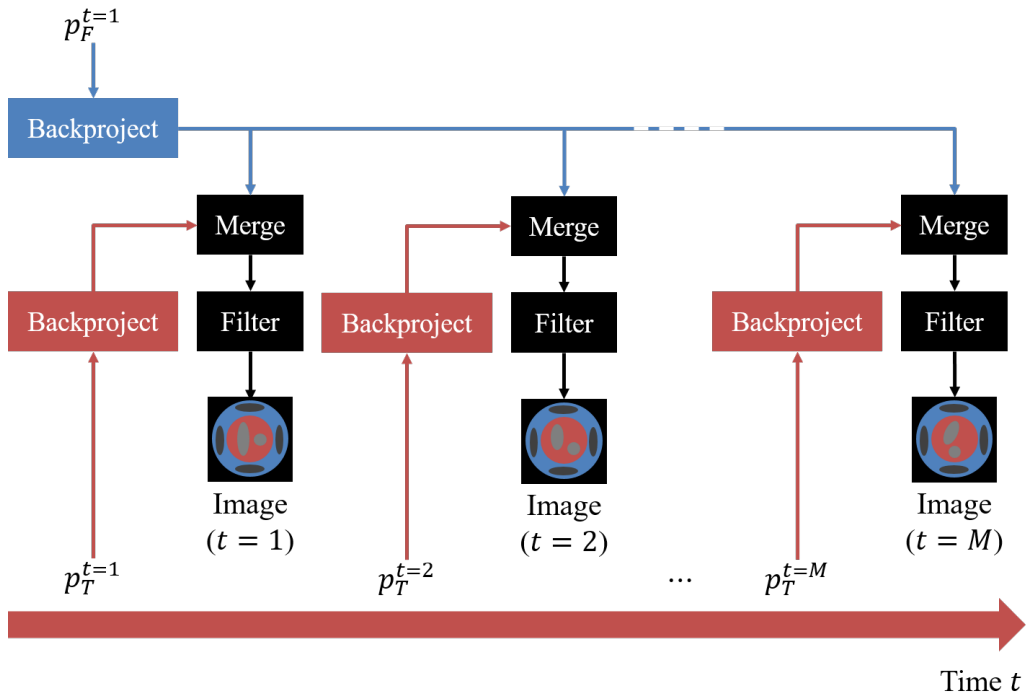


Figure 6.3 – General flowchart for dynamic ROI update. A single full-FOV spin $p_F^{t=1}$ is used to reconstruct a static background. Multiple truncated spins $p_T^{t=m}$ are acquired to update the reconstruction within the ROI.

Our direct ROI reconstruction is not limited to the context of INR procedures; image-guided therapy and breast CT may also benefit from the framework proposed in this thesis. An interesting application may also include the reconstruction of a moving ROI embedded in a static background, where the ROI would be updated as it moves, while using the same un-filtered backprojection of a single set of full-FOV data to extrapolate each acquired motion phase of the ROI (Figure 6.3). Cardiac imaging seems to be a good clinical context to investigate the feasibility of this approach (Delaney & Bresler, 1995). More generally, the flexibility of our framework may be beneficial to alternative imaging devices and modalities, especially coming from X-ray or molecular small-animal imaging as well as from non-destructive testing, where exotic designs are allowed to compensate for the peculiarities of the imaging situation, by simplifying and accelerating the reconstruction task with respect to iterative algorithms.

Proof of the fan-beam DBP-HT formula

Noo et al. (2004) define the differentiated backprojection (DBP) using parallel-beam projections as:

$$b_0^\pi(\mathbf{x}) = b_{[0,\pi]}^{(1)}(\alpha, \mathbf{x}) = \int_0^\pi p'_\theta(\mathbf{x} \cdot \boldsymbol{\theta}^\perp) d\theta. \quad (\text{A.1})$$

More generally, they define:

$$b_\phi^{\phi+\pi}(\mathbf{x}) = \frac{1}{2} \int_0^{2\pi} p'_\theta(\mathbf{x} \cdot \boldsymbol{\theta}^\perp) \operatorname{sgn}(\sin(\theta - \phi)) d\theta \quad (\text{A.2})$$

The authors derive a formula for $b_\phi^{\phi+\pi}(\mathbf{x})$ starting from fan-beam projections, that we prove in this subsection. The proof is divided into three steps:

1. Find the actual differentiated function that is integrated in the fan-beam geometry;
2. Write the derivative of a product as a sum of two terms, one of which will put the discontinuities outside of the derivative operator;
3. Calculate the integral of the second term, that will provide the additional corrective terms of the full-scan, fan-beam DBP formula.

A.1 Step 1: find the actual differentiated function

We start from the parallel-beam case and we write $\operatorname{sgn}(X) = 2 \operatorname{Hv}(X) - 1$ and Hv stands for the Heaviside function (we recall that $\operatorname{Hv}' = \delta$, the Dirac delta

function). The previous formula can be written using the Heaviside function:

$$b_{\phi}^{\phi+\pi}(\mathbf{x}) = \int_0^{2\pi} p'_{\theta}(\mathbf{x} \cdot \boldsymbol{\theta}^{\perp}) \text{Hv}(\sin(\theta - \phi)) d\theta + \underbrace{\frac{1}{2} \int_0^{2\pi} p'_{\theta}(\mathbf{x} \cdot \boldsymbol{\theta}^{\perp}) d\theta}_{=0} \quad (\text{A.3})$$

We now write the derivative as a convolution step with kernel δ' :

$$b_{\phi}^{\phi+\pi}(\mathbf{x}) = \int_0^{2\pi} \int_{-\infty}^{+\infty} p_{\theta}(u) \delta'(\mathbf{x} \cdot \boldsymbol{\theta}^{\perp} - u) \text{Hv}(\sin(\theta - \phi)) du d\theta \quad (\text{A.4})$$

We use the change of variables between fan-beam and parallel-beam variables:

$$\begin{cases} \theta &= \hat{\theta} + \arctan\left(\frac{\hat{u}}{D}\right) \\ u &= \frac{\hat{u}d}{\sqrt{\hat{u}^2 + D^2}} \end{cases} \quad (\text{A.5})$$

so that the Jacobian is equal to:

$$\left| \frac{\partial(\theta, u)}{\partial(\hat{\theta}, \hat{u})} \right| = \frac{D^2 d}{(\hat{u}^2 + D^2)^{\frac{3}{2}}} \quad (\text{A.6})$$

and (δ' being homogeneous with degree -2 , meaning that $\delta'(\lambda X) = \lambda^{-2} \delta'(X)$)

$$\delta'(\mathbf{x} \cdot \boldsymbol{\theta}^{\perp} - u) = \delta' \left(\frac{s_{\hat{\theta}}(\mathbf{x})}{\sqrt{\hat{u}^2 + D^2}} \left(\frac{D}{s_{\hat{\theta}}(\mathbf{x})} \mathbf{x} \cdot \hat{\boldsymbol{\theta}}^{\perp} - \hat{u} \right) \right) \quad (\text{A.7})$$

$$= \frac{\hat{u}^2 + D^2}{s_{\hat{\theta}}(\mathbf{x})^2} \delta' \left(\frac{D}{s_{\hat{\theta}}(\mathbf{x})} \mathbf{x} \cdot \hat{\boldsymbol{\theta}}^{\perp} - \hat{u} \right) \quad (\text{A.8})$$

where $s_{\hat{\theta}}(\mathbf{x}) = \mathbf{x} \cdot \hat{\boldsymbol{\theta}} + d$. Hence:

$$\begin{aligned} b_{\phi}^{\phi+\pi}(\mathbf{x}) &= \int_0^{2\pi} \frac{Dd}{s_{\hat{\theta}}(\mathbf{x})^2} \int_{-\infty}^{+\infty} \frac{D}{\sqrt{\hat{u}^2 + D^2}} \hat{p}_{\hat{\theta}}(\hat{u}) \text{Hv} \left(\sin \left(\hat{\theta} + \arctan \left(\frac{\hat{u}}{D} \right) - \phi \right) \right) \\ &\quad \times \delta' \left(\frac{D}{s_{\hat{\theta}}(\mathbf{x})} \mathbf{x} \cdot \hat{\boldsymbol{\theta}}^{\perp} - \hat{u} \right) d\hat{u} d\hat{\theta} \end{aligned} \quad (\text{A.9})$$

so that:

$$b_{\phi}^{\phi+\pi}(\mathbf{x}) = \int_0^{2\pi} \frac{Dd}{s_{\hat{\theta}}(\mathbf{x})^2} \underbrace{\frac{\partial}{\partial \hat{u}} \left\{ \frac{D}{\sqrt{\hat{u}^2 + D^2}} \hat{p}_{\hat{\theta}}(\hat{u}) \text{Hv} \left(\sin \left(\hat{\theta} + \arctan \left(\frac{\hat{u}}{D} \right) - \phi \right) \right) \right\}}_{\Delta(\hat{\theta})} \Big|_{\hat{u}_{\hat{\theta}}(\mathbf{x})} d\hat{\theta}, \quad (\text{A.10})$$

where $\hat{u}_{\hat{\theta}}(\mathbf{x}) = \frac{D}{s_{\hat{\theta}}(\mathbf{x})} \mathbf{x} \cdot \hat{\boldsymbol{\theta}}^{\perp}$ is the coordinate of the projection of \mathbf{x} at view $\hat{\theta}$.

A.2 Step 2: find the residual integral

We now focus on $\Delta(\hat{\theta})$:

$$\begin{aligned} \Delta(\hat{\theta}) = & \text{Hv} \left(\sin \left(\hat{\theta} + \arctan \left(\frac{\hat{u}}{D} \right) - \phi \right) \right) \frac{\partial}{\partial \hat{u}} \left(\frac{D}{\sqrt{\hat{u}^2 + D^2}} \hat{p}_{\hat{\theta}}(\hat{u}) \right) \\ & + \frac{D}{\sqrt{\hat{u}^2 + D^2}} \hat{p}_{\hat{\theta}}(\hat{u}) \underbrace{\frac{\partial}{\partial \hat{u}} \left(\text{Hv} \left(\sin \left(\hat{\theta} + \arctan \left(\frac{\hat{u}}{D} \right) - \phi \right) \right) \right)}_{\eta} \end{aligned} \quad (\text{A.11})$$

The quantity η is computed using the property $\text{Hv}' = \delta$:

$$\eta = \frac{D}{\hat{u}^2 + D^2} \cos \left(\hat{\theta} + \arctan \left(\frac{\hat{u}}{D} \right) - \phi \right) \times \delta \left(\sin \left(\hat{\theta} + \arctan \left(\frac{\hat{u}}{D} \right) - \phi \right) \right) \quad (\text{A.12})$$

Putting all together eq. (A.10), (A.11), and (A.12) we end up with:

$$\begin{aligned} b_{\phi}^{\phi+\pi}(\mathbf{x}) = & \int_0^{2\pi} \frac{Dd}{s_{\hat{\theta}}(\mathbf{x})^2} \text{Hv} \left(\sin \left(\hat{\theta} + \arctan \left(\frac{\hat{u}^*}{D} \right) - \phi \right) \right) \frac{\partial}{\partial \hat{u}} \left\{ \frac{D}{\sqrt{\hat{u}^2 + D^2}} \hat{p}_{\hat{\theta}}(\hat{u}) \right\}_{\hat{u}_{\hat{\theta}}(\mathbf{x})} d\hat{\theta} \\ & + S, \end{aligned} \quad (\text{A.13})$$

where:

$$\begin{aligned} S = & \int_0^{2\pi} \frac{D^3 d}{s_{\hat{\theta}}(\mathbf{x})^2 (\hat{u}_{\hat{\theta}}(\mathbf{x})^2 + D^2)^{\frac{3}{2}}} \hat{p}_{\hat{\theta}}(\hat{u}_{\hat{\theta}}(\mathbf{x})) \cos \left(\hat{\theta} + \arctan \left(\frac{\hat{u}_{\hat{\theta}}(\mathbf{x})}{D} \right) - \phi \right) \\ & \times \delta \left(\sin \left(\hat{\theta} + \arctan \left(\frac{\hat{u}_{\hat{\theta}}(\mathbf{x})}{D} \right) - \phi \right) \right) d\hat{\theta}. \end{aligned} \quad (\text{A.14})$$

In the next step, we will focus on the second integral S , which will translate into corrective terms for the fan-beam DBP formula. Note that the first integral still uses the Heaviside function $\text{Hv}(X)$, but can be written using the sign function $\text{sgn}(X) = 2 \text{Hv}(X) - 1$ as well:

$$\begin{aligned} & \int_0^{2\pi} \frac{Dd}{s_{\hat{\theta}}(\mathbf{x})^2} \text{Hv} \left(\sin \left(\hat{\theta} + \arctan \left(\frac{\hat{u}_{\hat{\theta}}(\mathbf{x})}{D} \right) - \phi \right) \right) \frac{\partial}{\partial \hat{u}} \left\{ \frac{D}{\sqrt{\hat{u}^2 + D^2}} \hat{p}_{\hat{\theta}}(\hat{u}) \right\}_{\hat{u}_{\hat{\theta}}(\mathbf{x})} d\hat{\theta} \\ = & \boxed{\frac{1}{2} \int_0^{2\pi} \frac{Dd}{s_{\hat{\theta}}(\mathbf{x})^2} \text{sgn} \left(\sin \left(\hat{\theta} + \arctan \left(\frac{\hat{u}_{\hat{\theta}}(\mathbf{x})}{D} \right) - \phi \right) \right) \frac{\partial}{\partial \hat{u}} \left\{ \frac{D}{\sqrt{\hat{u}^2 + D^2}} \hat{p}_{\hat{\theta}}(\hat{u}) \right\}_{\hat{u}_{\hat{\theta}}(\mathbf{x})} d\hat{\theta}} \\ & + \underbrace{\int_0^{2\pi} \frac{Dd}{s_{\hat{\theta}}(\mathbf{x})^2} \frac{\partial}{\partial \hat{u}} \left\{ \frac{D}{\sqrt{\hat{u}^2 + D^2}} \hat{p}_{\hat{\theta}}(\hat{u}) \right\}_{\hat{u}_{\hat{\theta}}(\mathbf{x})} d\hat{\theta}}_{= \int_0^{2\pi} p'_{\hat{\theta}}(\mathbf{x} \cdot \boldsymbol{\theta}^{\perp}) d\theta = 0} \end{aligned} \quad (\text{A.15})$$

The boxed line corresponds to the first integral of the full-scan, fan-beam DBP formula in (Noo et al., 2004). Writing this integral with the sign function has the benefit of actually using all the projection views, *i.e.* the full circle $[0, 2\pi]$, while the Heaviside function would only select rays whose equivalent parallel-beam angles lie in $[0, \pi]$.

A.3 Step 3: deduce the corrective terms

We then need to put our last efforts on the computation of S . We will use the following lemma.

Lemma A.3.1. *For sufficiently regular functions f and g the following holds:*

$$\int_{\mathbb{R}^n} f(\mathbf{x})\delta(g(\mathbf{x}))d\mathbf{x} = \int_{g^{-1}(0)} \frac{f(\mathbf{x})}{|\nabla g(\mathbf{x})|}d\sigma(\mathbf{x}). \quad (\text{A.16})$$

Using Lemma A.3.1 yields:

$$\begin{aligned} S = & \sum_{k: \sin(\hat{\theta}_k + \arctan(\hat{u}_{\hat{\theta}_k}(\mathbf{x})/D) - \phi) = 0} \frac{D^3 d}{s_{\hat{\theta}_k}(\mathbf{x})^2 (\hat{u}_{\hat{\theta}_k}(\mathbf{x})^2 + D^2)^{\frac{3}{2}}} \hat{p}_{\hat{\theta}_k}(\hat{u}_{\hat{\theta}_k}(\mathbf{x})) \\ & \times \cos\left(\hat{\theta}_k + \arctan\left(\frac{\hat{u}_{\hat{\theta}_k}(\mathbf{x})}{D}\right) - \phi\right) \\ & \times \left| \frac{\partial}{\partial \hat{\theta}} \left\{ \sin\left(\hat{\theta} + \arctan\left(\frac{\hat{u}_{\hat{\theta}_k}(\mathbf{x})}{D}\right) - \phi\right) \right\} \right|_{\hat{\theta} = \hat{\theta}_k}^{-1} \end{aligned} \quad (\text{A.17})$$

Now:

$$\begin{aligned} \frac{\partial}{\partial \hat{\theta}} \left\{ \sin\left(\hat{\theta} + \arctan\left(\frac{\hat{u}_{\hat{\theta}}(\mathbf{x})}{D}\right) - \phi\right) \right\} &= \cos\left(\hat{\theta} + \arctan\left(\frac{\hat{u}_{\hat{\theta}}(\mathbf{x})}{D}\right) - \phi\right) \\ & \times \left(1 + \frac{D}{\hat{u}_{\hat{\theta}}^2 + D^2} \frac{\partial \hat{u}_{\hat{\theta}}(\mathbf{x})}{\partial \hat{\theta}} \right) \end{aligned} \quad (\text{A.18})$$

and:

$$\begin{aligned} \frac{\partial \hat{u}_{\hat{\theta}}(\mathbf{x})}{\partial \hat{\theta}} &= \frac{\partial}{\partial \hat{\theta}} \left(\frac{D(-x_1 \sin \hat{\theta} + x_2 \cos \hat{\theta})}{x_1 \cos \hat{\theta} + x_2 \sin \hat{\theta} + d} \right) = \frac{D}{s_{\hat{\theta}}(\mathbf{x})} (-\mathbf{x} \cdot \hat{\boldsymbol{\theta}}) - \frac{\hat{u}^{*2}}{D} \\ &= \frac{Dd}{s_{\hat{\theta}}(\mathbf{x})} - \frac{\hat{u}_{\hat{\theta}}^2 + D^2}{D}. \end{aligned} \quad (\text{A.19})$$

Hence:

$$\begin{aligned} 1 + \frac{D}{\hat{u}_{\hat{\theta}}(\mathbf{x})^2 + D^2} \frac{\partial u^*}{\partial \hat{\theta}} &= 1 + \frac{D}{\hat{u}_{\hat{\theta}}(\mathbf{x})^2 + D^2} \left(\frac{Dd}{s_{\hat{\theta}}(\mathbf{x})} - \frac{\hat{u}_{\hat{\theta}}(\mathbf{x})^2 + D^2}{D} \right) \\ &= \frac{D^2 d}{s_{\hat{\theta}}(\mathbf{x}) (\hat{u}_{\hat{\theta}}(\mathbf{x})^2 + D^2)} \end{aligned} \quad (\text{A.20})$$

Putting together eq. (A.17), (A.18) and (A.20), we end up with:

$$S = \sum_{k: \sin\left(\hat{\theta}_k + \arctan(\hat{u}_{\hat{\theta}_k}(\mathbf{x})/D) - \phi\right) = 0} \frac{D}{s_{\hat{\theta}_k}(\mathbf{x}) \sqrt{\hat{u}_{\hat{\theta}_k}^2 + D^2}} \hat{p}_{\hat{\theta}_k}(\hat{u}_{\hat{\theta}_k}) \times \operatorname{sgn} \left(\cos \left(\hat{\theta}_k + \arctan \left(\frac{\hat{u}_{\hat{\theta}_k}}{D} \right) - \phi \right) \right). \quad (\text{A.21})$$

Using the Thales theorem (see Figure 2.17a):

$$\|\mathbf{x} - \boldsymbol{\xi}\| = \frac{s_{\hat{\theta}}(\mathbf{x})}{D} \sqrt{\hat{u}_{\hat{\theta}}(\mathbf{x})^2 + D^2}, \quad (\text{A.22})$$

so that:

$$S = \sum_{k: \sin\left(\hat{\theta}_k + \arctan(\hat{u}_{\hat{\theta}_k}(\mathbf{x})/D) - \phi\right) = 0} \frac{p_{\hat{\theta}_k}(\hat{u}_{\hat{\theta}_k}(\mathbf{x}))}{\|\mathbf{x} - \boldsymbol{\xi}_{\hat{\theta}=\hat{\theta}_k}\|} \times \operatorname{sgn} \left(\cos \left(\hat{\theta}_k + \arctan \left(\frac{\hat{u}_{\hat{\theta}_k}}{D} \right) - \phi \right) \right). \quad (\text{A.23})$$

Because the equation:

$$\sin \left(\hat{\theta}_k + \arctan \left(\frac{\hat{u}_{\hat{\theta}_k}(\mathbf{x})}{D} \right) - \phi \right) = 0, \quad (\text{A.24})$$

has only two solutions $\hat{\theta}_1$ and $\hat{\theta}_2$, which lie on the same diameter of the trigonometric circle, we end up with:

$$S = \frac{\hat{p}_{\hat{\theta}_1}(\hat{u}_{\hat{\theta}_1}(\mathbf{x}))}{\|\mathbf{x} - \boldsymbol{\xi}_{\hat{\theta}=\hat{\theta}_1}\|} - \frac{\hat{p}_{\hat{\theta}_2}(\hat{u}_{\hat{\theta}_2}(\mathbf{x}))}{\|\mathbf{x} - \boldsymbol{\xi}_{\hat{\theta}=\hat{\theta}_2}\|}. \quad (\text{A.25})$$

Summing the two boxed equations of this proof provides the full-scan, fan-beam DBP formula of [Noo et al. \(2004\)](#).

Publications

B.1 Journals (with review committee)

Langet, H., Riddell, C., **Reshef, A.**, Troussset, Y., Tenenhaus, A., Lahalle, E., Fleury, G., & Paragios, N. (2015). Compressed-sensing-based content-driven hierarchical reconstruction: Theory and application to C-arm cone-beam computed tomography. *Medical Physics*, *42*(9), pp. 5222–5237.

Reshef, A., Riddell, C., Troussset, Y., Ladjal, S., & Bloch, I. (2017). Dual-rotation C-arm cone-beam computed tomography to increase low-contrast detection. *Medical Physics*, *44*(9), pp. e164-e173.

B.2 Conferences (with review committee)

Reshef, A., Riddell, C., Troussset, Y., Ladjal, S., & Bloch, I. (2016). Dual-rotation C-arm cone-beam computed tomography to increase low-contrast resolution. *4th International Conference on Image Formation in X-Ray Computed Tomography*. Bamberg, Germany.

Reshef, A., Riddell, C., Troussset, Y., Ladjal, S., & Bloch, I. (2017). Reconstruction tomographique 2D : une nouvelle méthode de rétro-projection filtrée. *Actes du XXVIème Colloque GRETSI*. Juan-les-Pins, France.

Reshef, A., Riddell, C., Troussset, Y., Ladjal, S., & Bloch, I. (2018). Divergent-beam backprojection-filtration formula with applications to region-of-interest imaging. *5th International Conference on Image Formation in X-Ray Computed Tomography*. Salt Lake City, USA.

Reshef, A., Nikoukhah, T., Riddell, C., Troussset, Y., Ladjal, S., & Bloch, I. (2018). Parallel-beam ROI reconstruction with differentiated backprojection and

angularly subsampled complementary sinograms. *5th International Conference on Image Formation in X-Ray Computed Tomography*. Salt Lake City, USA.

B.3 Invited talk

Reshef, A., Riddell, C., Trouset, Y., Ladjal, S., & Bloch, I. (2018). Divergent-beam backprojection-filtration formula with applications to region-of-interest imaging. S³: Signal Seminar of Université Paris-Saclay, Gif-sur-Yvette, France.

B.4 Supervised Master's theses

Pierre Meriguet (2016). Analytical projection and backprojection operators in divergent-beam geometries. Supélec.

Alexiane Pasquier (2017). Neural net-based scatter correction for interventional C-arm CBCT. Grenoble INP – Phelma.

Tina Nikoukhah (2017). Parallel-beam region-of-interest direct reconstruction with dual-rotation C-arm cone-beam computed tomography. Grenoble INP – ENSIMAG.

Acquisitions et reconstructions tomographiques par rotation double sur arceau interventionnel pour la détection des faibles contrastes en imagerie des tissus mous de la tête

C.1 Contexte clinique

La neuroradiologie interventionnelle ([Wible, 2017](#)) traite des pathologies vasculaires du cerveau de manière minimalement invasive par voie endovasculaire. Des outils sont insérés directement dans le réseau vasculaire, ou des aiguilles sont insérées à travers le patient pour atteindre le lieu de l'intervention. Cette discipline dresse un pont entre les étapes de diagnostic pré-opératoire et les procédures chirurgicales, qui sont plus invasives pour le patient.

Les pathologies traitées concernent principalement :

1. La restauration du flux sanguin dans des vaisseaux dont la lumière est réduite suite à des dépôts de plaques lipidiques (on parle de vaisseaux sténosés). Un ballon est apporté jusqu'au lieu de la sténose, gonflé pour compresser les plaques, puis retiré du réseau artériel (angioplastie). Une prothèse tubulaire (stent) peut être enroulée autour du ballon, puis déployé au gonflement de ce-dernier; il reste alors en place une fois le ballon retiré.
2. La restauration du flux sanguin dans des vaisseaux obstrués par un caillot ou thrombus (on parle d'accident vasculaire ischémique provoqué par une thrombose). Un outil est introduit dans le réseau artériel et amené jusqu'au thrombus; celui-ci est alors capturé par l'outil et ramené hors du patient (thrombectomie mécanique). La thrombectomie mécanique est maintenant

la procédure recommandée par l'Association Américaine des Accidents Vasculaires Cérébraux ([Powers et al., 2018](#)).

3. L'isolation d'une cavité issue d'un gonflement anormal de la paroi d'un vaisseau (anévrisme). Celle-ci est souvent obtenue en remplissant la cavité par des "coils" métalliques à mémoire de forme, qui bloquent le flux sanguin dans l'anévrisme. Le placement d'un stent dans le vaisseau porteur complète souvent la procédure.
4. La condamnation de connexions anormales entre les réseaux artériel et veineux (malformation artério-veineuse ou MAV). Un produit d'embolisation est injecté au niveau de l'artère alimentant la malformation, afin de bloquer l'artère à cet endroit et de réduire ainsi le flux sanguin dans la MAV.

Le développement des interventions minimallement invasives est rendu possible par le degré de maturité des technologies d'imagerie utilisées à des fins pré-opératoires (échographie, résonance magnétique, tomодensitométrie) et per-opératoires (arceau interventionnel rayon X). En imagerie pré-opératoire, la tomодensitométrie (ou "computed tomographie", notée CT) reste la modalité de référence pour l'imagerie des tissus mous du cerveau ; elle produit des images tridimensionnelles, et c'est un excellent compromis entre le coût de l'examen, le temps consacré à celui-ci, et la résolution en contraste obtenue par les scanners CT.

L'arceau interventionnel (ou "C-arm") a d'abord été conçu pour de l'imagerie rayon X bidimensionnelle temps réel. Cependant, il est possible de fournir des images tridimensionnelles de l'anatomie imagée avec le même système. On parle alors de tomодensitométrie (ou tomographie) conique sur arceau interventionnel, ou CBCT ("cone-beam CT") sur arceau interventionnel. Si le CBCT sur arceau interventionnel est utilisé en routine clinique pour l'imagerie vasculaire ([Anxionnat et al., 1998](#)), son application à l'imagerie des tissus mous, qui permettrait d'obtenir une information clinique sans transférer le patient d'une salle interventionnelle (où se trouve l'arceau) à une salle d'imagerie diagnostique (où se trouve le scanner CT), est encore minoritaire. En effet, les images reconstruites manquent encore de précision aux niveaux de contrastes des tissus mous du cerveau.

L'imagerie des tissus mous est indispensable pour certifier qu'aucun saignement n'apparaît à l'issue d'une procédure de neuroradiologie interventionnelle. Elle est aussi nécessaire en tant qu'imagerie diagnostique et imagerie de planification du geste interventionnel, dans le cas des accidents vasculaires ischémiques, afin d'évaluer la présence et l'étendue d'une zone d'infarct dans le cerveau.

Ce travail de thèse contribue à réduire l'écart entre l'imagerie CT diagnostique et le CBCT sur arceau interventionnel, en termes d'imagerie des tissus mous du cerveau. En prenant le CT diagnostic comme notre modalité de référence, nous étudions les particularités de la chaîne d'imagerie 3D du CBCT sur arceau interventionnel, qui s'appuie sur la chaîne d'imagerie 2D du système. Nous identifions les principaux facteurs d'influence sur la résolution en contraste du CBCT sur arceau : le rayonnement diffusé, l'échantillonnage, et la dose. Sans modification

matérielle du système, nous proposons de combiner deux jeux d’acquisition rotationnelle, que nous appelons une acquisition par rotation double, et que nous utilisons pour améliorer la détection des faibles contrastes. Nous imitons ainsi la modulation de faisceau obtenue en CT diagnostic par le biais de filtres physiques dits “bow-tie” (en noeud papillon).

En laissant une grande flexibilité sur les paramètres d’acquisition, nous portons notre effort sur l’étape algorithmique de reconstruction tomographique. Nous proposons une stratégie de reconstruction itérative fondée sur de précédents travaux (Langet et al., 2015), capable de gérer à la fois la reconstruction d’un volume entier, et la reconstruction de régions d’intérêt (“region-of-interest”, ou ROI) dans le contexte d’acquisitions par rotation double (Reshef et al., 2016, 2017a). En revisitant les méthodes classiques de reconstruction directe, nous proposons également une reconstruction directe alternative pour les acquisitions par rotation double, qui mélangent astucieusement l’information des deux jeux de données (Reshef et al., 2017b; Reshef, Riddell, et al., 2018; Reshef, Nikoukhah, et al., 2018). Nous observons que sans rien changer à l’approche proposée, celle-ci est également adaptée à l’imagerie des faibles contrastes dans le contexte de l’imagerie de régions d’intérêt.

C.2 Imagerie sur arceau interventionnel

C.2.1 Généralités et imagerie 2D

Un arceau interventionnel est un système d’imagerie rayon X. Un bras ouvert et rigide en forme de “C”, appelé le “C-arm” en anglais, porte deux masses à chaque extrémité : d’un côté, un tube à rayon X produit et envoie des photons X ; de l’autre, un détecteur reçoit les rayons ayant traversé l’anatomie imagée. L’arceau laisse accès au patient, allongé sur une table pendant la procédure interventionnelle. L’arceau peut être mobile, tenu par un bras robotisé, tenu par un plafonnier, ou fixé au sol. En neuroradiologie interventionnelle, des systèmes biplans combinant un arceau fixé au sol et un arceau fixé au plafond (les arceaux frontal et latéral, respectivement), sont utilisés, en raison de la complexité de l’anatomie de l’arbre vasculaire dans la tête.

Historiquement, l’arceau interventionnel est utilisé comme une caméra vidéo rayon X. Le faisceau de rayons X interagit avec la matière traversée, et l’image formée au détecteur résulte de l’atténuation de ce faisceau. Le tube à rayon X produit des photons selon un spectre d’énergie, et pour une énergie donnée (paramétrée en kilovolts ou kV), l’intensité $I(\text{kV})$ après interaction le long d’une ligne \mathcal{L} est donnée par la loi de Beer-Lambert :

$$I(\text{kV}) = I_0(\text{kV})e^{-\int_{\mathcal{L}} \mu(\text{kV}, x) dx}, \quad (\text{C.1})$$

où $I_0(\text{kV})$ est l’intensité en sortie du tube (ou intensité dans l’air), et $\mu(\text{kV}, x)$ résume en chaque point de l’espace x et pour un niveau d’énergie kV, l’atténuation locale de l’intensité résultant des interactions multiples avec la matière. On appelle $\mu(\text{kV})$ le coefficient linéaire d’atténuation; il est caractéristique d’un matériau. On notera que I_0 est linéaire avec le produit du courant du tube par

le temps d'exposition, exprimé en milli-ampères-secondes (mAs), et non-linéaire avec la différence de potentiel appliquée entre l'anode et la cathode du tube.

A l'autre bout de la chaîne image, un détecteur de type panneau plan à conversion indirecte est utilisé; celui-ci est constitué d'un cristal appelé scintillateur, qui permet la conversion des photons X en photons lumineux. Ces photons lumineux excitent une matrice de photodiodes, qui convertissent le signal lumineux en un signal électrique. Enfin, une conversion analogique-numérique (CAN), aussi appelée étape de quantification, convertit ce signal électrique en un signal numérique.

Avec cette technologie, le détecteur mesure l'intensité moyenne par rapport à la distribution du spectre du rayons X du tube. Un pixel du détecteur mesure non seulement l'intensité du rayon atténué provenant directement de la source (aussi appelé intensité primaire), mais aussi des intensités venant de directions aléatoires dues au phénomène de diffusion élastique et inélastique (effet Compton).

C.2.2 Imagerie 3D

L'arceau interventionnel est utilisé comme une caméra vidéo rayons X, permettant de suivre en temps réel la navigation d'outils dans le réseau vasculaire du patient dans des images projectives. Il est également possible, en laissant l'arceau acquérir une collection de projections à différentes positions, de reconstruire l'image tridimensionnelle de l'anatomie ainsi imagée. Typiquement, les arceaux interventionnels acquièrent une collection de projections selon une trajectoire circulaire couvrant 180° plus l'angle du faisceau divergent, soit environ 200° (trajectoire dite circulaire "short-scan", par opposition à une trajectoire circulaire couvrant 360°). On parle d'imagerie tomographique.

En géométrie parallèle 2D, l'inversion du problème de reconstruction tomographique se fonde sur le théorème coupe-projection, qui relie la transformée de Fourier 1D d'une projection en densité (on parle de projection en densité lorsqu'on s'intéresse à $p = \log(I_0) - \log(I)$), à une ligne de la transformée de Fourier 2D de l'image à reconstruire. On obtient alors une inversion analytique du problème tomographique, aussi appelée formule de rétro-projection filtrée ("filtered backprojection" ou FBP) :

$$f = \frac{1}{2} \int_0^{2\pi} \mathcal{B}_\theta \mathcal{D}[p_\theta] d\theta = \frac{1}{2} \int_0^{2\pi} \mathcal{D}[p_\theta](u_\theta) d\theta, \quad (\text{C.2})$$

où $u_\theta(\mathbf{x})$ est la coordonnée de la projection du point \mathbf{x} sur le détecteur, \mathcal{D} est le filtre rampe ($\mathcal{D}[q]$ revient à multiplier par $|\rho|$ la transformée de Fourier de q), et \mathcal{B}_θ est l'opérateur de rétro-projection.

Un changement de variable permet, à partir de la formule précédente, d'en déduire une formule de rétro-projection filtrée en géométrie divergente 2D (aussi connue sous le nom de géométrie en éventail). En revanche, il n'existe pas d'inversion exacte pour la géométrie divergente 3D ou géométrie conique; mais la formule de Feldkamp-Davis-Kress (FDK, (Feldkamp et al., 1984)), qui est une extension directe de FBP en géométrie divergente 2D, est une formule raisonnable

de reconstruction approchée. L'image obtenue par FDK est :

$$f_{\text{FDK}} = \frac{1}{2} \int_0^{2\pi} \frac{D^2}{s_{\hat{\theta}}^2} \hat{\mathcal{B}}_{\hat{\theta}} \mathcal{D} [\tilde{p}_{\hat{\theta}}(\cdot, \hat{v}_{\hat{\theta}})] d\hat{\theta}, \quad (\text{C.3})$$

où :

$$\tilde{p}_{\hat{\theta}}(\hat{u}, \hat{v}) = \frac{d}{D} \cdot \frac{D}{\sqrt{\hat{u}^2 + \hat{v}^2 + D^2}} \hat{p}_{\hat{\theta}}(\hat{u}, \hat{v}). \quad (\text{C.4})$$

Dans la suite, la formulation semi-discrète, consistant à considérer un nombre fini d'échantillons angulaires, sera utile pour l'obtention d'une formule originale de reconstruction directe restant intrinsèquement une formule vue par vue. Dans cette formulation, l'image FDK obtenue à partir de N échantillons équirépartis sur 2π est :

$$f_{\text{FDK},N} = \frac{1}{2} \sum_{\hat{\theta} \in \Theta} \frac{D^2}{s_{\hat{\theta}}^2} \hat{\mathcal{B}}_{\hat{\theta}} \mathcal{D} [\tilde{p}_{\hat{\theta}}(\cdot, \hat{v}_{\hat{\theta}})] \Delta\theta = \frac{\pi}{N} \sum_{\hat{\theta} \in \Theta} \frac{D^2}{s_{\hat{\theta}}^2} \hat{\mathcal{B}}_{\hat{\theta}} \mathcal{D} [\tilde{p}_{\hat{\theta}}(\cdot, \hat{v}_{\hat{\theta}})], \quad (\text{C.5})$$

où :

$$\Theta = \left\{ \theta_i = \left(i - \frac{1}{2} \right) \Delta\theta, i = 1, \dots, N \right\}, \text{ where } \Delta\theta = \frac{2\pi}{N}. \quad (\text{C.6})$$

En reconstruction itérative, le problème tomographique est directement exprimé en un problème complètement discret ; ici, nous minimiserons une énergie de la forme (Langet et al., 2015) :

$$f_{\text{IFDK}} = \underset{f}{\operatorname{argmin}} \left\{ \frac{1}{2} (\mathcal{R}f - p)^T \mathcal{D} (\mathcal{R}f - p) + \chi(f) \right\}, \quad (\text{C.7})$$

où \mathcal{R} est l'opérateur de projection, et \mathcal{D} est le filtre rampe, qui est diagonal dans l'espace de Fourier, et inclus dans la forme quadratique qui compose le terme d'attache aux données. $\chi(f)$ est une régularisation convexe qui peut être ou non différentiable.

C.2.3 Qualité image des faibles contrastes

Pour quantifier les performances de l'arceau interventionnel en terme de résolution en contraste, nous utilisons un fantôme d'assurance qualité appelé le Catphan[®] (Goodenough, 2012). Le module CTP 515 du Catphan[®] (Figure 2.19c) est constitué d'un cylindre équivalent à de l'eau, avec des inserts de contrastes cylindriques de différents diamètres. Les contrastes relatifs des inserts sont 1%, 0.5% et 0.3%. Leurs diamètres varient de 2 mm à 15 mm. Les diamètres des inserts centraux (dits "subslices") varient de 3 mm to 9 mm.

Une analyse système le long de la chaîne image 3D de l'arceau interventionnel a permis d'identifier les principaux facteurs influant sur la qualité image des faibles contrastes (Figure 2.22). Il s'agit du bruit quantique, des non-idéalités du détecteur (dérives de gain, conversion analogique-numérique), de la qualité du faisceau de rayons X (polychromaticité du faisceau) et de la dynamique exponentielle de son atténuation (compensée en scanner diagnostic par des filtres

“bow-tie”), du rayonnement diffusé (qui est un facteur essentiel de perte de résolution en contraste, et qui est donc forcément corrigé sur un arceau interventionnel), et des problématiques d’échantillonnage (champ de vue tronqué, nombre de vues acquises).

De cette analyse, nous déduisons que les principaux facteurs d’influence sont :

- Le rayonnement diffusé, qui doit être rejeté le plus possible, ou, à défaut, corrigé ;
- L’échantillonnage, puisque la troncation doit être évitée le plus possible, et le nombre de vues rester aussi fin que possible ;
- La conversion analogique-numérique, qui semble plus grossière sur arceau interventionnel qu’elle ne l’est sur un scanner diagnostic ;
- La dose (et donc le bruit), puisque nous ne disposons pas d’un filtre “bow-tie” sur les arceaux interventionnels.

Nous avons laissé le côté la problématique du mouvement de l’objet pendant l’acquisition du spin : en-dehors des vibrations mécaniques de l’arceau, dont on suppose qu’une calibration géométrique a pu les prendre en compte à la reconstruction, nous supposons qu’il n’y a pas d’autre mouvement parasite dans notre étude.

C.3 Bow-tie virtuel en tomographie conique rayons X

C.3.1 Une question de bruit

Si, comme indiqué dans la section précédente, les principaux éléments influant sur la détection des faibles contrastes sont le diffusé, l’échantillonnage, la quantification et la dose, nous pouvons restreindre l’analyse aux deux derniers éléments, et via cette analyse, montrer que la dose est un élément plus déterminant que la quantification lorsqu’il s’agit de visualiser les faibles contrastes en 3D.

Pour réduire le problème, nous utilisons le module de faibles contrastes du fantôme Catphan[®] (CTP 515), et nous acquérons des spins en environnement contrôlé : pas de collimation latérale, un champ de vue vertical réduit à son minimum pour réduire la contribution du diffusé dans l’image, observation des coupes centrales, écartant l’influence des artefacts coniques. Une pré-correction du durcissement de faisceau dû à l’eau permet de s’affranchir des enjeux de la polychromaticité des rayons X. Enfin, les images sont acquises à la plus faible vitesse de rotation, aboutissant à un fort échantillonnage angulaire pour une reconstruction tomographique plus précise. Ne restent alors que la quantification et la dose comme points ouverts.

L’étape de quantification consiste à définir une subdivision de l’axe des réels $-\infty = q_{-1} < q_0 < \dots < q_B < q_{B+1} = +\infty$, et à assigner une valeur quantifiée Q_i à chaque intervalle $[q_{i-1}, q_i[$. On peut donc la résumer à une fonction \mathcal{Q} définie de la manière suivante :

$$\mathcal{Q}(I) = \sum_{i=0}^{B+1} Q_i \mathbb{1}_{[q_{i-1}, q_i[}(I). \quad (\text{C.8})$$

Afin de ne pas quantifier au-delà du bruit statistique, une rampe quadratique peut être utilisée (on rappelle que la variance du bruit au détecteur est proportionnelle à l'intensité du faisceau de rayons X). En réalité, afin de corriger en offsets les pixels du détecteur, il est nécessaire de lire précisément le panneau à vide (en absence de rayon X), de sorte qu'une rampe linéaire-quadratique est utilisée en pratique.

Nous simulons des projections analytiques de disques avec des inserts de contrastes similaires à ceux du Catphan[®] CTP 515, bruitées, dans une géométrie 2D en éventail. Nous générons ensuite des projections quantifiées sur 850 niveaux de quantifications répartis sur une dynamique de 14 bits (Figure 3.3). Grâce au processus d'accumulation de projections bruitées, on remarque que les images reconstruites avec FBP diffèrent peu selon qu'elles ont été quantifiées ou non sur 850 niveaux. En revanche, les faibles contrastes et les inserts centraux sont bien plus facilement identifiables lorsque quatre reconstructions sont moyennées. En revanche, réaliser une acquisition à quatre fois la dose originale demanderait une rampe de quantification qui aille quatre fois plus haut ; si cela n'est pas le cas, une saturation numérique intervient, créant une non-uniformité du fond de l'image inacceptable en pratique.

Ainsi, il s'agirait davantage d'un problème de dose, que d'un problème de quantification. Cette hypothèse est confirmée par des expériences sur données réelles acquises sur un système biplan IGS 630. Le Catphan[®] CTP 515 a été acquis quatre fois à (76 kVp, 3.4 mAs) avec 0.3 mm de filtration de cuivre au niveau du tube, et avec un détecteur de 30 cm de largeur. Afin d'utiliser une dose quatre fois supérieure, un spectre différent, de 120 kVp, a été utilisé pour acquérir un cinquième spin, tous les autres paramètres étant gardés fixes par ailleurs. L'influence de différents spectres de rayons X a été négligée ici. L'algorithme FDK avec des poids de Parker a été utilisé pour reconstruire les images.

C.3.2 Bow-tie virtuel par rotation double

La flexibilité mécanique d'un arceau interventionnel ne permet pas de rejeter efficacement tout le rayonnement diffusé, et le coût d'un filtre bow-tie dédié à l'imagerie des tissus mous de la tête, rapporté au nombre d'acquisitions nécessaires, n'est pas une option aujourd'hui. Il y a donc un intérêt à concevoir une acquisition à exposition non uniforme conduisant à de meilleures mesures à moindre dose au patient.

Nous proposons une acquisition double définie comme suit. Un spin est plein champ ("full-FOV", indexé par F) et un spin est tronqué (indexé par T), et n'imagine qu'un champ de vue 3D inclus dans le champ de vue 3D du spin plein champ. Le spin plein champ est acquis à faible dose, ce qui évite d'irradier inutilement le patient, tandis que le spin tronqué est, lui, acquis à une dose plus élevée pour atteindre une exposition cible au centre de l'objet, où l'épaisseur traversée par les rayons X est plus importante.

Nous concevons cette acquisition double de sorte qu'elle puisse être aussi flexible que possible, aussi nous nous donnons deux degrés de liberté :

- (i) L'ouverture du champ de vue tronqué : nous notons t , $0 < t \leq 1$, le niveau

de réduction du champ de vue par rapport au champ non tronqué.

- (ii) Le ratio d'intensités entre les deux acquisitions : si I_0^F est l'intensité dans l'air correspondant à l'exposition au centre de l'objet obtenue avec le spin plein champ, et si I_0^T est l'intensité du spin tronqué, nous notons $x = I_0^T/I_0^F$, de sorte que l'exposition au centre de l'objet est égale à $(1+x)I_0^F$ dans une acquisition double. En travaillant aux mêmes énergies pour les deux acquisitions, x est simplement un ratio des mAs.

Pour simuler un bow-tie, nous choisissons $x \geq 1$. Nous définissons la réduction de dose d par rapport à une acquisition simple plein champ apportant le même niveau de dose au centre de l'objet comme suit :

$$d = \frac{I_0^F + I_0^T}{I_0^F + t \cdot I_0^T} = \frac{1+x}{1+tx}. \quad (\text{C.9})$$

Nous définissons les contributions relatives de chaque spin à la dose totale via les poids suivants :

$$\alpha_F = \frac{I_0^F}{I_0^F + t \cdot I_0^T} = \frac{1}{1+tx}, \quad \alpha_T = 1 - \alpha_F. \quad (\text{C.10})$$

Nous résolvons le problème de minimisation suivant :

$$\operatorname{argmin}_f \left\{ \sum_{n \in \{F, T\}} \alpha_n \mathcal{Q}_n(f) + \chi(f) \right\}, \quad (\text{C.11})$$

où $\chi(f) = \lambda \|\nabla f\|^2$, et le terme d'attache aux données est une combinaison convexe des formes quadratiques ($n \in \{F, T\}$) :

$$\mathcal{Q}_n(f) = \frac{1}{2} (\mathcal{R}_n f + \log(I_n))^T \mathcal{D}_n (\mathcal{R}_n f + \log(I_n)), \quad (\text{C.12})$$

où \mathcal{R}_F (resp. \mathcal{R}_T) est l'opérateur de projection pour la géométrie non tronquée (resp. tronquée), et \mathcal{D}_F (resp. \mathcal{D}_T) est le filtre rampe pour les signaux non tronqués (resp. tronqués). Un schéma itératif de type forward-backward splitting (Langet et al., 2015) suffit à résoudre ce problème.

Ecrire ce problème de minimisation directement en utilisant $\log(I_n)$ permet de s'affranchir de la connaissance de l'intensité dans l'air, qui se transforme en un offset après application du logarithme, et qui est annulé par la rampe intégrée à la forme quadratique. Ceci est vrai si le filtre n'est pas implémenté comme la transformée de Fourier d'un noyau fini, ce qui est recommandé en pratique, mais aboutit à une valeur non nulle de la composante continue.

Nous écrivons donc plutôt $\mathcal{D}_F = \mathcal{H} \partial_u$, où ∂_u est un dérivateur, et \mathcal{H} est la transformée de Hilbert. Afin d'assurer une transition lisse aux bords de $\partial_u(\log(I_T))$, une fenêtre de Hanning est appliquée avant de calculer la transformée de Hilbert, de sorte que nous avons : $\mathcal{D}_T = \mathcal{H} W \partial_u$, où W est l'opérateur d'apodisation de Hanning.

Les expériences faites sur le Catphan[®] 515 sont décrites en détail en Section 3.2.3. En guise de métrique de qualité image, nous avons choisi le ratio

contraste-à-bruit (“contrast-to-noise ratio” ou CNR), que nous avons appliqué aux inserts de contrastes du module rappelés dans le Tableau 3.2. Nous montrons qu’une acquisition double améliore la détection de faibles contrastes et réduit, par conception, la contribution du diffusé dans l’image reconstruite. L’apodisation, dans le filtre rampe utilisée sur le spin tronqué, est nécessaire pour récupérer une uniformité souhaitée dans l’image finale. Enfin, une régularisation aussi simple que celle proposée suffit à fournir une image de bonne qualité ; en particulier, cette régularisation ne modifie pas fondamentalement la texture de l’image reconstruite, ce qui est souvent le cas avec des régularisations plus avancées de type variation totale.

La conséquence de cette approche par rotation double est bien sûr qu’elle requiert deux fois le temps d’une acquisition standard : en réalité, elle demande même davantage, à cause de la complexité de calcul requise par la reconstruction itérative, qui augmente la complexité de la solution proposée.

C.4 Une reconstruction directe pour le bow-tie virtuel

Une approche par reconstruction itérative a été proposée parce qu’un mélange direct des projections n’était pas envisageable, dans la mesure où nous n’imposons pas de contrainte sur la répétabilité des positions angulaires des vues d’une acquisition à l’autre. Mélanger deux images reconstruites indépendamment nécessiterait de savoir reconstruire avec suffisamment de précision le spin tronqué, ce qui n’est pas possible sans autre a priori (Natterer, 2001).

C.4.1 Rétro-projection différenciée à K passes de Hilbert

Nous proposons ici une formule de filtrage des rétro-projections (en anglais, “backprojection-filtration”, ou BPF), que nous appelons la formule de rétro-projection différenciée à K passes de Hilbert (DBP-HT- K), en géométrie parallèle. Elle est équivalente à la rétro-projection différenciée à une passe de Hilbert de la littérature (Noo et al., 2004) lorsque $K = 1$, et au FBP semi-discret lorsque K est égal au nombre de projections. Notre analyse repose sur l’idée que dans le cadre semi-discret, l’image FBP est obtenue en sommant des contributions élémentaires :

$$f_N = \frac{\pi}{N} \sum_{\theta \in \Theta} \mathcal{B}_\theta \mathcal{D}[p_\theta] = \frac{\pi}{N} \sum_{k=1}^K g_{\Theta_k}, \quad (\text{C.13})$$

où :

$$g_{\Theta_k} = \sum_{\theta \in \Theta_k} \mathcal{B}_\theta \mathcal{D}[p_\theta]. \quad (\text{C.14})$$

Ici, nous notons Θ_k un élément d’une subdivision de Θ .

En décomposant le filtre rampe en un dérivateur d’ordre n (typiquement, $n = 0$ ou $n = 1$), et un filtre résiduel non local, nous montrons qu’il est possible d’obtenir g_{Θ_k} en rétro-projetant une image dérivée, et en appliquant le filtre non local à cette rétro-projection (Théorème 4.2.1). Ce filtre, tout en étant bidimensionnel, traite l’espace 2D ligne par ligne ; d’autre part, il est possible de choisir plusieurs orientations de lignes, de sorte que nous pouvons en choisir

une garantissant que chaque ligne a un support fini. La formule DBP-HT- K est déduite par sommation des reconstructions partielles sur chaque Θ_k de la subdivision.

Ce résultat est assez intuitif en géométrie parallèle. Est-il transposable en géométrie divergente ? Lorsque l'échantillonnage angulaire tend vers l'infini (cas continu), les sommes sont remplacées par des intégrales sur $[0, 2\pi]$. Traditionnellement, de cette vue continue en géométrie parallèle, un changement de variables entre (u, θ) en géométrie parallèle, et $(\hat{u}, \hat{\theta})$ en géométrie divergente, permet d'exprimer la même quantité dans le cas divergent. C'est ce que fait (Noo et al., 2004), et c'est ce que nous avons fait également. Les deux formules sont équivalentes lorsque $K = 1$, et souffrent toutes deux d'une limitation lorsque l'échantillonnage angulaire devient un enjeu. En effet, les intégrales en jeu ré-échantillonnent les données en géométrie divergente, ce qui suppose des échantillonnage spatial et angulaire fins. Si cela ne pose pas de problème en imagerie scanner diagnostic, cela peut être un enjeu en imagerie sur arceau interventionnel, et a fortiori, pour un nombre arbitrairement petit N de vues.

Au lieu de calculer la même quantité qu'en géométrie parallèle, nous calculons une quantité différente, intrinsèquement adaptée à la géométrie divergente, et qui tend vers la formule DBP-HT- K de la géométrie parallèle lorsque la position de la source tend vers l'infini. Cette formule en géométrie divergente utilise la même approche que pour DBP-HT- K en géométrie parallèle. On écrit encore :

$$f_N = \frac{\pi}{N} \sum_{k=1}^K g_{\Theta_k}, \quad (\text{C.15})$$

mais cette fois :

$$g_{\Theta_k} = \sum_{\hat{\theta} \in \Theta_k} \frac{D^2}{s_{\hat{\theta}}^2} \hat{\mathcal{B}}_{\hat{\theta}} \mathcal{D} [\tilde{p}_{\hat{\theta}}]. \quad (\text{C.16})$$

En géométrie divergente, rétro-projeter une projection revient à redistribuer sur chaque ligne de l'image 2D une transformation homographique de cette projection. Ainsi, afin d'appliquer la partie non local de la rampe (le filtre de Hilbert) après rétro-projection, il est nécessaire de vérifier la commutativité d'une transformation homographique et d'une transformation de Hilbert. C'est ce que nous montrons (Théorème 4.2.4). De même qu'en géométrie parallèle, on peut trouver une direction de filtrage commune à tout un sous-secteur angulaire Θ_k , et sommer sur les éléments de la subdivision Θ pour obtenir la version divergente de DBP-HT- K (Théorème 4.2.5). De même, une version où la rampe complète est passée après rétro-projection est proposée.

L'extension à la géométrie conique de l'arceau interventionnel peut se faire de la même manière que FDK étend FBP à cette géométrie. On a alors des formules de reconstruction approchée, différentes de FDK, qui vérifient les mêmes propriétés que FDK, à savoir : la formule approchée devient exacte si l'objet à reconstruire est invariant selon z , et elle revient à la formule exacte sur chaque coupe axiale lorsque la position de la source part à l'infini.

Dans la suite, par souci de simplicité, et par analogie avec les formules de reconstruction en géométrie rectifiée (Riddell & Troussset, 2006), nous prenons

$K = 2$ et nous coupons le spin entre les vues frontales, $\Theta_{\text{FRT}} = \left[\frac{\pi}{4}, \frac{3\pi}{4} \right] \cup \left[\frac{5\pi}{4}, \frac{7\pi}{4} \right]$, et les vues latérales, $\Theta_{\text{LAT}} = \Theta \setminus \Theta_{\text{FRT}}$.

De nombreuses simulations, en géométries planaires et en géométrie conique, illustrent ces résultats. L'erreur relative moyenne entre les reconstructions FDK et DBP-HT-2, définie comme la moyenne des erreurs relatives par rapport à FDK sur tous les voxels d'une région d'intérêt (sur un fantôme anatomique de tête, cela correspond aux voxels supérieurs à -250 HU), est inférieure à 0,5%, avec les erreurs les plus hautes situées là où l'angle du cône est le plus grand.

C.4.2 Application au bow-tie virtuel

Nous disposons donc d'un spin de N projections p_{F} plein champ, non tronquées, à faible dose, et de N projections p_{T} tronquées, à haute dose. Comme présenté au début de cette partie, il n'est pas possible de mélanger les projections directement, ni de reconstruire séparément les deux images issues de p_{F} et p_{T} . Avec les méthodes de type FBP, le filtre non local s'appliquant directement sur les projections, la gestion de la troncation (par exemple par une extrapolation ad hoc des projections aux extrémités) se fait forcément dans l'espace des projections.

Avec les méthodes de type BPF, il est possible de gérer la troncation dans un nouvel espace, qui est l'espace des rétro-projections avant filtrage non local. Puisque seules des opérations locales ont été appliquées aux projections, leurs rétro-projections sont justes dans leurs champs de vue 3D respectifs (au bruit près). On se propose donc d'utiliser un opérateur de mélange \mathcal{M} comme suit :

$$\mathcal{M}(b_{\text{F}}, b_{\text{T}}) = \begin{cases} w_{\text{F}} \cdot b_{\text{F}} + w_{\text{T}} \cdot b_{\text{T}} & \text{dans le champ 3D tronqué;} \\ b_{\text{F}} & \text{ailleurs.} \end{cases} \quad (\text{C.17})$$

Ici, b_{F} et b_{T} sont les rétro-projections des projections localement filtrées, et w_{F} , w_{T} sont des fonctions de poids (constantes ou non) qui vérifient $w_{\text{F}} + w_{\text{T}} = 1$. Cette opération est effectuée indépendamment sur les rétro-projections frontales et latérales.

Des simulations sur fantôme de tête, et des expériences sur de véritables acquisitions de Catphan[®] 515, et de fantôme anatomique de tête, illustrent l'efficacité de cette approche. Qualitativement, on observe aussi une réduction des non-uniformités basses fréquences liées au rayonnement diffusé dans la reconstruction proposée. L'erreur relative moyenne dans les simulations, entre une reconstruction FDK plein champ, haute dose, et la reconstruction directe du bow-tie virtuel, est également de l'ordre de 0,5% à l'intérieur du champ tronqué. Il est intéressant de noter qu'après le filtrage de Hilbert, le bruit de l'image à faible dose ne semble pas se propager particulièrement dans le champ tronqué. En revanche, la dose du champ tronqué ne se propage pas non plus en-dehors de ce champ, et n'améliore donc pas le reste de l'image, comme le permettait l'approche itérative.

Ainsi, la reconstruction directe pour acquisitions doubles est essentiellement une reconstruction de régions d'intérêt ("region-of-interest", ou ROI). Bien que nous nous attendions à ce que cette approche, intégrée à un schéma itératif, améliore à la fois le résultat final et la convergence des itérations, nous nous intéressons maintenant au comportement de nos deux solutions (reconstruction

itérative et reconstruction directe DBP-HT- K) pour la reconstruction de régions d'intérêt.

C.5 Du bow-tie virtuel à l'imagerie de régions d'intérêt

L'imagerie de régions d'intérêt (ROI) consiste à reconstruire le champ de vue d'une 3D d'une image dont les projections transaxiales sont tronquées. Dans ce cas-là, la méthode FBP ne parvient pas à reconstruire l'objet correspondant aux projections. Dans le cas de la tomographie intérieure (Figure 5.1c), il n'existe pas de reconstruction exacte (Natterer, 2001). Une façon de parvenir à une reconstruction raisonnable est d'utiliser une information supplémentaire pour extrapoler les données tronquées. Cette information peut être donnée a priori, ou venir de mesures complémentaires. Notre approche s'inscrit dans la deuxième catégorie. Dans le contexte d'une acquisition double, nous réduisons à quelques vues seulement le jeu de projections plein champ. Nous notons s le ratio d'échantillonnage angulaire, c'est-à-dire le ratio entre le nombre de vues tronquées et le nombre de vues plein champ. On a donc typiquement $s \gg 1$ dans le cas de l'imagerie de région d'intérêt.

C.5.1 Reconstruction itérative

Dans ce contexte, il est nécessaire de modifier les contributions relatives α_F et $\alpha_T = 1 - \alpha_F$ définies dans le schéma itératif. La contribution des projections plein champ à la dose totale est maintenant égale à :

$$\alpha_F = \frac{N_F I_0^F}{N_F I_0^F + t \cdot N_T I_0^T} = \frac{1}{1 + t s}. \quad (\text{C.18})$$

Cette modification étant faite, nous appliquons le même algorithme que précédemment dans le cas du bow-tie virtuel. En particulier, notre régularisation reste lisse, de sorte que nous n'attendons pas d'amélioration de l'image en-dehors de la région d'intérêt.

Les résultats sur fantômes (Catphan[®] 515 et fantôme de tête uniforme) montrent qu'avec moins de 10 projections non tronquées, c'est-à-dire un soixantième des vues tronquées, la région d'intérêt peut être reconstruite avec peu de variations parasites basses fréquences, malgré un décalage de la composante continue. Notre compréhension de ces résultats, qui n'allaient pas de soi à la lecture de la littérature, est que malgré la corruption de l'image hors de la région d'intérêt, due au sévère sous-échantillonnage angulaire des vues plein champ, celle-ci reste une estimation suffisante des basses fréquences de l'image hors de la région d'intérêt ; de plus, l'échantillonnage polaire de l'acquisition tomographique ne nécessite pas autant de vues pour échantillonner correctement ces basses fréquences : ainsi, le petit a priori spatial de la littérature (Kudo et al., 2008) peut être remplacé par une petite quantité de vues non tronquées dans une acquisition double.

C.5.2 Reconstruction directe

Nous proposons deux approches de reconstruction directe pour l'imagerie de régions d'intérêt par acquisition double. La première approche consiste à adapter la méthode de (Noo et al., 2004) aux acquisitions doubles, en géométrie parallèle. Dans (Noo et al., 2004), les auteurs montrent l'égalité (à un facteur près), dans le domaine continu, entre la rétro-projection des projections dérivées, et la transformée de Hilbert ligne par ligne de l'objet f . Cette relation reste vraie dans le cadre semi-discret, où l'on a :

$$\text{DBP}_N(\mathbf{x}) = -2\pi\mathcal{H}_{\frac{\pi}{2}}[f_N](\mathbf{x}), \quad (\text{C.19})$$

où DBP_N est la rétro-projection différenciées des N vues disponibles, et f_N est l'image obtenue par FBP à partir de ces mêmes N vues. On rappelle que \mathcal{H}_α est l'opérateur 2D qui revient à filtrer chaque ligne orientée selon $\boldsymbol{\alpha}^\perp = (-\sin \alpha, \cos \alpha)^T$ par la transformée de Hilbert 1D. Lorsque N est grand par rapport à la taille de la grille de reconstruction, l'échantillonnage angulaire est fin, et le support de f_N peut être considéré comme compact. Ainsi, l'inversion ligne par ligne de la transformée de Hilbert peut être réalisée via l'application de la transformée de Hilbert tronquée (Noo et al., 2004). Afin de pouvoir toujours utiliser cette inversion lorsque N se limite à quelques vues, il est donc nécessaire de réduire la taille de la grille de reconstruction ; ou, de manière équivalente, il suffit d'appliquer un filtre passe-bas à DBP_N avant d'utiliser la transformée de Hilbert tronquée.

Nous proposons donc l'opérateur de mélange suivant entre les rétro-projections différenciées de nos deux acquisitions :

$$\mathcal{M}_{\text{ROI}}(\text{DBP}_F, \text{DBP}_T) = \begin{cases} w_F \cdot G_\sigma[\text{DBP}_F] + w_T \cdot \text{DBP}_T & \text{dans la ROI;} \\ G_\sigma[\text{DBP}_F] & \text{hors de la ROI.} \end{cases} \quad (\text{C.20})$$

Ici, G_σ est un opérateur de flou gaussien d'écart type σ .

Les simulations sur des acquisitions en géométries parallèles d'une coupe de scanner diagnostic d'une tête, montrent qu'il est possible, avec la bonne valeur σ associée à chaque ratio d'échantillonnage angulaire s , de garder l'erreur relative moyenne inférieure à 1% même à $s = 32$. Cependant, la question de la sélection automatique de l'écart type σ est encore une question ouverte ; d'autre part, lorsque s devient trop grand, il n'existe plus de valeur de σ permettant le bon compromis entre la préservation de structures et le retrait des stries de sous-échantillonnage dans DBP_F , et l'image résultante devient traversée de non-uniformités basses fréquences (Figure 5.9b). Enfin, cette approche ne dispose pas d'extension en géométrie divergente. En revanche, en n'opérant aucune subdivision de l'espace angulaire ($K = 1, \Theta_1 = \Theta$), il s'agit de la seule approche qui permette la reconstruction d'une ligne.

Il est intéressant de noter que le schéma de mélange mis en place pour la reconstruction directe d'une acquisition double pour le bow-tie virtuel, utilisant l'opérateur \mathcal{M} dans l'espace des rétro-projections des projections localement filtrées, peut tout à fait s'appliquer dans le cas où s est supérieur à 1. Les lignes de Hilbert, en-dehors de la région d'intérêt, sont évidemment corrompues par des

oscillations dues au sous-échantillonnage angulaire (Figure 5.10b), mais la forme basse fréquence de la transformée de Hilbert est préservée, et de même que dans le cas du bow-tie virtuel, on ne s'attend pas à ce que les phénomènes hautes fréquences de ces oscillations se propagent loin de leurs positions initiales.

Contrairement au cas du bow-tie virtuel, l'information de l'image en-dehors de la région d'intérêt n'a d'autre nécessité que de permettre une extrapolation des transformées de Hilbert. Nous proposons donc une stratégie multi-résolution, où la rétro-projection des données plein champ est faite sur une grille de reconstruction échantillonnée grossièrement. Ainsi, la rétro-projection, dont le coût d'exécution est non négligeable, se trouve accélérée. Le choix du sous-échantillonnage de la grille de reconstruction dépend bien sûr du contenu de l'image ; plus le contenu d'une image a de hautes fréquences, moins une image basse résolution sera capable d'extrapoler les données manquantes dans les projections tronquées. Une fois la rétro-projection basse résolution obtenue, l'image est rééchantillonnée à la bonne résolution (une interpolation trilineaire suffit), avant d'être utilisée par l'opérateur de mélange \mathcal{M} .

C.6 Conclusion

C.6.1 Contributions

Cette thèse a porté sur l'étude des défis liés à la détection des faibles contrastes en tomographie conique rayons X sur arceau interventionnel. La chaîne image 3D est complexe : le tube à rayons X, les déformations mécaniques de l'arceau, les non-idéalités du détecteur, l'algorithme de reconstruction, peuvent tous, à leur niveau, influencer la qualité image des faibles contrastes. A travers des simulations et des conceptions d'expériences en environnement contrôlé, nous avons isolé les principaux facteurs influençant la qualité image des faibles contrastes. En particulier, nous avons pu écarter l'étape de conversion analogique-numérique de la liste des principaux suspects.

Notre proposition d'acquisition double est une preuve de concept. C'est une manière d'utiliser le système d'imagerie actuel au maximum de ses capacités, sans avoir à changer de composant physique. Cette acquisition double peut être vue comme un bow-tie virtuel, et a nécessité le développement d'une méthode de reconstruction itérative améliorant l'ensemble du volume reconstruit.

En passant d'une approche de type FBP à une approche de type BPF, nous avons revisité les reconstructions classiques et proposé une formule originale de reconstruction directe, que nous appelons la rétro-projection différenciée à K passes de Hilbert (DBP-HT- K), qui se comporte comme FBP même aux faibles échantillonnages angulaires. Cette formule nous a permis de proposer une reconstruction alternative pour le bow-tie virtuel.

Enfin, nous avons changé de point de vue, et étudié dans quelle mesure nos méthodes de reconstruction d'acquisitions doubles pouvaient répondre au problème de l'imagerie de régions d'intérêt. Les deux approches ont montré qu'il était possible de reconstruire une région d'intérêt en utilisant quelques vues non tronquées en plus, sans recourir à une information supplémentaire a priori (qu'il

s'agisse d'un a priori spatial, ou d'une régularisation parcimonieuse).

C.6.2 Perspectives

Les résultats de cette thèse sont un point de départ. Afin de faire face à d'autres contraintes, des choix de conception auront à être pris pour raffiner le travail et l'adapter au milieu de la neuroradiologie interventionnelle. En particulier, la présence de mouvement au cours de l'acquisition (fréquent dans le cas d'un accident vasculaire ischémique) devra être pris en compte.

Le retour à une rotation simple est une option pour accélérer le temps d'acquisition et réduire les risques de mouvement du patient pendant le spin. Si les limites d'une acquisition simple ont été mises en évidence dans cette thèse, il reste envisageable d'acquérir deux spins en une rotation : dans ce cas, une collimation dynamique, rapide, sera nécessaire, de même qu'il faudra augmenter la vitesse de rotation et la fréquence de lecture du détecteur plan.

Cette thèse n'a pas cherché à proposer de stratégies de correction du rayonnement diffusé. En revanche, la conception de la solution à double acquisition prend en compte le bénéfice de l'acquisition tronquée en terme de réjection du diffusé. En combinant les deux acquisitions, tronquées et non tronquées, et en bénéficiant de lectures du signal sous l'ombre des lames de collimation, on peut raisonnablement espérer pouvoir estimer plus précisément le diffusé dans l'image (Siewerdsen et al., 2006).

D'un point de vue théorique, notre plus grande contribution concerne la rétro-projection différenciée à K passes de Hilbert (DBP-HT- K). L'étude de l'utilisation de DBP-HT- K dans un schéma itératif est une piste de recherche naturelle. D'autre part, l'étude du comportement de FBP et DBP-HT- K à de petites troncations latérales et à la présence de structures hors champ, comme le lit du patient, est un travail en cours.

Les applications de DBP-HT- K à la reconstruction de régions d'intérêt illustre la flexibilité de l'approche proposée. Ce schéma n'est pas limité à des acquisitions doubles, et pourrait tout à fait s'appliquer à des acquisitions multiples, ou multi-résolutions (Maaß et al., 2011). Nous pensons qu'une démarche consistant à utiliser peu de mesures supplémentaires, avec un coût marginal en terme de dose, est pertinente : nous proposons une alternative aux approches utilisant des a priori de différentes sortes, et discutables en pratique.

Enfin, nous insistons sur le fait que les travaux de cette thèse dépassent le cadre de la neuroradiologie interventionnelle. La radiothérapie, le scanner diagnostique du sein, l'imagerie cardiaque, sont autant d'applications où nos solutions sont susceptibles d'apporter une réponse. Plus généralement, la flexibilité de notre approche devrait pouvoir bénéficier à d'autres modalités et systèmes d'imagerie, où des conceptions exotiques sont destinées à compenser les particularités de la situation, en simplifiant et en accélérant la tâche de reconstruction par rapport aux algorithmes itératifs actuels.

Bibliography

- Altunbas, C. (2014). Image corrections for scattered radiation. In C. C. Shaw (Ed.), *Cone-beam computed tomography* (p. 129-147). Taylor & Francis. Cited on pages [32](#), [48](#), [49](#), and [143](#).
- American Stroke Association. (2018). *What You Should Know About Cerebral Aneurysms*. Retrieved from <http://www.strokeassociation.org> Cited on page [5](#).
- Anxionnat, R., Bracard, S., Macho, J., Da Costa, E., Vaillant, R., Launay, L., ... Picard, L. (1998). 3d angiography. *Clinical interest. First application in interventional neuroradiology. J Neuroradiol*25, 251–262. Cited on pages [11](#), [75](#), [143](#), and [158](#).
- Arcadu, F., Marone, F., & Stampanoni, M. (2017). Fast iterative reconstruction of data in full interior tomography. *Journal of Synchrotron Radiation*, 24(1), 205–219. doi: 10.1107/S1600577516015794 Cited on page [115](#).
- Baek, J.-H., Yoo, J., Song, D., Kim, Y. D., Nam, H. S., Kim, B. M., ... Heo, J. H. (2017). Predictive value of thrombus volume for recanalization in stent retriever thrombectomy. *Scientific reports*, 7(1), 15938. Cited on page [3](#).
- Barrett, H. H., Gordon, S., & Hershel, R. (1976). Statistical limitations in transaxial tomography. *Computers in biology and medicine*, 6(4), 307–323. Cited on page [45](#).
- Benjamin, E. J., Blaha, M. J., Chiuve, S. E., Cushman, M., Das, S. R., Deo, R., ... others (2017). Heart disease and stroke statistics-2017 update: a report from the american heart association. *Circulation*, 135(10), e146–e603. Cited on page [3](#).
- Berkhemer, O. A., Fransen, P. S., Beumer, D., Van Den Berg, L. A., Lingsma, H. F., Yoo, A. J., ... others (2015). A randomized trial of intraarterial treatment for acute ischemic stroke. *New England Journal of Medicine*, 372(1), 11–20. Cited on page [4](#).
- Bhatia, N. (2016). *Scattering correction in cone beam tomography using continuously thickness-adapted kernels* (Unpublished doctoral dissertation). Université de Lyon. Cited on page [49](#).

- Bian, J., Han, X., Sidky, E. Y., Siewerdsen, J. H., & Pan, X. (2010). Investigation of low-contrast tumor detection in algorithm-enabled low-dose cbct. In *Nuclear science symposium conference record (nss/mic), 2010 ieee* (pp. 3479–3482). Cited on page [75](#).
- Bian, J., Xia, D., Sidky, E. Y., & Pan, X. (2010). Region of interest imaging for a general trajectory with the rebinned bpf algorithm. *Tsinghua science and technology*, *15*(1), 68–73. Cited on page [79](#).
- Bier, B., Schwemmer, C., Maier, A., Hofmann, H. G., Xia, Y., Hornegger, J., & Struffert, T. (2013). Convolution-based truncation correction for C-Arm CT using scattered radiation. *Informatik aktuell*, 338–343. doi: 10.1007/978-3-642-36480-8_59 Cited on page [113](#).
- Bilgot, A., Desbat, L., & Perrier, V. (2012). FBP and the interior problem in 2D tomography. *IEEE Nuclear Science Symposium Conference Record*(2), 4080–4085. doi: 10.1109/NSSMIC.2011.6153776 Cited on page [113](#).
- Bracard, S., Ducrocq, X., Mas, J. L., Soudant, M., Oppenheim, C., Moulin, T., . . . others (2016). Mechanical thrombectomy after intravenous alteplase versus alteplase alone after stroke (THRACE): a randomised controlled trial. *The Lancet Neurology*, *15*(11), 1138–1147. Cited on page [4](#).
- Chalela, J. A., Kidwell, C. S., Nentwich, L. M., Luby, M., Butman, J. A., Demchuk, A. M., . . . Warach, S. (2007). Magnetic resonance imaging and computed tomography in emergency assessment of patients with suspected acute stroke: a prospective comparison. *The Lancet*, *369*(9558), 293–298. Cited on page [7](#).
- Chen, L., Shaw, C. C., Altunbas, M. C., Lai, C.-J., Liu, X., Han, T., . . . Whitman, G. J. (2008). Feasibility of volume-of-interest (VOI) scanning technique in cone beam breast CT – A preliminary study. *Medical Physics*, *35*(8), 3482–3490. Cited on page [116](#).
- Chen, L., Shen, Y., Lai, C.-J., Han, T., Zhong, Y., Ge, S., . . . Shaw, C. C. (2009). Dual resolution cone beam breast CT: a feasibility study. *Medical Physics*, *36*(9), 4007–4014. doi: 10.1118/1.3187225 Cited on page [116](#).
- Chityala, R., Hoffmann, K., Rudin, S., & Bednarek, D. (2005). Region of interest (roi) computed tomography (ct): Comparison with full field of view (ffov) and truncated ct for a human head phantom. In *Medical imaging* (pp. 583–590). Cited on page [116](#).
- Chityala, R. N., Hoffmann, K. R., Bednarek, D. R., & Rudin, S. (2004). Region of interest (ROI) computed tomography. In *Medical imaging 2004* (pp. 534–541). Cited on page [116](#).
- Cho, S., Bian, J., Pelizzari, C. a., Chen, C.-T., He, T.-C., & Pan, X. (2007). Region-of-interest image reconstruction in circular cone-beam microCT. *Medical Physics*, *34*(12), 4923–4933. doi: 10.1118/1.2804924 Cited on page [113](#).
- Cho, S., Pearson, E., Pelizzari, C. A., & Pan, X. (2009). Region-of-interest image reconstruction with intensity weighting in circular cone-beam CT for image-guided radiation therapy. *Medical Physics*, *36*(4), 1184–1192. Cited on pages [75](#) and [116](#).
- CHRU de Nancy. (2018). *Une nouvelle salle de neuroradiologie*

- interventionnelle pour le traitement des pathologies cérébrales*. Retrieved from <http://maternite.chru-nancy.fr/index.php/une-nouvelle-salle-de-neuroradiologie-interventionnelle-pour-le-traitement-des-pathologies-cerebrales> Cited on page 10.
- Clackdoyle, R., Noo, F., Momey, F., Desbat, L., & Rit, S. (2017). Accurate transaxial region-of-interest reconstruction in helical CT? *IEEE Transactions on Radiation and Plasma Medical Sciences*(99). Cited on page 115.
- Courdurier, M., Noo, F., Defrise, M., & Kudo, H. (2008). Solving the Interior Problem of Computed Tomography Using a Priori Knowledge. *Inverse Problems*, 24(6), 65001. doi: 10.1088/0266-5611/24/6/065001 Cited on pages 113 and 115.
- Dance, D., Christofides, S., & Maidment, A. (2014). Diagnostic radiology physics: A handbook for teachers and students. Cited on page 17.
- Defrise, M., Noo, F., Clackdoyle, R., & Kudo, H. (2006). Truncated Hilbert transform and image reconstruction from limited tomographic data. *Inverse Problems*, 22(March), 1037–1053. doi: 10.1088/0266-5611/22/3/019 Cited on pages 113 and 115.
- Delaney, A. H., & Bresler, Y. (1995). Multiresolution tomographic reconstruction using wavelets. *IEEE Transactions on image processing*, 4(6), 799–813. Cited on pages 116 and 147.
- Dendy, B., Philip Palin; Heaton. (2011). *Physics for Diagnostic Radiology* (3rd ed.). CRC Press. Cited on pages 17, 21, and 29.
- Dowsett, D., Kenny, P. A., & Johnston, R. E. (2006). *The physics of diagnostic imaging second edition*. CRC Press. Cited on page 17.
- Fahmi, F., Beenen, L., Streekstra, G., Janssen, N., de Jong, H., Riordan, A., ... others (2013). Head movement during ct brain perfusion acquisition of patients with suspected acute ischemic stroke. *European journal of radiology*, 82(12), 2334–2341. Cited on page 143.
- Fahrig, R., Starman, J., Girard, E., Al-Ahmad, A., Gao, H., Kothary, N., & Ganguly, A. (2014). C-arm CT in the interventional suite: Current status and future directions. In C. C. Shaw (Ed.), *Cone-beam computed tomography* (p. 199-221). Taylor & Francis. Cited on pages 32 and 47.
- Fanous, A. A., & Siddiqui, A. H. (2016). Mechanical thrombectomy: stent retrievers vs. aspiration catheters. *Cor et Vasa*, 58(2), e193–e203. Cited on page 3.
- Feldkamp, L., Davis, L., & Kress, J. (1984). Practical cone-beam algorithm. *JOSA A*, 1(6), 612–619. Cited on pages 39, 64, 88, 108, and 160.
- Fessler, J. A. (2000). Statistical image reconstruction methods for transmission tomography. *Handbook of medical imaging*, 2, 1–70. Cited on page 45.
- Fessler, J. A. (2006). Iterative methods for image reconstruction. In *Ieee international symposium on biomedical imaging tutorial, arlington virginia*. Cited on page 40.
- Garverick, S. L., & Michon, G. J. (1994). *Architecture for arbitrary nonlinear quantization of multi-channel data*. Google Patents. (US Patent 5,371,501) Cited on page 57.

- González, R. G., Hirsch, J. A., Koroshetz, W., Lev, M. H., & Schaefer, P. W. (2011). *Acute ischemic stroke*. Springer. Cited on pages 3 and 4.
- Goodenough, D. (2012). Catphan 500 and 600 manual. *Greenwich, NY: The Phantom Laboratory*. Cited on pages 42 and 161.
- Granfors, P. R. (1999). Performance characteristics of an amorphous silicon flat-panel x-ray imaging detector. In *Medical imaging'99* (pp. 480–490). Cited on pages 28 and 57.
- Granfors, P. R., & Albagli, D. (2009). Scintillator-based flat-panel x-ray imaging detectors. *Journal of the Society for Information Display*, 17(6), 535–542. Cited on pages 28, 29, and 32.
- Granfors, P. R., & Aufrichtig, R. (2000). Performance of a 41× 41-cm² amorphous silicon flat panel x-ray detector for radiographic imaging applications. *Medical physics*, 27(6), 1324–1331. Cited on pages 28 and 57.
- Hoskovec, J., Clackdoyle, R., Desbat, L., & Rit, S. (2016). Exact fan-beam reconstruction with arbitrary object translations and truncated projections. *IEEE Transactions on Nuclear Science*, 63(3), 1408–1418. Cited on page 115.
- Hsieh, J. (2009). *Computed tomography: principles, design, artifacts, and recent advances*. SPIE Press. Cited on pages 34, 47, and 113.
- Hsieh, J., Armstrong, R. H., Arduini, P. J., & Senzig, R. F. (2004). *Methods and apparatus for truncation compensation*. Google Patents. (US Patent 8,624,769) Cited on pages 131 and 145.
- Hsieh, J., Chao, E., Thibault, J., Grekowicz, B., Horst, A., McOlash, S., & Myers, T. J. (2004). A novel reconstruction algorithm to extend the CT scan field-of-view. *Medical Physics*, 31(9), 2385–2391. doi: 10.1118/1.1776673 Cited on pages 113 and 131.
- Hu, Z., Zhang, Y., Liu, J., Ma, J., Zheng, H., & Liang, D. (2016). A feature refinement approach for statistical interior CT reconstruction. *Physics in Medicine and Biology*, 61(14), 5311–5334. doi: 10.1088/0031-9155/61/14/5311 Cited on page 115.
- Hubbell, J. H., & Seltzer, S. M. (1995). *Tables of x-ray mass attenuation coefficients and mass energy-absorption coefficients 1 keV to 20 MeV for elements Z= 1 to 92 and 48 additional substances of dosimetric interest* (Tech. Rep.). National Inst. of Standards and Technology-PL, Gaithersburg, MD (United States). Ionizing Radiation Div. Cited on page 26.
- Hurst, R. W., & Rosenwasser, R. H. (2007). *Interventional neuroradiology*. CRC Press. Cited on pages 6, 7, 8, and 9.
- Jin, J.-Y., Ren, L., Liu, Q., Kim, J., Wen, N., Guan, H., . . . Chetty, I. J. (2010). Combining scatter reduction and correction to improve image quality in cone-beam computed tomography (cbct). *Medical physics*, 37(11), 5634–5644. Cited on page 145.
- Jin, S. B., Shin, K., Yoo, S., Kim, J., Kim, K., Huh, Y., . . . Kwon, O.-K. (2014). Dual-resolution image reconstruction for region-of-interest CT scan. *Journal of Instrumentation*, 9(7). doi: 10.1088/1748-0221/9/07/C07008 Cited on page 117.
- Joseph, P. M., & Spital, R. D. (1978). A method for correcting bone induced

- artifacts in computed tomography scanners. *Journal of computer assisted tomography*, 2(1), 100–108. Cited on page 46.
- Kak, A. C., & Slaney, M. (2001). *Principles of computerized tomographic imaging*. SIAM. Cited on pages 17, 36, 38, 78, 85, and 124.
- Kästner, T., Hornegger, J., Maier, A., Xia, Y., & Bauer, S. (2015). Truncation Robust C-Arm CT Reconstruction for Dynamic Collimation Acquisition Schemes. In *Bildverarbeitung für die medizin 2015* (pp. 516–521). Springer. Cited on pages 122 and 143.
- Katsevich, A. (2010). Singular value decomposition for the truncated hilbert transform. *Inverse Problems*, 26(11), 115011. Cited on page 80.
- Knaup, M., Ritschl, L., & Kachelrieß, M. (2012). Digitization and visibility issues in flat detector CT: A simulation study. In *Nuclear science symposium and medical imaging conference (nss/mic), 2012 ieee* (pp. 2661–2666). Cited on page 58.
- Kolditz, D., Kyriakou, Y., & Kalender, W. A. (2010). Low dose, low noise, and high resolution volume of interest (VOI) imaging in C-arm flat-detector CT. In *Spie medical imaging* (pp. 762226–762226). Cited on pages 122 and 145.
- Kolditz, D., Meyer, M., Kyriakou, Y., & Kalender, W. A. (2010). Comparison of extended field-of-view reconstructions in c-arm flat-detector ct using patient size, shape or attenuation information. *Physics in Medicine and Biology*, 56(1), 39. Cited on pages 113 and 117.
- Kolditz, D., Struffert, T., Kyriakou, Y., Bozzato, A., Dörfler, A., & Kalender, W. (2012). Volume-of-interest imaging of the inner ear in a human temporal bone specimen using a robot-driven C-arm flat panel detector CT system. *American Journal of Neuroradiology*, 33(10), E124–E128. Cited on page 116.
- Kudo, H., Courdurier, M., Noo, F., & Defrise, M. (2008). Tiny a priori knowledge solves the interior problem in computed tomography. *Physics in Medicine and Biology*, 53(9), 2207. Cited on pages 115, 122, 145, and 168.
- Kudo, H., Suzuki, T., & Rashed, E. A. (2013). Image reconstruction for sparse-view ct and interior ct—introduction to compressed sensing and differentiated backprojection. *Quantitative Imaging in Medicine and Surgery*, 3(3), 147–161. Cited on page 122.
- Langer, M., & Peyrin, F. (2010). A wavelet algorithm for zoom-in tomography. In *Biomedical imaging: From nano to macro, 2010 ieee international symposium on* (pp. 608–611). Cited on page 116.
- Langet, H., Riddell, C., Reshef, A., Troussset, Y., Tenenhaus, A., Lahalle, E., . . . Paragios, N. (2015). Compressed-sensing-based content-driven hierarchical reconstruction: Theory and application to C-arm cone-beam tomography. *Medical Physics*, 42(9), 5222–5237. Cited on pages 13, 40, 41, 42, 65, 145, 159, 161, and 164.
- Lauritsch, G., Boese, J., Wigstrom, L., Kemeth, H., & Fahrig, R. (2006). Towards cardiac C-arm computed tomography. *IEEE Transactions on Medical Imaging*, 25(7), 922–934. Cited on page 75.
- Lauzier, P. T., Tang, J., Qi, Z., & Chen, G.-H. (2010). Image reconstruction in cardiac interventions using a small flat-panel detector. In *Proc. spie* (Vol.

- 7622, pp. 762228–762228–8). doi: 10.1117/12.844581 Cited on page 115.
- Lee, M., Ward, J. P., Unser, M., & Ye, J. C. (2014). Multiscale interior tomography using 1d generalized total variation. In *Proc. 3rd int. conf. image formation in x-ray computed tomography* (pp. 347–350). Cited on page 115.
- Létourneau, D., Wong, J. W., Oldham, M., Gulam, M., Watt, L., Jaffray, D. A., ... Martinez, A. A. (2005). Cone-beam-CT guided radiation therapy: technical implementation. *Radiotherapy and Oncology*, 75(3), 279–286. Cited on page 116.
- Lipshitz, S. P., Wannamaker, R. A., & Vanderkooy, J. (1992). Quantization and dither: A theoretical survey. *Journal of the audio engineering society*, 40(5), 355–375. Cited on page 55.
- Liu, X., Shaw, C. C., Wang, T., Chen, L., Altunbas, M. C., & Kappadath, S. C. (2006). An accurate scatter measurement and correction technique for cone beam breast CT imaging using scanning sampled measurement (SSM) technique. In *Medical imaging* (pp. 614234–614234). Cited on pages 49 and 145.
- Love, L. A., & Kruger, R. A. (1987). Scatter estimation for a digital radiographic system using convolution filtering. *Medical physics*, 14(2), 178–185. Cited on page 48.
- Lu, W., Yan, H., Gu, X., Tian, Z., Ouyang, L., Yang, L., ... others (2014). Reconstructing cone-beam CT with spatially varying qualities for adaptive radiotherapy: a proof-of-principle study. *Physics in Medicine and Biology*, 59(20), 6251. Cited on pages 117 and 145.
- Lück, F., Kolditz, D., Hupfer, M., & Kalender, W. A. (2013). Effect of shaped filter design on dose and image quality in breast CT. *Physics in Medicine and Biology*, 58(12), 4205. Cited on page 116.
- Maaß, C., Knaup, M., & Kachelrieß, M. (2011). New approaches to region of interest computed tomography. *Medical Physics*, 38(6), 2868–2878. Cited on pages 116, 145, and 171.
- Maier, A., Scholz, B., & Dennerlein, F. (2012). Optimization-based Extrapolation for Truncation Correction. In *Ct meeting* (Vol. i, pp. 390–394). Cited on pages 113 and 115.
- Mail, N., Moseley, D., Siewerdsen, J., & Jaffray, D. (2009). The influence of bowtie filtration on cone-beam CT image quality. *Medical Physics*, 36(1), 22–32. Cited on pages 47 and 116.
- Maltz, J. S., Bose, S., Shukla, H. P., & Bani-Hashemi, A. R. (2007). CT Truncation artifact removal using water-equivalent thicknesses derived from truncated projection data. *Annual International Conference of the IEEE Engineering in Medicine and Biology - Proceedings*(July 2015), 2907–2911. doi: 10.1109/IEMBS.2007.4352937 Cited on page 113.
- Matsinos, E., & Kaissl, W. (2006). The dual-gain mode: a way to enhance the dynamic range of x-ray detectors. *arXiv preprint physics/0607021*. Cited on page 62.
- Mayo Clinic. (2018). *Endovascular embolization*. Retrieved from <https://www.mayoclinic.org/diseases-conditions/brain-avm/multimedia/endovascular-embolization/img-20090359> Cited on

- page 6.
- Medtronic. (2018). *Solitaire™ Platinum Revascularization Device. Stent Retriever Thrombectomy for Acute Ischemic Stroke*. Retrieved from <http://www.medtronic.com/us-en/healthcare-professionals/products/neurological/revascularization-stroke/solitaire.html> Cited on page 4.
- Menjot, d. C. N., Saver, J., Goyal, M., Jahan, R., Diener, H., Bonafe, A., . . . others (2017). Efficacy of stent-retriever thrombectomy in magnetic resonance imaging versus computed tomographic perfusion-selected patients in swift prime trial (solitaire fr with the intention for thrombectomy as primary endovascular treatment for acute ischemic stroke). *Stroke*, 48(6), 1560. Cited on page 7.
- Menser, B., Wiegert, J., Wiesner, S., & Bertram, M. (2010). Use of beam shapers for cone-beam ct with off-centered flat detector. In *Medical imaging 2010: Physics of medical imaging* (Vol. 7622, p. 762233). Cited on pages 47 and 116.
- Moore, C. J., Marchant, T. E., & Amer, A. M. (2006). Cone beam CT with zonal filters for simultaneous dose reduction, improved target contrast and automated set-up in radiotherapy. *Physics in Medicine and Biology*, 51(9), 2191. Cited on page 116.
- Mulder, M., Jansen, I., Goldhoorn, R., Venema, E., Chalos, V., Compagne, K., . . . others (2018). Time to Endovascular Treatment and Outcome in Acute Ischemic Stroke: MR CLEAN Registry Results. *Circulation*. Cited on page 4.
- Murphy, K., & Robertson, F. (2013). *Interventional neuroradiology*. Springer. Cited on pages 4 and 5.
- Nakayama, Y., Awai, K., Funama, Y., Liu, D., Nakaura, T., Tamura, Y., & Yamashita, Y. (2006). Lower tube voltage reduces contrast material and radiation doses on 16-mdct aortography. *American Journal of Roentgenology*, 187(5), W490–W497. Cited on page 46.
- National Heart, Lung and Blood Institute. (2018). *Carotid artery stenting*. Retrieved from <http://www.nhlbi.nih.gov/health/health-topics/topics/carotid-artery-disease> Cited on page 2.
- Natterer, F. (2001). *The mathematics of computerized tomography*. SIAM. Cited on pages 78, 113, 165, and 168.
- Ning, R., Tang, X., & Conover, D. (2004). X-ray scatter correction algorithm for cone beam CT imaging. *Medical physics*, 31(5), 1195–1202. Cited on pages 48 and 145.
- Nogueira, R. G., Jadhav, A. P., Haussen, D. C., Bonafe, A., Budzik, R. F., Bhuva, P., . . . others (2018). Thrombectomy 6 to 24 hours after stroke with a mismatch between deficit and infarct. *New England Journal of Medicine*, 378(1), 11–21. Cited on page 4.
- Noo, F., Clackdoyle, R., & Pack, J. D. (2004). A two-step Hilbert transform method for 2D image reconstruction. *Physics in Medicine and Biology*, 49(17), 3903. Cited on pages 79, 84, 85, 86, 104, 111, 113, 115, 122, 123, 127, 129, 142, 145, 149, 152, 153, 165, 166, and 169.

- Noo, F., Hoppe, S., Dennerlein, F., Lauritsch, G., & Hornegger, J. (2007). A new scheme for view-dependent data differentiation in fan-beam and cone-beam computed tomography. *Physics in Medicine and Biology*, *52*(17), 5393. Cited on page [80](#).
- Ohnesorge, B., Flohr, T., & Klingenbeck-Regn, K. (1999). Efficient object scatter correction algorithm for third and fourth generation ct scanners. *European radiology*, *9*(3), 563–569. Cited on pages [96](#) and [113](#).
- Olson, T. (1995). Optimal time-frequency projections for localized tomography. *Annals of biomedical engineering*, *23*(5), 622–636. Cited on page [116](#).
- Olson, T., & DeStefano, J. (1994). Wavelet localization of the radon transform. *IEEE Transactions on Signal Processing*, *42*(8), 2055–2067. Cited on pages [116](#) and [146](#).
- Orth, R. C., Wallace, M. J., & Kuo, M. D. (2008). C-arm cone-beam ct: General principles and technical considerations for use in interventional radiology. *J Vasc Interv Radiol*, *19*, 814–821. Cited on page [11](#).
- Pack, J. D., Noo, F., & Clackdoyle, R. (2005). Cone-beam reconstruction using the backprojection of locally filtered projections. *IEEE Transactions on Medical Imaging*, *24*(1), 70–85. Cited on pages [79](#) and [80](#).
- Pan, X., Zou, Y., & Xia, D. (2005). Image reconstruction in peripheral and central regions-of-interest and data redundancy. *Medical Physics*, *32*(3), 673–684. doi: 10.1118/1.1844171 Cited on page [113](#).
- Parker, D. L. (1982). Optimal short scan convolution reconstruction for fan beam CT. *Medical physics*, *9*(2), 254–257. Cited on pages [49](#), [64](#), and [131](#).
- Patel, V., Hoffmann, K., Ionita, C., Keleshis, C., Bednarek, D., & Rudin, S. (2008). Rotational micro-CT using a clinical C-arm angiography gantry. *Medical Physics*, *35*(10), 4757–4764. Cited on page [116](#).
- Powers, W. J., Rabinstein, A. A., Ackerson, T., Adeoye, O. M., Bambakidis, N. C., Becker, K., ... others (2018). 2018 guidelines for the early management of patients with acute ischemic stroke: a guideline for healthcare professionals from the american heart association/american stroke association. *Stroke*, *49*(3), e46–e110. Cited on pages [4](#) and [158](#).
- Prell, D., Kyriakou, Y., & Kalender, W. A. (2009). Comparison of ring artifact correction methods for flat-detector ct. *Physics in Medicine & Biology*, *54*(12), 3881. Cited on page [46](#).
- Reshef, A., Nikoukhah, T., Riddell, C., Trouset, Y., Ladjal, S., & Bloch, I. (2018). Parallel-beam ROI reconstruction with differentiated backprojection and angularly subsampled complementary sinograms. In *5th International Conference on Image Formation in X-Ray Computed Tomography*. Salt Lake City, USA. Cited on pages [14](#), [80](#), and [159](#).
- Reshef, A., Riddell, C., Trouset, Y., Ladjal, S., & Bloch, I. (2016). Dual-Rotation C-Arm Cone-Beam Computed Tomography to Increase Low-Contrast Resolution. In *4th International Conference on Image Formation in X-Ray Computed Tomography*. Bamberg, Germany. Cited on pages [13](#), [62](#), and [159](#).
- Reshef, A., Riddell, C., Trouset, Y., Ladjal, S., & Bloch, I. (2017a). Dual-rotation C-arm cone-beam computed tomography to increase low-contrast detection. *Medical Physics*, *44*(9), e164-e173. Cited on pages [13](#), [62](#), [118](#),

- and 159.
- Reshef, A., Riddell, C., Trouset, Y., Ladjal, S., & Bloch, I. (2017b). Reconstruction tomographique 2D : une nouvelle méthode de rétro-projection filtrée. In *Actes du XXVIème Colloque GRETSI*. Cited on pages 14, 80, and 159.
- Reshef, A., Riddell, C., Trouset, Y., Ladjal, S., & Bloch, I. (2018). Divergent-beam backprojection-filtration formula with applications to region-of-interest imaging. In *5th International Conference on Image Formation in X-Ray Computed Tomography*. Salt Lake City, USA. Cited on pages 14, 80, and 159.
- Riddell, C., Benali, H., & Buvat, I. (2004). Diffusion regularization for iterative reconstruction in emission tomography. *IEEE Transactions on Nuclear Science*, 51(3), 712–718. Cited on page 65.
- Riddell, C., & Trouset, Y. (2006). Rectification for cone-beam projection and backprojection. *IEEE Transactions on Medical Imaging*, 25(7), 950–962. Cited on page 166.
- Rinkel, J., Gerfault, L., Esteve, F., & Dinten, J. (2007). A new method for x-ray scatter correction: first assessment on a cone-beam CT experimental setup. *Physics in medicine and biology*, 52(15), 4633. Cited on page 49.
- Ritschl, L., Knaup, M., & Kachelrieß, M. (2013). Extending the dynamic range of flat detectors in CBCCT using a compressed-sensing-based mult-exposure technique. *Proc Fully 3D*, 3, 26–9. Cited on page 62.
- Roos, P. G., Colbeth, R. E., Mollov, I., Munro, P., Pavkovich, J., Seppi, E. J., ... others (2004). Multiple-gain-ranging readout method to extend the dynamic range of amorphous silicon flat-panel imagers. In *Medical imaging 2004* (pp. 139–149). Cited on page 62.
- Rowlands, J. A., & Yorkston, J. (2000). Flat panel detectors for digital radiography. *Handbook of Medical Imaging*, 1, 223–328. Cited on page 29.
- Rührschopf, E.-P., & Klingensbeck, K. (2011a). A general framework and review of scatter correction methods in cone beam ct. part 2: scatter estimation approaches. *Medical physics*, 38(9), 5186–5199. Cited on pages 48 and 49.
- Rührschopf, E.-P., & Klingensbeck, K. (2011b). A general framework and review of scatter correction methods in x-ray cone-beam computerized tomography. part 1: Scatter compensation approaches. *Medical physics*, 38(7), 4296–4311. Cited on pages 31 and 49.
- Sartor, K. (2002). *Diagnostic and Interventional Neuroradiology. A Multimodality Approach* (1st edition ed.). Thieme. Cited on pages 6, 7, 8, and 11.
- Saver, J. L. (2006). Time is brain—quantified. *Stroke*, 37(1), 263–266. Cited on page 4.
- Schafer, S., Noël, P. B., Walczak, A. M., & Hoffmann, K. R. (2010). Filtered region of interest cone-beam rotational angiography. *Medical Physics*, 37(2), 694–703. Cited on page 116.
- Schmidgunst, C., Ritter, D., & Lang, E. (2007). Calibration model of a dual gain flat panel detector for 2D and 3D x-ray imaging. *Medical Physics*, 34(9), 3649–3664. Cited on page 62.
- Schöndube, H., Stierstorfer, K., Dennerlein, F., White, T. A., Noo, F., Beekman, F., & Kachelrieß, M. (2007). Towards an efficient two-step hilbert algo-

- rithm for helical cone-beam ct. In *Proc. 2007 meeting on fully 3d image reconstruction in radiology and nuclear medicine (lindau, germany)* (pp. 120–123). Cited on page 79.
- Schöndube, H., Stierstorfer, K., & Noo, F. (2010). Evaluations of a 2d inverse hilbert transform. In *1st international conference on image formation in x-ray computed tomography*. Salt Lake City, USA. Cited on page 80.
- Schörner, K. (2012). *Development of methods for scatter artifact correction in industrial x-ray cone-beam computed tomography* (Unpublished doctoral dissertation). Technische Universität München. Cited on page 49.
- Sen Sharma, K., Holzner, C., Vasilescu, D. M., Jin, X., Narayanan, S., Agah, M., ... Wang, G. (2013). Scout-view assisted interior micro-CT. *Physics in Medicine and Biology*, 58(12), 4297–314. doi: 10.1088/0031-9155/58/12/4297 Cited on page 116.
- Shen, Y., Yi, Y., Zhong, Y., Lai, C.-J., Liu, X., You, Z., ... Shaw, C. C. (2011). High resolution dual detector volume-of-interest cone beam breast CT–Demonstration with a bench top system. *Medical Physics*, 38(12), 6429–6442. doi: 10.1118/1.3656040 Cited on page 116.
- Sidky, E. Y., Kraemer, D. N., Roth, E. G., Ullberg, C., Reiser, I. S., & Pan, X. (2014). Analysis of iterative region-of-interest image reconstruction for x-ray computed tomography. *Journal of Medical Imaging*, 1(3), 031007. Cited on page 115.
- Sidky, E. Y., & Pan, X. (2005). Recovering a compactly supported function from knowledge of its hilbert transform on a finite interval. *IEEE Signal Processing Letters*, 12(2), 97–100. Cited on page 80.
- Siewerdsen, J., Daly, M., Bakhtiar, B., Moseley, D., Richard, S., Keller, H., & Jaffray, D. (2006). A simple, direct method for x-ray scatter estimation and correction in digital radiography and cone-beam CT. *Medical physics*, 33(1), 187–197. Cited on pages 48, 49, 62, 75, 144, and 171.
- Siewerdsen, J., Zbijewski, W., & Xu, J. (2014). Cone-beam CT image quality. In C. C. Shaw (Ed.), *Cone-beam computed tomography* (p. 37-58). Taylor & Francis. Cited on pages 47 and 48.
- Simonsen, C. Z., Yoo, A. J., Rasmussen, M., Sørensen, K. E., Leslie-Mazwi, T., Andersen, G., & Sørensen, L. H. (2018). Magnetic resonance imaging selection for endovascular stroke therapy. *Stroke*, 49(6), 1402–1406. Retrieved from <http://stroke.ahajournals.org/content/49/6/1402> doi: 10.1161/STROKEAHA.118.021038 Cited on page 7.
- Sisniega, A., Abella, M., Desco, M., & Vaquero, J. J. (2013). Dual-exposure technique for extending the dynamic range of x-ray flat panel detectors. *Physics in Medicine and Biology*, 59(2), 421. Cited on page 62.
- Society of NeuroInterventional Surgery (SNIS). (2018). *Brain aneurysms*. Retrieved from <http://www.brainaneurysm.com> Cited on page 5.
- Sourbelle, K., Kachelriess, M., & Kalender, W. A. (2005). Reconstruction from truncated projections in CT using adaptive detruncation. *European Radiology*, 15(5), 1008–1014. doi: 10.1007/s00330-004-2621-9 Cited on page 113.
- Sukovic, P., & Clinthorne, N. H. (2001). A method for extending the dynamic range of flat panel imagers for use in cone beam computed tomography. In

- Nuclear science symposium conference record, 2001 ieee* (Vol. 3, pp. 1647–1651). Cited on page 62.
- Taguchi, K., Xu, J., Srivastava, S., Tsui, B. M. W., Cammin, J., & Tang, Q. (2011). Interior region-of-interest reconstruction using a small, nearly piecewise constant subregion. *Medical Physics*, 38(3), 1307–1312. doi: 10.1118/1.3549763 Cited on page 115.
- Tang, S., Yang, Y., & Tang, X. (2012). Practical interior tomography with radial Hilbert filtering and a priori knowledge in a small round area. *Journal of X-Ray Science and Technology*, 20(4), 405–422. doi: 10.3233/XST-2012-00348 Cited on page 115.
- Tuy, H. K. (1983). An inversion formula for cone-beam reconstruction. *SIAM Journal on Applied Mathematics*, 43(3), 546–552. Cited on pages 39 and 49.
- Ueda, R., Nemoto, T., & Kudo, H. (2017). Practical interior tomography with small region piecewise model prior. In *Spie medical imaging* (Vol. 10132, p. 101320P). International Society for Optics and Photonics. doi: 10.1117/12.2255706 Cited on page 115.
- US Food and Drug Administration. (2017). *What are the radiation risks from ct?* Retrieved from <https://www.fda.gov/Radiation-EmittingProducts/RadiationEmittingProductsandProcedures/MedicalImaging/MedicalX-Rays/ucm115329.htm> (Retrieved June 10, 2018) Cited on page 8.
- Wang, G., & Yu, H. (2013). The meaning of interior tomography. *Physics in Medicine and Biology*, 58(16), R161–R186. Cited on pages 112 and 122.
- Ward, J. P., Lee, M., Ye, J. C., & Unser, M. (2015). Interior tomography using 1D generalized total variation. Part I: Mathematical foundation. *SIAM Journal on Imaging Sciences*, 8(1), 226–247. Cited on page 115.
- Wible, B. C. (2017). *Interventional procedures*. Elsevier Health Sciences. Cited on pages 1, 6, 7, and 157.
- Wiegert, J. (2007). *Scattered radiation in cone-beam computed tomography: analysis, quantification and compensation* (Unpublished doctoral dissertation). PhD Thesis, Rheinisch-Westfälischen Technischen Hochschule Aachen, Aachen. Cited on page 49.
- Wrigley, C. J., Hancock, B. R., Newton, K. W., & Cunningham, T. J. (2014). *Mixed linear/square-root encoded single slope ramp provides a fast, low noise analog to digital converter with very high linearity for focal plane arrays*. Google Patents. (US Patent 8,624,769) Cited on page 57.
- Xia, D., Chang, Y.-B., Manak, J., Siddiqui, A. H., Zhang, Z., Chen, B., . . . Pan, X. (2018). Reduction of angularly-varying-data truncation in c-arm cbct imaging. *Sensing and Imaging*, 19(1), 14. Cited on page 115.
- Xia, D., Cho, S., Bian, J., Zou, Y., Sidky, E. Y., Zuo, N., & Pan, X. (2007). 3d roi-image reconstruction from cone-beam data. *Nuclear Instruments and Methods in Physics Research Section A: Accelerators, Spectrometers, Detectors and Associated Equipment*, 580(2), 866–875. Cited on page 80.
- Xia, Y. (2016). *Region-of-interest imaging with c-arm computed tomography* (Unpublished doctoral dissertation). Friedrich-Alexander-Universität Erlangen-Nürnberg (FAU). Cited on pages 112 and 115.

- Xia, Y., Bauer, S., Maier, a., Berger, M., & Hornegger, J. (2015a). Patient-bounded extrapolation using low-dose priors for volume-of-interest imaging in C-arm CT. *Medical Physics*, *42*(4), 1787–1796. doi: 10.1118/1.4914135 Cited on page [117](#).
- Xia, Y., Bauer, S., Maier, A., Berger, M., & Hornegger, J. (2015b). Patient-bounded extrapolation using low-dose priors for volume-of-interest imaging in c-arm ct. *Medical Physics*, *42*(4), 1787–1796. Cited on page [140](#).
- Xia, Y., Hofmann, H., Dennerlein, F., Mueller, K., Schwemmer, C., Bauer, S., ... Maier, A. (2014). Towards clinical application of a laplace operator-based region of interest reconstruction algorithm in c-Arm Ct. *IEEE Transactions on Medical Imaging*, *33*(3), 593–606. doi: 10.1109/TMI.2013.2291622 Cited on page [115](#).
- Xu, J., Sisniega, A., Zbijewski, W., Dang, H., Stayman, J., Wang, X., ... Siewerdsen, J. (2016a). Design and characterization of a dedicated cone-beam CT scanner for detection of acute intracranial hemorrhage. In *Spie medical imaging* (pp. 97830T–97830T). Cited on page [58](#).
- Xu, J., Sisniega, A., Zbijewski, W., Dang, H., Stayman, J. W., Wang, X., ... Siewerdsen, J. H. (2016b). Evaluation of detector readout gain mode and bowtie filters for cone-beam ct imaging of the head. *Physics in Medicine and Biology*, *61*(16), 5973. Cited on page [62](#).
- Xu, Q., Mou, X., Wang, G., Sieren, J., Hoffman, E. A., & Yu, H. (2011). Statistical interior tomography. *IEEE Transactions on Medical Imaging*, *30*(5), 1116–1128. doi: 10.1109/TMI.2011.2106161 Cited on page [115](#).
- Yang, Q., Tong, X., Schieb, L., Vaughan, A., Gillespie, C., Wiltz, J. L., ... others (2017). Vital signs: Recent trends in stroke death rates-united states, 2000-2015. *MMWR. Morbidity and mortality weekly report*, *66*(35), 933–939. Cited on page [3](#).
- Ye, Y., Yu, H., Wei, Y., & Wang, G. (2007). A general local reconstruction approach based on a truncated hilbert transform. *Journal of Biomedical Imaging*, *2007*(1), 2–2. Cited on pages [79](#) and [115](#).
- Ye, Y., Zhao, S., Yu, H., & Wang, G. (2005). A general exact reconstruction for cone-beam ct via backprojection-filtration. *IEEE Transactions on Medical Imaging*, *24*(9), 1190–1198. Cited on page [80](#).
- Yoo, S., & Yin, F.-F. (2006). Dosimetric feasibility of cone-beam CT-based treatment planning compared to CT-based treatment planning. *International Journal of Radiation Oncology, Biology, Physics*, *66*(5), 1553–1561. Cited on page [116](#).
- You, J., & Zeng, G. L. (2006). Explicit finite inverse hilbert transforms. *Inverse Problems*, *22*(3), L7. Cited on pages [79](#) and [125](#).
- Yu, H., & Wang, G. (2009). Compressed sensing based interior tomography. *Physics in Medicine and Biology*, *54*(9), 2791. doi: 10.1088/0031-9155/54/9/014 Cited on page [115](#).
- Yu, H., Ye, Y., Zhao, S., & Wang, G. (2006). Local ROI reconstruction via generalized FBP and BPF algorithms along more flexible curves. *International Journal of Biomedical Imaging*, *2006*, 1–7. doi: 10.1155/IJBI/2006/14989 Cited on page [116](#).

- Yu, L., Zou, Y., Sidky, E. Y., Pelizzari, C. A., Munro, P., & Pan, X. (2006). Region of interest reconstruction from truncated data in circular cone-beam CT. *IEEE Transactions on Medical Imaging*, *25*(7), 869–881. doi: 10.1109/TMI.2006.872329 Cited on pages [80](#) and [113](#).
- Zaidat, O. O., Castonguay, A. C., Nogueira, R. G., Haussen, D. C., English, J. D., Satti, S. R., ... others (2018). TREVO stent-retriever mechanical thrombectomy for acute ischemic stroke secondary to large vessel occlusion registry. *Journal of neurointerventional surgery*, neurintsurg–2017. Cited on page [3](#).
- Zamyatin, A. a., Silver, M. D., & Nakanishi, S. (2006). Extension of the reconstruction field-of-view using sinogram decomposition. *Medical Imaging*, *6142*(2007), 614220–614220–8. doi: 10.1117/12.653880 Cited on page [113](#).
- Zellerhoff, M., Scholz, B., Ruehrnschopf, E.-P., & Brunner, T. (2005). Low contrast 3d reconstruction from c-arm data. In *Medical imaging* (pp. 646–655). Cited on pages [62](#) and [113](#).
- Zeng, G. L. (2010). *Medical image reconstruction: a conceptual tutorial*. Springer. Cited on page [17](#).
- Zeng, G. L. (2015). Revisit of the ramp filter. *IEEE Transactions on Nuclear Science*, *62*(1), 131. Cited on page [65](#).
- Zeng, G. L., You, J., Huang, Q., & Gullberg, G. T. (2007). Two finite inverse hilbert transform formulae for region-of-interest tomography. *International journal of imaging systems and technology*, *17*(4), 219–223. Cited on page [79](#).
- Zhang, B., & Zeng, G. L. (2007). Two-dimensional iterative region-of-interest (ROI) reconstruction from truncated projection data. *Medical Physics*, *34*(3), 935–944. doi: 10.1118/1.2436969 Cited on page [115](#).
- Zhang, G., Marshall, N., Jacobs, R., Liu, Q., & Bosmans, H. (2013, 05). Bowtie filtration for dedicated cone beam CT of the head and neck: A simulation study. , *86*. Cited on pages [47](#) and [116](#).
- Zhang, H., Li, L., Yan, B., Wang, L., Cai, A., & Hu, G. (2016). A two-step filtering-based iterative image reconstruction method for interior tomography. *Journal of X-Ray Science and Technology*, *24*(5), 733–747. doi: 10.3233/XST-160584 Cited on page [115](#).
- Zhang, Z., Kusnoto, B., Han, X., Sidky, E., & Pan, X. (2015). Volume-of-interest reconstruction from severely truncated data in dental cone-beam ct. In *Medical imaging 2015: Physics of medical imaging* (Vol. 9412, p. 94124M). Cited on page [115](#).
- Zhao, S., Yu, H., & Wang, G. (2005). A unified framework for exact cone-beam reconstruction formulas. *Medical physics*, *32*(6), 1712–1721. Cited on page [80](#).
- Zhao, W., & Siewerdsen, J. (2014). Acquisition of projection images. In C. C. Shaw (Ed.), *Cone-beam computed tomography* (p. 9-19). Taylor & Francis. Cited on pages [29](#) and [32](#).
- Zhuang, T., & Chen, G.-H. (2006). New families of exact fan-beam and cone-beam image reconstruction formulae via filtering the backprojection image of differentiated projection data along singly measured lines. *Inverse Prob-*

- lems*, 22(3), 991. Cited on page 80.
- Zhuang, T., Leng, S., Nett, B. E., & Chen, G.-H. (2004). Fan-beam and cone-beam image reconstruction via filtering the backprojection image of differentiated projection data. *Physics in Medicine and Biology*, 49(24), 5489. Cited on pages 79 and 113.
- Ziegler, A., Nielsen, T., & Grass, M. (2008). Iterative reconstruction of a region of interest for transmission tomography. *Medical physics*, 35(4), 1317–1327. Cited on page 115.
- Zivelonghi, C., & Tamburin, S. (2018). Mechanical thrombectomy for acute ischemic stroke: the therapeutic window is larger but still “time is brain”. *Functional neurology*, 33(1), 5. Cited on page 4.
- Zou, Y., & Pan, X. (2004a). Exact image reconstruction on pi-lines from minimum data in helical cone-beam ct. *Physics in Medicine and Biology*, 49(6), 941. Cited on page 79.
- Zou, Y., & Pan, X. (2004b). An extended data function and its generalized backprojection for image reconstruction in helical cone-beam ct. *Physics in Medicine and Biology*, 49(22), N383. Cited on page 79.
- Zou, Y., Pan, X., & Sidky, E. Y. (2005). Theory and algorithms for image reconstruction on chords and within regions of interest. *JOSA A*, 22(11), 2372–2384. Cited on pages 79 and 140.

Dual-rotation C-arm cone-beam tomographic acquisition and reconstruction frameworks for low-contrast detection in brain soft-tissue imaging

Aymeric RESHEF

RESUME : L'arceau interventionnel est un système d'imagerie rayons X temps réel. Il dispose d'une option tomographique qui, grâce à une rotation de l'arceau autour du patient, permet d'acquérir des images en coupes dont la résolution en contraste est plus faible que celle des tomodensitomètres diagnostiques, rendant l'information clinique des tissus mous du cerveau inexploitable. Nous proposons un nouveau mode d'acquisition et de reconstruction tomographiques sur arceau interventionnel pour l'amélioration de la détection des faibles contrastes en imagerie interventionnelle des tissus mous de la tête. Afin d'émuler un filtre « bow-tie » (en nœud papillon), une double acquisition est envisagée. Les spécificités de la double acquisition imposent la conception d'un algorithme de reconstruction itérative dédié, incluant le filtre rampe dans l'énergie de minimisation. En bifurquant des approches par rétro-projection filtrée vers celles par filtration des rétro-projections, une méthode de reconstruction directe, alternative à la précédente, est proposée pour les acquisitions doubles. Pour une acquisition simple, la méthode est assurée de faire aussi bien que l'algorithme de rétro-projection filtrée quel que soit l'échantillonnage angulaire en géométrie planaire, et offre une approximation alternative à l'algorithme de Feldkamp-Davis-Kress en géométrie conique. Nous montrons qu'avec peu ou pas de modifications aux schémas précédents, les deux méthodes de reconstruction (itérative et directe) s'adaptent bien à la reconstruction de régions d'intérêt, à laquelle l'acquisition double reste étroitement liée à travers son acquisition tronquée.

MOTS-CLEFS : filtre « bow-tie », imagerie du cerveau, tomographie, reconstruction, rétro-projection, détection des faibles contrastes, région d'intérêt

ABSTRACT : Interventional C-arm systems are real-time X-ray imaging systems, that can perform tomographic acquisitions by rotating the C-arm around the patient; however, C-arm cone-beam computed tomography (CBCT) achieves a lower contrast resolution than diagnostic CT, which is necessary in order to benefit from the clinical information of soft tissues in the brain. We propose a new C-arm CBCT acquisition and reconstruction framework to increase low-contrast detection in brain soft-tissue imaging. In order to emulate a bow-tie filter, a dual-rotation acquisition is proposed. To account for all the specificities of the dual-rotation acquisition, a dedicated iterative reconstruction algorithm is designed, that includes the ramp filter in the cost function. By switching from filtered backprojection (FBP) to backprojection-filtration (BPF) reconstruction methods, we propose an alternative, direct reconstruction method for dual-rotation acquisitions. For single-rotation acquisitions, the method ensures to perform as good as FBP with arbitrarily coarse angular sampling in planar geometries, and provides a different approximation from the Feldkamp-Davis-Kress (FDK) algorithm in the cone-beam geometry. Although we used it to emulate a virtual bow-tie, our dual-rotation acquisition framework is intrinsically related to region-of-interest (ROI) imaging through the truncated acquisition. With few or no modification of the proposed reconstruction methods, we successfully addressed the problem of ROI imaging in the context of dual-rotation acquisitions.

KEY-WORDS : bow-tie filter, brain imaging, tomography, reconstruction, backprojection-filtration, low-contrast detection, region-of-interest

